

# **Planetary Materials Studied by Time-Resolved X-ray Diffraction under Compression in Dynamic Diamond Anvil Cells**

## **DISSERTATION**

zur Erlangung des akademischen Grades einer Doktorin  
der Naturwissenschaften (Dr. rer. nat.)  
in der Bayreuther Graduiertenschule für  
Mathematik und Naturwissenschaften (BayNAT)  
der Universität Bayreuth

vorgelegt von

**Alba San José Méndez**

aus Fuenlabrada (Madrid)

Hamburg, 2020



This doctoral thesis was prepared partly at the Deutsches Elektronen Synchrotron in Hamburg and at the Bavarian Research Institute of Experimental Geochemistry and Geophysics (BGI) at the University of Bayreuth from June 2017 until November 2020 and was supervised by Prof. Dr. Hauke Marquardt and co-supervised by Dr. Hanns-Peter Liermann.

This is a full reprint of the thesis submitted to obtain the academic degree of Doctor of Natural Sciences (Dr. rer. nat.) and approved by Bayreuth Graduate School of Mathematical and Natural Sciences (bayNAT) of the University of Bayreuth.

Date of submission: 20 Nov. 2020

Date of defense: 18 Dec. 2020

Acting director: Prof. Dr. Markus Lippitz

Doctoral committee:

Prof. Dr. Daniel Frost	(Reviewer)
Prof. Dr. Hauke Marquardt	(Reviewer)
PD Dr. Catherine McCammon	(Chairwoman)
Prof. Dr. Leonid Dubrovinsky	(Reviewer)





**Planetary Materials Studied by  
Time-Resolved X-ray Diffraction under  
Compression in Dynamic Diamond Anvil Cells**

Alba San José Méndez



*To Luis, María Josefa and Marina*





# Abstract

Investigating the physical properties of minerals at extreme pressures and temperatures is crucial for understanding the interior structure of planetary bodies and unravelling their formation and evolution. Earth's interior is characterized by hosting an iron-rich core enveloped by a mantle with a composition dominated by  $\text{MgSiO}_3$  and  $(\text{Mg,Fe})\text{O}$ . One of the aspects that make Earth different from other terrestrial bodies in our Solar System is the presence of liquid  $\text{H}_2\text{O}$ . Out of the Solar System, Earth-like exoplanets have caught attention as their composition might be analogous to Earth. Depending on the materials available during their formation, Earth-like exoplanets could have accumulated larger amounts of  $\text{H}_2\text{O}$  as compared to Earth (ocean planets). Current models for ocean planets assume an interior structure analogous to Earth, with an additional layer overlying the silicate mantle: an icy mantle of high-pressure ice VII/ice X at the bottom of a liquid ocean. Experimental data on the phase diagram and physical properties of these candidate mantle minerals at high-pressure/-temperature are essential to constrain current planetary interior models.

Here, a novel experimental approach was implemented to investigate the compression behavior of planetary materials at extreme conditions. A piezo-driven dynamic Diamond Anvil Cell (dDAC) was employed to generate high pressures. Time-resolved X-ray diffraction was used to characterize the evolution of unit cell volumes ( $V$ ) with pressure ( $P$ ). The combination of the dDAC with extremely sensitive X-ray detectors allowed for the collection of diffraction images with high temporal resolution while the sample is being compressed. The uniquely dense sampling of pressure and volume in our data allowed to directly determine changes in the bulk modulus by local differentiation of  $V(P)$  without having to rely on an equation-of-state formulation. A resistively-heated dDAC (RHdDAC) was implemented for conducting experiments at simultaneous high- $P/T$ . Using this approach, the compression behavior of two planetary materials,  $\text{H}_2\text{O}$  ice and  $(\text{Mg,Fe})\text{O}$  ferropericlase, was investigated in this thesis.

$\text{H}_2\text{O}$  crystallizes as ice VII at a pressure of about 2 GPa, a molecular solid characterized by a body centered cubic ( $bcc$ ) arrangement of oxygens. Increasing pressure triggers the dissociation of  $\text{H}_2\text{O}$  molecules towards the formation of ice X, an atomic solid also presenting a  $bcc$  crystal lattice. The ice VII – ice X transition proceeds through the symmetrization of the hydrogen-bonds and the formation of intermediate stages without a change in crystallographic symmetry. The continuous nature of this transformation makes its characterization very complicated and no consensus on the transition pressure range has emerged in the literature. Moreover, only a few studies have measured the compression behavior of  $\text{H}_2\text{O}$  across the ice VII – ice X transition, and whether or not the H-bond symmetrization has any effect remains unclear.

Here, the ice VII – ice X transition was studied in the dDAC up to pressures of about 180 GPa while collecting time-resolved X-ray diffraction. The bulk modulus of H<sub>2</sub>O ice was directly derived from quasi-continuous  $V(P)$  data showing three changes in compression behavior in the ranges of 35-45, 50-55 and 90-110 GPa. The observed changes are in perfect agreement with previous computational results, showing that the H-bond symmetrization influences the high-pressure compressibility of H<sub>2</sub>O. Preliminary high-temperature data were collected in the RHdDAC across the ice VII –ice X transition, covering a large portion of the phase diagram, to show the potential of the RHdDAC to study thermal effects on the compression behavior of H<sub>2</sub>O ice.

(Mg,Fe)O ferropericlase undergoes changes in compression behavior as a consequence of a change in the spin state of iron at high pressure. The iron spin crossover is a gradual transformation accompanied by an elastic softening of the bulk modulus of ferropericlase starting at 40 GPa at room temperature. Several experimental and computational studies have shown that the pressure range over which the spin crossover occurs and the magnitude of the elastic softening are sensitive to iron content and stress conditions. However, the reported transition ranges differ considerably. Furthermore, although it has been suggested that iron-iron interactions may cause a broadening of the transition pressure range, these effects have not been investigated.

Here, the compression behavior (Mg,Fe)O was investigated in the dDAC up to pressures of about 100 GPa while collecting time-resolved X-ray diffraction. Complementary ab-initio calculations were performed to investigate the effect of iron-iron interactions on the elastic softening across the spin crossover. Both experiments and computations are in perfect agreement, showing a broad and asymmetric softening of the bulk modulus of (Mg,Fe)O at pressures between about 40 and 80 GPa, with possible implications for the seismic signature of the spin crossover in the lower mantle. First high- $T$  data were collected in the RHdDAC up to temperatures of 1400 K showing the potential of the RHdDAC to explore thermal effects on the compression behavior of (Mg,Fe)O at high pressure.

## **Zusammenfassung**

Die Untersuchung der physikalischen Eigenschaften von Mineralien unter extremen Drücken und Temperaturen ist grundlegend für das Verständnis der inneren Struktur von planetaren Körpern, ihrer Entstehung und Evolution. Das Erdinnere ist charakterisiert durch einen eisenreichen Kern umgeben von einem Mantel, dessen Zusammensetzung vor allem durch MgSiO<sub>3</sub> und (Mg,Fe)O bestimmt wird. Einer der Aspekte, der die Erde von anderen Himmelskörpern unseres Sonnensystems unterscheidet, ist das Vorhandensein von flüssigem

H<sub>2</sub>O. Außerhalb des Sonnensystems haben erdähnliche Exoplaneten unser Interesse geweckt, da ihre Zusammensetzung der Erde ähnlich sein könnten. Abhängig von den Materialien, die während ihrer Entstehung zur Verfügung standen, könnten erdähnliche Exoplaneten größere Mengen Wasser akkumuliert haben (Ozeanplaneten). Aktuelle Modelle für Ozeanplaneten nehmen eine innere Struktur analog der der Erde an mit einer zusätzlichen Schicht oberhalb des Silikatmantels: ein Eismantel aus Hochdruck Eis VII/Eis X am Grunde des flüssigen Ozeans. Experimentelle Daten des Phasendiagramms und der physikalischen Eigenschaften der möglichen Mineralkandidaten dieses Mantels unter hohen Drücken/Temperaturen sind unabdingbar, um die derzeitigen Planetenmodelle zu verbessern.

In dieser Arbeit wurde eine neue, experimentelle Herangehensweise umgesetzt, um das Kompressionsverhalten planetarer Materialien unter extremen Bedingungen zu untersuchen. Eine piezo-getriebene dynamische Diamantstempelzelle (dynamic diamond anvil cell; dDAC) wurde eingesetzt, um hohe Drücke zu erreichen. Zeitaufgelöste Röntgendiffraktion wurde verwendet, um die Entwicklung des Einheitszellenvolumens (V) und des Drucks (P) zu charakterisieren. Die Kombination aus dDAC und hochempfindlichen Röntgendetektoren erlaubte es, Diffraktionsbilder mit hoher zeitlicher Auflösung während der Kompression aufzunehmen. Diese einmalig hohe Dichte an Messpunkten erlaubte es, die Änderungen des Kompressionsmoduls direkt aus der lokalen Ableitung von V(P) zu bestimmen ohne dafür auf eine Zustandsgleichung zurückgreifen zu müssen. Eine widerstandsgeheizte dDAC (RHdDAC) wurde eingesetzt, um Experimente mit hohem Druck und Temperatur parallel durchzuführen. Mit dieser Herangehensweise wurde das Kompressionsverhalten von zwei Mineralien, H<sub>2</sub>O Eis und (Mg,Fe)O Ferroperiklas, in dieser Arbeit untersucht.

Wasser kristallisiert bei Drücken von etwa 2 GPa als Eis VII, einem Molekülkristall bestimmt durch eine kubisch raumzentrierte Anordnung des Sauerstoffs. Eine Erhöhung des Drucks bedingt die Dissoziation der H<sub>2</sub>O Moleküle und Entstehung von Eis X, einem Ionenkristall ebenfalls mit kubisch raumzentriertem Gitter. Die Eis VII – Eis X Umwandlung geschieht durch die Symmetrisierung der Wasserstoffbindungen und Bildung von Intermediaten ohne einer Änderung der kristallographischen Symmetrie. Der kontinuierliche Charakter dieser Transformation macht die Bestimmung äußerst kompliziert und bisher gibt es in der Literatur keinen Konsens über den Druckbereich, in welchem die Umwandlung stattfindet. Darüber hinaus haben nur wenige Studien das Kompressionsverhalten von H<sub>2</sub>O über den Übergang von Eis VII zu Eis X hinweg untersucht. Ob die Symmetrisierung der H-Bindungen einen Einfluss hat, ist weiterhin unklar. Hier wurde der Eis VII – Eis X Übergang in einer dDAC bis zu Drücken von 180 GPa unter kontinuierlicher Aufnahme von Röntgendiffraktogrammen untersucht. Das Kompressionsmodul von H<sub>2</sub>O Eis wurde direkt aus den quasi-kontinuierlichen V(P) Daten abgeleitet und zeigt drei Phasen des Kompressionsverhaltens in den Druckbereichen 35-45, 50-

55 und 90-110 GPa. Die beobachteten Veränderungen sind in perfekter Übereinstimmung mit vorhergehenden Berechnungen und zeigen, dass die H-Bindungssymmetrisierung einen Einfluss auf die Hochdruck-Kompressibilität von H<sub>2</sub>O hat. Hochtemperaturdaten wurden in einer RHdDAC über den Eis VII – Eis X Übergang aufgenommen und decken einen großen Teil des Phasendiagramms ab. Diese Daten zeigen das Potential der RHdDAC für Studien thermischer Effekte auf das Kompressionsverhalten von H<sub>2</sub>O mit Relevanz für das Innere von Planeten.

(Mg,Fe)O Ferroperiklas durchläuft Veränderungen im Kompressionsverhalten als Konsequenz aus der Änderung des Spinzustandes des Eisens bei hohen Drücken. Der Übergang des Spins ist eine graduelle Transformation begleitet von elastischer Erweichung des Kompressionsmoduls von Ferroperiklas ab 40 GPa bei Raumtemperatur. Verschiede experimentelle und rechnergestützte Studien haben gezeigt, dass der Druckbereich, in dem der Spinübergang stattfindet, und der Grad der elastischen Erweichung vom Eisengehalt und den Druckbedingungen abhängen. Allerdings weichen die veröffentlichten Übergangsbereiche stark voneinander ab. Obwohl vermutet wurde, dass die Eisen-Eisen Wechselwirkungen der Ursprung der Verbreiterung des Übergangsdruckbereichs sind, wurden diese Effekte bisher nicht untersucht.

Hier wurde das Kompressionsverhalten von (Fe,Mg)O in einer dDAC bis zu Drücken von etwa 100 GPa unter kontinuierlicher Aufnahme von Röntgendiffraktogrammen untersucht. Ergänzende ab-initio Berechnungen wurden durchgeführt, um den Effekt der Eisen-Eisen Wechselwirkung auf die elastische Erweichung während des Spinübergangs zu untersuchen. Die rechnergestützten Ergebnisse basieren auf mehreren Modellen mit zufälliger Anordnung des Eisens und nehmen eine reguläre Lösung für *high* und *low* Spins an. Experimente und Berechnungen sind in hervorragender Übereinstimmung und zeigen eine breite und asymmetrische Erweichung des Kompressionsmoduls von (Fe,Mg)O bei Drücken zwischen ca. 40 und 80 GPa. Dies hat möglicherweise Implikationen für die seismische Signatur des Spinübergangs im unteren Mantel. Hochtemperatur Daten aufgenommen in einer RHdDAC bei Temperaturen bis zu 1400 K zeigen das Potential der RHdDAC zur Untersuchung thermischer Effekte auf die Kompressibilität von (Fe,Mg)O bei hohen Temperaturen.

# Acknowledgements

In the first place, I would like to thank my supervisors, Prof. Dr. Hauke Marquardt (University of Oxford and Bayerisches Geoinstitut, BGI) and Dr. Hanns-Peter Liermann (Extreme Conditions Beamline, DESY), for giving me the opportunity to be part of an exceptional scientific network where, with their advice and guidance, I have enjoyed and grown as an independent researcher in a highly creative and innovative scientific environment. I thank Dr. Konstatin Glazyrin (DESY), Dr. Anna Pakhomova (DESY) and Dr. Rachel J. Husband (DESY) for their willingness and tireless efforts to support me on beamtime preparations, long night-shifts and for fruitful coffee-break discussions. I further thank Iris Schwark (DESY) for all the time spent on the design, test and improvements of the resistively-heated dynamic DAC (*“the monster”*). I also thank Mario Wendt (DESY) and Sergej Wenz (DESY) for materializing scientific concepts and always approaching me with a smile. I appreciate the help of Dr. Maxim Bykov (Carnegie Institution for Science) with the scanning electron microscope. I would like to thank Christoph Otzen (University of Jena), Dr. Alexander Schökel (DESY) and Dr. Nico Giordano (DESY) for their scientific support and friendship. I thank Dr. Alexander Kurnosov (BGI), Dr. Niccolò Satta (University of Oxford), Dr. Johannes Buchen (California Institute of Technology), Dr. Kirsten Schulze (BGI) and Dr. Julia Immoor (BGI) for their selfless support in preparing cells and performing experiments during long beamtimes. I would also like to thank Dr. Florian Trybel (University of Linköping) and Prof. Dr. Gerd Steinle-Neumann (BGI) for their original and fundamental contributions to the present study. I further thank Dr. Martin French (University of Rostock) for sharing his computational results. I would like to express my sincere appreciation to the whole FS-PETRA-D PETRA III (DESY) and BGI staff for their dedication and professionalism.

I thank my parents, Luis and María Josefa, my sister, Marina, my entire family in Spain, family Hein in Hamburg, and my friends for their unconditional love and support.



# Contents

<b>1 Introduction</b>	<b>1</b>
1.1 Ice VII and X .....	3
1.2 Ferropericlase .....	5
1.3 Bulk modulus.....	6
1.4 Goals of this work .....	7
<b>2 Experimental Methods</b>	<b>9</b>
2.1 Diamond Anvil Cells.....	9
2.1.1 DAC assembly .....	10
2.2 The piezo-driven dynamic DAC .....	12
2.3 The Resistively-Heated dynamic DAC.....	13
2.3.1 Temperature calibration of the thermocouples in the RHdDAC.....	15
2.4 Powder X-ray diffraction .....	16
2.4.1 Time-Resolved X-Ray Diffraction at the ECB .....	17
2.4.2 dDAC data integration and analysis .....	18
2.4.3 Challenges in dDAC data analysis .....	19
2.5 Bulk modulus calculation .....	21
<b>3 Synopsis</b>	<b>23</b>
3.1 Compression behavior of H <sub>2</sub> O across the ice VII –ice X transition .....	25
3.2 Compression behavior of ferropericlase across the spin crossover.....	31
3.3 A Resistively-Heated dynamic Diamond Anvil Cell .....	35
3.4 Outlook.....	39
<b>References</b>	<b>41</b>

<b>4 Bulk modulus of H<sub>2</sub>O across the ice VII – ice X transition measured by time-resolved X-ray diffraction in dynamic Diamond Anvil Cell experiments</b>	<b>51</b>
4.1 INTRODUCTION .....	51
4.2 METHODS.....	53
4.3 RESULTS AND DISCUSSION.....	57
4.4 CONCLUSIONS.....	61
References.....	61
Supplemental Material.....	65
<b>5 Elastic softening of ferropericlase across the iron spin crossover constrained by time-resolved XRD experiments and computations</b>	<b>69</b>
5.1 INTRODUCTION .....	70
5.2 MATERIALS AND METHODS.....	72
5.3 RESULTS AND DISCUSSION.....	78
5.4 CONCLUSIONS.....	85
References.....	85
Supplemental Material.....	91
<b>6 A resistively-heated dynamic diamond anvil cell (RHdDAC) for fast compression X-ray diffraction experiments at high temperatures</b>	<b>121</b>
6.1 INTRODUCTION .....	122
6.2 THE HIGH-TEMPERATURE DYNAMIC DIAMOND ANVIL CELL.....	123
6.3 EXPERIMENTAL METHOD.....	126
6.4 PERFORMANCE AND APPLICATION .....	128
6.5 CONCLUSIONS.....	132
References.....	133

# Figures

1.1	Interior model of an Earth-like exoplanet and an ocean exoplanet.....	2
1.2	Predicted $P$ - $T$ conditions for the interior of ocean-planets .....	3
1.3	Evolution of the energy potential across the hydrogen-bond symmetrization.....	4
1.4	Scheme of the spin crossover orbital splitting.....	6
2.1	Schematic drawing showing the components of a diamond anvil cell (DAC).....	10
2.2	An amorphous gasket insert.....	11
2.3	A dynamic diamond anvil cell (dDAC).....	13
2.4	Schematics of the experimental setup for dDAC experiments at the beamline.....	13
2.5	A DAC equipped with a resistive-heating system .....	14
2.6	A vacuum vessel for the resistive-heated dDAC (RHdDAC) .....	15
2.7	Thermal expansion of Au measured in the RHdDAC.....	16
2.8	The dDAC and the LAMBDA detectors in the experimental hutch at the beamline.....	18
2.9	Integrated diffraction pattern for H <sub>2</sub> O at 26 GPa in the dDAC.....	19
2.10	Peak profile fitting of integrated patterns collected from a dDAC experiment on H <sub>2</sub> O.....	20
2.11	Bulk modulus determination from quasi-continuous $V(P)$ data collected in the dDAC.....	22
3.1	$V(P)$ data for H <sub>2</sub> O across the ice VII - ice X transition.....	27
3.2	Bulk modulus $K_T(P)$ of H <sub>2</sub> O across the ice VII – ice X transition as a function of pressure ...	28
3.3	Bulk modulus $K_T(P)$ of (Mg,Fe)O ferropericlase across the iron spin crossover .....	33
3.4	Explored $P$ - $T$ conditions across the H <sub>2</sub> O phase diagram in the RHdDAC.....	36
3.5	$P$ -oscillations on (Mg,Fe)O ferropericlase at 125 GPa and 1400 K.....	37
4.1	Contour plot of H <sub>2</sub> O diffraction patterns in the dDAC.....	54
4.2	Integrated diffraction pattern of H <sub>2</sub> O in the dDAC.....	55
4.3	Integrated diffraction patterns of H <sub>2</sub> O after application of the IRR filter .....	56
4.4	$V(P)$ data for H <sub>2</sub> O ice in comparison with previous reported data.....	58
4.5	Bulk modulus of H <sub>2</sub> O ice in comparison with previous reported data.....	60
4.6	Bulk modulus of H <sub>2</sub> O ice before and after application of spline+smoothing.....	67
4.7	Bulk modulus of H <sub>2</sub> O ice as derived from three different dDAC experiments .....	67

5.1	A typical integrated diffraction pattern and a contour plot for (Mg,Fe)O .....	73
5.2	Unit cell volumes derived for (Mg,Fe)O by experiments and computations .....	79
5.3	Bulk moduli derived for (Mg,Fe)O by experiments and computations .....	80
5.4	Low spin fraction of (Mg,Fe)O as a function of pressure .....	84
5.5	Example of the procedure followed for the calculation of the bulk modulus .....	91
5.6	Effect of the chosen pressure interval on the derived bulk moduli curves.....	92
5.7	Frequency distribution of spin crossover pressure.....	92
5.8	$\Delta H_{LS-HS}$ as a function of pressure .....	93
6.1	A DAC equipped with a resistive-heating system .....	124
6.2	Illustration of the connection of the DAC to the piezoelectric actuator in the RHdDAC.....	125
6.3	RHdDAC connected to the lid of the vacuum vessel.....	126
6.4	An amorphous gasket insert.....	127
6.5	Schematics of the experimental setup for RHdDAC experiments at the beamline .....	128
6.6	Thermal expansion of Au measured in the RHdDAC .....	129
6.7	Explored $P$ - $T$ conditions across the $H_2O$ phase diagram in the RHdDAC.....	130
6.8	$P$ -oscillations on (Mg,Fe)O ferropericlyase at 125 GPa and 1400 K.....	132

## Tables

3.1	Compilation of data points collected in previous static DAC XRD experiments.....	27
4.1	Summary of experimental run conditions .....	53
4.2	Peak fitting results: Le Bail in comparison to the Gaussian approach. ....	66
5.1	Initial atomic coordinates of iron atoms in 64-atom ferropericlyase models.....	94
5.2	Iron arrangement, low-spin fraction at 300K and Fe-Fe radial distribution function for models with an $(Mg_{0.90625}Fe_{0.09375})O$ composition .....	95
5.3	Iron arrangement, low-spin fraction at 300K and Fe-Fe radial distribution function for models with an $(Mg_{0.8125}Fe_{0.1875})O$ composition.....	99
5.4	Iron arrangement for 64-atom (left), and 216-atom (middle) models and low-spin fraction at 300K (right), for models with an $(Mg_{0.90625}Fe_{0.09375})O$ composition .....	103
5.5	Iron arrangement for 64-atom (left), and 216-atom (middle) models and low-spin fraction at 300K (right), for models with an $(Mg_{0.90625}Fe_{0.09375})O$ composition .....	107
5.6	Iron arrangement for 64-atom (left), and 216-atom (middle) models and low-spin fraction at 300K (right), for models with an $(Mg_{0.8125}Fe_{0.1875})O$ composition.....	111
5.7	Iron arrangement for 64-atom (left), and 216-atom (middle) models and low-spin fraction at 300K (right), for models with an $(Mg_{0.8125}Fe_{0.1875})O$ composition.....	115





# Chapter 1

## Introduction

Earth is the largest terrestrial planet in our Solar System and the only planet known to host life. Earth's interior is compositionally divided into different layers with two major portions corresponding to a metallic core enriched in iron and a mantle dominated by silicates and oxides, such as  $\text{MgSiO}_3$  bridgmanite and  $(\text{Mg,Fe})\text{O}$  ferropericlase, respectively (Dziewonski and Anderson 1981; McDonough and Sun 1995). On the surface, Earth's atmosphere and temperature allowed the retention of liquid  $\text{H}_2\text{O}$ , indispensable for the development of life. Besides the intimate relation between liquid  $\text{H}_2\text{O}$  and life,  $\text{H}_2\text{O}$  may also play a fundamental role for the dynamics of Earth's interior (Regenauer-Lieb 2006; Korenaga et al. 2017). The recent discovery of inclusions of  $\text{H}_2\text{O}$  ice VII in diamonds sourced from between 410 and 660 km depth (Tschauner et al. 2018) suggests that  $\text{H}_2\text{O}$  might also be present in Earth's deep mantle where it can form through mineral dehydration reactions (Lin et al. 2005; Schwager and Boehler 2008; Pearson et al. 2014). Beyond Earth,  $\text{H}_2\text{O}$  composes a large portion of the interior of planetary bodies in the outer Solar System and may play an active role for the evolution of the icy Giants, Uranus and Neptune (Fortney and Nettelmann 2010; Redmer et al. 2011), and icy satellites, Europa, Ganymede, Callisto, Titan and Enceladus (Sotin et al. 2007; Fortes and Choukroun 2010; Noack et al. 2016; Journaux et al. 2017). However, the size, composition, low surface temperature and violent radiation environment make these planets very different from Earth. The lack of Earth analogues in our Solar System has pushed astronomy to look for Earth-like exoplanets in distant solar systems. However, astrophysical observables to infer the composition of exoplanets are limited by large interstellar distances. Therefore, the construction of interior structure models for exoplanets is essential for interpreting astrophysical observations and for unraveling the compositional diversity of planetary systems as well as for predicting their long-term evolution. Over the last two decades, more than 4000 planets have been discovered beyond the solar system<sup>1</sup>. Those classified as super-Earths are terrestrial exoplanets presenting masses in the range from 1 to 10  $M_E$ . The first super-Earth planet was discovered by Rivera et al. (2005). Their low masses pose an important challenge for planetary detection techniques. For this reason, only a few dozens of super-Earth exoplanets have been registered to date. Super-Earth planets are of great interest because their conditions, comparable to Earth, make them potentially habitable. Later improvements in automated techniques allowed to rescuing planets from false positive status, as it is the case of Kepler-1649 c, a planet that is 1.06 times the size of Earth orbiting within its host star's habitable zone (Vanderburg et al. 2020).

---

<sup>1</sup> The Extrasolar Planets Encyclopaedia: <http://exoplanet.eu/catalog/>

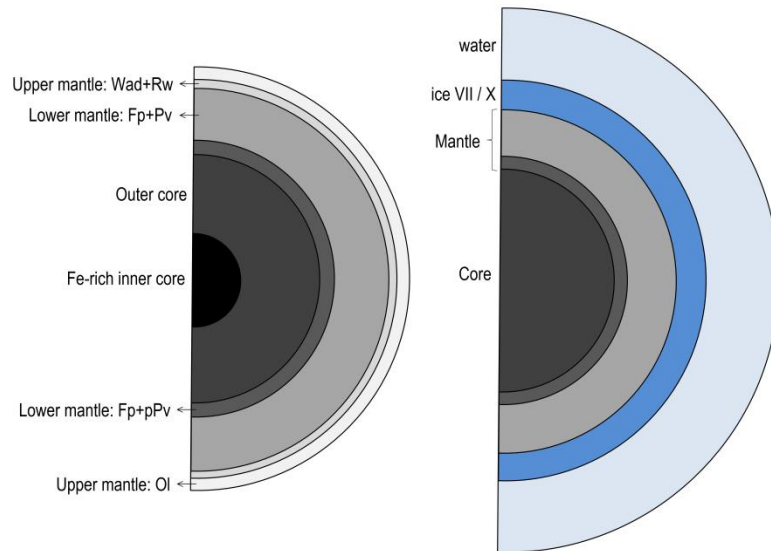


**Figure 1.1:** Interior model of an Earth-like exoplanet (left) and an ocean exoplanet (right, illustrations modified from Valencia et al. 2007). Abbreviations: Ol = olivine, Wad = wadsyelite, Rw = ringwoodite, Fp = ferropericlase, Pv= perovskite, pPV = post-perovskite. The thicknesses of the layers are not to scale. For a given mass, an ocean exoplanet has a smaller core and mantle and a larger radius than an Earth-like planet. In the case of ocean exoplanets, the upper mantle may not exist if the amount of H<sub>2</sub>O is such that the pressure at the ice/mantle interface is larger than that of the transition from Ol → Wad → Rw.

Understanding the composition of super-Earth exoplanets is essential to constrain the bulk parameters, i.e., mass and radius, and to model their interior structure and formation histories. Depending on the material available during their formation, i.e., if they formed inside or outside the snow line<sup>2</sup>, the composition of super-Earths may vary from a purely rocky iron-rich composition to a composition that accommodates large amounts of H<sub>2</sub>O (ocean planets, Léger et al. 2004). The first detailed interior models for super-Earth planets were constructed by Valencia et al. (2006). Later models (Valencia et al. 2006; Sotin et al. 2007) assumed an interior structure and composition analogous to that of the Earth: an upper mantle composed by olivine, a lower mantle made of perovskite and ferropericlase and an iron-rich core that may be divided into an outer liquid layer and an inner liquid layer depending on the temperature profile of the planet (Fig. 1.1). It is predicted that the purely rocky end-member could host a massive core comprising up to 80% of the total planet mass, analogous to Mercury in the Solar System (super-Mercury exoplanet, nomenclature introduced by Valencia et al. 2006). Existing interior models for super-Earths with a H<sub>2</sub>O fraction between 20 and 50% (ocean planets) of the total planet mass accommodate an additional layer overlying the rocky interior (Sotin et al. 2007; Valencia et al. 2007): an icy shell of high-pressure ice VII/ice X at the bottom of a liquid H<sub>2</sub>O shell. The pressure ( $P$ ) and temperature ( $T$ ) conditions in the icy shell as well as its thickness depend on

<sup>2</sup> The snow line in a protoplanetary disk is the distance from the host star at which the low temperatures allow volatile compounds such as H<sub>2</sub>O, NH<sub>3</sub> and CH<sub>4</sub> to crystallize as ice during planet formation (Hayashi 1981).

the water content and planet radius. Sotin et al. (2007) predicted that  $P$ - $T$  conditions in the icy shell of ocean-planets containing 50% mass  $H_2O$  may range from 2-500 GPa in pressure and from 1000-2000 K in temperature, with thicknesses of up to 6000 km (Fig. 1.2). If the pressure conditions at the bottom of the icy shell are above the transition from perovskite to post-perovskite ( $P = 125$  GPa at  $T = 2750$  K; Tsuchiya et al. 2004), the upper mantle would be absent and ferropericlase and post-perovskite the main composing minerals of the silicate mantle. Additionally, due to the low density of the water shells, the radius of an ocean planet would be larger than that of the rocky end-member having the same mass, what makes these planets easier to detect.

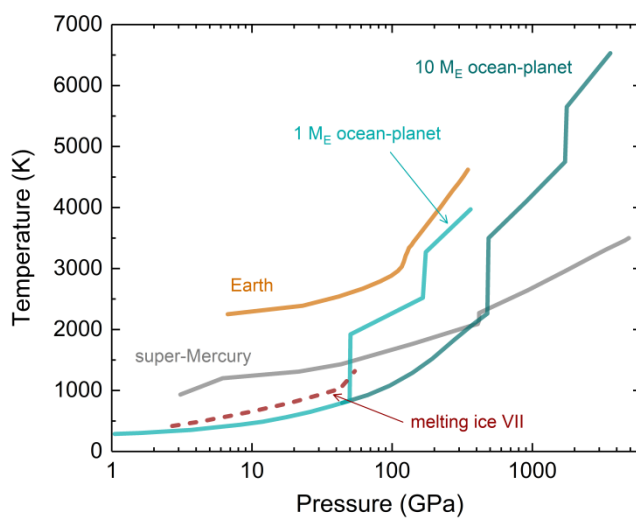


**Figure 1.2:** Predicted  $P$ - $T$  conditions for ocean-planets with 50% mass  $H_2O$  massing 1 and 10  $M_E$  (Sotin et al. 2007) and super-Mercury (Valencia et al. 2007), along with Earth's geotherm. A dashed red line corresponds to the melting curve for ice VII reported in Goncharov et al. (2009).

Considering the above, understanding the physical properties of  $H_2O$  as well as mantle minerals at extreme  $P$ - $T$  conditions is crucial to model the interior of ocean planets and super-Earths. Furthermore, the behavior of  $H_2O$  at extreme  $P$ - $T$  conditions is not only of interest for super-Earths but also relevant to understanding the interior of giant planets and icy satellites in the Solar System.

## 1.1 Ice VII and X

The polymorphs ice VII and ice X dominate the high-pressure phase diagram of  $H_2O$  with broad stability fields ( $P \sim 300$  GPa and  $T \sim 2000$  K) covering  $P$ - $T$  conditions relevant for planetary interiors (Redmer et al. 2011; French et al. 2016). Ice VII (space group  $Pn3m$ ) is a solid characterized by a body centered cubic ( $bcc$ ) arrangement of oxygens, where  $H_2O$  molecules are linked via hydrogen-bonds ( $O-H \cdots O$ ) and randomly oriented with a short-range order imposed by obeying the ice rules (Bernal and Fowler 1933; Pauling 1935; Hobbs et al. 1974; Benoit et al. 1998). Ice VII is stable up to pressures of about 60 GPa at 300 K. Further compression triggers

dissociation of the H<sub>2</sub>O molecules towards the formation of the ionic ice X phase. The ice VII - ice X transition is predicted to proceed through four distinct stages, involving gradual changes in the energy potential for the O-H...O bond with pressure, up to complete symmetrization of hydrogen-bonds (Holzapfel 1972; Benoit et al. 1998, 2002; Benoit and Marx 2005; Lin et al. 2011):

- i. In ice VII ( $P > 2\text{GPa}$ ), the energy potential is double-well shaped with an unimodal proton distribution coinciding with one of the two minima (Fig. 1.3).
- ii. As the O-O distance decreases with increasing pressure, the energy barrier decreases enhancing proton tunneling between the two minima, i.e., *translational* proton disorder. At this stage, the proton distribution is bimodal and the proton is delocalized between the two minima. This stage is associated with a *dynamically disordered* ice VII phase (ice VII').
- iii. As the energy barrier approaches zero with further compression, the energy potential transforms into an effective single-well with an unimodal proton distribution at the center. At this stage, the energy potential is still broad and the proton delocalized. This stage is associated with a *dynamically disordered* ice X phase (ice X').
- iv. Symmetrization of the hydrogen-bonds is complete when the energy potential adopts an effective narrow single-well form, where the proton distribution is localized at the midpoint between two oxygens (O-H-O), forming the static ice X phase.

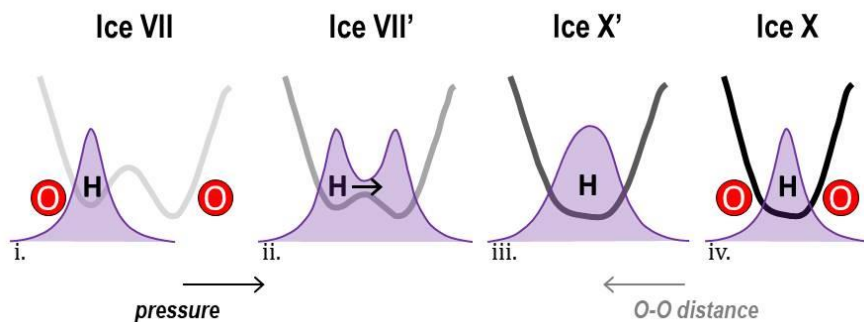


**Figure 1.3:** Evolution of the energy potential across the hydrogen-bond symmetrization, using the prime notation employed by Sugimura et al. (2008) to denote the *dynamically disordered* intermediate states ice VII' and ice X'.

Numerous experimental (Aoki et al. 1996; Goncharov et al. 1996, 2005; Wolanin et al. 1997; Loubeyre et al. 1999; Song et al. 1999, 2003; Zha et al. 2007, 2016; Sugimura et al. 2008; Meier et al. 2018; Guthrie et al. 2019) and computational (Bernasconi et al. 1998; Lin et al. 2011; Lu et al. 2011; French and Redmer 2015; Tsuchiya and Tsuchiya 2017; Hernandez and Caracas 2018) studies have investigated the hydrogen-bond symmetrization of H<sub>2</sub>O ice. The reported transition pressures for the formation of the intermediate *disordered* phases amongst the different studies differ considerably. Moreover, measurements of the bulk modulus of ice across the ice VII – ice X

transition disagree in terms of absolute values of  $K_T$  and a possible influence of the hydrogen-bond symmetrization remains unclear at 300 K (Asahara et al. 2010; Ahart et al. 2011; Li et al. 2019; Zhang et al. 2019). Furthermore, simultaneous high-pressure and temperature measurements are essential to address research questions related to deep Earth and H<sub>2</sub>O-rich planetary bodies (Zeng and Sasselov 2014). However, high- $P/T$  data on the physical properties of H<sub>2</sub>O are lacking due to the occurrence of chemical reactions between H<sub>2</sub>O and different metals that are regularly used as gasket materials, pressure markers, or as laser absorbers in laser-heated DACs (Schwager et al. 2004; Lin 2005; Sano et al. 2008).

## 1.2 Ferropericlase

(Mg,Fe)O ferropericlase is the second most abundant mineral in Earth's lower mantle and possibly in Super-Earth planets (Duffy et al. 2015; Irifune and Tsuchiya 2015). In Earth, (Mg,Fe)O forms, along with MgSiO<sub>3</sub> perovskite, from the decomposition of (Mg,Fe)<sub>2</sub>SiO<sub>4</sub> ringwoodite at approximately 660 km depth (23.4 GPa, Shim et al. 2001; Ishii et al. 2018). At pressures of about 40 GPa, ferrous iron (Fe<sup>2+</sup>) in ferropericlase undergoes a change of electronic spin state (Badro 2003; Lin et al. 2013). At room pressure, Fe<sup>2+</sup> adopts the high spin electronic configuration where the six 3d-electrons fill the  $t_{2g}$  and  $e_g$  orbitals maximizing the number of unpaired electrons (Fig. 1.4). Under hydrostatic compression, an isotropic distortion of the iron-containing octahedral sites in the crystal structure increases the crystal field stabilization energy (CFSE), i.e., the energy difference between the  $t_{2g}$  and  $e_g$  orbitals, triggering a change in the electronic configuration of iron to the low spin state, where electron pairing is favored in the lower energy  $t_{2g}$  orbitals (Badro 2003). The spin crossover is accompanied by a reduction in the Fe<sup>2+</sup> ionic radius (Shannon 1976), enhancing the compressibility of ferropericlase over the pressure range where the spin crossover occurs (Lin et al. 2013). This enhanced compressibility leads to an elastic softening in the bulk modulus,  $K_T$ .

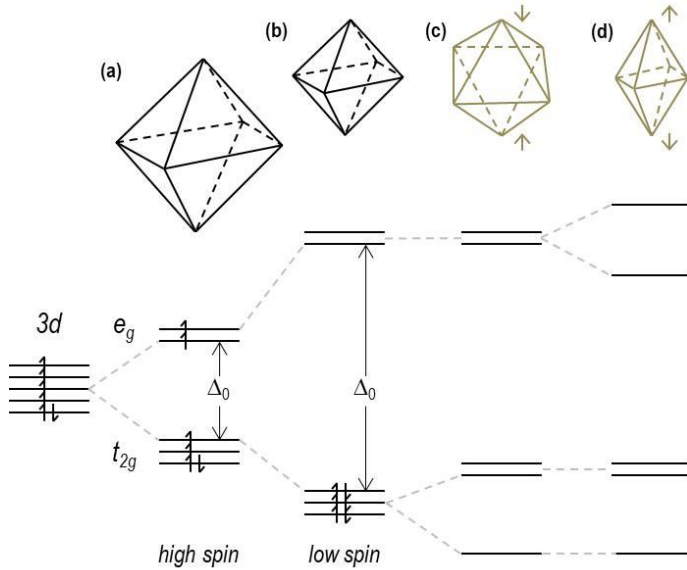


**Figure 1.4:** Scheme of the spin crossover orbital splitting associated to distortion of the octahedral sites (illustration modified from Burns 1993): (a) regular octahedron; (b) isotropically distorted octahedron; (c) trigonally distorted octahedron; (d) tetragonally distorted octahedron.  $\Delta_0$  represents the crystal field stabilization energy.

The reported pressure ranges over which the spin crossover occurs, i.e., broadness of the elastic softening in  $K_T$ , by computational (Tsuchiya et al. 2006; Marquardt et al. 2009; Wentzcovitch et al. 2009; Mao et al. 2011; Lin et al. 2013; Holmström and Stixrude 2015) and experimental studies (Crowhurst et al. 2008; Yang et al. 2015; Marquardt et al. 2018) show some disagreement. Computational studies suggest that the pressure range of the spin crossover may be particularly sensitive to second neighbor iron-iron interactions in ferropericlase with iron contents  $>18.75\%$  (Tsuchiya et al. 2006). However, this type of interaction has not yet been considered in computational models. Furthermore, if pressure is non-hydrostatic, an anisotropic distortion of the iron-containing octahedral sites leads to further splitting of the 3d orbitals which modifies the CFSE and (Fig. 1.4, Burns 1993), possibly affecting the spin crossover pressure (Glazyrin et al. 2016). The spin crossover pressure range and the magnitude of the softening in  $K_T$  is also sensitive to temperature. Computational and first experimental results predict a broader pressure range and shallower softening of  $K_T$  with increasing temperature (Marquardt et al. 2009; Wu et al. 2009; Mao et al. 2011; Lin et al. 2013; Muir and Brodholt 2015). However, measurements of the bulk modulus of ferropericlase at high-temperature, that are essential to predict the seismic signature of the spin crossover in the lower mantle, are lacking.

### 1.3 Bulk modulus

The elastic properties of minerals are key input parameters in geophysical planetary models. The isothermal bulk modulus or  $K_T$ , is a measure of the elastic compression behavior of a solid that can be formally defined as:

$$K_T = -V \left( \frac{\partial P}{\partial V} \right)_T \quad (1.1)$$

where  $P$  is the external pressure applied,  $V$  is the initial volume and the derivative denotes the material resistance to compression. The large sizes of super-Earth planets mean that the bulk modulus of the composing minerals must be evaluated at very high pressures. Diamond Anvil Cells (DACs), are powerful devices broadly used in mineral physics to generate high pressure in a sample. There is a variety of experimental techniques that can be combined with DAC experiments to determine the bulk modulus of minerals at high-pressures: X-ray scattering techniques, i.e., Inelastic X-ray Scattering (IXS) and Nuclear Resonant Inelastic X-ray Scattering (NRIXS); laser-light scattering techniques, i.e., Brillouin Spectroscopy (BS) and Impulsive Stimulated Light Scattering (ISLS); and ultrasonic techniques. A comprehensive review on advantages and limitations of these techniques has been reported in Marquardt and Thomson (2020). A common demand among these techniques is the long signal-collection times required for individual measurements that might extend up to 24 hours. Such temporal constraints pose a severe challenge for the application of high temperatures to the sample, leading to a lack of experimental data at simultaneous high- $P/T$  conditions relevant for planetary interiors. Therefore, the development of new experimental approaches is indispensable to extend the  $P$ - $T$  conditions accessible by direct bulk modulus determination in a laboratory.

### 1.4 Goals of this work

The investigation of changes in the compression behavior of H<sub>2</sub>O ice and (Mg,Fe)O across the above mentioned phase transitions at pressures (and temperatures) relevant for the interior of planets is a major goal of this thesis. For this purpose, a novel experimental approach has been implemented and optimized. A piezo-driven dynamic Diamond Anvil Cell (dDAC) is employed to dynamically compress samples over large pressures ranges (pressures up to  $\sim 200$  GPa), in significantly short experimental times (1-1000 s) (Marquardt et al. 2018; Jenei et al. 2019). The combination of the dDAC with time-resolved X-ray diffraction at the Extreme Conditions Beamline (ECB) at Deutsches Elektronen Synchrotron (DESY) in Hamburg permits tracking of unit cell volumes ( $V$ ) with high temporal resolution while the sample is being continuously compressed. A first major goal of this thesis was to employ these novel capabilities to quantify the high-pressure bulk modulus of H<sub>2</sub>O ice and (Mg,Fe)O ferropericlase and characterize any changes across the H-symmetrisation and spin crossover, respectively. The short experimental times that characterize this novel approach facilitate experiments at high temperatures. A second major goal of this thesis was thus to develop and implement a resistively-heated dDAC (RHdDAC) for simultaneous high- $P$  and high- $T$  experiments at the ECB, allowing for pressures in the sample above 100 GPa at temperatures of  $\sim 1400$  K.



# Chapter 2

## Experimental Methods

Dynamic compression in our experiments is performed by means of piezo-driven dynamic Diamond Anvil Cells (dDACs). The room temperature dDAC setup available at the Extreme Conditions Beamline (ECB) at PETRA III (DESY) and its operation are described in this chapter. The implementation of the RHdDAC setup constitutes a great part of this research project. The heating system implemented in the RHdDAC is based on the use of rigid graphite heaters and its assembly is described in detail below. Changes in the unit cell volume with pressure are tracked by time-resolved X-ray diffraction (XRD). Time-resolved XRD measurements are conducted by the employment of extremely sensitive GaAs LAMBDA detectors that allow for the collection of individual diffraction patterns on the millisecond time scale while compressing the sample in the dDACs. Hundreds, sometimes thousands of diffraction images are collected in one single experiment. The excellent  $P$ -resolution of our XRD data allows for the direct determination of the bulk modulus of solids across large pressure-ranges by direct differentiation of quasi-continuous  $V(P)$  data without assuming equation-of-state formalisms. In this study, the development and implementation of new data processing tools that enable the analysis of a large number of XRD patterns is indispensable. Data integration and analysis are discussed.

### 2.1 Diamond Anvil Cells

Diamond Anvil Cells (DACs) are broadly used in (geo-)physics, chemistry, and materials science to explore material properties under extreme conditions of pressure ( $P$ ). The transparency of diamond to visible light and X-rays allows to determine a variety of physical properties on compressed samples (Jayaraman 1983; Mao et al. 1996). In a DAC, high pressures are generated by compressing the sample between two opposing diamond anvils with flat tips (*culets*), aligned with one another. The sample is firstly loaded in a hole (*sample chamber*) drilled in a metallic sheet (*gasket*) that is placed between the diamonds at the culet center to contain the sample. The pressure generated in the sample ( $P$ ) is defined as the ratio between the force applied by the diamonds ( $F$ ) divided by the area ( $A$ ) over which the force acts (i.e., culet):

$$P = \frac{F}{A} \quad (2.1)$$

A general scheme of the Mao-type symmetric DACs that are employed in this study is shown in the following section.

### 2.1.1 DAC assembly

In this chapter, the assembly routine for standard DACs as carried out in our experiments is described in detail. In a first step, diamonds with culet sizes between 80 and 200  $\mu\text{m}$  diameters are glued into plate DAC seats using a thermally conductive epoxy adhesive. A tungsten carbide (WC) seat is placed at the upstream side and a cubic boron nitride (c-BN) seat, which is transparent to X-rays, is positioned on the downstream side (Fig. 2.1). The diamonds are aligned to one another under the microscope by using the optical interference fringes between the culets. Afterwards, a gasket sheet is pre-indented between the diamond culets to a final thickness of 30  $\mu\text{m}$  and a hole is drilled in the center of the indentation. The diameter of the hole is typically half the diameter of the diamond culet. Different drilling machines are used depending on the diameter of the hole. An Electro Discharge Machining (EDM) drill at Beamline P02.2 at PETRA III offers a well-shaped and clean cut of the gasket. Centering of the drill in the indentation of the gasket is achieved manually. For this reason, the use of EDM is more convenient in those cases where the indentation is relatively large or has a diameter equal to or greater than 100  $\mu\text{m}$ . If the indentation diameter is less than 100  $\mu\text{m}$ , the laser micro-hole drilling machine at Beamline P02.2 is used, which is equipped with a motorized stage that allows for controlled XY positioning of the hole in small indentations.

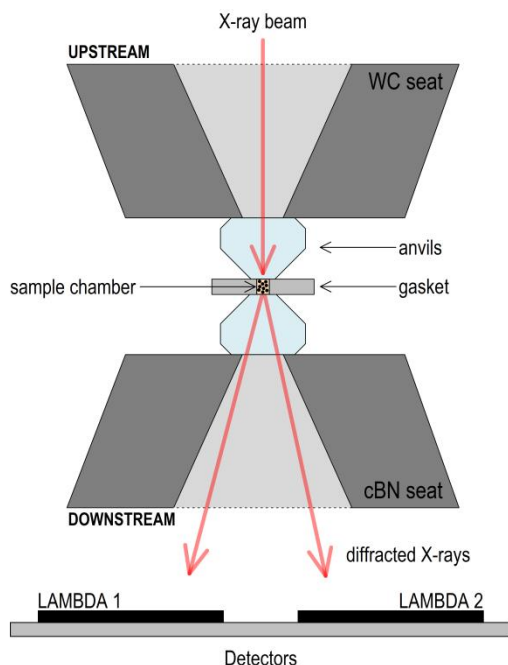


**Figure 2.1:** Schematic drawing showing the components of a diamond anvil cell (left) and a picture of the DAC, closed with the screws (right).

The gasket material is chosen according to the needs of the experiment. Re gaskets are often used in DAC experiments due to their mechanical stability in experiments to pressures above 100 GPa. In comparison with softer crystalline materials such as stainless steel, the hardness of Re decreases the occurrence of “sliding” of the gasket hole and subsequent blow-out of the

sample during the experiment (Jenei et al. 2019; Soignard and McMillan, 2004). However, Re gaskets can be problematic in X-ray diffraction experiments since the high-Z character of Re may lead to the appearance of strong parasitic peaks in the diffraction patterns that tend to overlap partly or fully with the sample peaks, complicating the data analysis. This situation becomes critical when it comes to DAC experiments where the contribution of the gasket increases as the sample hole shrinks under compression. Besides Re, amorphous alloys can be really advantageous gasket materials since they have nearly no contribution to the diffraction patterns (Fig. 4 in Méndez et al. 2020, reproduced here as Fig. 2.2). Moreover, amorphous alloys are characterized by being extremely homogeneous in microstructure and having no microstructural discontinuities (O’Handley 1987). When used as gasket materials, it has been observed that such structural homogeneity also prevents the gasket from moving off-center (Mao et al. 1979; Balzaretto et al. 1999), stabilizing the sample chamber (He et al. 2003). In our experiments, we prepared ring-like inserts of an amorphous boron alloy ( $\text{Fe}_{0.79}\text{Si}_{0.06}\text{B}_{0.15}$ ) and introduced them in the sample hole of a regular Re gasket, following the procedure described in detail in Méndez et al. (2020). In our study, the performance of amorphous boron alloy gaskets has been tested at room and high temperatures.

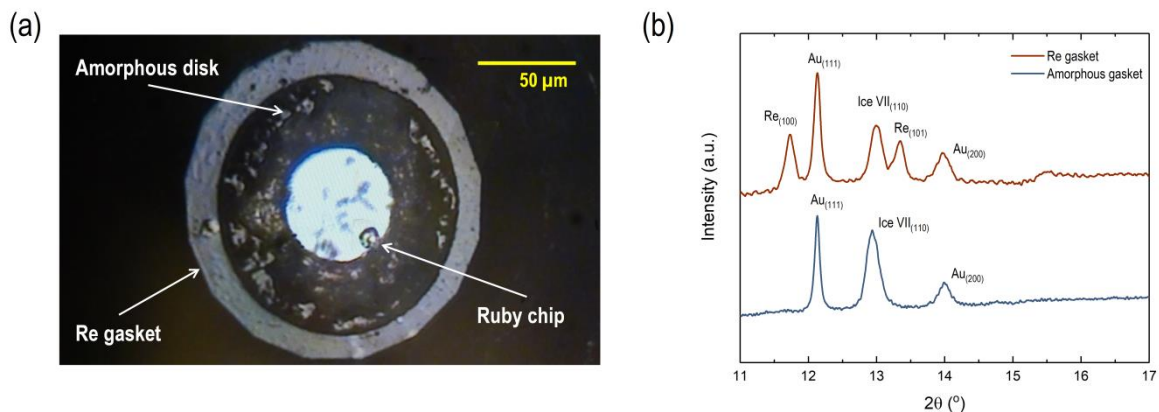


**Figure 2.2:** (a) Picture of the sample chamber in a DAC viewed through the diamond culet. The loaded sample is  $\text{H}_2\text{O}$  along with Au powder. (b) Raw integrated diffraction patterns from two samples containing  $\text{H}_2\text{O}$  ice and Au powder loaded in a Re gasket (top) and an amorphous gasket (bottom). A detector artifact appears in the top pattern as a bump at  $15.5^\circ$ .

Both gasket configurations, i.e. regular Re gaskets with or without amorphous alloy inserts, are suitable for gas-loading DACs. For some of the here-presented experiments, pre-compressed Ne is loaded at the gas-loading facilities installed at the Extreme Conditions Beamline (Liermann et al. 2015). Ne is broadly employed as pressure-transmitting medium as it creates a quasi-hydrostatic stress environment up to 15 GPa (Meng et al. 1993; Klotz et al. 2009). Even at higher pressures, deviatoric stresses and pressure gradients remain small in Ne (Buchen et al. 2017, 2018).

## 2.2 The piezo-driven dynamic DAC

In conventional static DAC experiments, a force is applied to the sample by manually tightening the screws. In dynamic compression experiments, the DAC is physically attached to a piezoelectric actuator (dynamic DACs, dDACs, Evans et al. 2007) that continuously apply a force on the DAC, allowing generating a time-dependent pressure profile to the sample. In the dDAC, compression rates of  $>100$  TPa/s can be achieved (Jenei et al. 2019) bridging the gap between traditional static DAC experiments and dynamic shock/ramp compression measurements. The combination of the dDAC with time-resolved analytical techniques such as X-ray diffraction (XRD) and Raman spectroscopy has been used to study a wide variety of physical phenomena such as crystal growth mechanisms (Lee et al. 2007; Tomasino and Yoo 2013), fast compression-induced rapid solidification (Chen and Yoo 2011), compression-rate dependencies and kinetics of phase transitions (Lee et al. 2006; Lin et al. 2016), to probe metastable phases (Chen and Yoo 2012; Chen et al. 2014), simulate processes during impact events (Sims et al. 2019) and measure the elastic response of mantle minerals at seismic frequencies (Marquardt et al. 2018).

The body of the dDAC employed in this study consists of a cylindrical housing made of stainless steel where the DAC is introduced along with a high-voltage piezoelectric actuator (PEA) that sits parallel to the anvil compression axis (Fig. 2.3a). The PEA has a through-hole of 9 mm in diameter, which allows the X-rays to reach the sample. A detailed description of the dDAC setup can be found in Jenei *et al.* (2019). The housing is open at one end (upstream). When DAC and PEA are placed into the housing, they are pushed together by tightening a finely threaded cap at the upstream end of the housing. Diverse voltage-time waveforms can be tailored with the computer program *Keysight* in order to design experiments with a specific pressure profile (Fig. 2.3b). The voltage-time waveform is sent to a piezo-controller (Piezosystem Jena GmbH) by means of a waveform generator (Agilent 33522B) that is directly connected to the PC. The voltage-time waveform is performed by the PEA that expands and pushes against the piston of DAC, compressing the sample. Different peak pressures and compression rates are achieved during the experiment by changing the applied voltage and timing of the waveform. The maximum peak pressure achieved in a dDAC experiment also depends on the size of the diamond culets. Calibration measurements of peak pressures as a function of voltage and culet size can be found in Jenei *et al.* (2019). Simultaneously, continuous collection of diffraction images is initiated on the detectors by a delay generator (SRS, DG645/5 with Rb clock) that interconnects and synchronizes the operation of all electronic devices. A schematic drawing of the connections in the experimental setup is shown in Fig. 2.4.

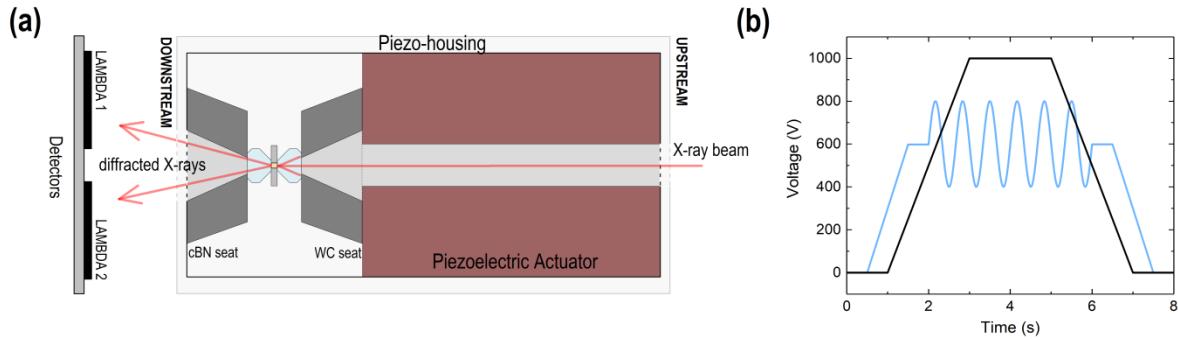


**Figure 2.3:** (a) Simplified schematic drawing of the dynamic diamond anvil cell (dDAC). (b) Examples of voltage-time waveforms employed in this study: a trapezoidal waveform with a compression rate of 500 V/s (black) and a sinusoidal waveform consisting of 6 oscillations with a frequency of 1.5 Hz and amplitude of 400 V (blue).

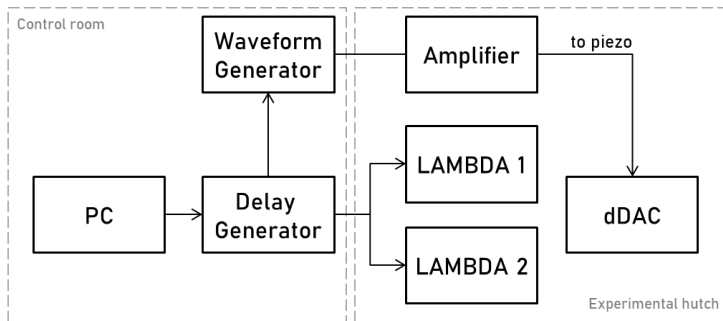


**Figure 2.4:** Schematics of the experimental setup for dDAC experiments at the ECB.

## 2.3 The Resistively-Heated dynamic DAC

In order to address research questions related to interior of planetary bodies, achieving experimental conditions of simultaneous high-pressure ( $P$ ) and-temperature ( $T$ ) is essential. High- $P/T$  experiments are more complicated because of the high- $T$  degradation of the DAC elements over time and the contamination of the sample due to temperature-induced reactions with the gasket material and/or the diamonds (Schwager et al. 2004; Lin 2005; Sano et al. 2008; Frost et al. 2019). One of the major goals of this research project includes the implementation of a resistively-heated dynamic Diamond Anvil Cell (RHdDAC) that allows us to reduce the exposure time of samples to high temperatures by performing fast compression with a piezoelectric actuator (PEA, Méndez et al. 2020). The implementation of the RHdDAC has posed a great experimental challenge due to the limited thermal stability of the PEA.

The RHdDAC uses a modified version of a Mao-type symmetric DAC suitable for housing resistive heaters similar to those used previously (Fig. 1 in Méndez et al. 2020, reproduced here as Fig. 2.5, Du et al. 2013). The here-employed resistive heaters, that are designed and manufactured at DESY, consist of disks made of rigid graphite that are placed around the diamond anvils (Fig. 2.5b). The heat is generated by letting an electric current flow through the heaters. The electric current is applied through two molybdenum rods that are wedged between

## Chapter 2. EXPERIMENTAL METHODS

the heaters and connected to a DC power supply. In order to avoid heat loss through the cell, ceramic rings are placed between the heaters and the diamond seats. The temperature is measured by two type-R thermocouples (T1 and T2 in Fig. 2.5a) that are placed on the anvil pavilion close to the tip of the diamonds.

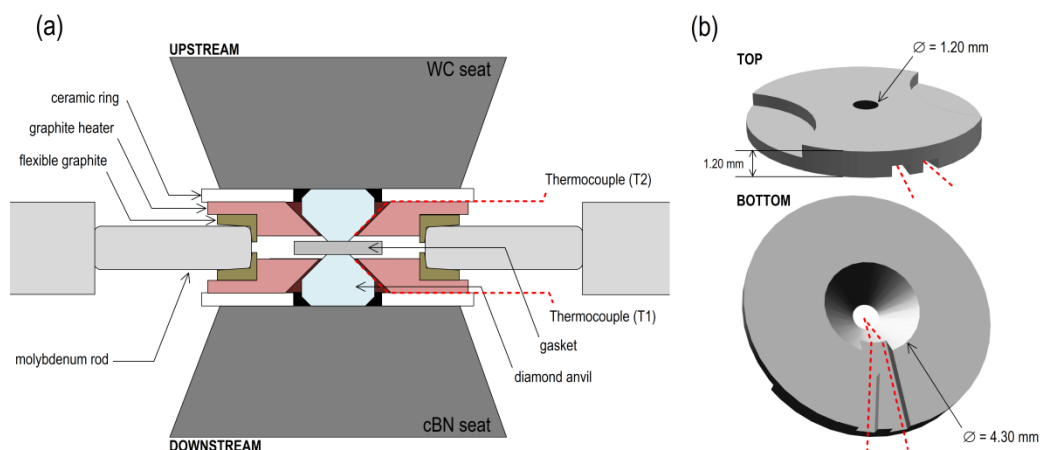


**Figure 2.5:** (a) Cross section of the inside of the symmetric DAC showing the seated diamond anvils and the heating assembly. (b) 3D illustration of the rigid graphite heater, top and bottom views. The location of the thermocouples is indicated by dashed red lines.

The PEA is enclosed in a hardened stainless steel case (PEA-housing) that is open at both ends. The symmetric DAC equipped with the heating system (RHDAC) is inserted into the downstream end of the PEA-housing by means of a cap with a bayonet connector (Fig. 3 in Méndez et al. 2020, reproduced here as Fig. 2.6). The exterior of the cap is connected to a water-cooled aluminium holder (Fig. 2.6a). The upstream end of the PEA-housing is closed through an end cap with fine threading that is tightened to engage DAC and PEA and pre-compress the sample if required. As the maximum operating temperature of the piezo is of 175 °C, a cooling plate is placed between DAC and PEA in order to avoid heat transfer to the piezo. In addition, a box like water-cooled jacket is placed around the PEA-housing (Fig. 2.6a). The DAC attached to the PEA-housing is inserted into a vacuum vessel that was constructed to minimize heat loss through air convection and avoid oxidation as well as diamond graphitization (Fig. 2.6b). The vacuum vessel consists of a water-cooled stainless steel chamber that has a volume of 4.5 l. The vacuum vessel is equipped with two Kapton windows that are located on the upstream and downstream sides to let the incident beam and diffracted X-rays pass. The total weight of the RHdDAC assembly together with the vacuum vessel is about 35 kg.

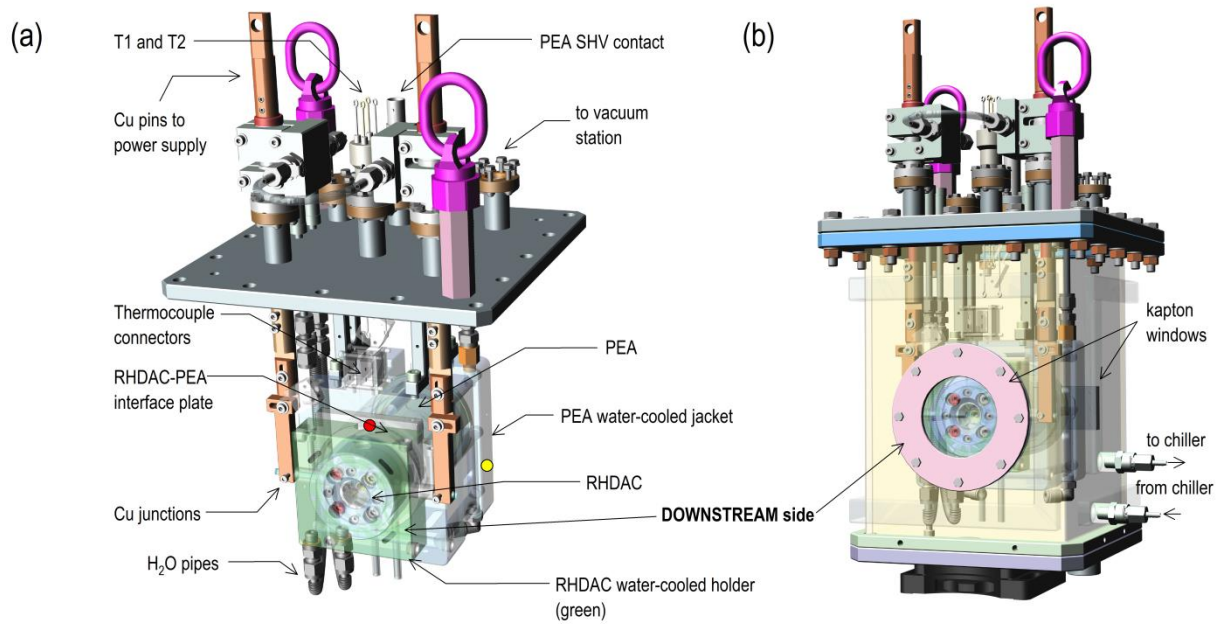


**Figure 2.6:** (a) RHdDAC connected to the lid of the vacuum vessel. Additional thermocouples are placed to measure the temperature of the water-cooled jacket (yellow circle) and at the front of the PEA (red circle). (b) RHdDAC inserted into the vacuum vessel.

### 2.3.1 Temperature calibration of the thermocouples in the RHdDAC

Despite the thermocouples being placed close to the tip of the diamonds, there may be a temperature difference between the temperature read by the thermocouples and the real temperature in the sample. In order to evaluate a possible temperature offset, the thermal expansion of Au was measured at ambient pressure employing X-ray diffraction (XRD). The temperature dependence of the lattice parameter of Au is well described in the literature (Simmons and Balluffi 1962; Anderson et al. 1989; Pamato et al. 2018), making it a good temperature standard. In the calibration experiment, Au powder (99.99% pure from Sigma Aldrich) was loaded into the RHdDAC and the temperature was increased in 50 K steps up to a maximum temperature of 1200 K. XRD images were collected after each temperature increment. The unit cell volume of Au was derived from the (111), (200), (220), and (311) reflections and plotted as a function of temperature (Fig. 6 in Méndez et al. 2020, reproduced here are Fig. 2.7) in comparison to previously reported values (Pamato et al. 2018). The difference between the average temperature of both thermocouples, T1 and T2, and results from Pamato *et al.* (2018) is smaller than  $\pm 50$  K (Fig. 2.7b), verifying that there is an efficient heating of the sample in the RHdDAC.

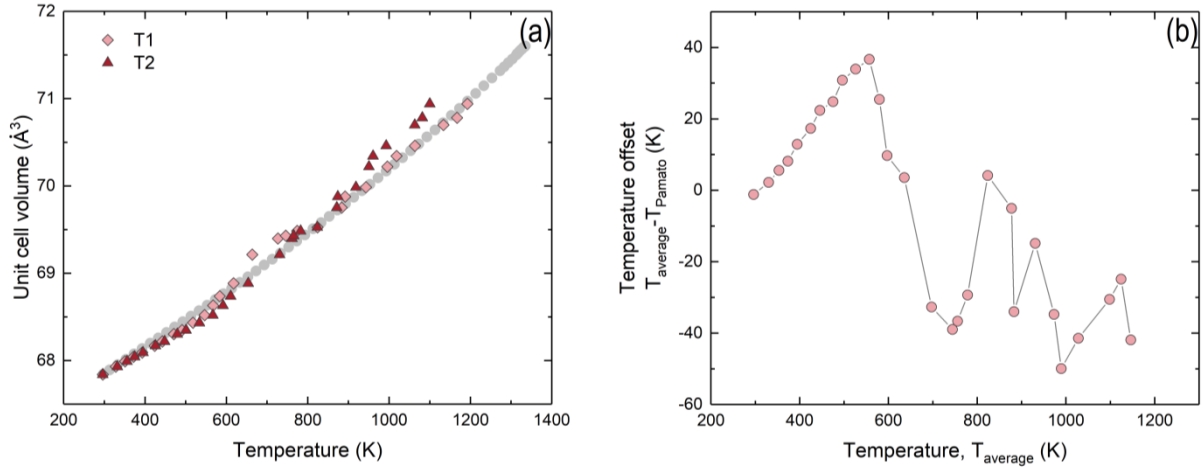


**Figure 2.7:** (a) Experimentally determined unit cell volumes of Au as a function of the temperatures read from thermocouples T1 and T2 (diamonds and triangles) in comparison with the experimental data from Pamato *et al.* (2018) (solid circles). (b) Temperature offset with respect to data in Pamato *et al.* (2018) as a function of the average temperature of T1 and T2.

## 2.4 Powder X-ray diffraction

Powder X-ray diffraction is a nondestructive technique employed for the analysis of crystalline structures, phase identification, and determination of physical parameters such as strain or average grain size. Widely applied in high-pressure mineral physics, X-ray diffraction provides valuable information about the size (volume) and shape (geometry) of the unit cell (Lavina *et al.* 2014). The phenomenon of diffraction consists on the elastic scattering of monochromatic X-rays from the lattice planes contained in a particular crystallographic orientation ( $hkl$ ), at specific angles ( $\theta$ ), via constructive interference (the order of diffraction is conventionally set to  $n=1$ ), satisfying Bragg's Law (Bragg 1914):

$$n\lambda = 2d_{hkl} \sin \theta \quad (2.2)$$

where  $\lambda$  is the wavelength of the X-rays and  $d_{hkl}$  is the distance between crystallographic planes. Every set of diffraction planes or family is represented by a diffraction peak in the diffraction pattern. A diffraction pattern plots intensity against scattering angle. The scattering angle  $\theta$  or the position of the reflections in the diffraction pattern is related to the distance  $d_{hkl}$  between atomic planes by Equation (2.2). The diffraction intensities are related to the distribution of atoms within the lattice as well as the average atomic electron density. Therefore, minerals containing light elements with a low electron density, i.e., low-Z character, such as H in H<sub>2</sub>O ice and Mg in (Mg, Fe)O ferropericlase, will be weak X-ray scatterers (low scattering factor or cross section) and their diffraction patterns will be characterized by relatively low diffraction intensities.

The crystal geometry can be derived from a group of reflections and their spatial relation to one another. For the simplest case where the crystal symmetry is cubic, the spacing of a given family of planes relates to the lattice parameters ( $a$ ,  $b$ , and  $c$ ) as:

$$\frac{1}{d_{hkl}^2} = \frac{h^2}{a^2} + \frac{k^2}{b^2} + \frac{l^2}{c^2} \quad (2.3)$$

where  $a=b=c$  in a cubic unit cell. The volume of a cubic unit cell is then defined as:

$$V = a^3 \quad (2.4)$$

Hence, a diffraction pattern is the fingerprint of periodic atomic arrangements in a given material and alterations of the symmetry or atomic distribution under stress, i.e., external pressure, may be trackable by time-resolved X-ray diffraction.

### 2.4.1 Time-Resolved X-Ray Diffraction at the ECB

As mentioned in the previous section, the scattering intensity is determined by the Z-character of the sample. In addition to this, there are other factors such as sample size (thickness) that can be limiting in experiments with DACs, where the sample thickness is only a few tenths of micrometers. The intensity of the diffraction patterns can be enhanced by collecting diffraction over long exposure times. However, in fast compression experiments, short exposure times are convenient to ensure a good data coverage along the compression path. Therefore, all here-presented experiments have been performed at a third-generation synchrotron light source (Liermann et al. 2010) where the increased brilliance of the incident X-ray beam in combination with advanced detection technologies enables measuring high-intensity diffraction with single-exposure times on the millisecond timescale. PETRA III is a good example of such a third-generation light source, utilizing a highly focused ( $8 \times 3 \mu\text{m}^2$ ) and intense monochromatic X-ray beam (Liermann et al. 2015). High time-resolution of the diffraction measurements is accomplished through the use of two fast and sensitive GaAs 2.3 MPix LAMBDA detectors (Pennicard et al. 2013, 2018) that enable collection of diffraction images at a frequency of up to 2 kHz. A scheme of the setup available at the ECB with a dDAC and the detectors is shown in Fig. 2.8.

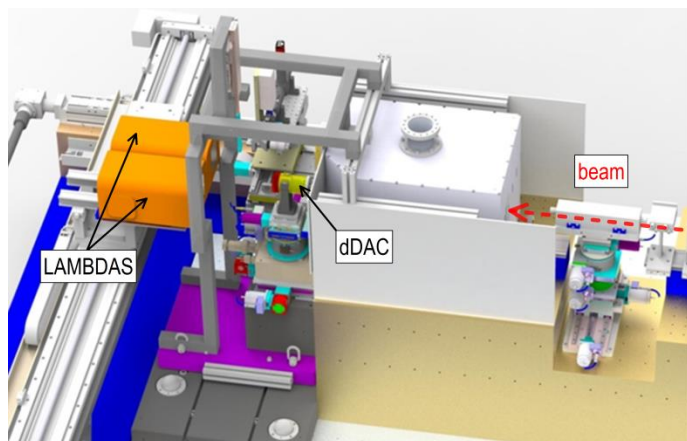


**Figure 2.8:** dDAC and the LAMBDA detectors in the experimental hutch at the ECB.

### 2.4.2 dDAC data integration and analysis

In a first step, the detector images are radially integrated using the Dioptas software (Prescher and Prakapenka 2015) to obtain 1D diffraction patterns as a function of the  $2\theta$ -angle. In dDAC experiments, the number of integrated diffraction patterns may vary from a few tenths to several thousands. One of the major challenges of this project was the development and implementation of new data analysis strategies for batch processing of diffraction patterns including peak fitting, volume ( $V$ ) and pressure ( $P$ ) determination and  $V(P)$  data treatment. For this purpose, two different tools were tested/developed during this work and are described here:

1) A Matlab code for individual peak fitting and tracking (courtesy of R. J. Husband) was initially used. In a first step, the user defines the  $2\theta$ -range that contains the peak of interest in the first pattern of the batch, by picking on the graph a lower limit ( $LL$ ) and an upper limit ( $UL$ ) in  $2\theta$ , as well as the position of maximum intensity ( $I$ ). Then, the code uses a Gaussian model to fit the peak and determine  $2\theta$  peak position ( $PP$ ) and full width half maximum (FWHM) of the peak assuming a linear background. The model parameters are optimized *with a non-linear least-squares fit*. Within two consecutive patterns, the peak shift due to compression ( $\Delta_{2\theta}=PP_{i+1}-PP_i$ ) is usually smaller than the distance between  $LL$  and  $UL$ . Thus, the program can find the peak in the following pattern, by picking the position of maximum intensity between  $LL$  and  $UL$ . Then,  $LL$  and  $UL$  positions are recalculated by adding  $\Delta_{2\theta}$  before the peak fitting is performed. After tracking the peak over the entire compression range, the program plots peak position as a function of file number. If an anomaly occurred along the tracking, the problematic pattern can be easily identified on the plot. As output parameters,  $PP$ , FWHM and corresponding uncertainties can be collected from the command window.

The Matlab approach was employed for the analysis of X-ray diffraction data on (Mg,Fe)O ferropericlase, where the signal/noise ratio of the integrated patterns permitted a reliable determination of peak positions, resulting in low uncertainties in  $V$ . However, the weaker nature

of the diffraction of H<sub>2</sub>O ice, as well as peak overlaps, required the implementation of a more sophisticated approach. For this reason, we implemented an alternative fitting program, described in the following:

2) A more sophisticated code for multiple peak fitting was written in Python (courtesy of Florian Trybel). Firstly, the program improves the signal/noise ratio of each integrated pattern by averaging over three points in  $2\theta$ -space and applying an infinite impulse response (IIR) filter forwards and backwards with zero phase shift. This step improves the reliability as well as the speed of the fitting routine (Fig. 2 in Mendez et al. 2020b reproduced here as Fig. 2.9, see also chapter 4). After phase identification with Dioptas, the diffraction peaks of each phase are assigned to a crystal structure and fitted separately. In order to track the peaks over the entire compression range, the program calculates the position of the peaks from the space group and a given initial compression using a routine from the pymatgen (Python Materials Genomics) library (Ong et al. 2013). The calculated peak positions (*CPP*) serve as initial positions for a Gaussian peak fit with a linear background correction. The *CPP* are optimized with a non-linear least-squares fit to obtain optimal peak positions (*OPP*) employing the *LMFIT* package (Newville et al. 2020). The *OPP* of the individual Gaussians is subsequently compared with the prediction (*CPP*). If the *OPP* is at larger (smaller)  $2\theta$ -angle than *CPP*, compression is increased (decreased) until  $|OPP - CPP| < \epsilon$  is reached ( $\epsilon \leq 10^{-3}$ ). The resulting compression serves as the starting compression for the next *P*-step, making the fitting significantly more efficient. The optimization of the compression rate is performed as an adaptive step width to improve accuracy and runtime.

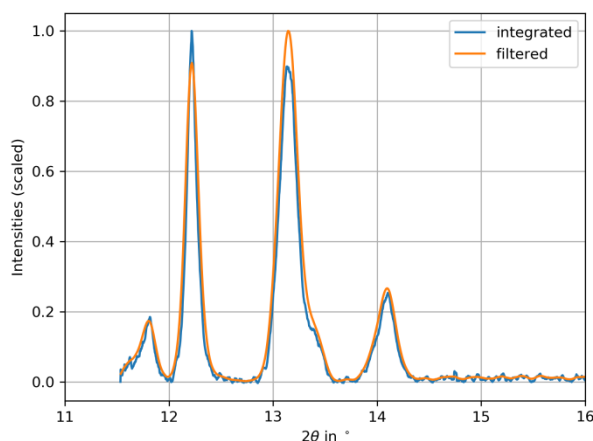


**Figure 2.9:** Example of an integrated diffraction pattern for H<sub>2</sub>O at 26 GPa in the dDAC. Blue shows the original pattern after integration of the detector image with Dioptas. Orange is the pattern after application of an IIR filter with zero phase shift.

### 2.4.3 Challenges in dDAC data analysis

Handling of peak overlaps is a major difficulty in experimental data analysis. In our dDAC experiments, diffraction patterns contain information from multiple phases such as the sample, the *P*-marker and sometimes also the gasket (see Section 2.1.3). Differences in compressional

behavior between the present phases lead to the occurrence of peak overlap during compression (Fig. 3 in Méndez et al. 2020b reproduced here as Fig. 2.10). In this regard, the choice of peak fitting technique may affect the results. In principle, both the here-employed Matlab and Python codes can resolve individual peaks while they are partly overlapping. However, the Python code becomes more successful when it comes to greater overlaps by estimating a linear compression rate and calculating the expected peak position for the overlapping phases. In general, the Gaussian approach chosen for our analysis is less sensitive to surrounding peaks, since it only considers the maximum of intensity and the FWHM, in contrast to more widely used XRD pattern fitting techniques such as Le Bail or Rietveld refinements, where the peak shape is relevant for the fitting. It is worth noting that a reliable fit is not possible when the peaks are completely overlapping, irrespective of the chosen approach. Sometimes, one can mask the most intense areas of the parasitic rings on the detectors in order to minimize the convolution with the sample rings. However, this approach strongly depends on the nature of the diffraction pattern (i.e., continuous and smooth or spotty rings) and how much of the detector area needs to be masked. Moreover, while a detector mask is fixed on concrete areas, diffraction peaks change their position with compression what may make this procedure inefficient over large  $P$ -ranges.

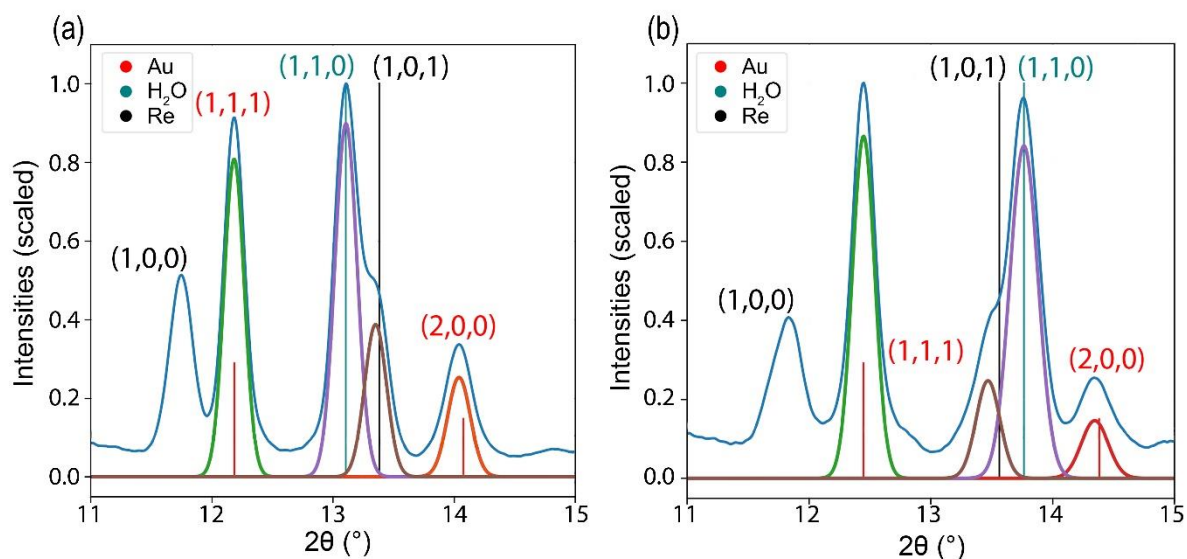


**Figure 2.10:** Exemplary peak profile fitting of integrated patterns collected from a dDAC experiment on H<sub>2</sub>O loaded in a Re gasket along with Au as  $P$ -marker, after application of the IRR filter (blue) at (a) 24 GPa and (b) 45 GPa with assigned indices and the calculated/theoretical peak positions (CPP) shown as vertical lines. The solid curves represent the Gaussian model peaks.

In addition to peak overlap, we found other issues in the implementation of these automatic fitting routines. The fine  $P$ -steps that characterize our compression data are usually below the confidence interval of the fitting software, especially for high values of  $K_T$ , i.e., when the sample is highly incompressible and the change in unit cell volume with pressure is small. These

programs generally need a sufficiently large difference in the peak position between consecutive patterns to identify a shift with compression. If the difference is too small, the programs tend to keep the positions constant, followed by a sudden jump to another peak position when a large enough shift is detected, introducing artifacts in  $V(P)$  (Fig. 2.11a). This issue can be resolved by lowering the convergence limit (significantly increasing the computer runtime) or by skipping patterns, which effectively increase the  $P$ -spacing between data points.

## 2.5 Bulk modulus calculation

The isothermal bulk modulus ( $K_T$ ) is a key input parameter in interior planetary models. As discussed in the introduction, diverse experimental techniques can be combined with DACs to determine the bulk modulus at high pressures. In addition, the bulk modulus is a thermodynamic parameter that can be indirectly inferred by fitting an equation of state formalism, i.e., Birch-Murnaghan or Vinet, to volume-pressure data. Previous X-ray diffraction studies employing static DACs used the later approach to infer the bulk modulus of H<sub>2</sub>O ice (Wolanin et al. 1997; Frank et al. 2004; Klotz et al. 2017) and (Mg, Fe)O ferropericlase (Fei et al. 2007; Chen et al. 2012; Solomatova et al. 2016). This approach works well when measuring first-order phase transitions, where a discontinuous change in volume marks the boundary between different phases. In this case, two equations of state will be used to fit the data before and after the transition. However, if the change in  $V(P)$  is continuous, as for second-order phase transitions, and subtle, as for *infinite*-order phase transitions (proton order-disorder, spin crossover), it may be difficult to identify different phases and decide how many equations of state adequately describe the data and over which  $P$ -range to apply them. This situation worsens when the transition is unexpected and/or the  $P$ -resolution is not sufficient to resolve a continuous change in  $V$ . Then, one may totally miss a phase transition and use one single equation state, smoothing out present features in the data that are not obvious to the eye.

The quasi-continuous  $P$ -resolution of our data allows us to calculate the bulk modulus by direct differentiation of  $V(P)$  via Equation (1.1), without the need to invoke an equation of state formalism and assumptions about the  $P$ -range over which one set of equation-of-state parameters adequately describes the material's behavior. Previous X-ray diffraction studies had to rely on the use of equations of state to infer the bulk modulus since direct differentiation of  $V(P)$  was not possible due to the typically low  $P$ -resolution achieved in static DAC experiments that essentially relies on the dexterity of the operator. In our experiments on (Mg, Fe)O, direct differentiation of raw X-ray diffraction data was possible since the good quality of the integrated patterns produced a  $V(P)$  dataset with low scatter. However, the weak nature of the diffraction peaks of H<sub>2</sub>O ice resulted in a larger scatter in  $V(P)$  that appeared strongly magnified in the

derivative  $K_T$ . As  $K_T$  is a thermodynamic property, it should be continuous and vary smoothly within phase boundaries. In order to achieve a completely smooth  $P$ -dependence of  $K_T$  of  $H_2O$  ice, we needed to eliminate the experimental scatter before differentiation of the  $V(P)$  data. For this purpose, we employed sensitive smoothing functions that reliably describe subtle features in  $V(P)$ . A mathematical solution was the employment of smoothing spline (monotonic) interpolation functions (Dierckx 1975, 1982). A spline is a continuously differentiable curve, broadly used in computer science to approach complex forms. A spline has two main features: i) it is defined in portions by low-degree polynomials which avoids Runge's phenomenon, i.e., data oscillations introduced by overfitting with high-degree polynomials; ii) it is continuous in the range where it is defined, as well as its derivatives (Dierckx 1975). In Fig. 2.11 an example of such interpolation is shown.

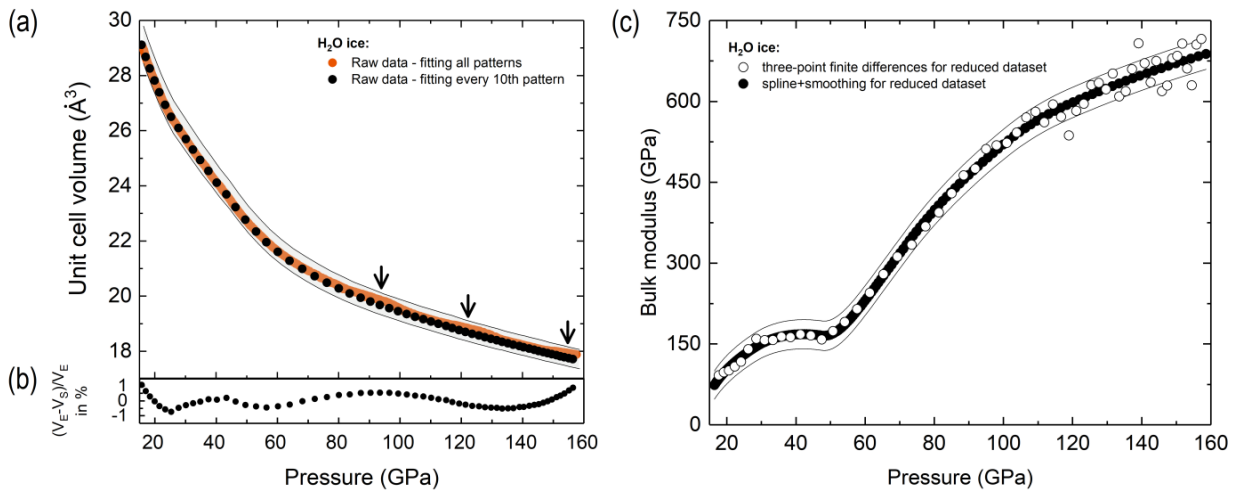


**Figure 2.11:** Exemplary dataset for the bulk modulus calculation. (a) Unit cell volume as a function of pressure for  $H_2O$  compressed up to 160 GPa in the dDAC. Orange circles represent the raw data by fitting all patterns. Black arrows point out artificial jumps introduced by the fitting Python code due to too small  $P$ -spacing of the data. Black circles represent raw data, but fitting every 10<sup>th</sup> pattern only (*reduced* dataset), which increases the  $P$ -spacing between data points and makes the artificial jumps disappear. (b) The difference between the data points and the spline with a smoothing factor of 1.0 is  $<1\%$  over the entire  $P$ -range. (c) Bulk modulus as a function of pressure derived from the *reduced* dataset by following two different procedures: (i) Computed by three-point finite differences (white circles), small fluctuations appear at high pressures; (ii) derived from the splined *reduced* dataset (black circles) with a smooth  $P$ -dependence.

# Chapter 3

## Synopsis

The following chapter summarizes the main findings of the publications that are presented in the following chapters 4-6. We investigated two different pressure-induced phase transitions: the hydrogen-bond symmetrization in H<sub>2</sub>O ice (chapter 4) and the spin crossover in (Mg,Fe)O ferropericlase (chapter 5). These transitions are continuous transformations of *infinite*-order that occur without symmetry changes in the crystal structures, making their characterization extremely difficult by conventional X-ray diffraction experiments. In our experiments, we combine a piezo-driven dDAC with synchrotron time-resolved X-ray diffraction with high-temporal resolution to study the evolution of crystal structures and compression behavior of samples as a function of pressure. The here-presented work also contributed to the implementation of this novel setup (section 2.2), reported in Jenei et al. (2019). The quasi-continuous pressure-resolution achieved in our experiments permits the detection of subtle changes in the unit cell volume ( $V$ ) with pressure ( $P$ ) and the determination of the bulk modulus ( $K_T$ ) by direct differentiation of  $V(P)$  data (see also Marquardt et al. 2018). We employed this approach to investigate changes in the bulk modulus of H<sub>2</sub>O and (Mg,Fe)O across the above mentioned transformations. Furthermore, we implemented a resistive-heated dDAC (RHdDAC) setup for conducting experiments at simultaneous high pressures and high temperatures (chapter 6). The potential and capabilities of the RHdDAC are highlighted at the end of this chapter.



### 3.1 Compression behavior of H<sub>2</sub>O across the ice VII –ice X transition

The following subsection summarizes the main results of the manuscript included in chapter 4:

*“Bulk modulus of H<sub>2</sub>O across the ice VII – ice X transition measured by time-resolved X-ray diffraction in dynamic Diamond Anvil Cell experiments”*

A. S. J. Méndez, F. Trybel, R. J. Husband, G. Steinle-Neumann, H.-P. Liermann and  
H. Marquardt

Status: Submitted to *Physical Review B*  
(19 October 2020)

**Individual contributions:** *Together with Hauke Marquardt, Rachel J. Husband and Hanns-Peter Liermann, I designed and performed the experiments. Florian Trybel wrote the diffraction pattern analysis and peak-fitting software. Together with Florian Trybel, Gerd Steinle-Neumann and Hauke Marquardt, I analyzed the data and wrote the manuscript.*

Ice VII and ice X are predicted to form an icy mantle in ocean exoplanets as well as icy satellites in the Solar System (Valencia et al. 2006, 2007; Sotin et al. 2007; Redmer et al. 2011; Journaux et al. 2017). The elastic properties of these high-pressure polymorphs, in particular the bulk modulus ( $K_T$ ), are key parameters to constrain interior models of H<sub>2</sub>O-rich planetary bodies. The ice VII – ice X transition is a continuous proton order-disorder transformation that is predicted to proceed through changes in the energy potential of the hydrogen-bond (Holzapfel 1972; Benoit et al. 1998, 2002; Benoit and Marx 2005). The bulk modulus of H<sub>2</sub>O across the ice VII – ice X transition is poorly constrained as previous studies have been limited to  $P < 100$  GPa (Asahara et al. 2010; Ahart et al. 2011; Li et al. 2019; Zhang et al. 2019) and it is yet unclear if the pressure-dependence of  $K_T$  is somehow sensitive to changes in proton-order. In order to understand the compression behavior of H<sub>2</sub>O ice, we performed three dynamic compression experiments across the ice VII – ice X transition up to pressures of 180 GPa at room temperature. We employed a dynamic DAC as described in section 2.2 in combination with time-resolved X-ray diffraction to measure changes in the unit cell volume as a function of pressure.

We conducted three dDAC experiments on H<sub>2</sub>O (dDAC-1, dDAC-2 and dDAC-3) with Au powder used as  $P$ -marker. Trapezoidal voltage-time waveforms were applied on the samples with nominal compression rates of 0.4-0.6 GPa/s. The total duration of our compression experiments was 300 s for dDAC-1, 850 s for dDAC-2 and 868 s for dDAC-3. Monochromatic synchrotron X-rays with a fixed wavelength (0.4828 Å) were used to measure time-resolved diffraction along the compression paths. We collected 1800 diffraction images for dDAC-1, 590 for dDAC-2 and 305 for dDAC-3. The Python routine developed by F. Trybel (section 2.4.2) was used to analyze

### **Chapter 3. SYNOPSIS**

the integrated diffraction patterns.  $P$  is calculated using the optimized position of  $(111)_{\text{Au}}$  combined with the equation-of-state of Fei et al. (2007). Volume ( $V$ ) of  $\text{H}_2\text{O}$  ice was determined from  $(110)_{\text{iceVII}}$ .

Unit cell volumes as a function of pressure for our three experimental runs are plotted in Fig. 3.1a. Differences in measured  $V$  between our three runs fall within the refinement uncertainties determined by the resolution limit of the fitting routine ( $0.05^\circ$  in  $2\theta$ ). Data from previous X-ray diffraction experiments employing static DACs (Wolanin et al. 1997; Loubeyre et al. 1999; Sugimura et al. 2008) are plotted in comparison to our data in Fig. 3.1b. Overall, our  $V(P)$  data are in good agreement with previous X-ray diffraction experiments. The observed differences in  $V$  between our three compression runs (dDAC-1, dDAC-2 and dDAC-3) are similar to differences between previously published measurements (Wolanin et al. 1997; Loubeyre et al. 1999; Sugimura et al. 2008), and between the three single-crystal X-ray diffraction experiments reported in Loubeyre et al. (1999). It is worth noting the higher data density in our experiments in comparison to previous works. A compilation of data points measured in the  $P$ -ranges from 30-50, 40-60 and 80-130 GPa in dDAC-1, dDAC-2 and dDAC-3 is given in Table 3.1, with a comparison to previous works. The capability of our experimental setup to collect a large number of points in short experimental time makes our data unique in terms of  $P$ -resolution and constitutes a significant advance relative to previous works. In our measurements, the sample is compressed by the PEA at a constant rate, with alignment ensured by the design of the housing (Jenei et al. 2019). During compression, X-ray diffraction patterns are continuously and automatically collected, resulting in only small scatter of collected volume data. The scatter that we see in our data within one run is significantly smaller than in previously reported data (Wolanin et al. 1997; Loubeyre et al. 1999; Sugimura et al. 2008). In static DAC experiments, an evenly spaced compression of the sample relies on the dexterity of the operator tightening the screws. After compression, the sample is aligned and the diffraction image is collected with rotation to improve the statistics of diffraction. As these steps may take several minutes, ice crystals may break or grow before diffraction is collected (this behavior was also reported in Hemley et al. 1987). This strictly means that a different sample is measured each time which may contribute to the data scatter observed in static DAC experiments.

### 3.1 COMPRESSION BEHAVIOR OF H<sub>2</sub>O ACROSS THE ICE VII – ICE X TRANSITION

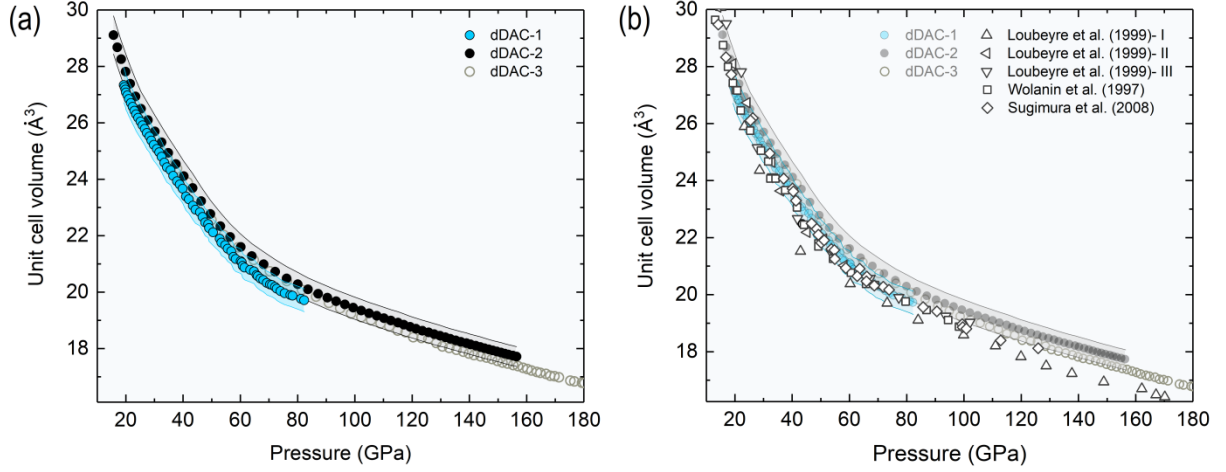


**Figure 3.1:** (a) Volume-pressure points for H<sub>2</sub>O ice as derived from the reduced datasets of the dDAC-1 (blue solid circles), dDAC-2 (black solid circles) and dDAC-3 data (grey open circles). Error bands using the resolution limit (0.05° in 2θ) of the fitting routine are shown for dDAC-1 and dDAC-2 (shaded regions). (b) Previous XRD measurements in static DAC experiments by Wolanin et al. (1997) (powder, squares), Sugimura et al. (2008) (powder, diamonds) and Loubeyre et al. (1999) (three single-crystal datasets, three differently pointing triangles) are plotted in comparison to our data.

	30-50 GPa	40-60 GPa	80-130 GPa	Total # data points
Wolanin <i>et al.</i> 1997	9	7	4	<b>32</b>
Loubeyre <i>et al.</i> 1999 (exp-I)	1	1	4	<b>18</b>
Loubeyre <i>et al.</i> 1999 (exp-II)	3	1	1	<b>12</b>
Loubeyre <i>et al.</i> 1999 (exp-III)	3	2	-	<b>7</b>
Sugimura <i>et al.</i> 2008	9	12	7	<b>33</b>
Hemley <i>et al.</i> 1987	3	3	12	<b>36</b>
dDAC-1 (raw)	<b>463</b>	<b>493</b>	<b>442</b>	<b>1800</b>
dDAC-2 (raw)	<b>74</b>	<b>62</b>	<b>159</b>	<b>590</b>
dDAC-3 (raw)	<b>29</b>	<b>24</b>	<b>79</b>	<b>305</b>

**Table 3.1:** Compilation of the number of data points collected in previous static DAC diffraction experiments in comparison to our work, separated over various  $P$ -ranges.

Previous works had to rely on equation of state formalisms to fit  $V(P)$  data and obtain  $K_T$ . In contrast, we directly derive the isothermal bulk modulus ( $K_T$ ) from the obtained high-density  $V(P)$  data via  $K_T = -V \cdot \partial P / \partial V$ , with the advantage that no assumption has to be made with respect to the analytical form of an equation-of-state. The resulting bulk modulus as a function of pressure is shown in Figure 3.2 for our three experimental runs. We find three distinct changes in the slope of  $K_T$ :

- (i) A softening starting at  $P=35-40$  GPa indicates a transition towards a more compressible state. We associate this change with the formation of disordered ice VII'. The enhanced compressibility of the ice VII' may be explained by a decrease in the "proton pressure" when protons start moving after  $H_2O$  molecule dissociation. The concept of "proton pressure" in this context was earlier introduced by Benoit and Marx (2005) and by Sugimura et al. (2008).
- (ii) A steep increase in  $K_T$  starting at  $P=50-55$  GPa marks the formation of a less compressible phase. The observed decrease in compressibility in  $H_2O$  ice may be explained by the transformation of a broad double-well potential into an effective single-well, denoting the onset of the hydrogen-bond symmetrization, as predicted almost 50 years ago by Holzapfel (1972). We attribute this feature to the formation of ice X'.
- (iii) A distinct change in  $P$ -dependence of  $K_T$  at  $P=90-110$  GPa, which has not been documented by previous experiments on the elastic properties of ice VII as they were limited to  $P < 100$  GPa. We attribute this change to the formation of static ice X.

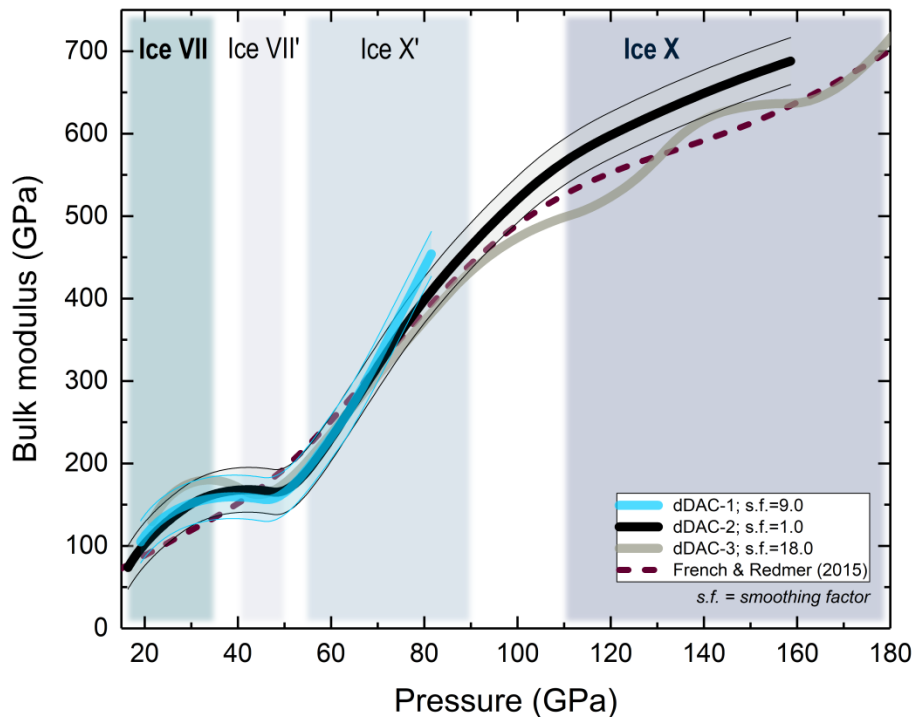


**Figure 3.2:** Bulk modulus of  $H_2O$  ice as a function of pressure calculated from the smoothed spline interpolation of the  $V(P)$  data from dDAC-1, dDAC-2 and dDAC-3. Thin lines along the curves represent the error in  $K_T$  propagated from the minimal separable peak distance in the Python routine ( $0.05^\circ$  in  $2\theta$ ). Dashed line represents reported data in French and Redmer (2015). Background colours guide the eyes to the approximate  $P$ -ranges for the stability of ice VII, ice VII', ice X' and ice X based on the  $P$ -ranges where a quasi-linear  $P$ -dependence of  $K_T$  is observed in our work.

### 3.1 COMPRESSION BEHAVIOR OF H<sub>2</sub>O ACROSS THE ICE VII – ICE X TRANSITION

In our experiments, the observed  $P$ -evolution of  $K_T$  across the ice VII – ice X transition is smooth with four quasi-linear regimes that can be correlated to the predicted changes in the energy potential (Holzapfel 1972; Benoit et al. 1998, 2002; Benoit and Marx 2005). Previous computational works documented only three transition regimes: ice VII – ice VII'/ice X' – ice X (Caracas 2008; French and Redmer 2015). Computational models rely on calculating properties related to the energy potential with a number of approximations that make it difficult to identify subtle modifications in proton localization, i.e., ice VII-ice VII' and ice X'-ice X. Furthermore, the subtle changes in compression behavior documented in our work are hardly resolvable by the limited  $P$ -coverage in previous experimental datasets. For instance, Hemley et al. (1987), used one equation of state to fit 33 data points in the  $P$ -range from 4-128 GPa (Table 3.1). These data were used by current interior models of ocean planets (Sotin et al. 2007; Valencia et al. 2007) that were based on the assumption that ice VII and ice X have a similar behavior (Brugger et al. 2017: „As for silicate rocks, water ice presents high-pressure phases that have been measured through laboratory experiments, such as the ice VII–ice X transition around 70 GPa, ice X having a behavior still close to that of ice VII (Sotin et al. 2007).“). Our data show that the bulk modulus of ice X is distinctly higher than that of ice VII and suggest that at least two equations of state should be used to fit  $V(P)$  in the  $P$ -range over which the ice VII – ice X transition occurs.

Our experiments provide the first experimental data of the bulk modulus of H<sub>2</sub>O ice up to pressures of 180 GPa. Our results provide valuable information to constrain interior models of H<sub>2</sub>O-rich planets. Furthermore, the bulk modulus of ice X is comparable to that of Earth's mantle minerals such as bridgmanite (Ballaran et al. 2012) and ferropericlase (Marquardt et al. 2009). The high bulk modulus of ice in combination with its low density in comparison to known mantle minerals may have important implications for the geodynamics of H<sub>2</sub>O-rich exoplanets.



## 3.2 Compression behavior of ferropericlase across the spin crossover

The following subsection summarizes the main results of the manuscript included in chapter 5:

*“Elastic softening of ferropericlase across the iron spin crossover constrained by time-resolved XRD experiments and computations”*

A. S. J. Méndez, S. Stackhouse, A. Kurnosov, N. Satta, H.-P. Liermann, R. J. Husband and H. Marquardt

Status: *In preparation*

**Individual contributions:** *Together with Hauke Marquardt and Hanns-Peter Liermann, I designed and performed the experiments. Alexander Kurnosov and Niccolò Satta, supported the experiments. Together with Hauke Marquardt, I analyzed the data. Stephen Stackhouse performed and analyzed the ab-initio computations of iron electronic configurations. Together with Hauke Marquardt and Stephen Stackhouse, I wrote the manuscript.*

(Mg,Fe)O ferropericlase is the second most abundant mineral in Earth’s lower mantle as well as super-Earth exoplanets (Duffy et al. 2015; Irifune and Tsuchiya 2015). At pressures of about 40 GPa (1300 km depth), the electronic configuration of iron in ferropericlase changes from a high spin to a low spin state (Badro 2003; Lin et al. 2013). The iron spin crossover is a gradual transformation that extends over several GPa in pressure and is accompanied by an elastic softening in the bulk modulus of ferropericlase (Crowhurst et al. 2008; Wentzcovitch et al. 2009), with possible implications for the interpretation of seismic data (Cammarano et al. 2010). As previously discussed in section 1.3, direct measurements of the bulk modulus of (Mg,Fe)O (Crowhurst et al. 2008; Yang et al. 2015; Marquardt et al. 2018) as well as computations (Tsuchiya et al. 2006; Marquardt et al. 2009; Wentzcovitch et al. 2009; Mao et al. 2011; Lin et al. 2013; Holmström and Stixrude 2015) suggest largely different pressure ranges over which the spin crossover occurs and different magnitudes of the elastic softening. Furthermore, the influence of iron-iron interactions as a function of iron content is poorly understood. Here, we performed dynamic compression on polycrystalline (Mg<sub>0.9</sub>Fe<sub>0.1</sub>)O and (Mg<sub>0.8</sub>Fe<sub>0.2</sub>)O employing a piezo-driven dynamic Diamond Anvil Cell (dDAC) and monitored the compression behavior of the sample using time-resolved X-ray diffraction. We complemented our experimental results by *ab-initio* calculations where we use multiple models with random configurations of iron, and presumed a regular solution for high- and low-spin, in order to understand the effect of iron-iron interactions on the elastic softening.

Powders of (Mg<sub>0.9</sub>Fe<sub>0.1</sub>)O and (Mg<sub>0.8</sub>Fe<sub>0.2</sub>)O are mixed with Pt-powder (*P*-marker) and loaded with Ne as pressure-transmitting medium. Trapezoidal voltage-time waveforms were applied to

### **Chapter 3. SYNOPSIS**

compress the samples in the dDAC. Intense monochromatic synchrotron X-radiation with a fixed wavelength (0.4821 Å) was used to measure time-resolved diffraction along the compression paths. We collected 549 diffraction images for (Mg<sub>0.9</sub>Fe<sub>0.1</sub>)O with a single-exposure time of 400 ms and 320 diffraction images for (Mg<sub>0.8</sub>Fe<sub>0.2</sub>)O with a single-exposure time of 200 ms. A MATLAB code for batch data processing (section 2.4.2) was employed to analyze the integrated X-ray diffraction patterns.  $P$  was determined from the measured position of the (111) diffraction line of platinum, Pt<sub>(111)</sub>, using published equation of state parameters (Fei et al. 2007). The lattice parameter of the sample is determined by fitting the (111), (200), and (220) diffraction lines of ferropericlase. We calculate the bulk modulus from the slope of a linear fit of  $V(P)$  applied over a pressure interval of 2.5 GPa every 1 GPa. The error in slope of the linear fit is propagated into the reported bulk modulus uncertainty. The bulk moduli are plotted as a function of pressure in Fig. 3.3, together with the here-performed ab-initio calculations.

Both measured and calculated bulk moduli for (Mg<sub>0.9</sub>Fe<sub>0.1</sub>)O and (Mg<sub>0.8</sub>Fe<sub>0.2</sub>)O show a remarkable drop at a pressure of about 40-45 GPa associated with the spin crossover, where the onset pressure seems to slightly shift to higher pressures with iron content. Our experiments as well as computations suggest a broad and asymmetric shape of the softening over a pressure range of at least 30 GPa. Our data also reveal a multi-dip structure where (at least) two local minima are noticeable in the experimental data. Our ab-initio calculations predict a bulk modulus behavior that is in good agreement with our experiments. In our ab-initio calculations, we average the results for multiple models with random iron configurations, and assumed a regular solution for high- and low-spin iron, as opposed to an ideal solution. All of the above observations suggest that the broadness and shape of the elastic softening is a result of a mixed spin state and is sensitive to the distribution of iron atoms. Our results suggest that the seismic signature of the iron spin crossover in the lower mantle might be different than previously assumed and possible implications for current interior models should be evaluated.

### 3.2 COMPRESSION BEHAVIOR OF FERROPERICLASE ACROSS THE SPIN CROSSOVER

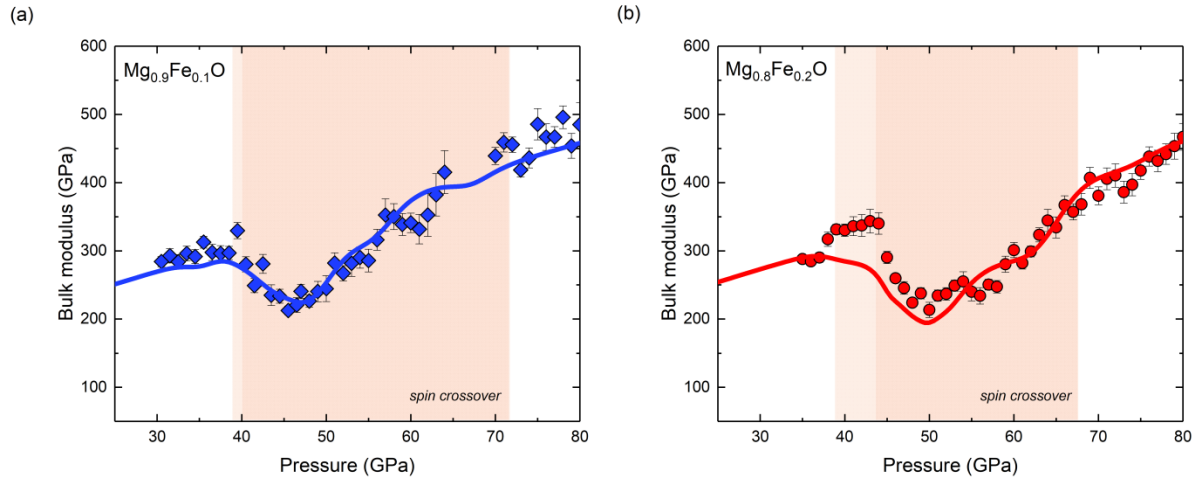


**Figure 3.3:** Bulk moduli derived by direct differentiation of our experimentally measured volumes, derived from the (200) reflection, (symbols) in comparison to our ab-initio calculations (line), using multiple models with random configurations of iron, and presuming a regular solution for high- and low-spin. (a) Results for  $(\text{Mg}_{0.9}\text{Fe}_{0.1})\text{O}$ . (b) Bulk moduli derived for  $(\text{Mg}_{0.8}\text{Fe}_{0.2})\text{O}$ . The shaded area shows the approximate region where the iron spin crossover occurs (dark shaded: experiments; light shaded: computations).



### 3.3 A Resistively-Heated dynamic Diamond Anvil Cell

The following subsection summarizes the main results of the manuscript included in chapter 6:

*“A resistively-heated dynamic diamond anvil cell (RHdDAC) for fast compression x-ray diffraction experiments at high temperatures”*

A. S. J. Méndez, H. Marquardt, R. J. Husband, I. Schwark, J. Mainberger, K. Glazyrin,  
A. Kurnosov, C. Otzen, N. Satta, J. Bednarcik, and H.-P. Liermann

Status: Published by *Review of Scientific Instruments*  
(14 July 2020)

**Individual contributions:** *The design of the RHdDAC setup was carried out by Hanns-Peter Liermann, Iris Schwark, and me. Together with Rachel J. Husband, Hanns-Peter Liermann and Hauke Marquardt, I designed and performed all the presented experiments including the calibration measurements. I processed and analyzed the presented diffraction data. Together with Hauke Marquardt and Hanns-Peter Liermann, I wrote the manuscript.*

Density, phase diagram and compression behavior measurements at combined high pressures and temperature are poorly constrained for most planetary materials, including H<sub>2</sub>O and (Mg,Fe)O ferropericlase. Particularly, experimental data on the elastic properties of H<sub>2</sub>O ice and (Mg,Fe)O at high-*P/T* are essential to constrain planetary interior models. Conventional experimental techniques to measure the elastic response of minerals at high-pressures in DAC experiments, demand long signal-collection times, making it difficult to perform high-temperature experiments (*see* Introduction). We implemented a resistive-heated DAC setup that is compatible with the employment of a piezoelectric actuator (PEA) that permits fast compression of samples at high-temperatures, reducing experimental times significantly. The RHdDAC setup is equipped with a sophisticated cooling system that enables the employment of piezo actuators for compression of samples at high temperatures. Details of the setup are given in section 2.3.

We used the novel setup to perform dynamic compression across the ice VII – ice X transition at 450, 625, 865 and 1043 K up to pressures of about 110 GPa, while simultaneously collecting quasi-continuous diffraction data employing the GaAs LAMBDA detectors at the ECB (Pennicard et al. 2013, 2018; Liermann et al. 2015). H<sub>2</sub>O was loaded in the RHdDAC along with Au powder (*P*-marker). Amorphous gaskets were employed to avoid the appearance of parasitic peaks in the diffraction patterns (Fig. X). The temperature was increased in steps of 100 K until reaching the target temperature, collecting diffraction images at each step. A pressure increase observed during heating in all the experiments was possibly due to the overall thermal expansion of the

DAC. Once the target temperature was reached, the sample was continuously compressed using the PEA while collecting time-resolved X-ray diffraction data. Trapezoidal voltage–time waveforms were applied with nominal compression rates ranging from 0.1 GPa/s to 0.3 GPa/s. Each of our experiments was completed in about 40 minutes, including the initial heating. We collected 521 diffraction images at 450 K, 544 at 625 K, 531 at 865 K and 193 at 1043 K. The  $P$ - $T$  regimes explored in our experiments are plotted in Fig. 3.4. It is worth noting that no reaction products between sample and gasket were detected in our experiments by X-ray diffraction and Raman spectroscopy measurements. Detailed data analysis is ongoing.

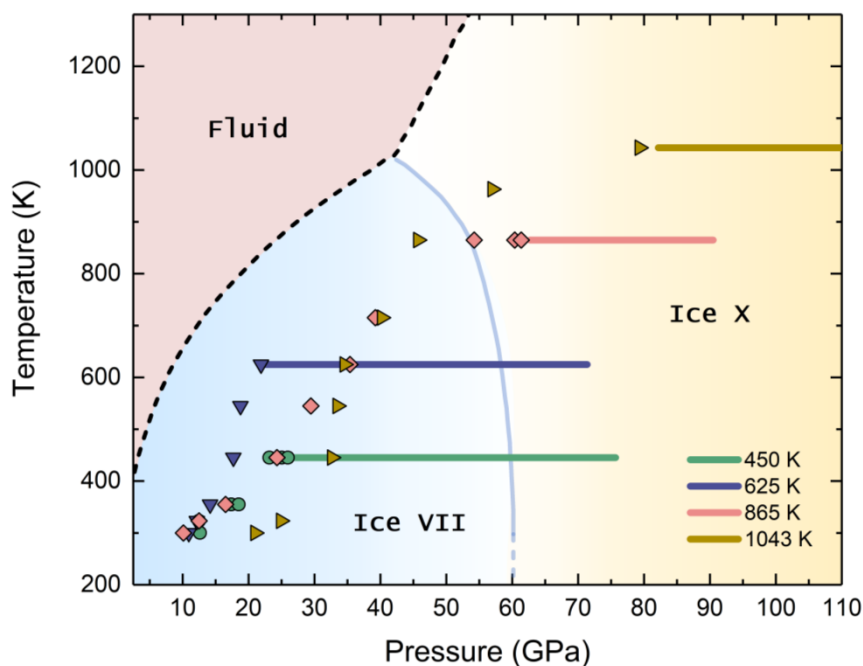


**Figure 3.4:** Experimental conditions reached during the experiments superimposed on the phase diagram of H<sub>2</sub>O. Symbols (triangles, diamonds and circles) represent experimental conditions where diffraction data are collected while increasing the temperature and lines depict the pressure range covered during the dynamic compression at constant  $T$ . Pressure is determined from the (111) diffraction line of gold using published equation of state parameters (Anderson et al. 1989). A solid blue line defines the ice VII-ice X boundary from Sugimura et al. (2012).

We also performed oscillation experiments on (Mg<sub>0.8</sub>Fe<sub>0.2</sub>)O at different  $P$ - $T$  in the RHdDAC (see also Marquardt et al. 2018). The sample was mixed with Pt powder ( $P$ -marker) and loaded in an amorphous gasket. After achieving a good vacuum and stable cooling conditions in the RHdDAC, the sample was heated up to a target temperature, taking diffraction images every 50 K. At each  $T$ -step, sinusoidal pressure oscillations with a frequency of 0.2 Hz were applied to the sample. Diffraction images were continuously collected by the GaAS LAMBDA detectors with single image exposure times of 200 ms. Integrated patterns were analyzed using the MATLAB code described in section 2.4.2. For a preliminary analysis at an experiment carried out at 1400 K and

~122 GPa, the (200) diffraction line of ferropericlase, and the (111) diffraction line of Pt were chosen to derive the unit cell volume and the pressure, respectively (Fig. 3.5). The collected data demonstrate the potential of the RHdDAC to directly quantify the sample's bulk modulus at high-temperature and pressures of the core-mantle-boundary, according to its thermodynamic definition ( $K=-V\cdot\partial P/\partial V$ ).

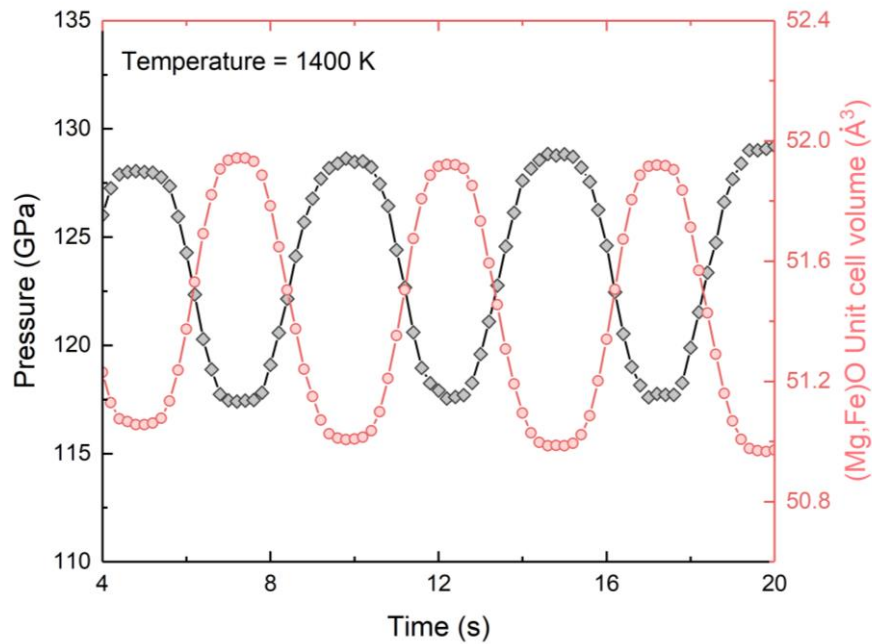


**Figure 3.5:** Platinum pressure and unit cell volume of ferropericlase as a function of time. Pressure is determined using published equation of state parameters of Fei et al. (2007). The response of both phases, platinum and ferropericlase, is in phase throughout the duration of the experiment.



### 3.4 Outlook

I have used piezo-driven dynamic DACs in combination with time-resolved X-ray diffraction to investigate the compression behavior of two different materials across  $n$ -order phase transitions: the H<sub>2</sub>O ice VII – ice X phase transition and the (Mg,Fe)O iron spin crossover. I have developed an approach to calculate the bulk modulus directly from quasi-continuous diffraction data.

These results show the potential of using time-resolved x-ray diffraction in the dynamic DAC to investigate the compression behavior of mantle minerals. The novel approach has three major advantages: (1) the bulk modulus can be calculated directly from diffraction data, (2) the quasi-continuous  $P$ -coverage resolves subtle features in the compression behavior associated to  $n$ -order phase transitions, and (3) experimental times can be minimized to a few minutes. The novel setup has the potential to study thermal effects on the compression behavior of planetary materials at high pressure, relevant to constrain planetary interior models.



## References

- Ahart, M., Somayazulu, M., Gramsch, S. A., Boehler, R., Mao, H., and Hemley, R. J. (2011) Brillouin scattering of H<sub>2</sub>O ice to megabar pressures. *The Journal of Chemical Physics*, 134, 124517.
- Anderson, O. L., Isaak, D. G., and Yamamoto, S. (1989) Anharmonicity and the equation of state for gold. *Journal of Applied Physics*, 65, 1534–1543.
- Aoki, K., Yamawaki, H., Sakashita, M., and Fujihisa, H. (1996) Infrared absorption study of the hydrogen-bond symmetrization in ice to 110 GPa. *Physical Review B*, 54, 15673–15677.
- Asahara, Y., Hirose, K., Ohishi, Y., Hirao, N., and Murakami, M. (2010) Thermoelastic properties of ice VII and its high-pressure polymorphs: Implications for dynamics of cold slab subduction in the lower mantle. *Earth and Planetary Science Letters*, 299, 474–482.
- Badro, J. (2003) Iron Partitioning in Earth's Mantle: Toward a Deep Lower Mantle Discontinuity. *Science*, 300, 789–791.
- Ballaran, T. B., Kurnosov, A., Glazyrin, K., Frost, D. J., Merlini, M., Hanfland, M., and Caracas, R. (2012) Effect of chemistry on the compressibility of silicate perovskite in the lower mantle. *Earth and Planetary Science Letters*, 333–334, 181–190.
- Balzaretti, N. M., Gonzalez, E.J., Piermarini, G.J., and Russell, T.P. (1999) Resistance heating of the gasket in a gem-anvil high pressure cell. *Review of Scientific Instruments*, 70, 4316–4323.
- Benoit, M., and Marx, D. (2005) The Shapes of Protons in Hydrogen Bonds Depend on the Bond Length. *ChemPhysChem*, 6, 1738–1741.
- Benoit, M., Marx, D., and Parrinello, M. (1998) Tunnelling and zero-point motion in high-pressure ice. *Nature*, 392, 258–261.
- Benoit, M., Romero, A. H., and Marx, D. (2002) Reassigning Hydrogen-Bond Centering in Dense Ice. *Physical Review Letters*, 89, 145501.
- Bernal, J. D., and Fowler, R. H. (1933) A Theory of Water and Ionic Solution, with Particular Reference to Hydrogen and Hydroxyl Ions. *The Journal of Chemical Physics*, 1, 515–548.
- Bernasconi, M., Silvestrelli, P. L., and Parrinello, M. (1998) *Ab Initio* Infrared Absorption Study of the Hydrogen-Bond Symmetrization in Ice. *Physical Review Letters*, 81, 1235–1238.
- Bragg, W. L., and Bragg, W. H. (1914) The analysis of crystals by the X-ray spectrometer. *Proceedings of the Royal Society of London. Series A, Containing Papers of a Mathematical and Physical Character*, 89, 468–489.
- Brugger, B., Mousis, O., Deleuil, M., and Deschamps, F. (2017) Constraints on Super-Earth Interiors from Stellar Abundances. *The Astrophysical Journal*, 850, 93.

## References

- Buchen, J., Marquardt, H., Ballaran, T. B., Kawazoe, T., and McCammon, C. (2017) The equation of state of wadsleyite solid solutions: Constraining the effects of anisotropy and crystal chemistry. *American Mineralogist*, 102, 2494–2504.
- Buchen, J., Marquardt, H., Schulze, K., Speziale, S., Boffa Ballaran, T., Nishiyama, N., and Hanfland, M. (2018) Equation of State of Polycrystalline Stishovite Across the Tetragonal-Orthorhombic Phase Transition. *Journal of Geophysical Research: Solid Earth*, 123, 7347–7360.
- Burns, R.G. (1993) *Mineralogical Applications of Crystal Field Theory*, 2nd ed. Cambridge University Press, Cambridge.
- Cammarano, F., Marquardt, H., Speziale, S., and Tackley, P. J. (2010) Role of iron-spin transition in ferropericlase on seismic interpretation: A broad thermochemical transition in the mid mantle? *Geophysical Research Letters*, 37.
- Caracas, R. (2008) Dynamical Instabilities of Ice X. *Physical Review Letters*, 101, 085502.
- Chen, B., Jackson, J. M., Sturhahn, W., Zhang, D., Zhao, J., Wicks, J. K., and Murphy, C.A. (2012) Spin crossover equation of state and sound velocities of  $(\text{Mg}_{0.65}\text{Fe}_{0.35})\text{O}$  ferropericlase to 140 GPa: EoS and Sound Velocities of  $(\text{Mg,Fe})\text{o}$ . *Journal of Geophysical Research: Solid Earth*, 117, n/a-n/a.
- Chen, J.-Y., and Yoo, C.-S. (2011) High density amorphous ice at room temperature. *Proceedings of the National Academy of Sciences*, 108, 7685–7688.
- Chen, J.-Y., and Yoo, C.-S. (2012) Formation and phase transitions of methane hydrates under dynamic loadings: Compression rate dependent kinetics. *The Journal of Chemical Physics*, 136, 114513.
- Chen, J.-Y., Kim, M., Yoo, C.-S., Liermann, H.-P., and Evans, W. J. (2014) Time-resolved x-ray diffraction across water-ice-VI/VII transformations using the *dynamic* -DAC. *Journal of Physics: Conference Series*, 500, 142006.
- Crowhurst, J. C., Brown, J. M., Goncharov, A. F., and Jacobsen, S. D. (2008) Elasticity of  $(\text{Mg,Fe})\text{O}$  Through the Spin Transition of Iron in the Lower Mantle. *Science*, 319, 451–453.
- Dierckx, P. (1982) A Fast Algorithm for Smoothing Data on a Rectangular Grid while Using Spline Functions. *SIAM Journal on Numerical Analysis*, 19, 1286–1304.
- Dierckx, P. (1975) An algorithm for smoothing, differentiation and integration of experimental data using spline functions.
- Du, Z., Miyagi, L., Amulele, G., and Lee, K. K. M. (2013) Efficient graphite ring heater suitable for diamond-anvil cells to 1300 K. *Review of Scientific Instruments*, 84, 024502.
- Duffy, T., Madhusudhan, N., and Lee, K. K. M. (2015) *Mineralogy of Super-Earth Planets*. In *Treatise on Geophysics* pp. 149–178. Elsevier.

## References

- Dziewonski, A. M., and Anderson, D. L. (1981) Preliminary reference Earth model. *Physics of the Earth and Planetary Interiors*, 25, 297–356.
- Evans, W. J., Yoo, C.-S., Lee, G. W., Cynn, H., Lipp, M. J., and Visbeck, K. (2007) Dynamic diamond anvil cell (dDAC): A novel device for studying the dynamic-pressure properties of materials. *Review of Scientific Instruments*, 78, 073904.
- Fei, Y., Zhang, L., Corgne, A., Watson, H., Ricolleau, A., Meng, Y., and Prakapenka, V. (2007) Spin transition and equations of state of (Mg,Fe)O solid solutions. *Geophysical Research Letters*, 34, L17307.
- Fei, Y., Ricolleau, A., Frank, M., Mibe, K., Shen, G., and Prakapenka, V. (2007) Toward an internally consistent pressure scale. *Proceedings of the National Academy of Sciences*, 104, 9182–9186.
- Fortes, A. D., and Choukroun, M. (2010) Phase Behaviour of Ices and Hydrates. *Space Science Reviews*, 153, 185–218.
- Fortney, J. J., and Nettelmann, N. (2010) The Interior Structure, Composition, and Evolution of Giant Planets. *Space Science Reviews*, 152, 423–447.
- Frank, M. R., Fei, Y., and Hu, J. (2004) Constraining the equation of state of fluid H<sub>2</sub>O to 80 GPa using the melting curve, bulk modulus, and thermal expansivity of Ice VII. *Geochimica et Cosmochimica Acta*, 68, 2781–2790.
- French, M., and Redmer, R. (2015) Construction of a thermodynamic potential for the water ices VII and X. *Physical Review B*, 91, 014308.
- French, M., Desjarlais, M. P., and Redmer, R. (2016) *Ab initio* calculation of thermodynamic potentials and entropies for superionic water. *Physical Review E*, 93, 022140.
- Frost, M., Kim, J. B., McBride, E. E., Peterson, J. R., Smith, J. S., Sun, P., and Glenzer, S. H. (2019) High-Pressure Melt Curve and Phase Diagram of Lithium. *Physical Review Letters*, 123, 065701.
- Glazyrin, K., Miyajima, N., Smith, J. S., and Lee, K. K. M. (2016) Compression of a multiphase mantle assemblage: Effects of undesirable stress and stress annealing on the iron spin state crossover in ferropericlase: Stresses and HS-LS Crossover in (Mg,Fe)O. *Journal of Geophysical Research: Solid Earth*, 121, 3377–3392.
- Goncharov, A. F., Struzhkin, V. V., Somayazulu, M. S., Hemley, R. J., and Mao, H. K. (1996) Compression of Ice to 210 Gigapascals: Infrared Evidence for a Symmetric Hydrogen-Bonded Phase. *Science*, 273, 218–220.
- Goncharov, A. F., Goldman, N., Fried, L. E., Crowhurst, J. C., Kuo, I.-F. W., Mundy, C. J., and Zaug, J. M. (2005) Dynamic Ionization of Water under Extreme Conditions. *Physical Review Letters*, 94, 125508.

## References

- Guthrie, M., Boehler, R., Molaison, J. J., Haberl, B., dos Santos, A. M., and Tulk, C. (2019) Structure and disorder in ice VII on the approach to hydrogen-bond symmetrization. *Physical Review B*, 99, 184112.
- He, D., Zhao, Y., Sheng, T. D., Schwarz, R. B., Qian, J., Lokshin, K. A., Bobev, S., Daemen, L. L., Mao, H.K., Hu, J.Z., and others (2003) Bulk metallic glass gasket for high pressure, *in situ* x-ray diffraction. *Review of Scientific Instruments*, 74, 3012–3016.
- Hemley, R. J., Jephcoat, A. P., Mao, H. K., Zha, C. S., Finger, L. W., and Cox, D. E. (1987) Static compression of H<sub>2</sub>O-ice to 128 GPa (1.28 Mbar), 4.
- Hernandez, J.-A., and Caracas, R. (2018) Proton dynamics and the phase diagram of dense water ice. *The Journal of Chemical Physics*, 148, 214501.
- Hobbs, P. V., Chang, S., and Locatelli, J. D. (1974) The dimensions and aggregation of ice crystals in natural clouds. *Journal of Geophysical Research (1896-1977)*, 79, 2199–2206.
- Holmström, E., and Stixrude, L. (2015) Spin Crossover in Ferropicardite from First-Principles Molecular Dynamics. *Physical Review Letters*, 114, 117202.
- Holzappel, W. B. (1972) On the Symmetry of the Hydrogen Bonds in Ice VII. *The Journal of Chemical Physics*, 56, 712–715.
- Irfune, T., and Tsuchiya, T. (2015) Phase Transitions and Mineralogy of the Lower Mantle. In *Treatise on Geophysics* pp. 33–60. Elsevier.
- Ishii, T., Huang, R., Fei, H., Koemets, I., Liu, Z., Maeda, F., Yuan, L., Wang, L., Druzhbin, D., Yamamoto, T., and others (2018) Complete agreement of the post-spinel transition with the 660-km seismic discontinuity. *Scientific Reports*, 8, 6358.
- Jayaraman, A. (1983) Diamond anvil cell and high-pressure physical investigations. *Reviews of Modern Physics*, 55, 65–108.
- Jenei, Zs., Liermann, H.P., Husband, R., Méndez, A. S. J., Pennicard, D., Marquardt, H., O'Bannon, E. F., Pakhomova, A., Konopkova, Z., Glazyrin, K., and others (2019) New dynamic diamond anvil cells for tera-pascal per second fast compression x-ray diffraction experiments. *Review of Scientific Instruments*, 90, 065114.
- Journaux, B., Daniel, I., Petitgirard, S., Cardon, H., Perrillat, J.-P., Caracas, R., and Mezouar, M. (2017) Salt partitioning between water and high-pressure ices. Implication for the dynamics and habitability of icy moons and water-rich planetary bodies. *Earth and Planetary Science Letters*, 463, 36–47.
- Klotz, S., Chervin, J.-C., Munsch, P., and Marchand, G. L. (2009) Hydrostatic limits of 11 pressure transmitting media. *Journal of Physics D: Applied Physics*, 42, 075413.
- Klotz, S., Komatsu, K., Kagi, H., Kunc, K., Sano-Furukawa, A., Machida, S., and Hattori, T. (2017) Bulk moduli and equations of state of ice VII and ice VIII. *Physical Review B*, 95, 174111.

## References

- Korenaga, J., Planavsky, N. J., and Evans, D. A. D. (2017) Global water cycle and the coevolution of the Earth's interior and surface environment. *Philosophical transactions. Series A, Mathematical, physical, and engineering sciences*, 375.
- Lavina, B., Dera, P., and Downs, R. T. (2014) Modern X-ray Diffraction Methods in Mineralogy and Geosciences. *Reviews in Mineralogy and Geochemistry*, 78, 1–31.
- Lee, G. W., Evans, W. J., and Yoo, C.-S. (2006) Crystallization of water in a dynamic diamond-anvil cell: Evidence for ice VII-like local order in supercompressed water. *Physical Review B*, 74, 134112.
- Lee, G. W., Evans, W. J., and Yoo, C.-S. (2007) Dynamic pressure-induced dendritic and shock crystal growth of ice VI. *Proceedings of the National Academy of Sciences*, 104, 9178–9181.
- Léger, A., Selsis, F., Sotin, C., Guillot, T., Despois, D., Mawet, D., Ollivier, M., Labèque, A., Valette, C., Brachet, F., and others (2004) A new family of planets? "Ocean-Planets." *Icarus*, 169, 499–504.
- Li, X., Shi, W., Liu, X., and Mao, Z. (2019) High-pressure phase stability and elasticity of ammonia hydrate. *American Mineralogist*, 104, 1307–1314.
- Liermann, H.-P., Morgenroth, W., Ehnes, A., Berghäuser, A., Winkler, B., Franz, H., and Weckert, E. (2010) The Extreme Conditions Beamline at PETRA III, DESY: Possibilities to conduct time resolved monochromatic diffraction experiments in dynamic and laser heated DAC. *Journal of Physics: Conference Series*, 215, 012029.
- Liermann, H.-P., Konôpková, Z., Morgenroth, W., Glazyrin, K., Bednarčík, J., McBride, E.E., Petitgirard, S., Delitz, J. T., Wendt, M., Bican, Y., and others (2015) The Extreme Conditions Beamline P02.2 and the Extreme Conditions Science Infrastructure at PETRA III. *Journal of Synchrotron Radiation*, 22, 908–924.
- Lin, C., Smith, J. S., Sinogeikin, S. V., Park, C., Kono, Y., Kenney-Benson, C., Rod, E., and Shen, G. (2016) Kinetics of the B1-B2 phase transition in KCl under rapid compression. *Journal of Applied Physics*, 119, 045902.
- Lin, J.-F. (2005) Melting behavior of H<sub>2</sub>O at high pressures and temperatures. *Geophysical Research Letters*, 32, L11306.
- Lin, J.-F., Speziale, S., Mao, Z., and Marquardt, H. (2013) Effects of the electronic spin transitions of iron in lower mantle minerals: implications for deep mantle geophysics and geochemistry: spin transition in lower mantle. *Reviews of Geophysics*, 51, 244–275.
- Lin, L., Morrone, J. A., and Car, R. (2011) Correlated Tunneling in Hydrogen Bonds. *Journal of Statistical Physics*, 145, 365–384.

## References

- Loubeyre, P., LeToullec, R., Wolanin, E., Hanfland, M., and Hausermann, D. (1999) Modulated phases and proton centring in ice observed by X-ray diffraction up to 170 GPa. *Nature*, 397, 503–506.
- Lu, X. Z., Zhang, Y., Zhao, P., and Fang, S. J. (2011) Vibrational Analysis of the Hydrogen-Bond Symmetrization in Ice. *The Journal of Physical Chemistry B*, 115, 71–74.
- Mao, H., Hemley, R. J., Jephcoat, A. P., Angel, R. J., and O’Nions, R. K. (1996) Experimental studies of Earth’s deep interior: accuracy and versatility of diamond-anvil cells. *Philosophical Transactions of the Royal Society of London. Series A: Mathematical, Physical and Engineering Sciences*, 354, 1315–1332.
- Mao, H. K., Bell, P. M., Dunn, K. J., Chrenko, R. M., and DeVries, R. C. (1979) Absolute pressure measurements and analysis of diamonds subjected to maximum static pressures of 1.3–1.7 Mbar. *Review of Scientific Instruments*, 50, 1002–1009.
- Mao, Z., Lin, J.-F., Liu, J., and Prakapenka, V. B. (2011) Thermal equation of state of lower-mantle ferropericlase across the spin crossover. *Geophysical Research Letters*, 38.
- Marquardt, H., and Thomson, A. R. (2020) Experimental elasticity of Earth’s deep mantle. *Nature Reviews Earth & Environment*, 1, 455–469.
- Marquardt, H., Speziale, S., Reichmann, H. J., Frost, D. J., and Schilling, F. R. (2009) Single-crystal elasticity of  $(\text{Mg}_{0.9}\text{Fe}_{0.1})\text{O}$  to 81 GPa. *Earth and Planetary Science Letters*, 287, 345–352.
- Marquardt, H., Buchen, J., Mendez, A. S. J., Kurnosov, A., Wendt, M., Rothkirch, A., Pennicard, D., and Liermann, H. -P. (2018) Elastic Softening of  $(\text{Mg}_{0.8}\text{Fe}_{0.2})\text{O}$  Ferropericlase Across the Iron Spin Crossover Measured at Seismic Frequencies. *Geophysical Research Letters*, 45, 6862–6868.
- Newville, M., Otten, R., Nelson, A., Ingargiola, A., Stensitzki, T., Allan, D., Fox, A., Carter, F., Michał, Pustakhod, D., and others (2020) *lmfit/lmfit-py 1.0.1*. Zenodo.
- McDonough, W., and Sun, S. S. (1995) The composition of the Earth. *Chem. Geol.*, 67, 1050–1056.
- Meier, T., Petitgirard, S., Khandarkhaeva, S., and Dubrovinsky, L. (2018) Observation of nuclear quantum effects and hydrogen bond symmetrisation in high pressure ice. *Nature Communications*, 9, 2766.
- Méndez, A. S. J., Marquardt, H., Husband, R. J., Schwark, I., Mainberger, J., Glazyrin, K., Kurnosov, A., Otzen, C., Satta, N., Bednarcik, J., and others (2020) A resistively-heated dynamic diamond anvil cell (RHdDAC) for fast compression x-ray diffraction experiments at high temperatures. *Review of Scientific Instruments*, 91, 073906.
- Meng, Y., Weidner, D. J., and Fei, Y. (1993) Deviatoric stress in a quasi-hydrostatic diamond anvil cell: Effect on the volume-based pressure calibration. *Geophysical Research Letters*, 20, 1147–1150.

## References

- Muir, J. M. R., and Brodholt, J.P. (2015) Elastic properties of ferrous bearing  $\text{MgSiO}_3$  and their relevance to ULVZs. *Geophysical Journal International*, 201, 496–504.
- Noack, L., Höning, D., Rivoldini, A., Heistracher, C., Zimov, N., Journaux, B., Lammer, H., Van Hoolst, T., and Bredehöft, J. H. (2016) Water-rich planets: How habitable is a water layer deeper than on Earth? *Icarus*, 277, 215–236.
- O’Handley, R. C. (1987) Physics of ferromagnetic amorphous alloys. *Journal of Applied Physics*, 62, R15–R49.
- Ong, S. P., Richards, W. D., Jain, A., Hautier, G., Kocher, M., Cholia, S., Gunter, D., Chevrier, V. L., Persson, K. A., and Ceder, G. (2013) Python Materials Genomics (pymatgen): A robust, open-source python library for materials analysis. *Computational Materials Science*, 68, 314–319.
- Pamato, M. G., Wood, I. G., Dobson, D. P., Hunt, S. A., and Vočadlo, L. (2018) The thermal expansion of gold: point defect concentrations and pre-melting in a face-centred cubic metal. *Journal of Applied Crystallography*, 51, 470–480.
- Pauling, L. (1935) The Structure and Entropy of Ice and of Other Crystals with Some Randomness of Atomic Arrangement. *Journal of the American Chemical Society*, 57, 2680–2684.
- Pearson, D. G., Brenker, F. E., Nestola, F., McNeill, J., Nasdala, L., Hutchison, M. T., Matveev, S., Mather, K., Silversmit, G., Schmitz, S., and others (2014) Hydrous mantle transition zone indicated by ringwoodite included within diamond. *Nature*, 507, 221–224.
- Pennicard, D., Lange, S., Smoljanin, S., Hirsemann, H., Graafsma, H., Epple, M., Zuvic, M., Lampert, M.-O., Fritzsche, T., and Rothermund, M. (2013) The LAMBDA photon-counting pixel detector. *Journal of Physics: Conference Series*, 425, 062010.
- Pennicard, D., Smoljanin, S., Pithan, F., Sarajlic, M., Rothkirch, A., Yu, Y., Liermann, H.-P., Morgenroth, W., Winkler, B., Jenei, Z., and others (2018) LAMBDA 2M GaAs—A multi-megapixel hard X-ray detector for synchrotrons. *Journal of Instrumentation*, 13, C01026–C01026.
- Prescher, C., and Prakapenka, V. B. (2015) *DIOPTAS*: a program for reduction of two-dimensional X-ray diffraction data and data exploration. *High Pressure Research*, 35, 223–230.
- Redmer, R., Mattsson, T. R., Nettelmann, N., and French, M. (2011) The phase diagram of water and the magnetic fields of Uranus and Neptune. *Icarus*, 211, 798–803.
- Regenauer-Lieb, K. (2006) Water and Geodynamics. *Reviews in Mineralogy and Geochemistry*, 62, 451–473.

## References

- Rivera, E. J., Lissauer, J. J., Butler, R. P., Marcy, G. W., Vogt, S. S., Fischer, D. A., Brown, T. M., Laughlin, G., and Henry, G. W. (2005) A  $\sim 7.5$  Earth-masses planet orbiting the nearby star, GJ 876. *The Astrophysical Journal*, 634, 625–640.
- Sano, A., Ohtani, E., Kondo, T., Hirao, N., Sakai, T., Sata, N., Ohishi, Y., and Kikegawa, T. (2008) Aluminous hydrous mineral  $\delta$ -AlOOH as a carrier of hydrogen into the core-mantle boundary. *Geophysical Research Letters*, 35, L03303.
- Schwager, B., and Boehler, R. (2008) H<sub>2</sub>O: another ice phase and its melting curve. *High Pressure Research*, 28, 431–433.
- Schwager, B., Chudinovskikh, L., Gavriiliuk, A., and Boehler, R. (2004) Melting curve of H<sub>2</sub>O to 90 GPa measured in a laser-heated diamond cell. *Journal of Physics: Condensed Matter*, 16, S1177–S1179.
- Shannon, R. D. (1976) Revised effective ionic radii and systematic studies of interatomic distances in halides and chalcogenides. *Acta Crystallographica Section A: Crystal Physics, Diffraction, Theoretical and General Crystallography*, 32, 751–767.
- Shim, S.-H., Duffy, T. S., and Shen, G. (2001) The post-spinel transformation in Mg<sub>2</sub>SiO<sub>4</sub> and its relation to the 660-km seismic discontinuity. *Nature*, 411, 571–574.
- Simmons, R. O., and Balluffi, R. W. (1962) Measurement of Equilibrium Concentrations of Lattice Vacancies in Gold. *Physical Review*, 125, 862–872.
- Sims, M., Jaret, S. J., Carl, E.-R., Rhymer, B., Schrodtt, N., Mohrholz, V., Smith, J., Konopkova, Z., Liermann, H.-P., Glotch, T. D., and others (2019) Pressure-induced amorphization in plagioclase feldspars: A time-resolved powder diffraction study during rapid compression. *Earth and Planetary Science Letters*, 507, 166–174.
- Soignard, E., and McMillan, P. F. (2004) An Introduction to Diamond Anvil Cells and Loading Techniques. In A. Katrusiak and P. McMillan, Eds., *High-Pressure Crystallography* pp. 81–100. Springer Netherlands, Dordrecht.
- Solomatova, N. V., Jackson, J. M., Sturhahn, W., Wicks, J. K., Zhao, J., Toellner, T. S., Kalkan, B., and Steinhardt, W. M. (2016) Equation of state and spin crossover of (Mg,Fe)O at high pressure, with implications for explaining topographic relief at the core-mantle boundary. *American Mineralogist*, 101, 1084–1093.
- Song, M., Yamawaki, H., Fujihisa, H., Sakashita, M., and Aoki, K. (1999) Infrared absorption study of Fermi resonance and hydrogen-bond symmetrization of ice up to 141 GPa. *Physical Review B*, 60, 12644–12650.
- Song, M., M., Yamawaki, H., Fujihisa, H., Sakashita, M., and Aoki, K. (2003) Infrared investigation on ice VIII and the phase diagram of dense ices. *Physical Review B*, 68, 014106.
- Sotin, C., Grasset, O., and Mocquet, A. (2007) Mass radius curve for extrasolar Earth-like planets and ocean planets. *Icarus*, 191, 337–351.

## References

- Sugimura, E., Iitaka, T., Hirose, K., Kawamura, K., Sata, N., and Ohishi, Y. (2008) Compression of H<sub>2</sub>O ice to 126 GPa and implications for hydrogen-bond symmetrization: Synchrotron x-ray diffraction measurements and density-functional calculations. *Physical Review B*, 77, 214103.
- Sugimura, E., Komabayashi, T., Ohta, K., Hirose, K., Ohishi, Y., and Dubrovinsky, L.S. (2012) Experimental evidence of superionic conduction in H<sub>2</sub>O ice. *The Journal of Chemical Physics*, 137, 194505.
- Tomasino, D., and Yoo, C.-S. (2013) Solidification and crystal growth of highly compressed hydrogen and deuterium: Time-resolved study under ramp compression in dynamic-diamond anvil cell. *Applied Physics Letters*, 103, 061905.
- Tschauner, O., Huang, S., Greenberg, E., Prakapenka, V. B., Ma, C., Rossman, G. R., Shen, A. H., Zhang, D., Newville, M., Lanzirotti, A., and others (2018) Ice-VII inclusions in diamonds: Evidence for aqueous fluid in Earth's deep mantle. *Science*, 359, 1136–1139.
- Tsuchiya, J., and Tsuchiya, T. (2017) First principles calculation of the elasticity of ice VIII and X. *The Journal of Chemical Physics*, 146, 014501.
- Tsuchiya, T., Tsuchiya, J., Umemoto, K., and Wentzcovitch, R. M. (2004) Elasticity of post-perovskite MgSiO<sub>3</sub>. *Geophysical Research Letters*, 31.
- Tsuchiya, T., Wentzcovitch, R. M., da Silva, C. R. S., and de Gironcoli, S. (2006) Spin Transition in Magnesiowüstite in Earth's Lower Mantle. *Physical Review Letters*, 96, 198501.
- Valencia, D., O'Connell, R. J., and Sasselov, D. (2006) Internal structure of massive terrestrial planets. *Icarus*, 181, 545–554.
- Valencia, D., Sasselov, D. D., and O'Connell, R. J. (2007) Radius and Structure Models of the First Super-Earth Planet. *The Astrophysical Journal*, 656, 545–551.
- Vanderburg, A., Rowden, P., Bryson, S., Coughlin, J., Batalha, N., Collins, K. A., Latham, D. W., Mullally, S. E., Colón, K. D., Henze, C., and others (2020) A Habitable-zone Earth-sized Planet Rescued from False Positive Status. *The Astrophysical Journal*, 893, L27.
- Wentzcovitch, R. M., Justo, J. F., Wu, Z., Silva, C. R. S. da, Yuen, D. A., and Kohlstedt, D. (2009) Anomalous compressibility of ferropericlase throughout the iron spin cross-over. *Proceedings of the National Academy of Sciences*, 106, 8447–8452.
- Wolainin, E., Pruzan, Ph., Chervin, J. C., Canny, B., Gauthier, M., Häusermann, D., and Hanfland, M. (1997) Equation of state of ice VII up to 106 GPa. *Physical Review B*, 56, 5781–5785.
- Wu, Z., Justo, J. F., da Silva, C. R. S., de Gironcoli, S., and Wentzcovitch, R. M. (2009) Anomalous thermodynamic properties in ferropericlase throughout its spin crossover. *Physical Review B*, 80, 014409.

## References

- Yang, J., Tong, X., Lin, J.-F., Okuchi, T., and Tomioka, N. (2015) Elasticity of Ferropericlase across the Spin Crossover in the Earth's Lower Mantle. *Scientific Reports*, 5, 17188.
- Zeng, L., and Sasselov, D. (2014) The effect of temperature evolution on the interior structure of H<sub>2</sub>O-rich planets. *The Astrophysical Journal*, 784, 96.
- Zha, C.-S., Hemley, R. J., Gramsch, S. A., Mao, H., and Bassett, W. A. (2007) Optical study of H<sub>2</sub>O ice to 120GPa: Dielectric function, molecular polarizability, and equation of state. *The Journal of Chemical Physics*, 126, 074506.
- Zha, C.-S., Tse, J. S., and Bassett, W. A. (2016) New Raman measurements for H<sub>2</sub>O ice VII in the range of 300 cm<sup>-1</sup> to 4000 cm<sup>-1</sup> at pressures up to 120 GPa. *The Journal of Chemical Physics*, 145, 124315.
- Zhang, J. S., Hao, M., Ren, Z., and Chen, B. (2019) The extreme acoustic anisotropy and fast sound velocities of cubic high-pressure ice polymorphs at Mbar pressure. *Applied Physics Letters*, 114, 191903.

## Chapter 4

# Bulk modulus of H<sub>2</sub>O across the ice VII – ice X transition measured by time-resolved X-ray diffraction in dynamic Diamond Anvil Cell experiments

A. S. J. Méndez<sup>1,2</sup>, F. Trybel<sup>2</sup>, R. J. Husband<sup>1</sup>, G. Steinle-Neumann<sup>2</sup>, H.-P. Liermann<sup>1</sup> and H. Marquardt<sup>3</sup>

<sup>1</sup>Deutsches Elektronen-Synchrotron (DESY), 22607 Hamburg, Germany; <sup>2</sup>Bayerisches Geoinstitut, Universität Bayreuth, 95440 Bayreuth, Germany; <sup>3</sup>Department of Earth Sciences, University of Oxford, OX1 3AN Oxford, UK.

Corresponding author: Alba San José Méndez (alba.mendez@desy.de)

This chapter has been published as:

Méndez et al. (2020) *Phys. Rev. B.* **103**, 064104.

### Abstract

We have studied the H<sub>2</sub>O ice VII – ice X phase transition at room temperature by performing three quasi-continuous synchrotron time-resolved X-ray diffraction experiments in the dynamic Diamond Anvil Cell, reaching pressures of 180 GPa. The dense pressure-coverage of our volume data allows us to directly derive the bulk modulus for H<sub>2</sub>O over the entire pressure range. Our data document three major changes in compression behavior in the ranges of 35-40, 50-55 and 90-110 GPa, likely corresponding to the formation of pre-transition dynamically disordered ice VII and ice X, and static ice X, respectively. Our results confirm that ice X has a very high bulk modulus.

### 4.1 INTRODUCTION

H<sub>2</sub>O ice is present in a large variety of planetary bodies, including the ice giants, Uranus and Neptune, mini-Neptune exoplanets [1,2] and icy satellites [3,4], having a fundamental impact on the heat and chemical exchange in their interiors [5–8]. H<sub>2</sub>O ice might also be present in Earth's deep mantle, as well as other terrestrial planets, where it can form through mineral dehydration reactions occurring at relatively cold regions of the mantle [9–11]. The polymorphs ice VII and ice X are the stable forms of H<sub>2</sub>O ice that exist at pressures ( $P$ ) larger than 2 GPa, and their physical properties play a pivotal role in the structure and evolution of H<sub>2</sub>O-rich planetary bodies.

#### **Chapter 4. BULK MODULUS OF H<sub>2</sub>O ACROSS THE ICE VII – ICE X TRANSITION**

Ice VII is a solid characterized by a body centered cubic (*bcc*) arrangement of oxygens, with H<sub>2</sub>O molecules linked via hydrogen bonds (O-H···O) such that the ice-rules are satisfied [12]. The high-*P* phase ice X is based on the same *bcc* oxygen lattice, but hydrogen atoms are located symmetrically between two oxygen atoms (O-H-O). It has been proposed that the ice VII - ice X transition proceeds through a proton order-disorder transition through which H<sub>2</sub>O molecules dissociate, triggered by changes in the energy potential for the O-H···O bond with *P*, leading to the formation of pre-transitional states prior to complete bond symmetrization in ice X [13–16]. At low *P*, the energy potential determining the position of the protons has been predicted to be of double-well character with a high energy barrier and a localized proton position coinciding with one of the two minima [17]. Computational studies [13–17] describe three main changes in the energy potential of the H-bond across the ice VII - ice X transition: (i) A lowering of the energy barrier with *P* triggers proton tunneling between the two minima, forming the translationally or dynamically disordered ice VII (ice VII'). (ii) As the potential barrier approaches zero with *P*, the proton distribution shifts to the center, forming the dynamically disordered ice X (ice X'). (iii) Symmetrization is complete when the energy potential adopts a narrow single-well form, localized at the mid-point between two oxygens (O-H-O), forming static ice X.

Numerous experimental studies employing different techniques, including X-ray [18,19] (XRD) and neutron diffraction [20], Raman [21] and infrared (IR) spectroscopy [22–25] as well as refractive index measurements [26], reported anomalies between 40 and 75 GPa, possibly associated with the formation of the dynamically disordered states. Diffraction [18,20,27] and IR-measurements [23,25] have reported O-H-O bond symmetrization in the *P*-range of 110-140 GPa, while Raman [28] and optical measurements [26] suggest an onset at *P* ≈ 90 GPa. However, these experimental techniques do not probe proton dynamics directly, and the formation of the pre-transitional states cannot be detected unambiguously. Recently, Meier *et al.* [29] reported first direct observations of proton mobility for *P*=8-90 GPa by a line-shape analysis of Nuclear Magnetic Resonance (NMR) experiments.

Here we perform dynamic compression experiments in combination with time-resolved XRD in order to explore the compression behavior of H<sub>2</sub>O across the ice VII – ice X transition up to 180 GPa using a dynamic Diamond Anvil Cell (dDAC) driven by a piezoelectric actuator [30,31]. This setup provides quasi-continuous volume-*P* data, with hundreds of diffraction patterns recorded in one experiment, and therefore allows us to compute compressibility by numerical differentiation without invoking an equation-of-state model to fit the data, a significant advance relative to prior static experiments with tens of data points. We track the bulk modulus evolution across the ice VII – ice X transition, and explore whether this transition as well as the

pre-transitional states (ice VII' and ice X') can be detected from changes in the compression behavior.

## 4.2 METHODS

### 4.2.1 Experimental setup

Three symmetric piston cylinder-type DACs are equipped with 150, 100 and 80  $\mu\text{m}$  diameter culet anvils (dDAC-1, dDAC-2 and dDAC-3), with two different gasket configurations (Table 1): (i) In dDAC-2 and dDAC-3, regular Re gaskets are pre-indented to a thickness of 30  $\mu\text{m}$  and holes of 50 and 40  $\mu\text{m}$  diameters are drilled, respectively; (ii) In dDAC-1, an amorphous gasket is employed in order to avoid the emergence of strong diffraction peaks from the Re gasket that may overwhelm the diffraction patterns of  $\text{H}_2\text{O}$  with smaller scattering factors. A disk of an amorphous boron alloy ( $\text{Fe}_{0.79}\text{Si}_{0.06}\text{B}_{0.15}$ ) with a thickness of 30  $\mu\text{m}$  and a 50  $\mu\text{m}$  diameter hole is inserted in a Re gasket, pre-indented to the same thickness, following the procedure described in Méndez *et al.* [32].

Milli-Q  $\text{H}_2\text{O}$  is loaded along with Au powder (99.99% pure from Sigma Aldrich) as  $P$ -marker and a ruby chip to monitor  $P$  in the sample during pre-compression. DACs are inserted in a “cap housing” coupled to a high-voltage piezoelectric actuator (PEA) as described in Jenei *et al.* [31] DAC and PEA are coupled by tightening the end cap at the back of the housing until a  $P$ -increase of 1-2 GPa is observed. The PEA is connected to an amplifier (Piezosystem Jena GmbH), remotely controlled via a waveform generator (Agilent 33522B). When voltage is applied, the PEA in contact with the DAC expands, pushing directly onto the piston and compressing the sample. Trapezoidal voltage-time waveforms are created by the Agilent Benchlink waveform builder software by Keysight and sent to the PEA. We apply voltage-time waveforms with a constant compression rate in each experiment, corresponding to nominal  $P$ -rates of 0.4-0.6 GPa/s that permits for sufficiently long X-ray exposure times while still achieving an excellent resolution in  $P$ -sampling (Table 1).

Run #	Culet size ( $\mu\text{m}$ )	Gasket type	Sample-detector distance (mm)	Maximum pressure (GPa)	Experiment total time (s)	Nominal compression rate (GPa/s)	Exposure time (ms)	Number of images analyzed
dDAC-1	150	Amorphous	418.42	90	300	0.5	100	1800
dDAC-2	100	Re	166.31	160	850	0.4	1000	590
dDAC-3	80	Re	404.89	180	868	0.6	2000	305

**Table 4.1:** Summary of experimental run conditions

**4.2.2 X-ray diffraction**

Monochromatic synchrotron X-rays with a fixed wavelength ( $0.4828 \text{ \AA}$ ) are used for time-resolved diffraction experiments at the Extreme Conditions Beamline P02.2 at PETRA III, Hamburg, Germany [33]. A compound refractive lens-focused X-ray beam ( $3 \text{ \mu m}$  (h) x  $8 \text{ \mu m}$  (v) FWHM) is aligned with the center of the sample chamber. GaAs 2.3 MPix LAMBDA detectors, with a pixel size of  $55 \text{ \mu m}$  x  $55 \text{ \mu m}$  and a repetition rate of up to 2 kHz, are employed to perform fast collection of XRD images [34,35]. For dDAC-2, one detector is aligned with the sample center and placed at a short sample-to-detector distance (Table 1), ensuring the collection of full diffraction rings. For dDAC-1 and dDAC-3, two detectors are symmetrically offset from the direct beam, capturing sections of the Debye–Scherrer diffraction rings. Tilting of the detector(s) and the sample-detector distance are calibrated using a  $Cr_2O_3$  standard (NIST 674b). With this setup we are able to collect more than 300 individual X-ray diffraction patterns in each compression experiment (Table 1). In-house data analysis software is used for quick visualization of the collected data (Fig. 4.1).

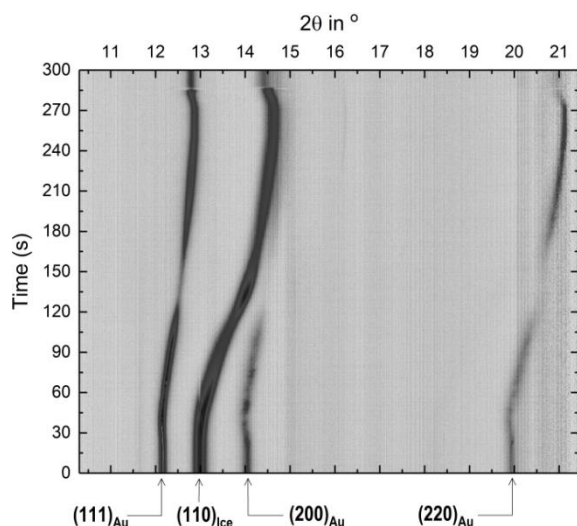


**Figure 4.1:** Contour plot showing the time-evolution of diffraction patterns (peaks) collected for dDAC-1 in time- $2\theta$  space; In our experiments, the  $(110)$  diffraction line of ice VII is the most intense and can be traced over the full  $P$ -range of the individual experiments.

**4.2.3 Diffraction pattern fitting**

The detector images are radially integrated using the Dioptas software [36] to obtain 1D diffraction patterns as a function of the  $2\theta$ -angle (Fig. 4.2). During integration, the dead areas of the detectors are masked to improve the signal/noise ratio. Additionally, the most intense areas of the  $(101)$  diffraction ring of Re –  $(101)_{Re}$  – are masked in dDAC-2 in order to minimize the convolution with the  $(110)_{iceVII}$  diffraction ring (Fig. 4.3).

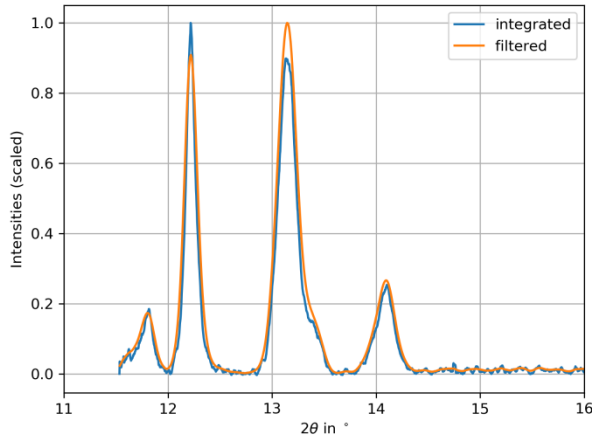


**Figure 4.2:** Exemplary integrated diffraction pattern for the dDAC-2 experiment at 26 GPa. Blue shows the original pattern after integration of the detector image with Dioptas; orange the pattern after application of an IIR filter with zero phase shift.

A Python routine is developed to deal with the large number of diffraction patterns (Table 1) and to automate peak fitting and tracking. Before integrated patterns are processed by the routine, we average over three points in  $2\theta$ -space and apply an infinite impulse response (IIR) filter forwards and backwards with zero phase shift to further improve the signal/noise ratio and the reliability as well as the speed of the fitting routine (Fig. 4.2). In order to analyze the recorded diffraction data, the peaks in the window  $2\theta=11.0^\circ$ - $20.0^\circ$  are assigned to a crystal structure, fitted and positions are tracked over the entire compression range in all diffraction patterns. In a first step, the positions of the expected peaks (indices identified via peak comparison with Dioptas) are calculated from the space group and a given initial compression using a routine from the *pymatgen* (Python Materials Genomics) library [37]. The calculated peak positions (*CPP*) are used as the initial positions for a model consisting of a Gaussian for each peak and a linear background correction. The model is optimized with a non-linear least-squares fit to obtain optimal peak positions (*OPP*) employing the *LMFIT* package [38]. The *OPP* of the individual Gaussians are subsequently compared with the prediction (*CPP*); if an individual *OPP* is at larger (smaller)  $2\theta$ -angle than *CPP*, compression is increased (decreased) until  $|OPP-CPP| < \epsilon$  is reached (with  $\epsilon$  a convergence parameter). The optimization of the compression is performed with an adaptive step width to improve accuracy and runtime.

As the *P*-standard and the sample differ in compressional behavior, the peak positions are optimized separately: *P* is calculated using the optimized position of  $(111)_{\text{Au}}$  combined with the equation-of-state of Fei *et al.* [39]. Volume (*V*) of  $\text{H}_2\text{O}$  ice is determined from  $(110)_{\text{iceVII}}$ . The  $(200)_{\text{Au}}$  peak of the *P*-standard and  $(101)_{\text{Re}}$  from the gasket (dDAC-2 and dDAC-3) are included to improve the model, but not considered in the optimization. In particular,  $(200)_{\text{Au}}$  is not suitable for that purpose as (i) it is small in amplitude, (ii) the amplitude decreases with *P* and (iii) it starts to overlap with the  $(110)_{\text{iceVII}}$  peak for  $P > 50$  GPa.

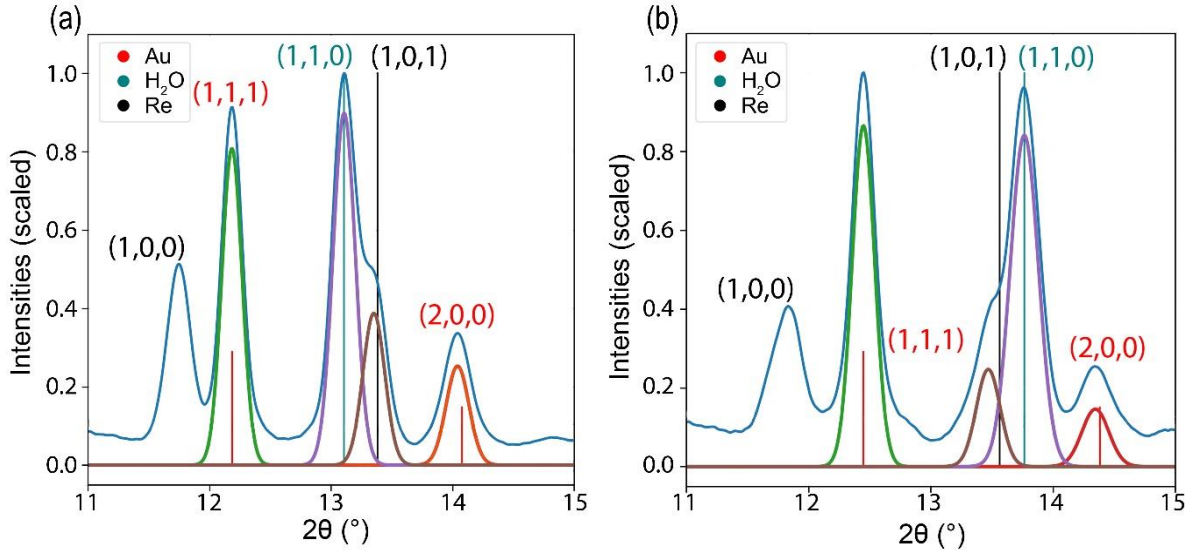


**Figure 4.3:** Diffraction patterns collected from dDAC-2 after application of the IRR filter (blue) at (a) 24 GPa and (b) 45 GPa with assigned indices and the calculated/theoretical peak positions (*CPP*) shown as vertical lines. The solid curves represent the Gaussian model peaks.

Diffraction patterns are individually loaded with user input on the initial compression estimate. Although the program can handle each spectrum individually, it is significantly more efficient to guess a starting compression from the previous *P*-step. This especially helps to resolve overlapping peaks, where a good initial guess is crucial. Such an interaction between  $(110)_{\text{IceVII}}$  and  $(101)_{\text{Re}}$  is shown in Fig. 4.3. At low *P*,  $(110)_{\text{IceVII}}$  appears at a smaller  $2\theta$ -value than  $(101)_{\text{Re}}$ ; during compression, the peaks start to overlap at  $P > 20$  GPa and reverse order in  $2\theta$  at  $P > 40$  GPa.

The routine can resolve the individual peaks while they are partly overlapping by estimating a linear compression rate. However, if the peaks are completely overlapping, a reliable fit is not possible, and, for this reason, for dDAC-3 a small *P*-range (41-49 GPa) is not processed. Nevertheless, we obtain, especially for dDAC-2 with a full diffraction ring, dense  $V(P)$  data with only very small data scatter introduced by the fitting routine due to peak asymmetry and overlap. The error in  $V$  is calculated from the minimal separable peak distance in the routine ( $0.05^\circ$  in  $2\theta$ ). If the peak shift between two consecutive patterns is too small, the program tends to keep the positions constant, followed by a sudden jump to another configuration. In principle, this problem can be avoided by decreasing  $\epsilon$  from  $10^{-3}$  to  $10^{-5}$  for  $|OPP-CPP|$ -determination. However, prohibitively increased computational requirements make fitting all patterns with  $\epsilon=10^{-5}$  impossible. Instead, we use every 25th diffraction pattern for dDAC-1, every 10th for dDAC-2 and every 5th for dDAC-3, preserving an excellent *P*-resolution, i.e., 1 GPa for dDAC-1 and 3 GPa for dDAC-2 and dDAC-3.

Fitting a series of Gaussians rather than performing a Rietveld or Le Bail refinement has large advantages for the current datasets: (i) The standard refinement techniques rely on the peak shape which may cause problems for the peak-overlap discussed above and (ii) processing the data is even more challenging in terms of automation. Nevertheless, on a limited number of diffraction patterns from dDAC-1 and dDAC-2 we have tested that  $P$  and  $V$  obtained from the Gaussian fitting performed here and a Le Bail refinement. The results are consistent with one another within the error coming from the minimal separable peak distance in our approach (Table 1 in the Supplemental Material).

#### 4.2.4 Bulk modulus calculation

The isothermal bulk modulus ( $K_T$ ) can be directly calculated from our dense  $V(P)$  dataset via  $K_T = -V \cdot \partial P / \partial V$ , with the advantage that no assumption has to be made with respect to the analytical form of an equation-of-state. Previous DAC studies on ice VII and ice X [18,19,27], by contrast, had to rely on an equation-of-state fit due to the significantly lower number of data points. Here, using the increased  $P$ -spacing by not fitting all diffraction patterns as discussed above, becomes a further advantage, as a small denominator ( $\Delta V$ ) can lead to significant fluctuations in the calculated bulk modulus. We further apply spline interpolation with smoothing [40,41] before calculating the bulk modulus to mediate still existing unphysical fluctuations (Fig. 4.6 in the Supplemental Material) via a central difference scheme. The smoothing factors are chosen such that smooth variations of  $K_T$  with  $P$  are obtained, while simultaneously keeping the difference between data points and the spline  $<1\%$  over the complete compression-range for all experiments (Fig. 4.4b).

The error in  $K_T$  is propagated from the error in  $V$  with a central difference scheme. As the (111)<sub>Au</sub> reflection ( $P$ -marker) does not suffer asymmetry or overlap,  $P$  is assumed to be error-free.

### 4.3 RESULTS AND DISCUSSION

#### 4.3.1 Volume compression curve of H<sub>2</sub>O ice

Figure 4.4 shows the unit cell  $V$  of H<sub>2</sub>O ice as a function of  $P$  from our experiments in comparison with previous XRD measurements [18,19,27] and equation-of-state predictions [42,43]. Differences between  $V$  measured in our three runs fall within the refinement uncertainties determined by the resolution limit of  $0.05^\circ$  in  $2\theta$  for the diffraction patterns (Fig. 4.4a), suggesting that the choice of the gasket material or the sample-detector configuration do not affect the results significantly. Overall, our  $V(P)$  data are in good agreement with previous experimental results [18,19,27] (Fig. 4.4c), and the observed differences in  $V$  between our three compression runs (dDAC-1, dDAC-2 and dDAC-3) are similar to differences between previously

published measurements [18,19,27], and between the three single-crystal X-ray diffraction experiments reported in Loubeyre *et al.* [27]. The scatter that we see in our data within one run is significantly smaller than in any of the experiments previously reported [18,19,27].

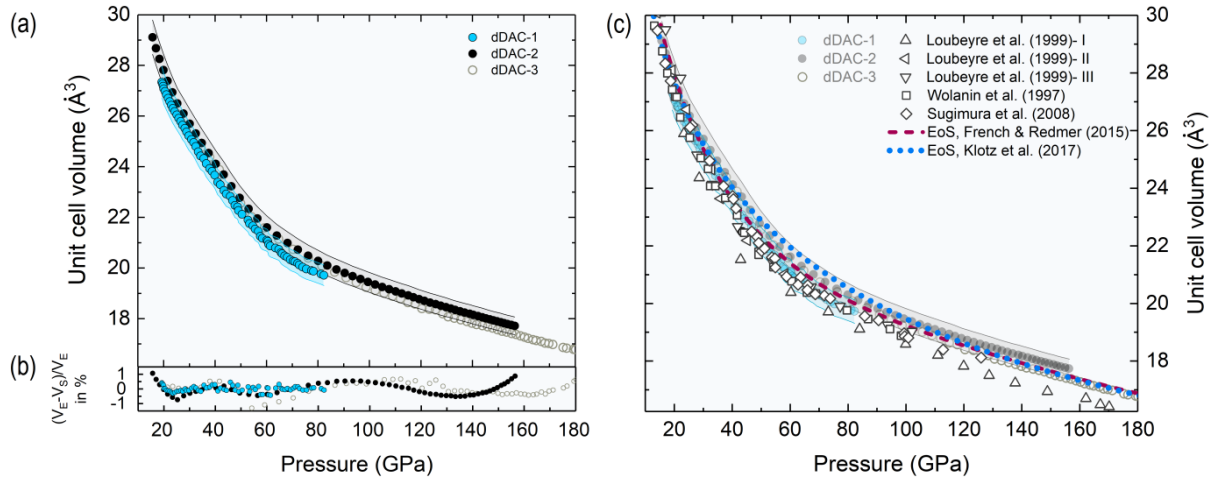


**Figure 4.4:** (a) Volume-pressure points for  $H_2O$  ice as derived from the reduced datasets of the dDAC-1 (blue solid circles), dDAC-2 (black solid circles) and dDAC-3 data (grey open circles). Error bands using the resolution limit ( $0.05^\circ$  in  $2\theta$ ) of the fitting routine are shown for dDAC-1 and dDAC-2 (shaded regions). (b) Difference between the data points and the spline with smoothing factors of 9.0 (dDAC-1), 1.0 (dDAC-2) and 18.0 (dDAC-3) is  $<1\%$  over the complete compression range for all experiments. (c) Previous XRD measurements in static DAC experiments by Wolanin *et al.* [19] (powder, squares), Sugimura *et al.* [18] (powder, diamonds) and Loubeyre *et al.* [27] (three single-crystal datasets, three differently pointing triangles) are plotted in comparison to our data. The dashed (maroon) and dotted (blue) curves represent the equations-of-state by French & Redmer [42] and Klotz *et al.* [43], respectively, the latter extrapolated significantly beyond the  $P$ -range of the experiments (14 GPa).

Our data generally agree with equations-of-state based on both experimental data [43] and computational results [42], even though some small but systematic deviations in  $P$ -trends exist in the  $P$ -range 50-100 GPa (Fig. 4.4c). This range coincides with the formation of the disordered ice state(s), likely triggered by nuclear quantum effects occurring in the range  $50 \lesssim P \lesssim 70$  GPa [13,14]. French & Redmer [42] computed an analytical thermodynamic potential from ab-initio calculations based on classical proton trajectories; although their calculations were supplemented with a quantum correction, they did not include tunnelling effects, which affect the proton motion and can explain the deviation from our results. The equation of state by Klotz *et al.* [43] is based on the extrapolation of neutron diffraction data measured up to 14 GPa, which is a too low  $P$  for observing significant proton tunnelling effects as indicated by the NMR results [29].

4.3.2 Bulk modulus of H<sub>2</sub>O ice at high pressures

Bulk moduli computed from our splined data (for clarity we only show  $K_T$ - $P$  from dDAC-2 in Fig. 4.5, with the results for dDAC-1 and dDAC-3 in Fig. 4.7 of the Supplemental Material) agree well with recent Brillouin spectroscopy measurements at  $P \lesssim 35$  GPa [44,45]. At higher  $P$ , three major changes in the slope of  $K_T$ - $P$  are captured by our experiments (Fig. 4.5):

- (i) A softening starting at  $P=35$ -40 GPa indicates a transition towards a more compressible state (Fig. 4.5), supporting previous findings [18]. We associate this change with the formation of disordered ice VII'. While Brillouin spectroscopy measurements disagree with one another in terms of absolute values for  $K_T$ , they show [45,46] – or at least hint [44] at – a  $P$ -range of high compressibility (40-50 GPa), supporting our observation of highly compressible ice VII'. A possible reason for the disagreement between the various Brillouin spectroscopy studies at all  $P$  is the marked elastic anisotropy of ice VII and, as a consequence, the possibility that velocities along certain directions were favored by crystallographic preferred orientation and/or selective elasto-optic coupling between the probing laser and specific phonon propagation direction [50]. In the  $P$ -range where we observe the softening, signal overlap with the diamond-anvils further complicates a reliable determination of the bulk modulus by Brillouin spectroscopy [44].
- (ii) A steep increase in  $K_T$  starting at  $P=50$ -55 GPa marks the formation of a less compressible phase, in agreement with the onset of hydrogen symmetrization predicted by computations at  $P \approx 50$  GPa [13], and may also be associated with anomalies in the infrared spectra of H<sub>2</sub>O ice reported for  $P=55$ -62 GPa [23,51,52]. We attribute this feature to the formation of ice X' [18].
- (iii) A distinct change in  $P$ -dependence of  $K_T$  at  $P=90$ -110 GPa, which is in excellent agreement with computational predictions [42,49], but has not been documented by previous experiments on the elastic properties of ice VII [18,24,26–28]. We attribute this change to the formation of static ice X.

These changes in the  $P$ -behavior of  $K_T$  are also visible in the dDAC-1 and dDAC-3 data at comparable onset  $P$  (Fig. 4.7 in the Supplemental Material).

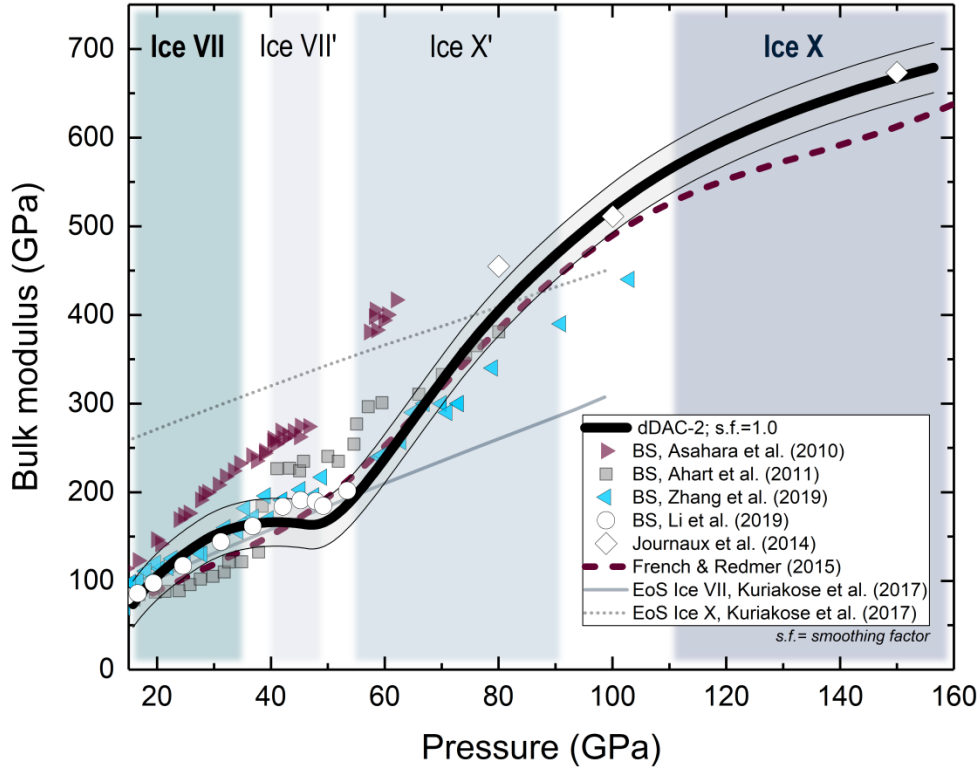


**Figure 4.5:** Bulk modulus of H<sub>2</sub>O ice as a function of pressure calculated from the smoothed spline interpolation of the  $V(P)$  data from dDAC-2 in comparison to previous studies (for results from dDAC-1 and dDAC-3, see Fig. 4.7 in Supplemental Material). Right-pointing triangles, solid squares, left-pointing triangles and solid circles represent Brillouin inelastic scattering (BS) data [44–47]. The solid and dotted thin grey lines show equations-of-state for ice VII and ice X, respectively [48]. Diamonds represent computational predictions of the bulk modulus of ice X [49]. The dashed maroon line refers to computational results [42]. Background colours guide the eyes to the approximate  $P$ -ranges for the stability of ice VII, ice VII', ice X' and ice X based on the  $P$ -ranges where a quasi-linear  $P$ -dependence of  $K_T$  is observed in our work.

The observed  $P$ -evolution of  $K_T$  across the ice VII – ice X transition in our experiments can be correlated with the variations in proton mobility observed by Meier *et al.* [29] for the O-H...O bond, and be rationalized by the predicted evolution of the energy barrier of a double-well potential [17,53]. Meier *et al.* [29] documented a significant increase in tunnelling probability for  $P=20-50$  GPa, i.e., in the  $P$ -range where the formation of ice VII' is expected. Our observation of a softening of  $K_T$  for ice VII observed for  $P=35-40$  GPa may be explained by a decrease in the “proton pressure” caused by higher proton mobility [18,53]. The steep increase in  $K_T$  that we observe for  $P>50$  GPa (Fig. 4.5) may reflect the proton centering process, and the formation of ice X'. Full proton localization may cause the change of the  $P$ -derivative in our  $K_T$ -data for  $P=90-110$  GPa.

## 4.4 CONCLUSIONS

We have collected quasi-continuous X-ray diffraction data across the ice VII – ice X transition and up to  $P=180$  GPa in three dynamically driven diamond-anvil-cell experiments. We derive the bulk modulus of H<sub>2</sub>O ice directly from our  $V(P)$  data. We find three main changes in the pressure-dependence at 35-40, 50-55 and 90-110 GPa and associate them with the formation of ice VII', ice X' and ice X, respectively. These transitions are not sharp; certainly not of first order (no volume collapse), unlikely of second order (no discontinuous changes in bulk modulus). This association suggests that the compression behavior of H<sub>2</sub>O at high pressure is sensitive to proton ordering. Our results further confirm computational predictions that the bulk modulus of ice X is distinctly higher than that of ice VII.

## Acknowledgements

This research was supported through the German Science Foundation (Deutsche Forschungsgemeinschaft, DFG) in Research Unit FOR 2440 (grants MA4534/5-1 and STE1105/13-1). We acknowledge DESY (Hamburg, Germany), a member of the Helmholtz Association HG, for providing the experimental facility PETRA III and beamline P02.2. We acknowledge B. Winkler and the BMBF project 05K13RF1 for the purchase of the laser cutting machine for preparing gaskets. We thank Martin French for sharing water high-pressure results, and Tiziana Boffa Balaran, Nicolò Satta and Thomas Meier for helpful discussions.

## References

- <sup>1</sup> J.J. Lissauer *et al.*, *Nature* 470, 53 (2011).
- <sup>2</sup> R. Redmer, T. R. Mattsson, N. Nettelmann, and M. French, *Icarus* 211, 798 (2011).
- <sup>3</sup> R. Jaumann, R. N. Clark, F. Nimmo, A. R. Hendrix, B. J. Buratti, T. Denk, J. M. Moore, P. M. Schenk, S. J. Ostro, and R. Srama, in *Saturn from Cassini-Huygens*, edited by M. K. Dougherty, L. W. Esposito, and S. M. Krimigis (Springer Netherlands, Dordrecht, 2009), pp. 637–681.
- <sup>4</sup> S.A. Kattenhorn and L.M. Prockter, *Nat. Geosci.* 7, 762 (2014).
- <sup>5</sup> B. Journaux, I. Daniel, S. Petitgirard, H. Cardon, J.-P. Perrillat, R. Caracas, and M. Mezouar, *Earth Planet. Sc. Lett.* 463, 36 (2017).
- <sup>6</sup> L. Noack, D. Höning, A. Rivoldini, C. Heistracher, N. Zimov, B. Journaux, H. Lammer, T. Van Hoolst, and J. H. Bredehöft, *Icarus* 277, 215 (2016).
- <sup>7</sup> C. Sotin, O. Grasset, and A. Mocquet, *Icarus* 191, 337 (2007).
- <sup>8</sup> A.D. Fortes and M. Choukroun, *Space. Sci. Rev.* 153, 185 (2010).
- <sup>9</sup> J.-F. Lin, V. V. Struzhkin, S. D. Jacobsen, M. Y. Hu, P. Chow, J. Kung, H. Liu, H.-k. Mao and R. J. Hemley, *Geophys. Res. Lett.* 32, L11306 (2005).

#### **Chapter 4. BULK MODULUS OF H<sub>2</sub>O ACROSS THE ICE VII – ICE X TRANSITION**

- <sup>10</sup> B. Schwager and R. Boehler, *High Pressure Res.* 28, 431 (2008).
- <sup>11</sup> O. Tschauner, S. Huang, E. Greenberg, V. B. Prakapenka, C. Ma, G. R. Rossman, A. H. Shen, D. Zhang, M. Newville, A. Lanzirrotti, and K. Tait, *Science* 359, 1136 (2018).
- <sup>12</sup> J. D. Bernal and R. H. Fowler, *J. Chem. Phys.* 1, 515 (1933).
- <sup>13</sup> W.B. Holzapfel, *J. Chem. Phys.* 56, 712 (1972).
- <sup>14</sup> M. Benoit, D. Marx, and M. Parrinello, *Nature* 392, 258 (1998).
- <sup>15</sup> M. Benoit, A. H. Romero, and D. Marx, *Phys. Rev. Lett.* 89, 145501 (2002).
- <sup>16</sup> M. Benoit and D. Marx, *ChemPhysChem* 6, 1738 (2005).
- <sup>17</sup> L. Lin, J.A. Morrone, and R. Car, *J. Stat. Phys.* 145, 365 (2011).
- <sup>18</sup> E. Sugimura, T. Iitaka, K. Hirose, K. Kawamura, N. Sata, and Y. Ohishi, *Phys. Rev. B* 77, 214103 (2008).
- <sup>19</sup> E. Wolanin, Ph. Pruzan, J. C. Chervin, B. Canny, M. Gauthier, D. Häusermann, and M. Hanfland, *Phys. Rev. B* 56, 5781 (1997).
- <sup>20</sup> M. Guthrie, R. Boehler, J. J. Molaison, B. Haberl, A. M. dos Santos, and C. Tulk, *Phys. Rev. B* 99, 184112 (2019).
- <sup>21</sup> A.F. Goncharov, N. Goldman, L.E. Fried, J.C. Crowhurst, I. Feng W. Kuo, C.J. Mundy, and J.M. Zaug, *Phys. Rev. Lett.* 94, 125508 (2005).
- <sup>22</sup> K. Aoki, H. Yamawaki, M. Sakashita, and H. Fujihisa, *Phys. Rev. B* 54, 15673 (1996).
- <sup>23</sup> A. F. Goncharov, V. V. Struzhkin, M. S. Somayazulu, R. J. Hemley, and H. K. Mao, *Science* 273, 218 (1996).
- <sup>24</sup> M. Song, H. Yamawaki, H. Fujihisa, M. Sakashita, and K. Aoki, *Phys. Rev. B* 60, 12644 (1999).
- <sup>25</sup> M. Song, H. Yamawaki, H. Fujihisa, M. Sakashita, and K. Aoki, *Phys. Rev. B* 68, 014106 (2003).
- <sup>26</sup> C.-S. Zha, R.J. Hemley, S.A. Gramsch, H. Mao, and W.A. Bassett, *J. Chem. Phys.* 126, 074506 (2007).
- <sup>27</sup> P. Loubeyre, R. LeToullec, E. Wolanin, M. Hanfland, and D. Hausermann, *Nature* 397, 503 (1999).
- <sup>28</sup> C.-S. Zha, J.S. Tse, and W.A. Bassett, *J. Chem. Phys.* 145, 124315 (2016).
- <sup>29</sup> T. Meier, S. Petitgirard, S. Khandarkhaeva, and L. Dubrovinsky, *Nat. Commun.* 9, 2766 (2018).
- <sup>30</sup> W.J. Evans, C.-S. Yoo, G.W. Lee, H. Cynn, M.J. Lipp, and K. Visbeck, *Rev. Sci. Instrum.* 78, 073904 (2007).
- <sup>31</sup> Zs. Jenei *et al.*, *Rev. Sci. Instrum.* 90, 065114 (2019).
- <sup>32</sup> A.S.J. Méndez, H. Marquardt, R.J. Husband, I. Schwark, J. Mainberger, K. Glazyrin, A. Kurnosov, C. Otzen, N. Satta, and J. Bednarcik, *Rev. Sci. Instrum.* 91, <https://doi.org/10.1063/5.0007557> (2020).
- <sup>33</sup> H.-P. Liermann *et al.*, *J. Synchrotron Radiat.* 22, 908 (2015).
- <sup>34</sup> D. Pennicard *et al.*, *J. Instrum.* 13, C01026 (2018).

- <sup>35</sup> D. Pennicard, S. Lange, S. Smoljanin, H. Hirsemann, H. Graafsma, M. Epple, M. Zuvic, M.-O. Lampert, T. Fritzsich, and M. Rothermund, *J. Phys. Conf. Ser.* 425, 062010 (2013).
- <sup>36</sup> C. Prescher and V.B. Prakapenka, *High Pressure Res.* 35, 223 (2015).
- <sup>37</sup> S.P. Ong, W.D. Richards, A. Jain, G. Hautier, M. Kocher, S. Cholia, D. Gunter, V.L. Chevrier, K.A. Persson, and G. Ceder, *Comput. Mater. Sci.* 68, 314 (2013).
- <sup>38</sup> Matt Newville *et al.*, *Lmfit/Lmfit-Py 1.0.1* (Zenodo, 2020).
- <sup>39</sup> Y. Fei, A. Ricolleau, M. Frank, K. Mibe, G. Shen, and V. Prakapenka, *PNAS* 104, 9182 (2007).
- <sup>40</sup> P. Dierckx, *J. Comput. Appl. Math.* 1, 3 (1975).
- <sup>41</sup> P. Dierckx, *SIAM J. Numer. Anal.* 19, 1286 (1982).
- <sup>42</sup> M. French and R. Redmer, *Phys. Rev. B* 91, 014308 (2015).
- <sup>43</sup> S. Klotz, K. Komatsu, H. Kagi, K. Kunc, A. Sano-Furukawa, S. Machida, and T. Hattori, *Phys. Rev. B* 95, 174111 (2017).
- <sup>46</sup> J. S. Zhang, M. Hao, Z. Ren, and B. Chen, *Appl. Phys. Lett.* 114, 191903 (2019).
- <sup>45</sup> X. Li, W. Shi, X. Liu, and Z. Mao, *Amer. Miner.* 104, 1307 (2019).
- <sup>44</sup> M. Ahart, M. Somayazulu, S.A. Gramsch, R. Boehler, H. Mao, and R.J. Hemley, *J. Chem. Phys.* 134, 124517 (2011).
- <sup>47</sup> Y. Asahara, K. Hirose, Y. Ohishi, N. Hirao, and M. Murakami, *Earth Planet. Sci. Lett.* 299, 474 (2010).
- <sup>48</sup> M. Kuriakose, S. Raetz, Q. M. Hu, S. M. Nikitin, N. Chigarev, V. Tournat, A. Bulou, A. Lomonosov, P. Djemia, V. E. Gusev, and A. Zerr, *Phys. Rev. B* 96, 134122 (2017).
- <sup>49</sup> B. Journaux, R. Caracas, P. Carrez, K. Gouriet, P. Cordier, and I. Daniel, *Phys. Earth Planet. In.* 236, 10 (2014).
- <sup>50</sup> S. Speziale, H. Marquardt, and T.S. Duffy, *Rev. Mineral. Geochem.* 78, 543 (2014).
- <sup>51</sup> A.F. Goncharov, V.V. Struzhkin, H. K. Mao, and R.J. Hemley, *Phys. Rev. Lett.* 83, 1998 (1999).
- <sup>52</sup> V.V. Struzhkin, A.F. Goncharov, R.J. Hemley, and H. K. Mao, *Phys. Rev. Lett.* 78, 4446 (1997).
- <sup>53</sup> M. Benoit and D. Marx, *ChemPhysChem* 6, 1738 (2005).



## Supplemental Material

### **Bulk modulus of H<sub>2</sub>O across the ice VII – ice X transition measured by time-resolved X-ray diffraction in dynamic Diamond Anvil Cell experiments**

A. S. J. Méndez<sup>1,2</sup>, F. Trybel<sup>2</sup>, R. J. Husband<sup>1</sup>, G. Steinle-Neumann<sup>2</sup>, H.-P. Liermann<sup>1</sup> and H. Marquardt<sup>3</sup>

<sup>1</sup>*Deutsches Elektronen-Synchrotron (DESY), 22607 Hamburg, Germany;* <sup>2</sup>*Bayerisches Geoinstitut, Universität Bayreuth, 95440 Bayreuth, Germany;* <sup>3</sup>*Department of Earth Sciences, University of Oxford, OX1 3AN Oxford, UK.*

\*Corresponding author: Alba San José Méndez ([alba.mendez@desy.de](mailto:alba.mendez@desy.de))

This file contains supplemental information on the following:

- (i) A comparison of  $P$  and  $V$  obtained from our X-ray diffraction peak fitting with Gaussian functions to LeBail refinement on a number of selected diffraction patterns of the dDAC-1 and dDAC-2 experiments (Table 4.2).
- (ii) Further information on data reduction, i.e., the  $V(P)$  curves for the full dataset from the dDAC-2 experiments and the calculations of the bulk modulus  $K_T$  (Figure 4.6).
- (iii) A comparison of the bulk modulus  $K_T$  calculated from the smoothed splined results of the dDAC-1, dDAC-2 and dDAC-3 experiments (Figure 4.7).

Peak analysis: In our diffraction patterns, each peak is individually fitted to a Gaussian with a linear background correction. This approach appears superior to a Rietveld or Le Bail refinement (i) when it comes to peak-overlaps and (ii) automation of data processing. In order to assess the consistency of our results, we have performed a Le Bail fit on a limited number of diffraction patterns from dDAC-1 and dDAC-2 and compared the  $P$  and  $V$  obtained from both approaches in Table S1. The Gaussian and Le Bail fits are consistent with one another within the error coming from the minimal separable peak distance in our approach ( $2\theta=0.05^\circ$ ) using individual Gaussian.

<b>Experiment/Frame</b>	<b><math>V_{\text{Gaussian}} (\text{\AA}^3)</math></b>	<b><math>P_{\text{Gaussian}} (\text{GPa})</math></b>	<b><math>V_{\text{LeBail}} (\text{\AA}^3)</math></b>	<b><math>P_{\text{LeBail}} (\text{GPa})</math></b>
dDAC-1/450	27.2(6)	19.8	27.3	19.9
dDAC-1/700	25.9(6)	25.9	26.2	25.5
dDAC-1/950	24.4(5)	34.3	24.8	34.2
dDAC-1/1275	22.4(5)	48.7	22.5	49.0
dDAC-1/1875	20.3(4)	71.1	20.4	71.1
dDAC-2/230	27.8(6)	19.9	27.9	19.7
dDAC-2/260	26.5(6)	25.3	26.5	25.2
dDAC-2/390	21.3(4)	64.0	21.3	64.0
dDAC-2/510	19.3(4)	105.0	19.3	104.4
dDAC-2/650	18.3(4)	135.2	18.4	134.7

**Table 4.2:** Comparison for ten points (five each for dDAC-1 and dDAC-2) for  $P$  and  $V$  using Le Bail and Gaussian fitting to X-ray diffraction patterns. The errors given in the  $V$ -estimate from our Gaussian fit ( $V_{\text{Gaussian}}$ ) reflect the minimal separable peak ( $2\theta=0.05^\circ$ ). Volume uncertainties from the LeBail fit ( $V_{\text{LeBail}}$ ) are below  $10^{-2} \text{\AA}^3$ .

Data reduction: The volume changes caused by the fine pressure steps that characterize our quasi-continuous compression data are, in general, below the fitting resolution, especially for high values of  $K_T$  where the sample is highly incompressible. Under such conditions, small shifts in  $2\theta$ -space of the traced reflections cannot be resolved by the fitting program. These factors can introduce artificial jumps in the  $V(P)$  data that are magnified in the derivative. In order to avoid this, we increase the  $P$ -steps by skipping patterns in the fitting. An example of such procedure is illustrated for dDAC-2 in Fig. 4.6a. The bulk modulus is then calculated from the reduced dataset by three-point finite differences before smoothing, and compared with  $K_T$  obtained after applying a spline interpolation and smoothing for the reduced dataset (Fig. 4.6b). The main features in the  $P$ -dependence of  $K_T$  are conserved after smoothing the reduced dataset.

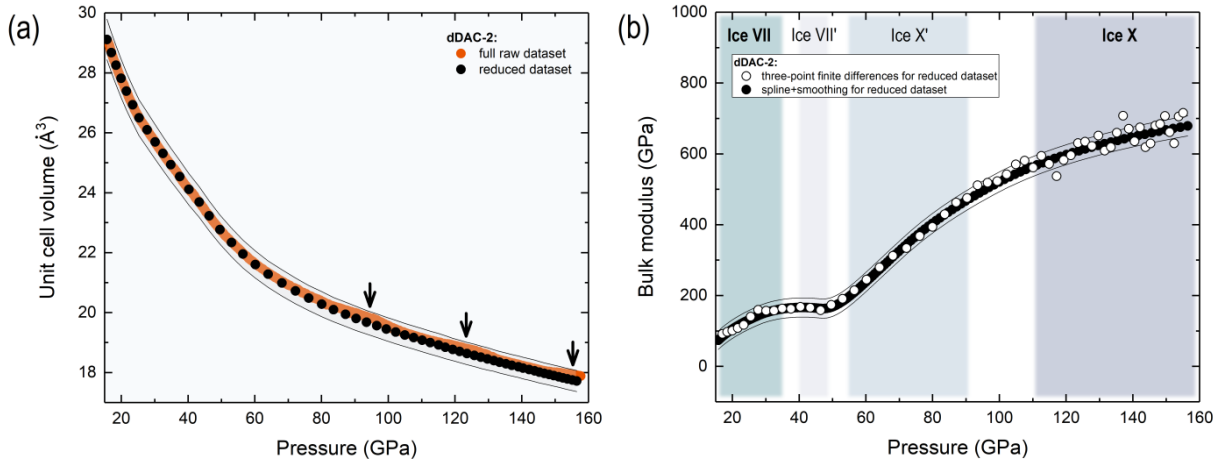


**Figure 4.6:** (a) Pressure-volume curves for dDAC-2. Orange circles correspond to the analysed full data consisting of 590 diffraction patterns, black circles represent  $V(P)$  data obtained after fitting every 10th pattern (reduced dataset) as described in Section 2.3. Black thin lines indicate the error in  $V$ . Black arrows point to small artificial jumps in the full  $V(P)$  data set, introduced by the fitting routine. (b) Bulk modulus as a function of pressure derived from the reduced dataset in dDAC-2, following two different procedures: (i) Computed by three-point finite differences (white circles) and (ii) derived from the procedure described in Section 2.4 using the reduced dataset (black circles).

Comparison of bulk modulus from different runs: Bulk moduli  $K_T$  derived from dDAC-1, dDAC-2 and dDAC-3 are plotted against  $P$  in Fig. 4.7, in comparison to computational results from French & Redmer [42]. Overall, the  $P$ -dependence of  $K_T$  agrees between the three experiments and with the computational results. The three main changes in  $P$ -dependence of  $K_T$  – discussed for the dDAC-2 data in the main text – are also visible in dDAC-3, despite fluctuations noticeable above 100 GPa which originate from modulations in the  $V(P)$  curve introduced by the fitting routine. The magnitude of these fluctuations falls within experimental uncertainty. With a maximum  $P=90$  GPa reached in the dDAC-1 experiment, only the signature of the ice VII – ice VII' and ice VII' – ice X' is observed.

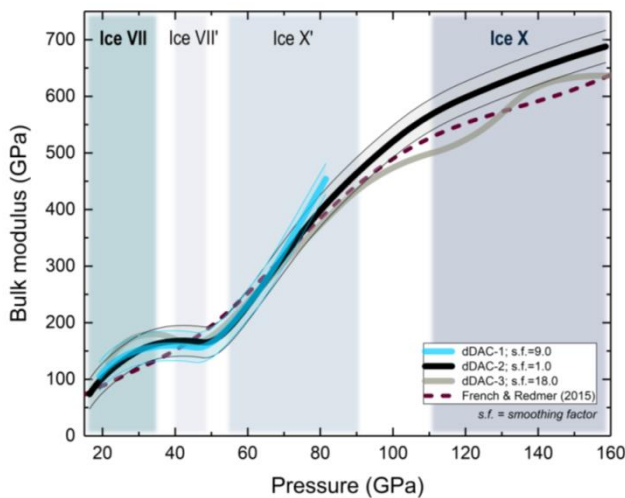


**Figure 4.7:** Bulk modulus as a function of pressure as derived from dDAC-1, dDAC2 and dDAC-3 data. The dashed maroon line shows computational results [42]. Background colors indicate approximate  $P$ -ranges for the stability of ice VII, ice VII', ice X' and ice X based on the  $P$ -ranges where a quasi-linear  $P$ -dependence of  $K_T$  is observed in our work.



## Chapter 5

# Broad softening of ferropicrlase across the iron spin crossover and a mixed-spin lower mantle

A.S.J. Méndez<sup>1,2</sup>, S. Stackhouse<sup>3</sup>, A. Kurnosov<sup>2</sup>, N. Satta<sup>4</sup>, H.-P. Liermann<sup>1</sup>, R. J. Husband<sup>1</sup> and H. Marquardt<sup>4</sup>

<sup>1</sup>Deutsches Elektronen-Synchrotron (DESY), 22607 Hamburg, Germany; <sup>2</sup>Bayerisches Geoinstitut BGI, University of Bayreuth, 95440 Bayreuth, Germany; <sup>3</sup>School of Earth and Environment, University of Leeds, LS2 9JT Leeds, United Kingdom; <sup>4</sup>Department of Earth Sciences, University of Oxford, OX1 3AN Oxford, United Kingdom.

Corresponding author: Alba San José Méndez (alba.mendez@desy.de)

This chapter has been submitted to:

*Earth and Planetary Science Letters*

### Abstract

The elastic bulk modulus softening of (Mg,Fe)O ferropicrlase across the iron spin crossover in Earth's lower mantle induces dramatic changes in key physical properties, including seismic P-velocities and viscosity. Direct measurements of the bulk modulus of (Mg,Fe)O, as well as computations, suggest largely different pressure ranges over which the elastic softening occurs. Here, we performed compression of powders of (Mg<sub>0.9</sub>Fe<sub>0.1</sub>)O and (Mg<sub>0.8</sub>Fe<sub>0.2</sub>)O in a piezo-driven dynamic Diamond Anvil Cell (dDAC) and monitored the compression behavior of the sample using time-resolved X-ray diffraction. The bulk modulus of ferropicrlase is derived directly from our high-resolution data by differentiation of pressure and volume data, without the need to assume a specific functional form to describe the elastic behavior throughout the spin crossover region. We complement our experimental results with theoretical calculations where we used multiple models with random configurations of iron, and presumed a regular solution for high- and low-spin iron. Both experiments and computations show a broad and asymmetric softening of the bulk modulus at pressures between about 40 and 80 GPa for (Mg<sub>0.8</sub>Fe<sub>0.2</sub>)O at room temperature, and suggest that the softening is sensitive to the distribution of iron in the ferropicrlase structure. Extending our theoretical work to high-temperature, we find that (Mg<sub>0.8</sub>Fe<sub>0.2</sub>)O is in a mixed-spin state throughout the majority of the lower mantle, with a low-spin fraction of only about 0.6 in the lowermost mantle along a typical geotherm. Our findings

imply that the properties of ferropericlae in the lowermost mantle, including its bulk modulus and viscosity, are close to those of the mixed-spin state.

**Keywords:** (Mg,Fe)O, ferropericlae, spin crossover, elastic softening, dynamic DAC, synchrotron time-resolved X-ray diffraction, ab-initio calculations, lower mantle, seismic signature

## 5.1 INTRODUCTION

(Mg,Fe)O ferropericlae is the second most abundant mineral in Earth's lower mantle (e.g. Irifune and Tsuchiya 2015). At high pressure, ferrous iron ( $\text{Fe}^{2+}$ ) in ferropericlae undergoes a change of electronic spin state. At room pressure,  $\text{Fe}^{2+}$  adopts the high-spin electronic configuration where the six 3d-electrons partially fill the  $t_{2g}$  and  $e_g$  orbitals, maximizing the number of unpaired electrons. At a pressure of about 40 GPa, a distortion of the iron-containing octahedral sites in the crystal structure triggers a change in iron electronic configuration to the low-spin state, where electron pairing in the  $t_{2g}$  orbitals is favored (Badro et al. 2003). The spin crossover is accompanied by a reduction in the  $\text{Fe}^{2+}$  ionic radius (Shannon 1976) enhancing the compressibility of ferropericlae over the pressure range where the spin crossover occurs (Crowhurst et al. 2008, Lin et al. 2013). Among others, the enhanced compressibility of ferropericlae in mixed-spin state causes a significant decrease in seismic P-wave velocities (Crowhurst et al. 2008, Marquardt et al. 2009, Wentzcovitch et al. 2009, Yang et al. 2015), and might lead to a marked decrease in viscosity (Wentzcovitch et al. 2009, Saha et al. 2013, Marquardt and Miyagi 2015, Deng and Lee 2017). Quantifying the presence and distribution of mixed-spin state ferropericlae in the lower mantle is thus pivotal to interpret seismic observables and design geodynamic models.

Diamond Anvil Cell (DAC) experiments provided direct constraints on the bulk modulus of (Mg,Fe)O across the spin crossover and reported a substantial elastic softening (Crowhurst et al. 2008, Yang et al. 2015, Marquardt et al. 2018), which is also supported by computations (Wentzcovitch et al. 2009). The pressure range over which the decrease of the bulk modulus is observed, however, varies significantly. Early measurements on  $(\text{Mg}_{0.94}\text{Fe}_{0.06})\text{O}$  using Impulsive Stimulated Light Scattering (ISLS) reported a bulk modulus softening between 40 and 60 GPa (Crowhurst et al. 2008), whereas more recent work on  $(\text{Mg}_{0.92}\text{Fe}_{0.08})\text{O}$  using the same technique observed the softening up to a pressure of almost 80 GPa (Yang et al. 2015). Pressure oscillation experiments in the dynamic DAC in combination with time-resolved X-ray diffraction diagnostics reported a similarly broad crossover range extending from about 40 GPa to 80 GPa (Marquardt et al. 2018). The latter is the only study to directly measure the bulk modulus softening for iron

contents above 8%, but has a limited pressure coverage within the spin crossover region and was performed in non-hydrostatic conditions.

The observation of such a broad crossover range is in apparent disagreement with the results of modelling of the bulk modulus based on traditional X-ray diffraction data that generally predicts a sharper softening across the spin crossover (Marquardt et al. 2009, Mao et al. 2011, Lin et al. 2013). However, the sharpness of the resulting bulk modulus softening depends on model assumptions and is poorly constrained by the actual data that typically cover only a few pressure points over the pressure region of the spin crossover (Lin et al. 2005, Fei et al. 2007, Marquardt et al. 2009, Solomatova et al. 2016).

Recent computational works also predict different spin crossover pressure ranges, with early works predicting a relatively sharp crossover at 300 K (Tsuchiya et al. 2006, Wentzcovitch et al. 2009). These theoretical studies used models where the distance between iron atoms is maximized, and it is assumed that high- and low-spin iron form an ideal solid solution (Tsuchiya et al. 2006, Wentzcovitch et al. 2009, Muir and Brodholt 2015). In contrast, previous experimental work showed that at ambient pressure ferroperricite samples quenched from high temperature ( $\sim 1000$  K), largely exhibit random ordering (Waychunas et al. 1994) and more recent calculations showed that there is a favourable enthalpy of mixing of high- and low-spin iron (Holmström and Stixrude 2015), which leads to a broadening of the spin crossover.

Here we used a dynamic Diamond Anvil Cell (dDAC) driven by a piezoelectric actuator (Evans et al. 2007, Jenei et al. 2019) to compress ferroperricite powders across the spin crossover using neon as pressure-transmitting medium. We employed extremely sensitive X-ray detectors in combination with the dDAC to perform time-resolved X-ray diffraction measurements along the compression path. The excellent pressure resolution of our data, about 0.1-0.5 GPa, together with the smooth compression path achieved by the dDAC (low data scatter), enables us to directly quantify the bulk modulus of ferroperricite across the spin crossover, without the need for model assumptions (Méndez et al. 2021). To complement our experimental results, we performed first-principles calculations that provide atomic-scale insight into the spin crossover and its associated bulk modulus anomaly. Both our experimental and computational data show a broad asymmetric spin crossover region. We use our high-temperature calculations to predict the low-spin fraction along a typical lower mantle geotherm and find it to be about 0.6 at the core-mantle boundary.

## **5.2 MATERIALS AND METHODS**

### *5.2.1 Experimental details*

#### *A) High-pressure dynamic diamond-anvil cell experiments*

Powders of  $(\text{Mg}_{0.9}\text{Fe}_{0.1})\text{O}$  and  $(\text{Mg}_{0.8}\text{Fe}_{0.2})\text{O}$  were synthesized from stoichiometric mixtures of reagent grade  $\text{MgO}$  and  $\text{Fe}_2\text{O}_3$  treated in a gas-mixing furnace at  $1250^\circ\text{C}$  at an oxygen fugacity of 2 log units below the fayalite-magnetite-oxygen (FMQ) buffer (see also Marquardt and Miyagi 2015). Fine-grained platinum powder was mixed with the sample and used as a pressure marker. Rhenium gaskets were preindented to a thickness of about  $30\ \mu\text{m}$  in a symmetric DAC with  $200\ \mu\text{m}$  anvil culets and holes with  $150\ \mu\text{m}$  diameters were drilled in the gaskets. Given the typically small amount of sample required for gas loading in DACs and the relatively low Z-character of  $(\text{Mg,Fe})\text{O}$  in comparison to Re, an amorphous  $\text{Fe}_{0.79}\text{Si}_{0.07}\text{B}_{0.14}$  insert was placed in the Re gasket hole in order to avoid emergence of Re peaks in the diffraction patterns (Mendez et al. 2020), Fig. 5.1a. The  $(\text{MgFe})\text{O}$ -Pt mixture was loaded into the gasket hole and neon was loaded as pressure-transmitting medium using the gas-loading setup at the Extreme Conditions Beamline (ECB) at PETRA III, DESY, Germany (Liermann et al. 2015). Samples were precompressed by uniformly tightening the screws as in standard DAC experiments. The DACs were inserted in a “cap housing” coupled to a high voltage piezoelectric (PE) actuator (Jenei et al. 2019). DAC and PE were engaged by tightening the cap at the back of the housing until a slight pressure increase was observed. When a given voltage is applied, the PE expands and pushes against the DAC in the housing compressing the sample. Trapezoidal voltage-time waveforms were generated using the program *Benchlink Waveform Builder* (Keysight Technologies) and loaded on a waveform generator (Agilent 33522B). A delay generator (SRS, DG645/5 with Rb clock) and a piezo amplifier (Piezosystem Jena GmbH) are employed when sending the waveform to the PE (Jenei et al. 2019).

Intense monochromatic synchrotron X-ray radiation ( $0.48\ \text{\AA}$  wavelength) was used for time-resolved X-ray diffraction measurements at the ECB (Liermann et al. 2015), focused using a compound refractive lens ( $2\ (\text{h})\ \mu\text{m} \times 8\ (\text{v})\ \mu\text{m}$ , FWHM). A GaAs 2.3 MPix LAMBDA detector that allows for data collection at a repetition rate of up to 2 kHz (Pennicard et al. 2013, Pennicard et al. 2018) was employed to perform fast collection of X-ray diffraction images. The detector was placed with an offset to the sample center, capturing sections of the Debye–Scherrer diffraction rings. Tilting and rotation of the detector and sample-detector distance were calibrated using a  $\text{Cr}_2\text{O}_3$  standard (NIST 674b). Data analysis software developed at the ECB was used for quick visualization of the collected data in contour plots (Fig. 5.1b). Diffraction images were integrated using the program Dioplas (Prescher and Prakapenka 2015). The integrated and background

corrected diffraction patterns were processed using a customised python code for batch processing to extract the peak positions of the sample and platinum.

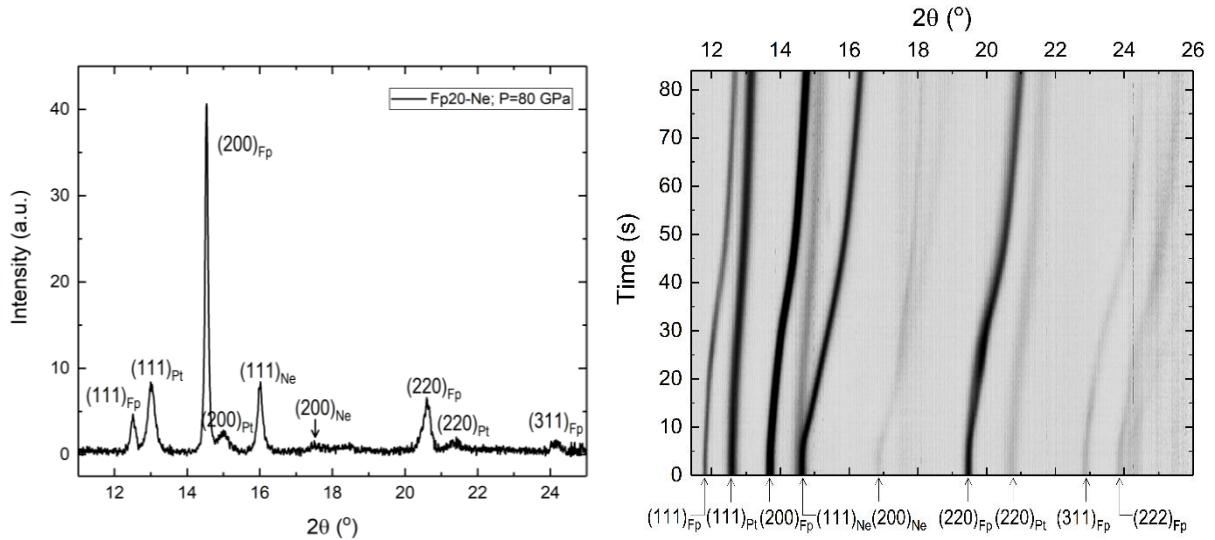


**Figure 5.1:** (a) A typical integrated diffraction pattern collected in 200 ms on  $(Mg_{0.8}Fe_{0.2})O$  at 80 GPa. (b) Contour plot showing the experimental run on  $(Mg_{0.8}Fe_{0.2})O$ , where >400 individual diffraction images have been collected upon compression.  $Pt_{(111)}$ ,  $Fp_{(200)}$ , and  $Fp_{(220)}$  remain strong diffraction lines throughout the entire experimental run and are not affected by peak overlap.

Data collection on  $(Mg_{0.8}Fe_{0.2})O$  was done continuously during a single continuous compression ramp from about 30 to 100 GPa. Single image exposure time was 200 ms. Data from  $(Mg_{0.9}Fe_{0.1})O$  were collected with single image exposure time of 400 ms in three compression steps, ranging from 30 to 47 GPa, 47 to 69 GPa, and 69 to 84 GPa. A second experimental run only provided useful data in the pressure range from 20 to 31 GPa, as the sample moved out of the X-ray beam during compression. The lattice parameter of the sample was determined by fitting the  $(200)$ , and  $(220)$  diffraction lines of ferropericlase  $Fp_{(200)}$ ,  $Fp_{(220)}$ . The fit to  $(111)$ , the weakest diffraction ring, were unreliable and this line was not used in the volume determination. Pressure was determined from the measured position of the  $(111)$  diffraction line of platinum,  $Pt_{(111)}$ , using published equation of state parameters (Fei et al. 2007).

### B) Derivation of high-pressure bulk moduli

The dense pressure-coverage in our data allows for a direct determination of the bulk modulus according to its thermodynamic definition ( $K_T = -V \cdot \partial P / \partial V$ ). We calculated the bulk modulus from the slope of a linear fit to  $V(P)$  applied over different pressure intervals (Fig. 5.5). As expected, a larger chosen pressure interval leads to smaller nominal uncertainties as derived from the standard error of the linear fit to the  $V(P)$  data. However, this comes at the expense of a reduced effective pressure resolution. The effect of the chosen pressure interval is illustrated in Fig. 5.6.

We found that the best results are obtained if the bulk moduli are derived from the unit cell volume calculated from a single line of ferropericlyase, i.e. either the (200) or the (220) line. By relying on a single line, volume scatter is minimized, leading to relatively smooth pressure derivatives. The choice of the ferropericlyase diffraction line does not substantially affect  $K(P)$  or its trend, see Fig. 5.7. Considering the signal-noise-ratio, use of the (200) line, the strongest ferropericlyase line, leads to overall smaller uncertainties, and was hence chosen for comparison to the computational results.

### 5.2.2 Calculation Details

#### A) Model Systems

To enable direct comparison with the experimental results, models of ferropericlyase were constructed with the chemical compositions  $(\text{Mg}_{0.90625}\text{Fe}_{0.09375})\text{O}$  and  $(\text{Mg}_{0.8125}\text{Fe}_{0.1875})\text{O}$ , corresponding to 3 or 6 Fe atoms in a 64 atom cell. For simplicity, we will sometimes refer to the two modelled compositions as  $(\text{Mg}_{0.9}\text{Fe}_{0.1})\text{O}$  and  $(\text{Mg}_{0.8}\text{Fe}_{0.2})\text{O}$  throughout the discussion. In order to investigate the possible role of short-range order on spin crossover pressure (Kantor et al. 2009, Glazyrin et al. 2017), 20 models were constructed for each ferropericlyase composition, with different random arrangements of Fe. For comparison, we also created a high symmetry model with a  $(\text{Mg}_{0.8125}\text{Fe}_{0.1875})\text{O}$  composition. The initial atomic coordinates of the Fe in these models are listed in Table S1 and depicted in Tables S2-S3.

In the 64-atom models, neighbouring on-axis iron atoms correspond to infinite rows of atoms with an Fe-O-Fe-O sequence. In order to assess the impact of this on the results, larger 216-atom models were constructed (see Tables S4-S7). These contained the same number and arrangement of iron atoms as the 64-atom models, but their larger size ensured that there were no iron arrangements corresponding to a infinite rows of atoms with an Fe-O-Fe-O sequence. To keep the same iron concentration in the 216-atom models, would have required an order of magnitude increase in the number of calculations, per model, which was not feasible.

#### B) First-principles Calculations

Theoretical calculations were performed with VASP (Kresse and Furthmüller 1996, Kresse and Furthmüller 1996), employing the projector augmented wave method (Blöchl 1994, Kresse and Joubert 1999), within the framework of density functional theory (DFT). The LDA exchange-correlation functional was used (Perdew and Zunger 1981). The valence electron configurations for the potentials were  $2p^63s^2$  for Mg,  $3p^63d^74s^1$  for Fe, and  $2s^22p^4$  for O. The kinetic-energy cut-off for the plane-wave basis set was set to 600 eV. For the 64-atom models, the Brillouin zone was sampled using a  $2\times 2\times 2$  Monkhorst-Pack grid (Monkhorst and Pack 1976), while for the

larger 216-atom models it was restricted to the gamma-point. The break condition for the electronic self-consistent loop was  $10^{-6}$  eV and that for ionic relaxation was  $10^{-5}$  eV. These parameters ensured that calculated enthalpy differences were converged to less than 1 meV per atom and bulk moduli to within 1 GPa. Symmetry was switched off.

In order to accurately describe the strongly correlated *d* electrons of iron in ferroperricite, we utilized the LDA+U method (Anisimov et al. 1991, Anisimov et al. 1997), in particular, the scheme of Dudarev et al. (1998) in which only the difference between onsite Coulomb interaction parameter *U* and onsite exchange parameter *J* is meaningful. In the present work, *U* is used to mean *U* - *J*. In our preliminary calculations, *U* = 3.4 eV was found to give the best agreement with experimental values for the spin crossover pressure and so was adopted for production calculations. This value is similar to the *U* = 3.0 eV used in previous calculations of ferroperricite (Muir and Brodholt 2015).

Since the LDA is known to underestimate pressure, we calculated a correction using the method outlined by Oganov et al. (2001), but excluding the thermal pressure term, which is expected to be small. The correction was calculated to be +6 GPa, based on the ambient condition volume of  $76.1\text{Å}^3$  reported by Speziale et al. (2007).

### *C) Magnetic Ordering*

For the iron concentrations investigated in this study, ferroperricite is paramagnetic at 300 K (Speziale et al. 2005, Kantor et al. 2009, Lyubutin et al. 2013). It is difficult to model paramagnetic systems and so in our theoretical calculations, the initial high-spin states were modelled both as ferromagnetic and antiferromagnetic and the results of both sets of calculations were averaged. For the antiferromagnetic calculations, initial magnetic moments were assigned in such a manner that iron atoms close to one another were given opposite spins.

In order to investigate the influence of magnetic state we calculated the spin crossover pressure for Models 7 and *symm* with a  $(\text{Mg}_{0.8125}\text{Fe}_{0.1875})\text{O}$  composition, for over 30 different magnetic orderings, representing disordered collinear paramagnets (Fig. 5.8). The spin crossover pressures are defined as going from the full high-spin state to full low-spin state. Model 7 has a random arrangement of iron atoms, with only off-axis neighbours. For this model the spin crossover pressures only varied by about 3 GPa. Model *symm* has an ordered arrangement of iron atoms, with only on-axis neighbours. For this model the spin crossover pressure varied by about 10 GPa, from about 46 GPa for ferromagnetic ordering, to close to 56 GPa for the highest symmetry antiferromagnetic ordering, with pressures for other orderings inbetween. This suggests that magnetic ordering is primarily important for models with a high number of neighbouring on-axis iron atoms.

*D) Spin Crossover*

The pressure and temperature dependence of the spin crossover was calculated following a similar approach to that of previous studies (Tsuchiya et al. 2006, Wentzcovitch et al. 2009), where the fraction of low-spin iron is calculated from the expression

$$n(P,T) = \frac{1}{1 + m(2S + 1)\exp\left(\frac{DH_{LS-HS}(P,T)}{k_B X_{Fe} T}\right)} \quad (5.1)$$

Here  $m$  is the electronic configuration degeneracy ( $m = 3$  for high-spin and  $m = 1$  for low-spin),  $S$  is the spin quantum number ( $S = 2$  for high-spin and  $S = 0$  for low-spin),  $DH_{LS-HS}$  is the difference in the enthalpy of the high- and low-spin states,  $k_B$  is the Boltzmann constant,  $X_{Fe}$  is the fraction of iron and  $T$  is temperature. However, in contrast to these studies and following the observations of Holmström and Stixrude (2015), we did not assume an ideal solution for high- and low-spin iron when calculating enthalpy differences, but instead treated it as a regular solution, calculating the enthalpy of mixed-spin states, as well as high- and low-spin. For each model studied, we calculated the enthalpy difference between all stable spin-states, including stable mixed-spin states, as a function of pressure (e.g. Fig. 5.9(a)) and used Equation 1 to determine  $n(P,T)$  for each spin crossover (e.g. Fig. 5.9(b)). In this procedure,  $DH_{LS-HS}$  is the enthalpy difference between a lower and higher spin state and  $X_{Fe}$  the fraction of iron in the model weighted by the fraction of iron involved in the individual spin crossover, i.e. for a model with  $(Mg_{(1-x)}Fe_x)O$  composition and a spin crossover where  $a$  out of  $b$  iron atoms go to low-spin:  $X_{Fe} = (a/b) \times x$ . The  $n$  value for a model is then the weighted average of the  $n$  values for the series of spin crossovers between high- and low-spin states, where the weights are their  $(a/b)$  values, e.g. Fig. 5.9(b). The  $n$  value for a particular ferroperricase composition was calculated as the arithmetic mean of the  $n$  values of all models with that composition, including both magnetic states. To allow direct comparison with the 64-atoms models, for the calculation of  $n$  using the 216-atom models,  $x$  was assumed to be the same value as that for the corresponding 64-atom model.

To reduce the number of calculations, this was achieved by first calculating the enthalpy of all spin states with one low-spin iron. Once the most favourable spin state with one low-spin iron was identified, it was used as the basis for constructing spin states with two low-spin irons. Once the most favourable spin state with two low-spin irons was identified, it was used as the basis for constructing spin states with three low-spin irons and so on and so forth. Enthalpy differences were calculated for each spin state at 20 GPa, 40 GPa, 60 GPa and 80 GPa. For the  $(Mg_{0.8125}Fe_{0.1875})O$  composition, it was not always possible to stabilize a high-spin

antiferromagnetic state at 80 GPa and a calculation was carried out at a lower pressure of 50 GPa instead. For one iron configuration (Model 1 of the  $(\text{Mg}_{0.8125}\text{Fe}_{0.1875})\text{O}$  composition) the results of this procedure were compared with those obtained when calculating all possible mixed-spin states, and were found to be identical.

Note that, as in previous studies (Tsuchiya et al. 2006) we neglect the vibrational free energy in the calculation of  $n(P,T)$ . Previous calculations (Wentzcovitch et al. 2009) have shown that this is important at lower mantle temperatures, but has a minor effect at room temperature.

### E) Equation of State

To determine the volume of ferropericlase through the spin crossover, the volume of mixing of the pure low- and high-spin states was assumed to be ideal

$$V(n) = (1 - n)V_{HS}(P) + nV_{LS}(P), \quad (5.2)$$

where  $V(n)$  is the volume of ferropericlase with a low-spin fraction  $n$ , and  $V_{HS}$  and  $V_{LS}$  are the volumes of ferropericlase in the pure high- and low-spin states. Our calculations for the  $(\text{Mg}_{0.8125}\text{Fe}_{0.1875})\text{O}$  composition, showed that the maximum deviation of the volume of a mixed-spin state from that predicted from ideal mixing of the volumes of the pure high- and low-spin states was on the order of 0.2%, with an average deviation of 0.05%. The latter equates to a volume of about  $0.05\text{\AA}^3$  per unit cell for the largest volume, and less for others.

For each ferropericlase composition, the volume difference between different models in the same spin-state (i.e. the same number of high- and low-spin iron) was on the order of 0.2%. In view of this, for simplicity, an equation-of-state was only calculated for one model for each ferropericlase composition. For the  $(\text{Mg}_{0.90625}\text{Fe}_{0.09375})\text{O}$  composition, this was Model 1, while for the  $(\text{Mg}_{0.8125}\text{Fe}_{0.1875})\text{O}$  composition, this was Model *symm*. The volumes of these models were calculated for the pure high- and low-spin states at 13 pressures between -10 GPa and 140 GPa. The resulting pressure-volume curves were fit to a third-order Birch-Murnaghan equation-of-state (Murnaghan 1944, Birch 1947), which were used to compute the volume of the pure high- and low-spin states ( $V_{HS}$ ,  $V_{LS}$ ) and corresponding bulk moduli ( $K_{HS}$ ,  $K_{LS}$ ), required for Equations (2) and (3). The same values were used for calculating  $V(n)$  and  $K(n)$ , when using  $n$  values from both 64-atom and 216-atom models.

All calculations were static and neglect thermal pressure. The effect of neglecting thermal pressure on the equation of state is expected to be small at 300 K and is, in part, accounted for through the *ad hoc* pressure correction, described above. These arguments follow through to the calculation of the bulk modulus below, which are based on these equations of state.

*F) Bulk Modulus*

Following previous theoretical studies (Wentzcovitch et al. 2009), the bulk modulus across the spin crossover was calculated from the relation

$$\frac{V(n)}{K(n)} = (1 - n) \frac{V_{HS}}{K_{HS}} + n \frac{V_{LS}}{K_{LS}} - (V_{LS} - V_{HS}) \left. \frac{\partial n}{\partial P} \right|_T \quad (5.3)$$

where all terms are as defined above and the pressure derivative of the fraction of low-spin iron was calculated at 300 K from a centred finite-difference approximation.

Note that, although  $n$  is calculated at 300 K,  $V(n)$ ,  $V_{HS}$ ,  $V_{LS}$ ,  $K_{HS}$  and  $K_{LS}$  are all static values, which will influence  $K(n)$ . As already mentioned above, we expect the difference between our static values and 300 K values to be small. In addition, we also note that previous calculations (Tsuchiya et al. 2006, Wentzcovitch et al. 2009) indicate that the temperature derivatives of the bulk modulus of the pure high- and low-spin states of ferroperriclite are on the order of 0.02 GPa/K. These derivatives imply that, without a pressure correction, static values for the bulk moduli will be about 6 GPa higher than 300 K values, which is smaller than the errors associated with the experimental measurements.

**5.3 RESULTS AND DISCUSSION**

The experimental and computational unit cell volumes are plotted as a function of pressure in Fig. 5.2. There is good agreement between the unit cell volumes derived from the (200) and the (220) diffraction lines of ferroperriclite, and volumes coincide with XRD data measured earlier for  $(\text{Mg}_{0.9}\text{Fe}_{0.1})\text{O}$  and  $(\text{Mg}_{0.83}\text{Fe}_{0.17})\text{O}$  in static DAC experiments (Lin et al. 2005, Marquardt et al. 2009). The unit cell volume of ferroperriclite shows a significant drop at a pressure of around 40 GPa indicating the onset of the iron spin crossover. The change of trend in  $V(P)$  becomes very clear in our data due to the quasi-continuous pressure coverage. The agreement of the here-measured volumes with previous experimental data collected in static DAC experiments suggests that our compression rate is sufficiently slow for the system to not suffer from non-equilibrium effects that may be encountered in dynamic compression experiments, at least not more than possibly present in traditional static DAC experiments where measurements are taken on the time-scale of minutes (Glazyrin et al. 2020).

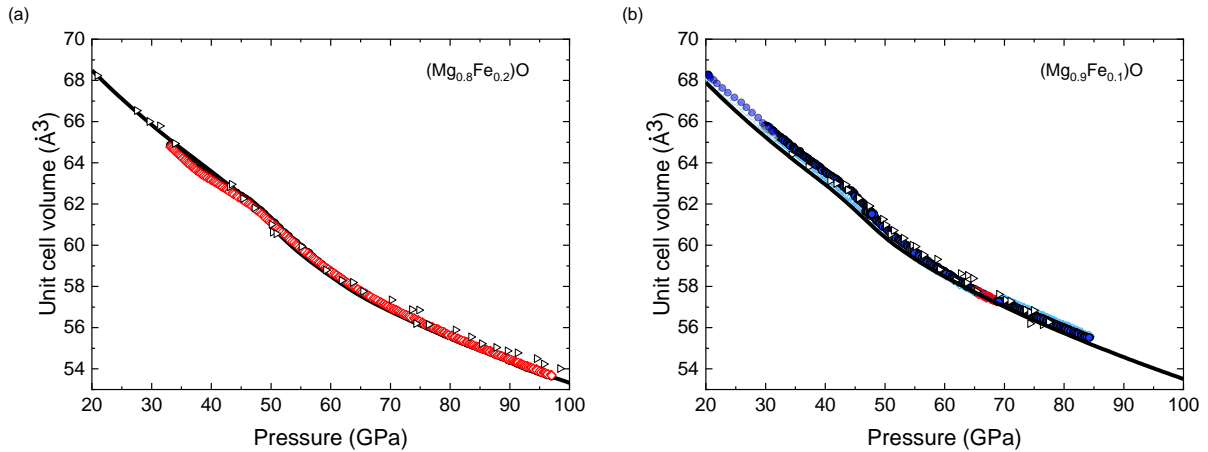


**Figure 5.2:** Unit cell volumes derived from (Mg,Fe)O by experiments (full symbols: derived from (200), open symbols: derived from (220) and computations (solid curves). (a) Unit cell volume of  $(\text{Mg}_{0.8}\text{Fe}_{0.2})\text{O}$  as a function of pressure, in comparison to previously published X-ray diffraction data on  $(\text{Mg}_{0.83}\text{Fe}_{0.17})\text{O}$  (Lin et al. 2005) shown as open black triangles. a) Unit cell volume of  $(\text{Mg}_{0.9}\text{Fe}_{0.1})\text{O}$  as a function of pressure, in comparison to previous X-ray diffraction data on ferropicrlase with the same composition (Marquardt et al. 2009) shown as open black triangles.

The dense pressure-coverage in our data, together with the smooth continuous compression achieved by the piezo-drive, allows for a direct determination of the bulk modulus according to its thermodynamic definition ( $K_T = -V \cdot \partial P / \partial V$ ). We calculated the bulk modulus from the slope of a linear fit of  $V(P)$  applied over a pressure interval of 2.5 GPa, which we found to represent the best compromise between pressure resolution and uncertainties in derived bulk moduli (Fig. 5.6). We derive the bulk modulus directly from our data without any smoothing or the need to assume its behavior across the spin crossover as required in previous works (Lin et al. 2005, Marquardt et al. 2009, Solomatova et al. 2016). The bulk moduli are plotted as a function of pressure in Fig. 5.3, together with the here-performed ab-initio calculations. Both measured and calculated bulk moduli for  $(\text{Mg}_{0.9}\text{Fe}_{0.1})\text{O}$  and  $(\text{Mg}_{0.8}\text{Fe}_{0.2})\text{O}$  show a clear drop at a pressure of about 40-45 GPa associated with the spin crossover, where the onset pressure seems to slightly shift to higher pressures with iron content. Our data show a broad and asymmetric shape of the softening, particular for  $(\text{Mg}_{0.8}\text{Fe}_{0.2})\text{O}$ , consistent with findings of pressure-oscillation experiments on ferropicrlase (Marquardt et al. 2018).

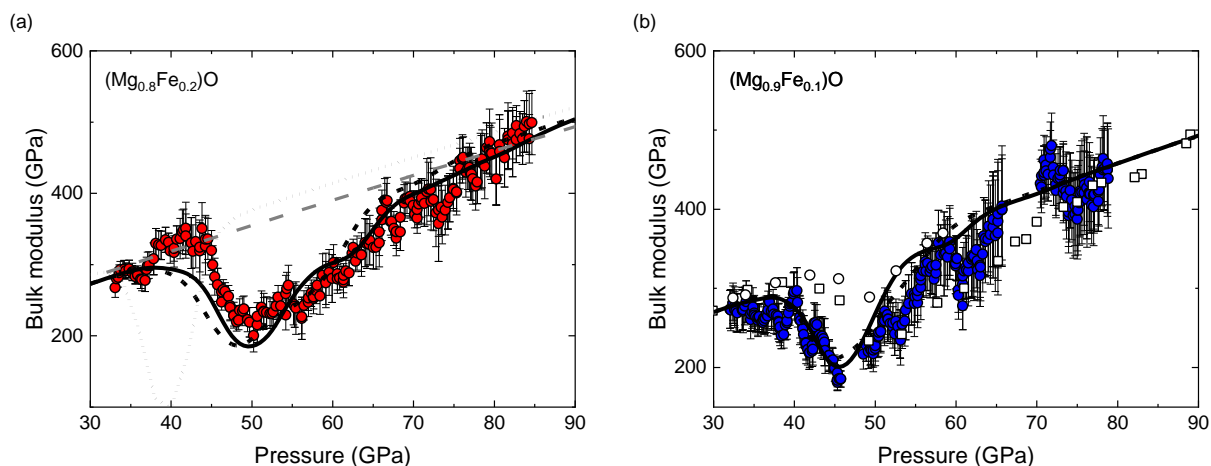


**Figure 5.3:** Bulk moduli derived by direct differentiation of our experimentally measured  $V(P)$ -data in comparison to our ab-initio calculations, using multiple models with random configurations of iron, and presuming a regular solution for high- and low-spin. Computational results are shown as solid black curves (64 atoms model) and short dashed black curves (216 atoms model). (a) Bulk moduli derived for  $(\text{Mg}_{0.8}\text{Fe}_{0.2})\text{O}$  in comparison to previous computational work on  $(\text{Mg}_{0.8175}\text{Fe}_{0.1825})\text{O}$  (Wentzcovitch et al. 2009), using a model where iron atoms are far apart and presuming ideal mixing of high- and low-spin irons (dotted curve). The dashed grey line shows the bulk modulus predicted for MgO by computations (Karki et al. 1999). (b) Results for  $(\text{Mg}_{0.9}\text{Fe}_{0.1})\text{O}$  in comparison to data for  $(\text{Mg}_{0.94}\text{Fe}_{0.06})\text{O}$  (open circles) and  $(\text{Mg}_{0.92}\text{Fe}_{0.08})\text{O}$  (open squares) derived from optical spectroscopy measurements (Crowhurst et al. 2008, Yang et al. 2015). The larger scatter in bulk moduli derived for  $(\text{Mg}_{0.9}\text{Fe}_{0.1})\text{O}$  results from the collection of data in three distinct compression steps (see section 5.2.1).

Overall our findings suggest that the bulk modulus is lowered over a pressure range of at least 30 GPa for  $(\text{Mg}_{0.8}\text{Fe}_{0.2})\text{O}$ , this is in apparent disagreement with some XRD results that suggested a range of about 20 GPa (Lin et al. 2005, Komabayashi et al. 2010, Mao et al. 2011). It is important to note, however, that the selected method to infer the bulk modulus of ferropericlae from traditional X-ray diffraction measurements can have a significant effect on the shape and width of the observed softening (Solomatova et al. 2016). Previous calculations predicted a sharp bulk modulus softening and do not reproduce our experimental results well (Wentzcovitch et al. 2009). In assuming an ideal solution for high- and low-spin iron, all iron atoms undergo the spin crossover at the same pressure, causing a very sharp bulk modulus softening (Wentzcovitch et al. 2009). A broader bulk modulus softening and hence wider spin crossover range at 300 K appears to be supportive of the work of Holmström and Stixrude (2015), who attribute the observed broadness of the spin crossover at low temperatures (300 K) to the favorable enthalpy of mixing  $\Delta H_{\text{mix}}$ . The magnitude of the enthalpy of mixing, however, is affected by the arrangement of Fe atoms, as predicted by Holmström and Stixrude (2015), who studied a highly symmetric arrangement of iron with periodic Fe-O-Fe-O sequences, leading to a broad spin crossover. More complicated arrangements, however, were not tested.

Our computations for  $(\text{Mg}_{0.8}\text{Fe}_{0.2})\text{O}$  predict a mixed-spin state for a pressure interval of about 40 GPa at room temperature, with a small difference between the values computed using the 64-

atom and 216-atom models, for reasons explained below. Our results are thus intermediate between the previous computational works, where Wentzcovitch et al. (2009) suggest a crossover range of only about 10 GPa, and Holmström and Stixrude (2015) predicted the range to span about 80 GPa. The main difference between these computations is the arrangement of iron in the models, and assumptions about the enthalpy of mixing of high- and low-spin atoms.

The agreement between our computations and the here-reported experimental results on both  $(\text{Mg}_{0.9}\text{Fe}_{0.1})\text{O}$  and  $(\text{Mg}_{0.8}\text{Fe}_{0.2})\text{O}$  suggest that (1) the mixed-spin region needs to be taken into account and (2) the assumption of a random distribution of iron atoms in the ferropерiclase structure is broadly valid. The slight disagreement observed between the here-reported experimental and computational results might be related to deviations from a random distribution in the experimental samples. Our results clearly show that the shape of the  $K(P)$  curve is sensitive to the distribution of iron in the ferropерiclase lattice.

Our data do not only show a broad spin crossover region, but also point towards a multi-dip structure where (at least) two local minima are noticeable in the experimental data as well as the theoretical calculations (Fig. 5.3). Differences between the bulk moduli calculated using values of  $n$  computed from 64-atom and 216-atom models are small, but evident. These are attributed to finite-size effects, in particular, pairs of neighbouring on-axis iron atoms present in some 64-atom models, which correspond to infinite rows of atoms with a Fe-O-Fe-O sequence.

To understand this further, consider the bulk modulus for the  $(\text{Mg}_{0.8125}\text{Fe}_{0.1875})\text{O}$  composition. Three anomalies are discernable between 40 GPa and 80 GPa. Our calculations indicate that the origin of these anomalies is iron atoms in different local environments undergoing spin crossovers at different pressures (Tables S2-S7). Most iron atoms undergo a spin crossover at about 40-50 GPa, with variations arising from small differences in their local environment, leading to the large first anomaly. The second and third anomalies correspond primarily to iron atoms that have neighbouring on-axis iron atoms in the low-spin state. For such iron atoms, the favourable enthalpy of mixing of high- and low-spin states stabilizes the high-spin iron atoms to higher pressures, but this is overestimated in the 64-atom models. The small size of the 64-atom models and use of periodic boundary conditions mean that all pairs of neighbouring on-axis iron atoms correspond to a repeating Fe-O-Fe-O sequence. Thus when one of the pair undergoes a spin crossover the other, in effect, experiences two low-spin neighbouring on-axis iron atoms (the iron atom in the model and its periodic image). Therefore the second and third anomalies occur at higher pressures in the 64-atom models than the 216-atoms models, where this is not an issue. For the 64-atom models, the second and third anomalies are centred at about 62 GPa and 80 GPa, but for the 216-atom models they occur at about 57 GPa and 70 GPa. We also notice that the first anomaly at about 50 GPa in the 64-atom models shifts to about 48 GPa, in the 216-

atom models. We attribute this to the overall decrease in iron concentration in the 216-atom models. Support for this comes from the observation that this effect is smaller for the  $(\text{Mg}_{0.90625}\text{Fe}_{0.09375})\text{O}$  composition. The pressures at which the anomalies occur are in broad agreement with the positions of the dips observed in the experimental measurements.

Our theoretical results provide atomic scale understanding of how the arrangement of iron influences the spin crossover. In Tables S2 and S3 we report the structures, low-spin fraction at 300 K and Fe-Fe radial distribution function for all 64-atom models studied. Fe-Fe radial distribution functions were calculated using VMD (Humphrey et al. 1996). In Tables S4-S7 we report the structures and compare the low-spin fraction at 300 K for 64-atom and 216-atom models. Labels indicate the order that the iron atoms undergo a spin crossover. Together these show that the pressure at which individual iron atoms undergo a spin crossover depends on several factors: the number and type (on or off-axis) of neighbouring iron atoms, whether the neighbouring iron atoms are in a high- or low-spin state and to a certain extent, and whether they have the same or opposite spin (Tables S2-S7).

Let us first consider how the arrangement of iron atoms influences the onset pressure of the spin crossover. Our results suggest that the spin crossover pressure of an individual iron atom increases with number of high-spin off-axis neighbouring iron atoms, with the increase being larger if it is of the same spin, but decreases with number of high-spin on-axis neighbouring iron atoms of the same spin, and increases with number of high-spin on-axis neighbouring iron atoms of the opposite spin. In practice, ferropericlase with the concentrations of iron we have studied is paramagnetic at ambient conditions (Speziale et al. 2005), which we approximate by averaging the results of ferromagnetic and antiferromagnetic calculations. For higher iron concentrations, it is antiferromagnetic at high pressures (Speziale et al. 2005). Based on these observations, the onset pressure of the spin crossover should increase with number of high-spin neighbouring iron atoms and degree of antiferromagnetic ordering, meaning that it should increase with iron concentration, as has been observed in experiments (Speziale et al. 2005). Differences in onset pressure are small for low iron concentrations, such as those studied in the present work, since the lowest number of neighbouring iron atoms is similar. Even though there is more clustering of iron atoms in the models for the  $(\text{Mg}_{0.8125}\text{Fe}_{0.1875})\text{O}$  composition, most contain at least one iron atom with either no or only one neighbouring iron atom, seen in the models for the  $(\text{Mg}_{0.90625}\text{Fe}_{0.09375})\text{O}$  composition.

While onset pressure depends on the number of high-spin neighbours of an iron atoms, the width of the spin crossover appears to depend on their number of low-spin neighbouring iron atoms. Our calculations show that as the spin crossover nears completion, it is the iron atoms with the most low-spin neighbouring iron atoms that persist in the high-spin state to the highest

pressures, in particular, those that have low-spin on-axis neighbouring iron atoms. Favourable enthalpy of mixing of high- and low-spin states has previously been reported to broaden the spin crossover (Holmström and Stixrude 2015). Our results suggest that this is most significant for on-axis neighbouring iron atoms pairs, which makes sense given that it is the on-axis  $d$ -orbitals ( $dz^2$  and  $dx^2-y^2$ ) that become unoccupied when iron atoms undergo a spin crossover. In a similar manner we find that in our calculations, when present, iron atoms with a high-spin on-axis neighbour are often the first to undergo a spin crossover.

Our current understanding of the architecture of the lower mantle largely relies on the interpretation of seismic tomography models based on shear and compressional wave velocities ( $V_s$ ,  $V_p$ ). Variations in temperature and pressure have a similar effect on the compressional wave and shear wave velocities of minerals and seismic tomography models are commonly interpreted based on the assumption that slow wave velocities are caused by higher temperatures (hot plumes), whereas seismically fast regions indicate cold areas (subducting slabs).

The iron spin crossover, however, has a stronger effect on  $V_p$  (through the reduction of the bulk modulus) than expected temperature variations in parts of the lower mantle (Marquardt et al. 2009, Wentzcovitch et al. 2009, Lin et al. 2013, Wu and Wentzcovitch 2014). Furthermore, the complex dependence on pressure and temperature can lead to a situation where an increase of temperature causes  $V_p$  to increase or remain unchanged, an effect that is incompatible with the simple relations commonly used to interpret seismic tomography models (slow = hot; fast = cold) (Marquardt et al. 2009, Wu and Wentzcovitch 2014). The ratio between shear-wave velocity  $V_s$  and compressional-wave velocity  $V_p$  variations ( $V_s/V_p$  ratio), as well as the correlation between  $V_s$  and bulk sound velocity  $V_c$  variations should be particularly sensitive to the iron spin crossover. Tomographic studies of the lower mantle generally find a negative  $V_s - V_c$  correlation. While in the lowermost mantle these observations are potentially explained by large-scale compositional variations or the phase transition from bridgmanite to post-perovskite (Koelemeijer et al. 2018), an explanation is lacking at mid-mantle depths between 1700 – 2300 km depth. The iron spin crossover might provide an explanation for the seismic observations, and recent works seem to provide first indications of its detectability in seismic observables (Shephard et al. 2020, Kennett 2021).

The exact seismic signature of the spin crossover, however, is sensitive to the broadness of the crossover and the associated elastic softening, as well as its dependence on temperature. Both our experiments and computations support a broad spin crossover and softening of the bulk modulus at room temperature. Based on the extension of our theoretical results on the spin states, which reproduce our room temperature experiments, to high temperatures (Fig. 5.4),

ferropericlasite would be in mixed-spin state along a typical geotherm throughout the bottom half of Earth's lower mantle. We could therefore expect the unique seismic signature of the spin crossover (most importantly the elevated  $V_S/V_P$  ratio) to affect seismic observables at all mantle depths below roughly 1000-1500 km.

Besides the impact on the seismic signature of the iron spin crossover expected in the lower mantle, our results have wide-ranging implications for the physical properties of ferropericlasite in the lowermost mantle. Importantly, our model predicts the fraction of low-spin iron to be only about 60% at the core-mantle boundary. We could therefore expect that the properties of ferropericlasite are closer to those predicted for the mixed-spin state than to the low-spin state. This implies a significantly reduced bulk modulus, altered electrical and thermal transport properties (Lin et al. 2013), as well as markedly reduced viscosity (Wentzcovitch et al. 2009, Saha et al. 2013, Marquardt and Miyagi 2015, Deng and Lee 2017). Our findings also suggest that the properties of ferropericlasite in the lowermost mantle can change geographically as lateral temperature variations lead to variations in the spin state of iron.

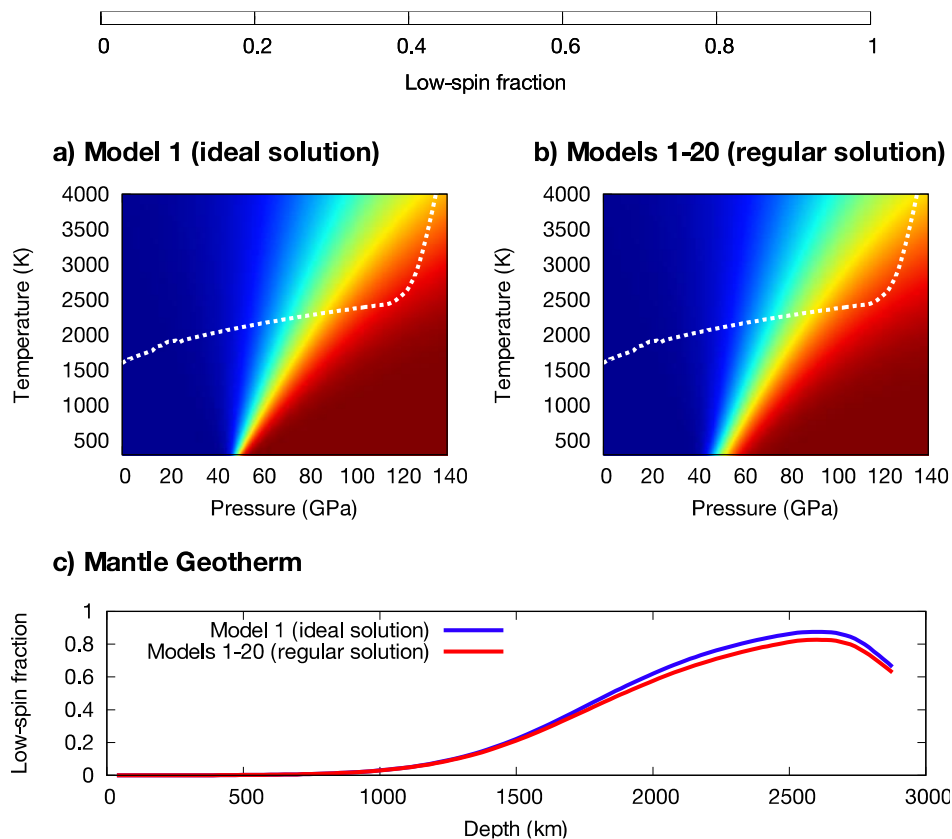


**Figure 5.4:** Low-spin fraction of  $(\text{Mg}_{0.8175}\text{Fe}_{0.1825})\text{O}$  at high pressure and temperature. Results are shown for (a) the ideal solution model and (b) a selected regular solution model. (c) Low-spin fraction of iron in  $(\text{Mg}_{0.8175}\text{Fe}_{0.1825})\text{O}$  expected along a mantle geotherm.

## 5.4 CONCLUSIONS

By combining novel time-resolved high-pressure XRD measurements with ab-initio computations, we show that the iron spin crossover leads to a broad, asymmetric softening of the bulk modulus with pressure. The broadness and shape of the elastic softening is a result of a mixed-spin state and is sensitive to the distribution of iron atoms within the crystal lattice. Based on our findings, we expect ferropericlase to be in mixed-spin state throughout the majority of the lower mantle and at the core-mantle boundary, with significant implications for its physical behavior, including seismic wave velocities and viscosity.

## Acknowledgments

This research was supported through the DFG Research Unit FOR 2440 (grant MA4534/5-1) as well the European Union's Horizon 2020 research and innovation Programme (ERC grant 864877). HM thanks Paula Koelemeijer for discussions. We like to thank M. Wendt for providing technical assistance. We acknowledge DESY (Hamburg, Germany), a member of the Helmholtz Association HGF, for the provision of experimental facilities. The research leading to this result has been supported by the project CALIPSOplus under the Grant Agreement 730872 from the EU Framework Program for Research and Innovation HORIZON 2020. The first-principles calculations were performed on ARC3 and ARC4 part of the High-Performance Computing facilities at the University of Leeds, UK, and also on ARCHER, the UK's national high-performance computing service.

## References

- Anisimov, V. I., F. Aryasetiawan and A. I. Lichtenstein (1997). "First-principles calculations of the electronic structure and spectra of strongly correlated systems: the LDA+U method." *Journal of Physics: Condensed Matter* **9**(4): 767-808.
- Anisimov, V. I., J. Zaanen and O. K. Andersen (1991). "Band theory and Mott insulators: Hubbard U instead of Stoner I." *Physical Review B* **44**(3): 943-954.
- Badro, J., G. Fiquet, F. Guyot, J.-P. Rueff, V. V. Struzhkin, G. Vanko and G. Monaco (2003). "Iron partitioning in Earth's mantle: toward a deep lower mantle discontinuity." *Science* **300**(5620): 789-791.
- Birch, F. (1947). "Finite Elastic Strain of Cubic Crystals." *Physical Review* **71**(11): 809.
- Blöchl, P. E. (1994). "Projector augmented-wave method." *Physical Review B* **50**(24): 17953-17979.
- Crowhurst, J. C., J. M. Brown, A. F. Goncharov and S. D. Jacobsen (2008). "Elasticity of (Mg,Fe)O through the spin transition of iron in the lower mantle." *Science* **319**(5862): 451-453.

## **Chapter 5. ELASTIC SOFTENING OF FERROPERICLASE ACROSS THE SPIN CROSSOVER**

- Deng, J. and K. K. M. Lee (2017). "Viscosity jump in the lower mantle inferred from melting curves of ferropericlase." *Nature Communications* **8**(1): 1997.
- Dudarev, S. L., G. A. Botton, S. Y. Savrasov, C. J. Humphreys and A. P. Sutton (1998). "Electron-energy-loss spectra and the structural stability of nickel oxide: An LSDA+U study." *Physical Review B* **57**(3): 1505-1509.
- Evans, W. J., C.-S. Yoo, G. W. Lee, H. Cynn, M. J. Lipp and K. Visbeck (2007). "Dynamic diamond anvil cell (dDAC): A novel device for studying the dynamic-pressure properties of materials." *Review of Scientific Instruments* **78**(7): 073904-073906.
- Fei, Y., A. Ricolleau, M. Frank, K. Mibe, G. Shen and V. Prakapenka (2007). "High-Pressure Geoscience Special Feature: Toward an internally consistent pressure scale." *Proceedings of the National Academy of Sciences* **104**(22): 9182-9186.
- Fei, Y., L. Zhang, A. Corgne, H. Watson, A. Ricolleau, Y. Meng and V. Prakapenka (2007). "Spin transition and equations of state of (Mg,Fe)O solid solutions." *Geophysical Research Letters* **34**: L17307.
- Glazyrin, K., S. Khandarkhaeva, L. Dubrovinsky and M. Sprung (2020). "Revisiting spin-state crossover in (MgFe)O by means of high-resolution x-ray diffraction from a single crystal." *Physical Review B* **101**(18): 184203.
- Glazyrin, K., R. Sinmyo, E. Bykova, M. Bykov, V. Cerantola, M. Longo, C. McCammon, V. B. Prakapenka and L. Dubrovinsky (2017). "Critical behavior of  $Mg_{1-x}Fe_xO$  at the pressure-induced iron spin-state crossover." *Physical Review B* **95**(21): 214412.
- Holmström, E. and L. Stixrude (2015). "Spin Crossover in Ferropericlase from First-Principles Molecular Dynamics." *Physical Review Letters* **114**(11): 117202.
- Humphrey, W., A. Dalke and K. Schulten (1996). "VMD: Visual molecular dynamics." *Journal of Molecular Graphics* **14**(1): 33-38.
- Irifune, T. and T. Tsuchiya (2015). 2.03 - Phase Transitions and Mineralogy of the Lower Mantle. *Treatise on Geophysics (Second Edition)*. G. Schubert. Oxford, Elsevier: 33-60.
- Jenei, Z., H. P. Liermann, R. Husband, A. S. J. Méndez, D. Pennicard, H. Marquardt, E. F. O'Bannon, A. Pakhomova, Z. Konopkova, K. Glazyrin, M. Wendt, S. Wenz, E. E. McBride, W. Morgenroth, B. Winkler, A. Rothkirch, M. Hanfland and W. J. Evans (2019). "New dynamic diamond anvil cells for tera-pascal per second fast compression x-ray diffraction experiments." *Review of Scientific Instruments* **90**(6): 065114.
- Kantor, I., L. Dubrovinsky, C. McCammon, G. Steinle-Neumann, A. Kantor, N. Skorodumova, S. Pascarelli and G. Aquilanti (2009). "Short-range order and Fe clustering in  $Mg_{1-x}Fe_xO$  under high pressure." *Physical Review B* **80**(1): 014204.
- Karki, B. B., R. M. Wentzcovitch, S. de Gironcoli and S. Baroni (1999). "First-principles determination of elastic anisotropy and wave velocities of MgO at lower mantle conditions." *Science* **286**(5445): 1705-1707.

- Kennett, B. L. N. (2021). "The relative behaviour of bulk and shear modulus as an indicator of the iron spin transition in the lower mantle." *Earth and Planetary Science Letters* **559**: 116808.
- Koelemeijer, P., B. S. A. Schuberth, D. R. Davies, A. Deuss and J. Ritsema (2018). "Constraints on the presence of post-perovskite in Earth's lowermost mantle from tomographic-geodynamic model comparisons." *Earth and Planetary Science Letters* **494**: 226-238.
- Komabayashi, T., K. Hirose, Y. Nagaya, E. Sugimura and Y. Ohishi (2010). "High-temperature compression of ferropericlase and the effect of temperature on iron spin transition." *Earth and Planetary Science Letters* **297**(3-4): 691-699.
- Kresse, G. and J. Furthmüller (1996). "Efficiency of ab-initio total energy calculations for metals and semiconductors using a plane-wave basis set." *Computational Materials Science* **6**(1): 15-50.
- Kresse, G. and J. Furthmüller (1996). "Efficient iterative schemes for ab initio total-energy calculations using a plane-wave basis set." *Physical Review B* **54**(16): 11169-11186.
- Kresse, G. and D. Joubert (1999). "From ultrasoft pseudopotentials to the projector augmented-wave method." *Physical Review B* **59**(3): 1758-1775.
- Liermann, H.-P., Z. Konopkova, W. Morgenroth, K. Glazyrin, J. Bednarcik, E. E. McBride, S. Petitgirard, J. T. Delitz, M. Wendt, Y. Bican, A. Ehnes, I. Schwark, A. Rothkirch, M. Tischer, J. Heuer, H. Schulte-Schrepping, T. Kracht and H. Franz (2015). "The Extreme Conditions Beamline P02.2 and the Extreme Conditions Science Infrastructure at PETRA III." *Journal of Synchrotron Radiation* **22**(4): 908-924.
- Lin, J.-F., S. Speziale, Z. Mao and H. Marquardt (2013). "Effects of the electronic spin transitions of iron in lower-mantle minerals: implications to deep-mantle geophysics and geochemistry." *Reviews of Geophysics* **51**(2): 244-275.
- Lin, J.-F., V. V. Struzhkin, S. D. Jacobsen, M. Y. Hu, P. Chow, J. Kung, H. Liu, H.-k. Mao and R. J. Hemley (2005). "Spin transition of iron in magnesiowüstite in the Earth's lower mantle." *Nature* **436**(7049): 377-380.
- Lyubutin, I. S., V. V. Struzhkin, A. A. Mironovich, A. G. Gavriliuk, P. G. Naumov, J.-F. Lin, S. G. Ovchinnikov, S. Sinogeikin, P. Chow, Y. Xiao and R. J. Hemley (2013). "Quantum critical point and spin fluctuations in lower-mantle ferropericlase." *Proceedings of the National Academy of Sciences* **110**(18): 7142.
- Mao, Z., J.-F. Lin, J. Liu and V. B. Prakapenka (2011). "Thermal equation of state of lower-mantle ferropericlase across the spin crossover." *Geophysical Research Letters* **38**(23): L23308.
- Marquardt, H., J. Buchen, A. S. J. Mendez, A. Kurnosov, M. Wendt, A. Rothkirch, D. Pennicard and H.-P. Liermann (2018). "Elastic Softening of  $(\text{Mg}_{0.8}\text{Fe}_{0.2})\text{O}$  Ferropericlase Across the Iron Spin Crossover Measured at Seismic Frequencies." *Geophysical Research Letters* **45**(14): 6862-6868.

- Marquardt, H. and L. Miyagi (2015). "Slab stagnation in the shallow lower mantle linked to an increase in mantle viscosity." *Nature Geoscience* **8**(4): 311-314.
- Marquardt, H., S. Speziale, H. J. Reichmann, D. J. Frost and F. R. Schilling (2009). "Single-crystal elasticity of  $(\text{Mg}_{0.9}\text{Fe}_{0.1})\text{O}$  to 81 GPa." *Earth and Planetary Science Letters* **287**(3-4): 345-352.
- Mendez, A. S. J., H. Marquardt, R. Husband, I. Schwark, J. Mainberger, K. Glazyrin, A. Kurnosov, C. Otzen, N. Satta, J. Bednarcik and H. P. Liermann (2020). "A resistively-heated dynamic diamond anvil cell (RHdDAC) for fast compression x-ray diffraction experiments at high temperatures." *Review of Scientific Instruments* **91**: doi: 10.1063/1065.0007557.
- Méndez, A. S. J., F. Trybel, R. J. Husband, G. Steinle-Neumann, H. P. Liermann and H. Marquardt (2021). "Bulk modulus of  $\text{H}_2\text{O}$  across the ice VII - ice X transition measured by time-resolved x-ray diffraction in dynamic diamond anvil cell experiments." *Physical Review B* **103**(6): 064104.
- Monkhorst, H. J. and J. D. Pack (1976). "Special points for Brillouin-zone integrations." *Physical Review B* **13**(12): 5188.
- Muir, J. M. R. and J. P. Brodholt (2015). "Elastic properties of ferropericlase at lower mantle conditions and its relevance to ULVZs." *Earth and Planetary Science Letters* **417**: 40-48.
- Murnaghan, F. D. (1944). "The Compressibility of Media under Extreme Pressures." *Proceedings of the National Academy of Sciences* **30**(9): 244-247.
- Oganov, A. R., J. P. Brodholt and G. D. Price (2001). "Ab initio elasticity and thermal equation of state of  $\text{MgSiO}_3$  perovskite." *Earth and Planetary Science Letters* **184**(3): 555-560.
- Pennicard, D., S. Lange, S. Smoljanin, H. Hirsemann, H. Graafsma, M. Eppe, M. Zuvic, M. O. Lampert, T. Fritsch and M. Rothermund (2013). "The LAMBDA photon-counting pixel detector." *Journal of Physics: Conference Series* **425**(6): 062010.
- Pennicard, D., S. Smoljanin, F. Pithan, M. Sarajlic, A. Rothkirch, Y. Yu, H.-P. Liermann, W. Morgenroth, B. Winkler, Z. Jenei, H. Stawitz, J. Becker and H. Graafsma (2018). "LAMBDA 2M GaAs—A multi-megapixel hard X-ray detector for synchrotrons." *Journal of Instrumentation* **13**(01): C01026.
- Perdew, J. P. and A. Zunger (1981). "Self-interaction correction to density-functional approximations for many-electron systems." *Physical Review B* **23**(10): 5048.
- Prescher, C. and V. B. Prakapenka (2015). "DIOPTAS: a program for reduction of two-dimensional X-ray diffraction data and data exploration." *High Pressure Research* **35**(3): 223-230.
- Saha, S., A. Bengtson and D. Morgan (2013). "Effect of anomalous compressibility on Fe diffusion in ferropericlase throughout the spin crossover in the lower mantle." *Earth and Planetary Science Letters* **362**(0): 1-5.

- Shannon, R. (1976). "Revised effective ionic radii and systematic studies of interatomic distances in halides and chalcogenides." *Acta Crystallographica Section A* **32**(5): 751-767.
- Shephard, G. E., C. Houser, J. Hernlund, J. J. Valencia-Cardona, Trønnes and R. Wentzkovitch (2020). "Seismological Expression of the Iron Spin Crossover in Ferropericlaise in the Earth's Lower Mantle.": <https://doi.org/10.31223/osf.io/deuck>.
- Solomatova, N., J. Jackson, W. Stuhrhahn, J. Wicks, J. Zhao, T. S. Toellner, B. Kalkan and W. M. Steinhardt (2016). "Equation of state and spin crossover of (Mg,Fe)O at high pressure, with implications for explaining topographic relief at the core-mantle boundary." *American Mineralogist* **101**(5): 1084-1093.
- Speziale, S., V. E. Lee, S. M. Clark, J. F. Lin, M. P. Pasternak and R. Jeanloz (2007). "Effects of Fe spin transition on the elasticity of (Mg,Fe)O magnesiowüstite and implications for the seismological properties of the Earth's lower mantle." *Journal of Geophysical Research* **112**.
- Speziale, S., A. Milner, V. E. Lee, S. M. Clark, M. P. Pasternak and R. Jeanloz (2005). "Iron spin transition in Earth's mantle." *Proceedings of the National Academy of Sciences* **102**(50): 17918-17922.
- Tsuchiya, T., R. M. Wentzkovitch, C. R. S. da Silva and S. de Gironcoli (2006). "Spin transition in magnesiowüstite in Earth's lower mantle." *Physical Review Letters* **96**(19): 198501-198504.
- Waychunas, G. A., W. A. Dollase and C. R. Ross (1994). "Short-range order measurements in MgO-FeO and MgO-LiFeO<sub>2</sub> solid solutions by DLS simulation-assisted EXAFS analysis." *American Mineralogist* **79**(3-4): 274-288.
- Wentzkovitch, R. M., J. F. Justo, Z. Wu, C. R. S. da Silva, D. A. Yuen and D. Kohlstedt (2009). "Anomalous compressibility of ferropericlaise throughout the iron spin cross-over." *Proceedings of the National Academy of Sciences* **106**(21): 8447-8452.
- Wu, Z. and R. M. Wentzkovitch (2014). "Spin crossover in ferropericlaise and velocity heterogeneities in the lower mantle." *Proceedings of the National Academy of Sciences* **111**: 10468-10472.
- Yang, J., X. Tong, J.-F. Lin, T. Okuchi and N. Tomioka (2015). "Elasticity of Ferropericlaise across the Spin Crossover in the Earth's Lower Mantle." *Scientific Reports* **5**: 17188.



## Supplemental Material

### Elastic softening of ferropericlase across the iron spin crossover constrained by time-resolved XRD experiments and computations

A.S.J. Méndez<sup>1,2</sup>, S. Stackhouse<sup>3</sup>, A. Kurnosov<sup>2</sup>, N. Satta<sup>4</sup>, H.-P. Liermann<sup>1</sup>, R. J. Husband<sup>1</sup> and H. Marquardt<sup>4</sup>

<sup>1</sup>Deutsches Elektronen-Synchrotron (DESY), 22607 Hamburg, Germany; <sup>2</sup>Bayerisches Geoinstitut BGI, University of Bayreuth, 95440 Bayreuth, Germany; <sup>3</sup>School of Earth and Environment, University of Leeds, LS2 9JT Leeds, United Kingdom; <sup>4</sup>Department of Earth Sciences, University of Oxford, OX1 3AN Oxford, United Kingdom.

Corresponding author: Alba San José Méndez (alba.mendez@desy.de)

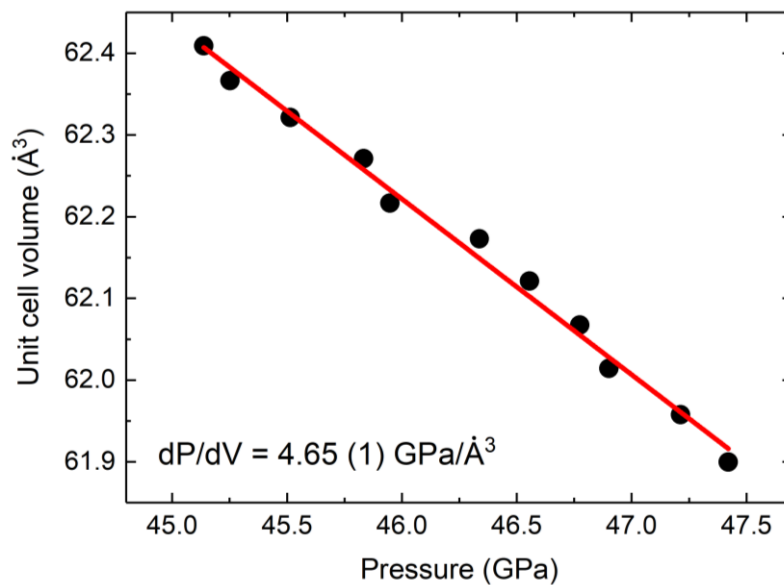
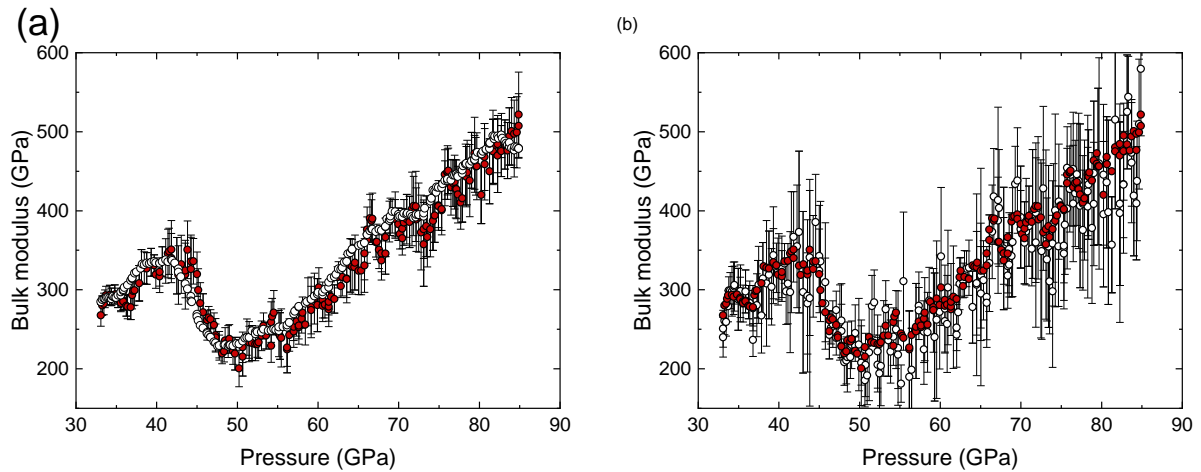
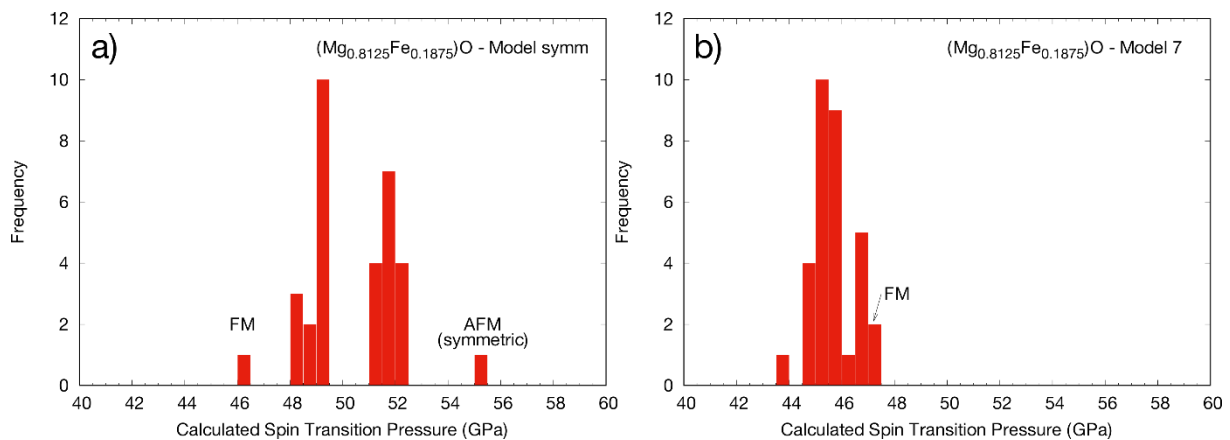


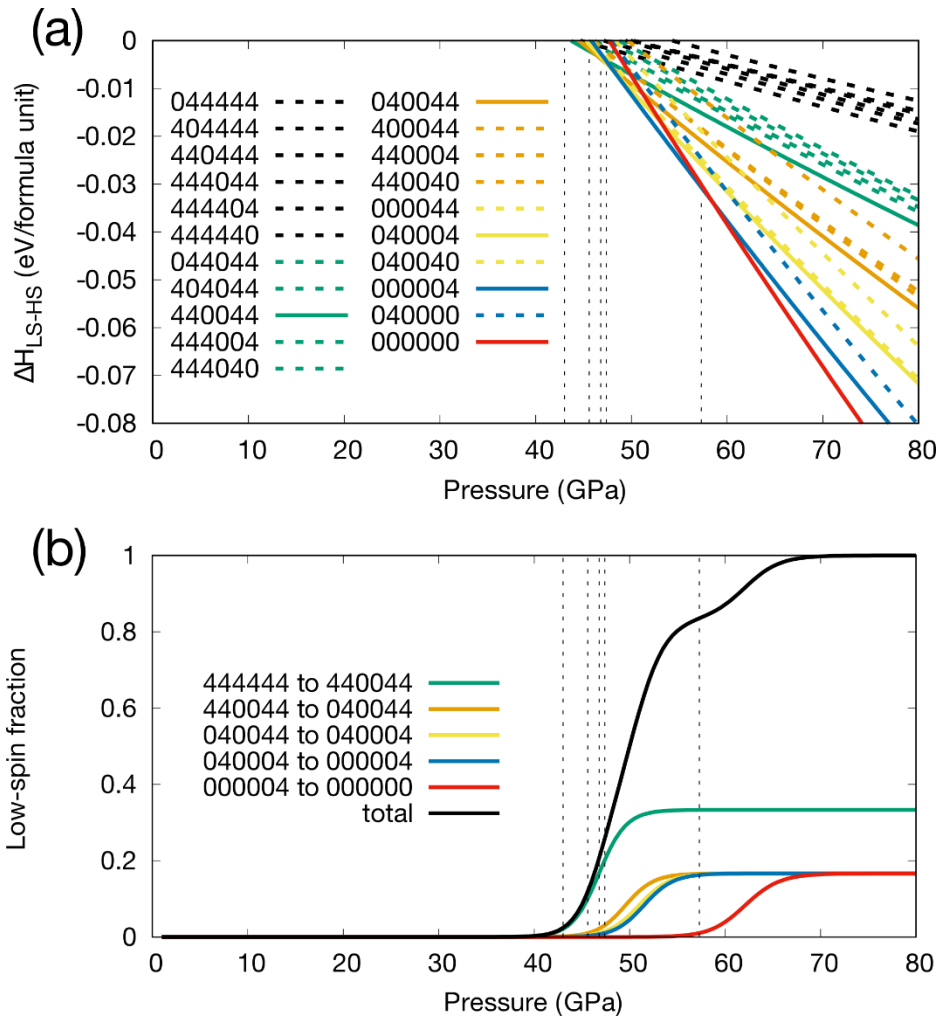
Figure 5.5: Typical linear fit to measured volume data.



**Figure 5.6:** Effect of the chosen pressure interval on the derived bulk moduli curves for  $(\text{Mg}_{0.8}\text{Fe}_{0.2})\text{O}$ . The solid red circles represent results obtained with the here-chosen pressure interval of 2.5 GPa. The open circles represent derivations using pressure intervals of 5 GPa (a) or 1.5 GPa (b). For clarity, error bars are only shown for the data obtained using the smaller pressure range in each figure. A smaller chosen pressure range for differentiation – and hence better pressure resolution – comes at the expense of a larger uncertainty in bulk modulus.



**Figure 5.7:** Frequency distribution of spin crossover pressure for 64-atom Models 7 (a) and symm (b) with a  $(\text{Mg}_{0.8125}\text{Fe}_{0.1875})\text{O}$  composition. The spin crossover pressures are those for going from various high-spin states (representing disordered collinear paramagnets) to the low-spin state. Model symm has a highly symmetric arrangement of iron atoms, where all iron atoms have only on-axis neighbours. Model 7 has a random arrangement of iron atoms, where all iron atoms have only off-axis neighbours.

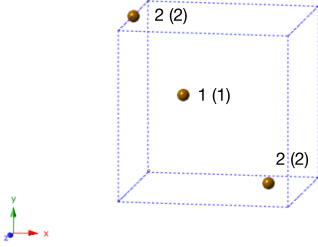
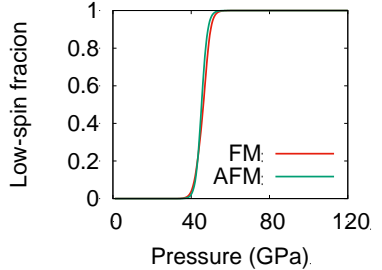
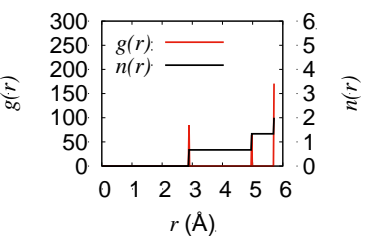
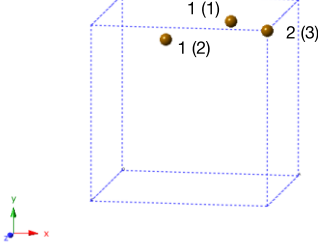
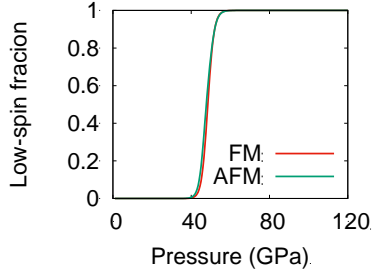
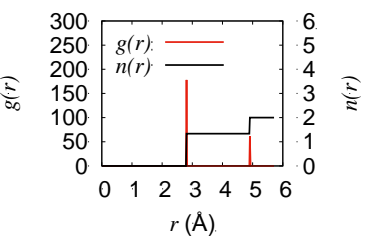
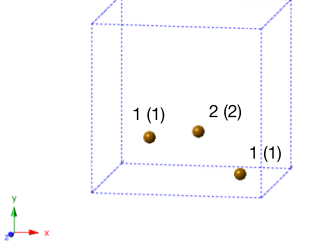
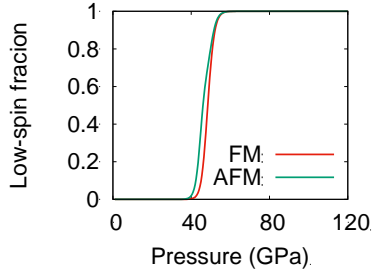
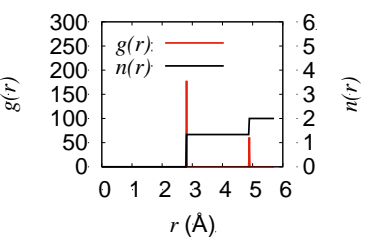
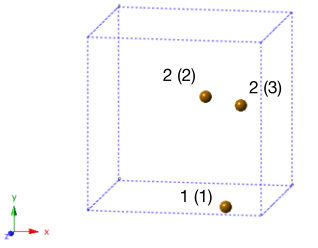
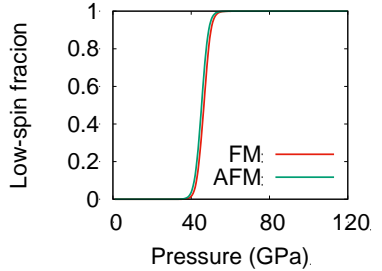
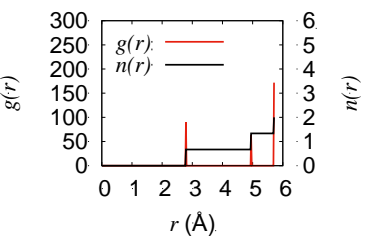
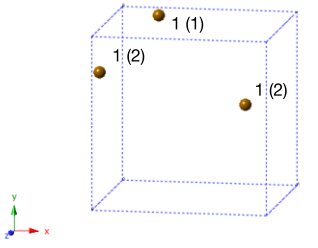
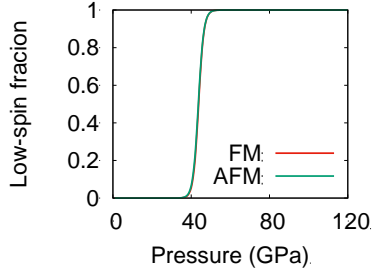
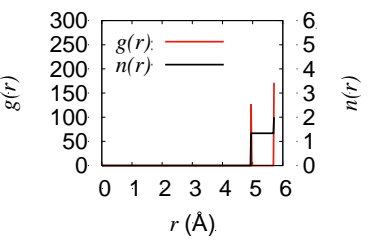


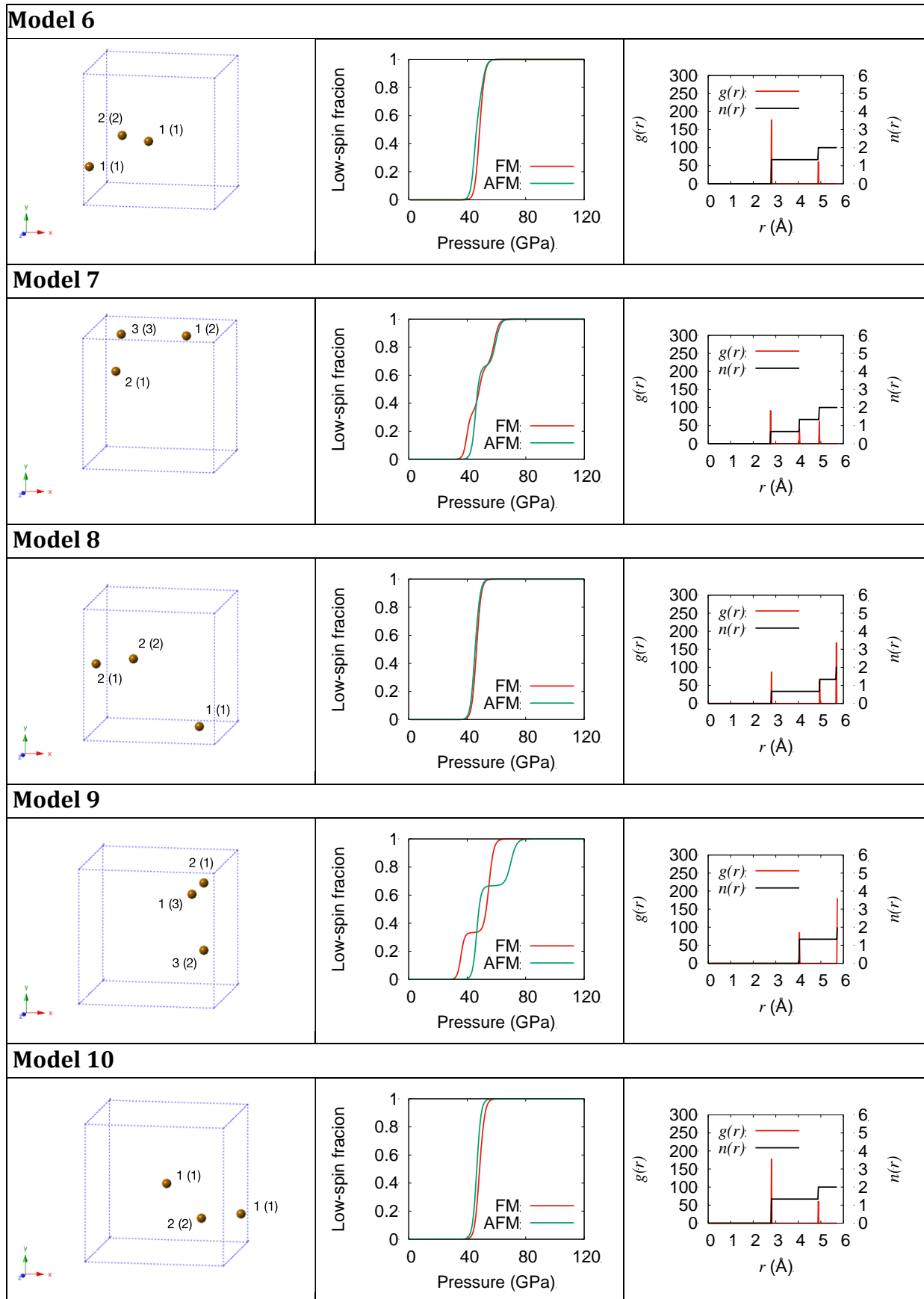
**Figure 5.8:**  $\Delta H_{LS-HS}$  (a) and low-spin fraction at 300K (b) as a function of pressure for 64-atom Model 1 with a  $(\text{Mg}_{0.8125}\text{Fe}_{0.1875})\text{O}$  composition, in a ferromagnetic state. Here  $\Delta H_{LS-HS}$  is the enthalpy difference between higher-spin and lower-spin states. Each string of six digits denotes the spin state of the model, with each digit specifying the spin state of one of the six iron atoms: 4 = high-spin and 0 = low-spin e.g. 440044 means that four iron atoms, with the same spin, are in a high-spin state and two are in a low-spin state. In panel (b) the low-spin fraction for each spin crossover is weighted by the fraction of total iron atoms involved.

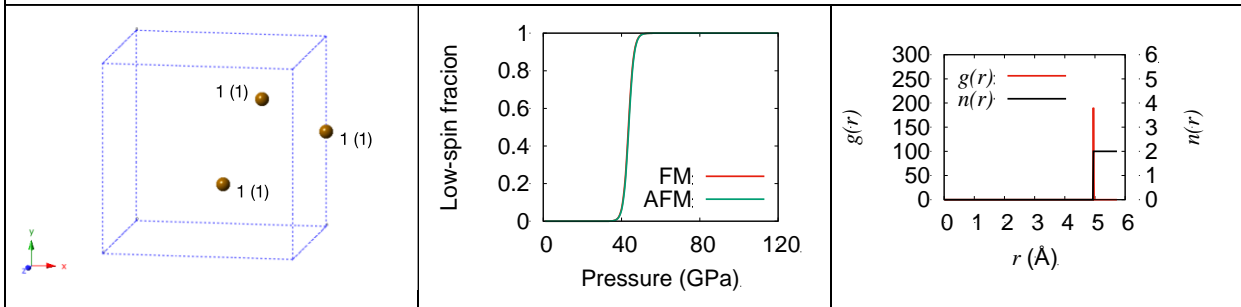
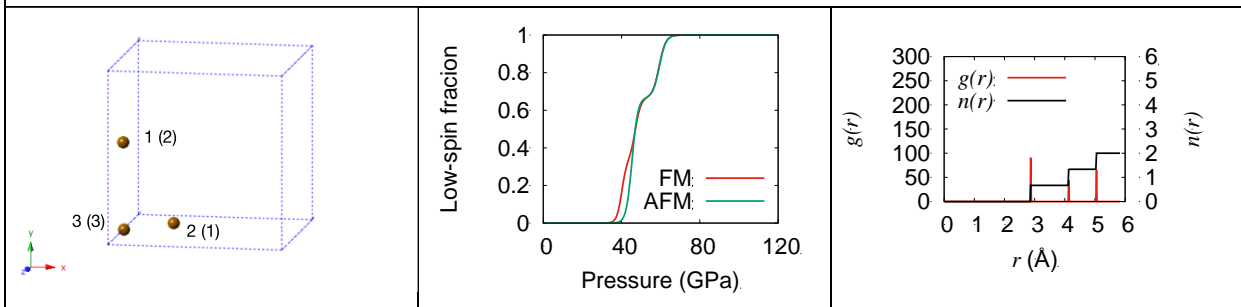
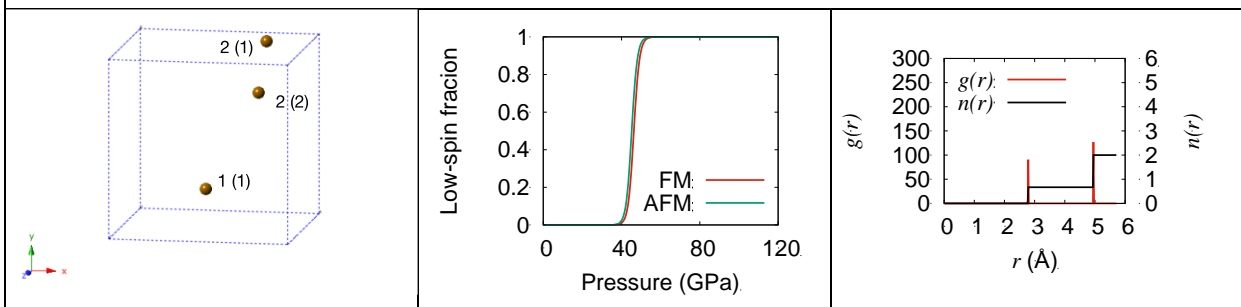
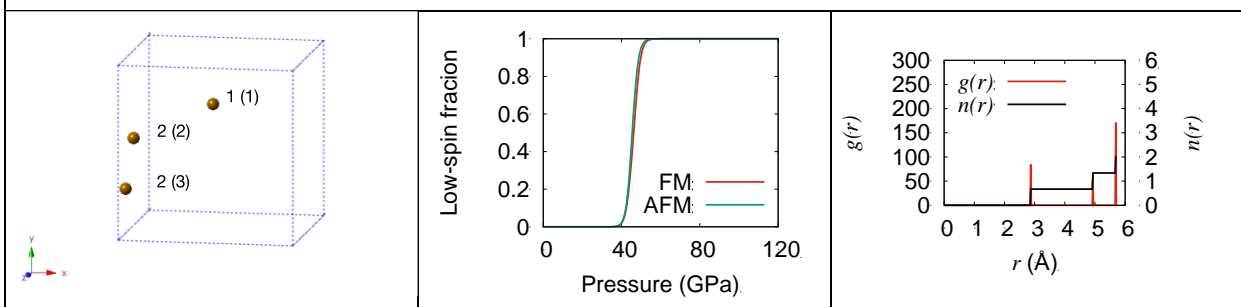
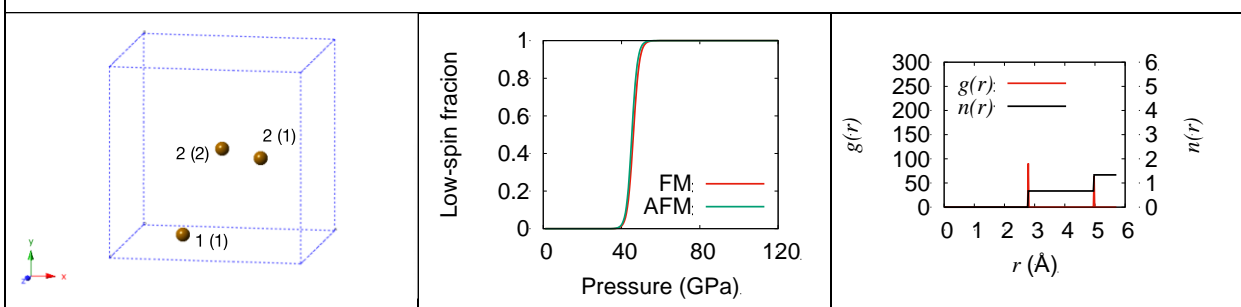
**Table 5.1:** Initial atomic coordinates of iron atoms in 64-atom ferroperriclate models.

Model	Fe1	Fe2	Fe3	Fe4	Fe5	Fe6
<b>(Mg<sub>0.90625</sub>Fe<sub>0.09375</sub>)O</b>						
1	0.25, 0.50, 0.25	0.75, 0.00, 0.25	0.00, 0.00, 0.50	-	-	-
2	0.75, 0.00, 0.75	0.25, 0.75, 0.00	0.00, 0.00, 0.00	-	-	-
3	0.50, 0.25, 0.25	0.25, 0.25, 0.50	0.75, 0.00, 0.25	-	-	-
4	0.75, 0.50, 0.25	0.50, 0.50, 0.00	0.75, 0.00, 0.75	-	-	-
5	0.75, 0.50, 0.25	0.00, 0.75, 0.75	0.25, 0.00, 0.25	-	-	-
6	0.50, 0.50, 0.00	0.00, 0.25, 0.75	0.25, 0.50, 0.75	-	-	-
7	0.25, 0.00, 0.75	0.75, 0.00, 0.75	0.25, 0.75, 0.00	-	-	-
8	0.00, 0.50, 0.50	0.25, 0.50, 0.25	0.75, 0.00, 0.25	-	-	-
9	0.75, 0.25, 0.00	0.75, 0.75, 0.00	0.75, 0.75, 0.50	-	-	-
10	0.00, 0.25, 0.25	0.75, 0.25, 0.50	0.50, 0.50, 0.50	-	-	-
11	0.75, 0.75, 0.50	0.00, 0.50, 0.00	0.50, 0.25, 0.25	-	-	-
12	0.00, 0.50, 0.50	0.00, 0.00, 0.50	0.25, 0.00, 0.25	-	-	-
13	0.75, 0.75, 0.50	0.50, 0.25, 0.75	0.75, 0.00, 0.25	-	-	-
14	0.00, 0.50, 0.50	0.00, 0.25, 0.75	0.50, 0.75, 0.75	-	-	-
15	0.25, 0.00, 0.25	0.75, 0.50, 0.75	0.50, 0.50, 0.50	-	-	-
16	0.00, 0.75, 0.75	0.00, 0.25, 0.75	0.25, 0.75, 0.00	-	-	-
17	0.75, 0.75, 0.50	0.75, 0.75, 0.00	0.50, 0.25, 0.25	-	-	-
18	0.75, 0.25, 0.00	0.75, 0.25, 0.50	0.50, 0.50, 0.00	-	-	-
19	0.00, 0.00, 0.50	0.00, 0.75, 0.75	0.75, 0.00, 0.25	-	-	-
20	0.50, 0.75, 0.25	0.25, 0.75, 0.50	0.50, 0.00, 0.0	-	-	-
<b>(Mg<sub>0.8125</sub>Fe<sub>0.1875</sub>)O</b>						
symm	0.50, 0.50, 0.00	0.50, 0.00, 0.50	0.00, 0.50, 0.50	0.50, 0.00, 0.00	0.00, 0.50, 0.00	0.00, 0.00, 0.05
1	0.25, 0.50, 0.25	0.75, 0.00, 0.25	0.00, 0.00, 0.50	0.75, 0.50, 0.75	0.25, 0.25, 0.00	0.00, 0.00, 0.00
2	0.50, 0.25, 0.25	0.25, 0.25, 0.50	0.75, 0.00, 0.25	0.25, 0.50, 0.75	0.50, 0.50, 0.00	0.25, 0.50, 0.25
3	0.75, 0.50, 0.25	0.00, 0.75, 0.75	0.25, 0.00, 0.25	0.50, 0.50, 0.00	0.50, 0.75, 0.75	0.75, 0.00, 0.75
4	0.25, 0.00, 0.75	0.75, 0.00, 0.75	0.25, 0.75, 0.00	0.00, 0.50, 0.50	0.75, 0.75, 0.00	0.75, 0.50, 0.75
5	0.75, 0.25, 0.00	0.75, 0.75, 0.00	0.75, 0.75, 0.50	0.25, 0.75, 0.50	0.25, 0.75, 0.50	0.50, 0.50, 0.00
6	0.75, 0.75, 0.50	0.00, 0.50, 0.00	0.50, 0.25, 0.25	0.00, 0.50, 0.50	0.00, 0.00, 0.00	0.75, 0.50, 0.75
7	0.75, 0.75, 0.50	0.50, 0.25, 0.75	0.75, 0.00, 0.25	0.00, 0.50, 0.00	0.00, 0.25, 0.25	0.50, 0.75, 0.25
8	0.25, 0.00, 0.25	0.75, 0.50, 0.75	0.50, 0.50, 0.50	0.00, 0.75, 0.25	0.00, 0.25, 0.25	0.25, 0.25, 0.00
9	0.75, 0.75, 0.50	0.75, 0.75, 0.00	0.50, 0.25, 0.25	0.25, 0.75, 0.00	0.25, 0.75, 0.50	0.50, 0.50, 0.00
10	0.00, 0.00, 0.50	0.00, 0.75, 0.75	0.75, 0.00, 0.25	0.50, 0.25, 0.75	0.25, 0.25, 0.50	0.50, 0.00, 0.00
11	0.00, 0.50, 0.50	0.50, 0.50, 0.50	0.25, 0.75, 0.00	0.75, 0.25, 0.00	0.25, 0.75, 0.50	0.00, 0.25, 0.25
12	0.25, 0.25, 0.00	0.50, 0.25, 0.75	0.75, 0.75, 0.50	0.50, 0.50, 0.50	0.25, 0.75, 0.00	0.50, 0.50, 0.00
13	0.50, 0.75, 0.75	0.25, 0.75, 0.00	0.75, 0.75, 0.00	0.00, 0.00, 0.00	0.25, 0.50, 0.25	0.75, 0.25, 0.50
14	0.00, 0.75, 0.75	0.00, 0.25, 0.75	0.75, 0.50, 0.25	0.50, 0.25, 0.25	0.00, 0.75, 0.25	0.75, 0.00, 0.75
15	0.25, 0.50, 0.25	0.25, 0.00, 0.25	0.25, 0.75, 0.00	0.50, 0.75, 0.25	0.75, 0.75, 0.50	0.00, 0.75, 0.25
16	0.50, 0.75, 0.75	0.75, 0.00, 0.75	0.25, 0.50, 0.25	0.00, 0.75, 0.75	0.25, 0.25, 0.00	0.75, 0.00, 0.25
17	0.50, 0.00, 0.00	0.50, 0.25, 0.75	0.00, 0.75, 0.25	0.75, 0.50, 0.75	0.75, 0.75, 0.00	0.50, 0.50, 0.50
18	0.50, 0.00, 0.50	0.50, 0.50, 0.50	0.50, 0.00, 0.00	0.00, 0.25, 0.25	0.50, 0.25, 0.25	0.25, 0.00, 0.25
19	0.00, 0.25, 0.75	0.50, 0.50, 0.50	0.25, 0.50, 0.75	0.75, 0.00, 0.25	0.00, 0.25, 0.25	0.00, 0.00, 0.50
20	0.50, 0.25, 0.25	0.00, 0.25, 0.25	0.25, 0.25, 0.00	0.50, 0.00, 0.50	0.25, 0.25, 0.50	0.25, 0.75, 0.00

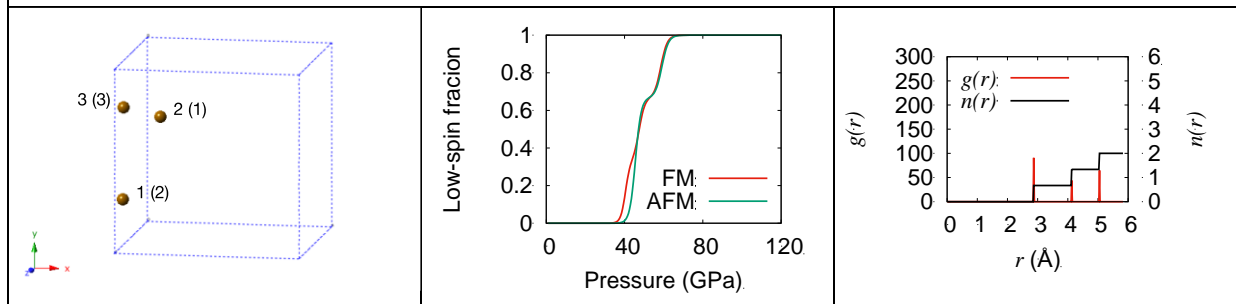
**Table 5.2:** Iron arrangement, low-spin fraction at 300K and Fe-Fe radial distribution function for models with an  $(\text{Mg}_{0.90625}\text{Fe}_{0.09375})\text{O}$  composition. Labels on iron atoms indicate the order that they undergo spin crossover: FM (AFM). If iron atoms have the same number it indicates simultaneous spin crossover. Fe-Fe radial distribution functions were calculated using VMD (Humphrey et al. 1996).

<b>Model 1</b>		
		
<b>Model 2</b>		
		
<b>Model 3</b>		
		
<b>Model 4</b>		
		
<b>Model 5</b>		
		

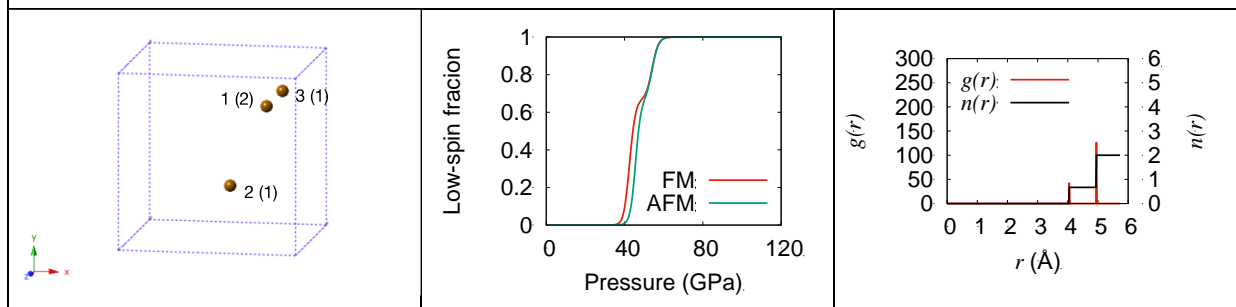


**Model 11****Model 12****Model 13****Model 14****Model 15**

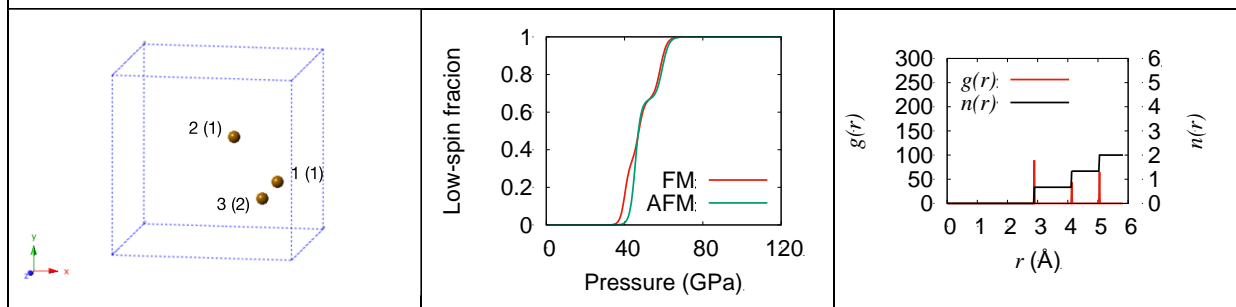
**Model 16**



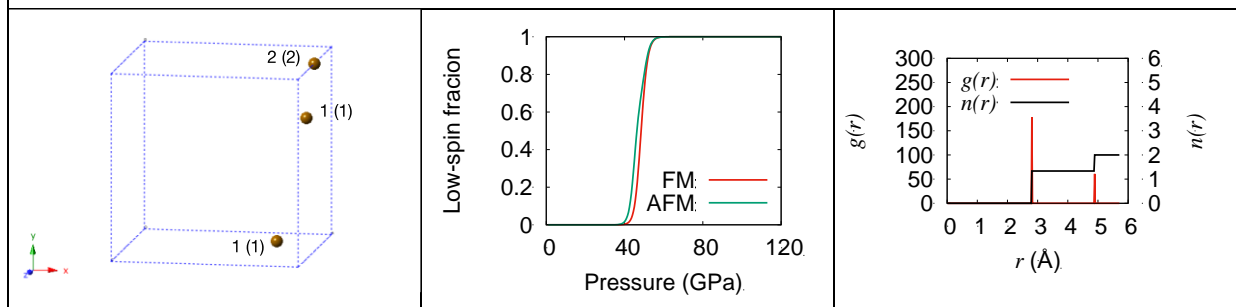
**Model 17**



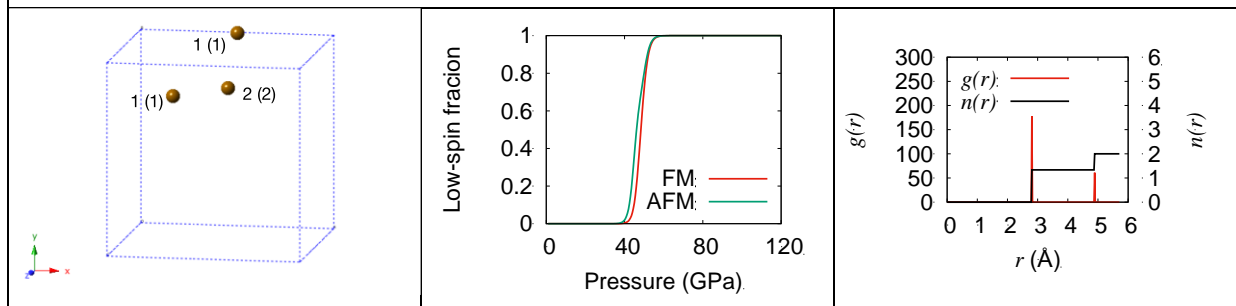
**Model 18**



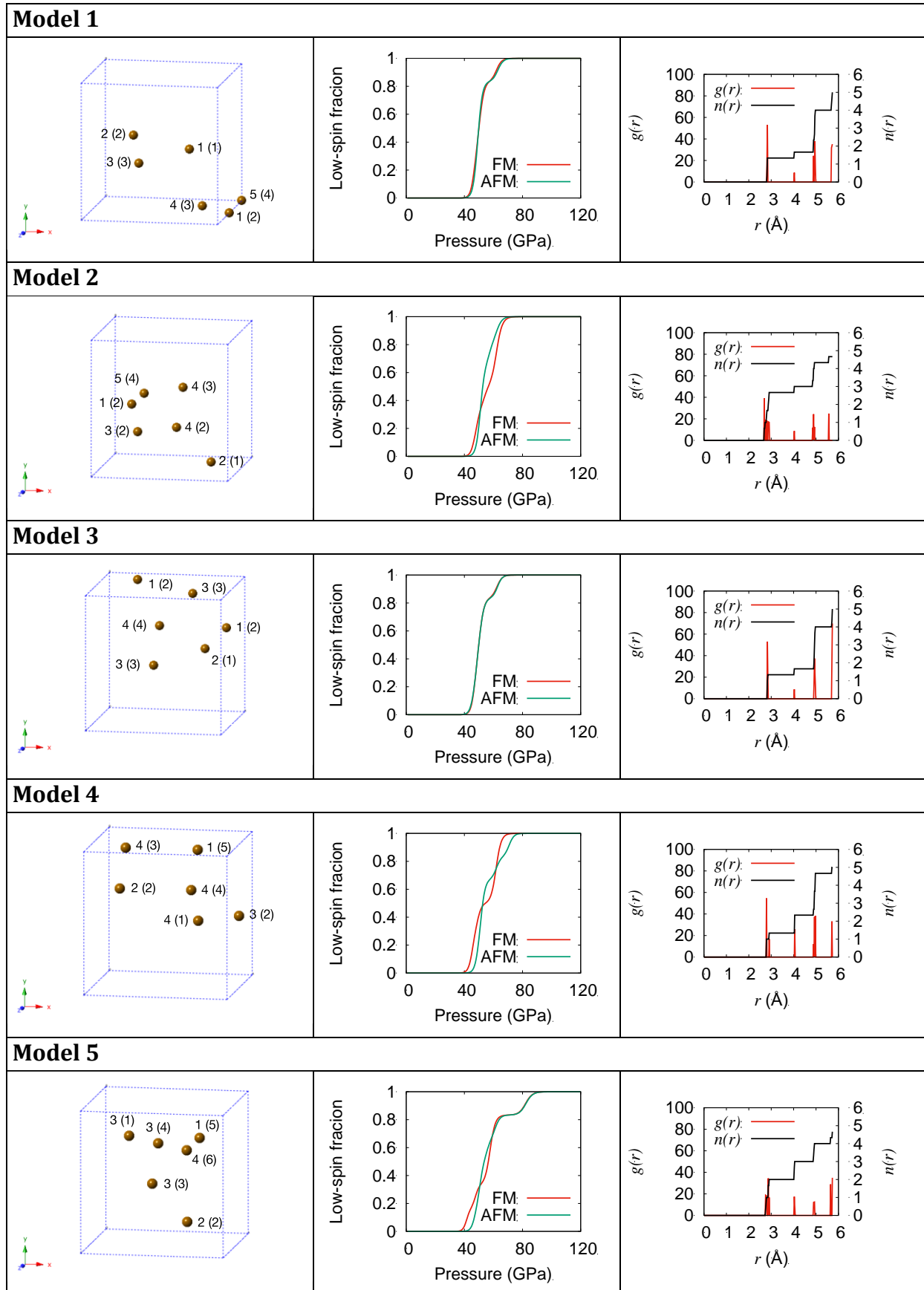
**Model 19**

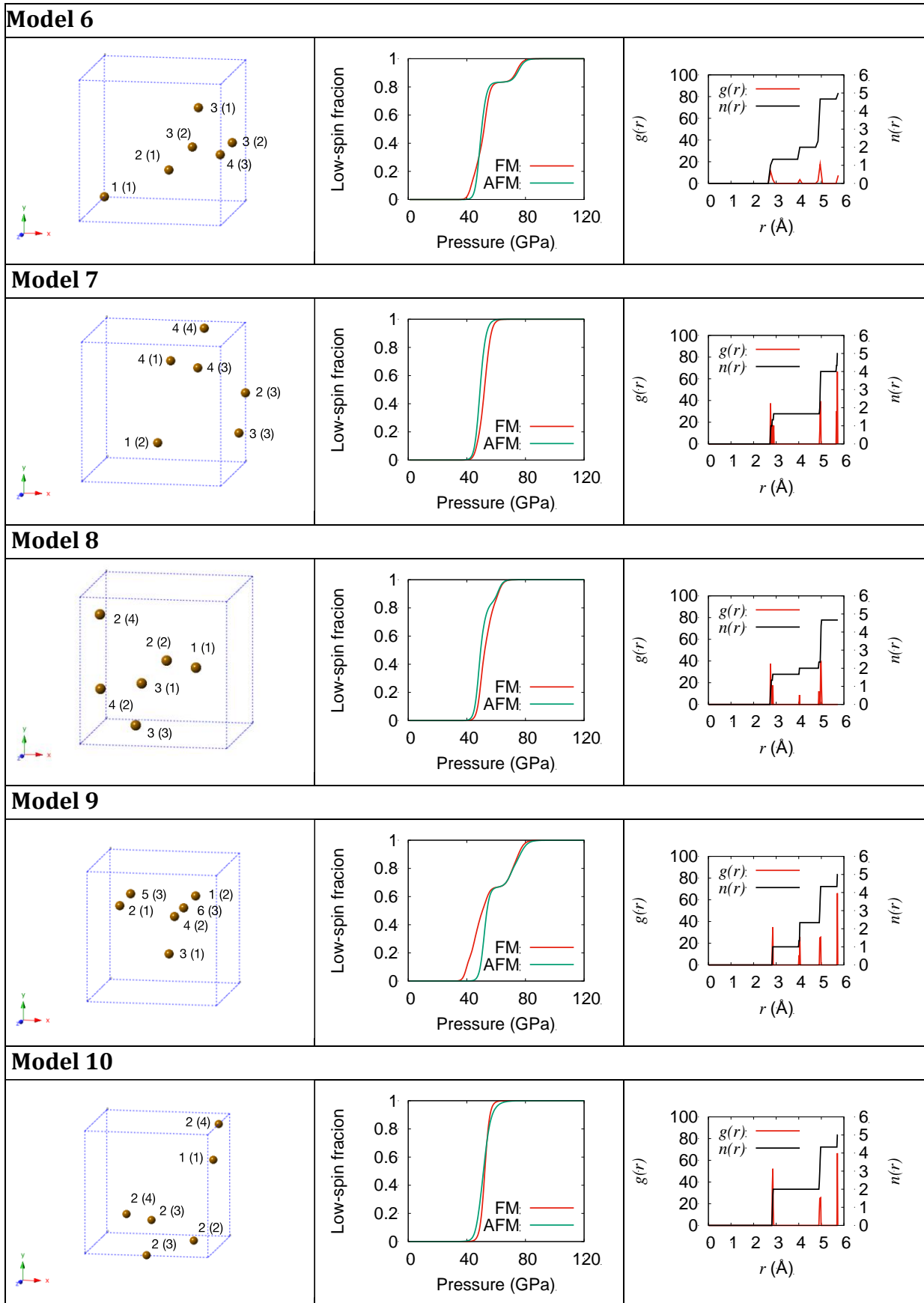


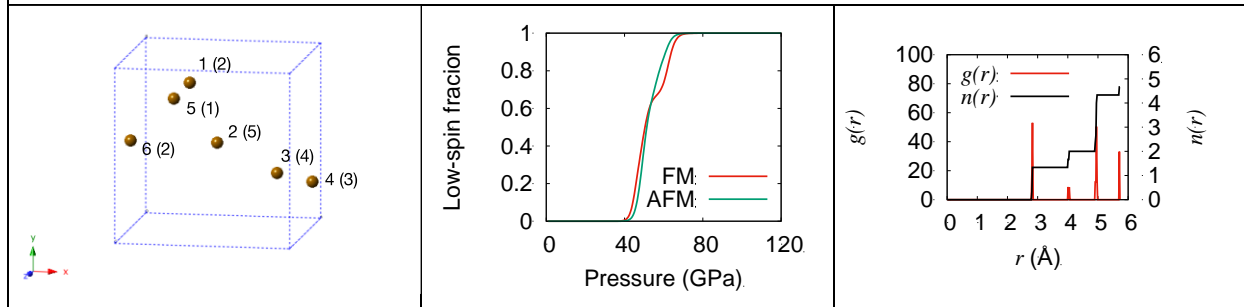
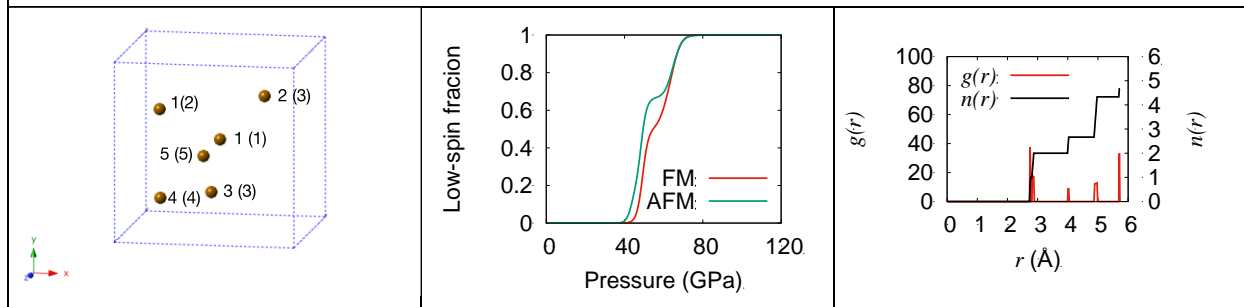
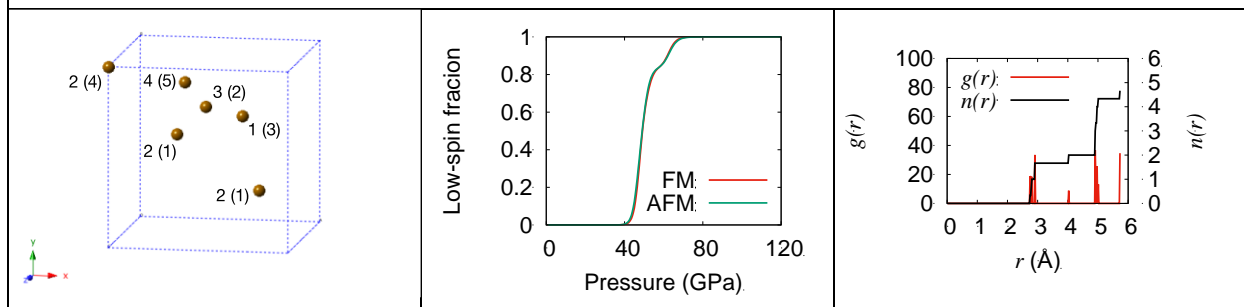
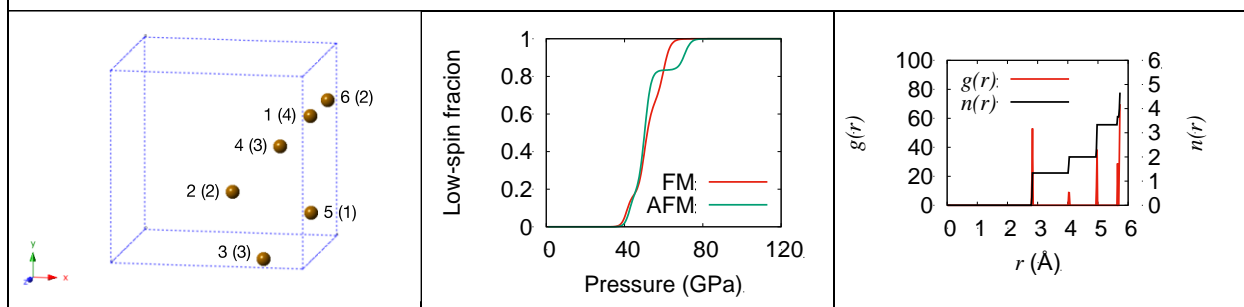
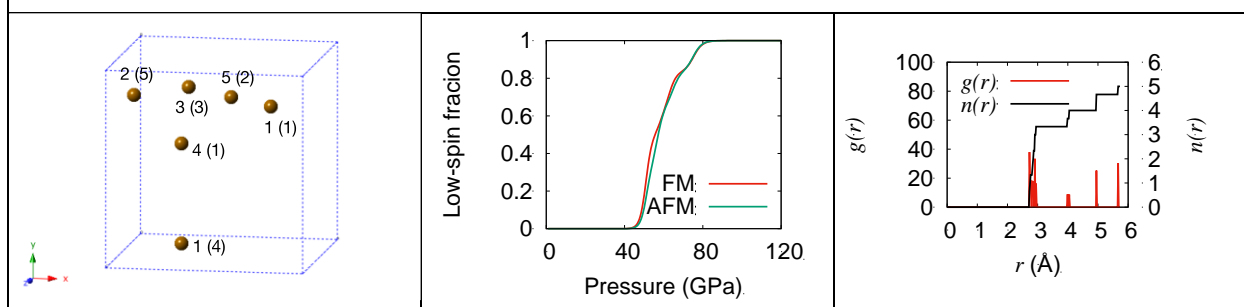
**Model 20**



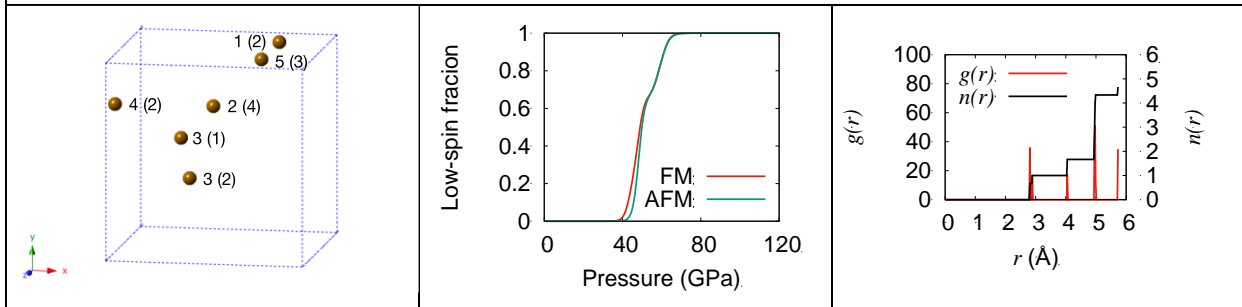
**Table 5.3:** Iron arrangement, low-spin fraction at 300K and Fe-Fe radial distribution function for models with an  $(\text{Mg}_{0.8125}\text{Fe}_{0.1875})\text{O}$  composition. Labels on iron atoms indicate the order that they undergo spin crossover: FM (AFM). If iron atoms have the same number it indicates simultaneous spin crossover. Fe-Fe radial distribution functions were calculated using VMD (Humphrey et al., 1996).



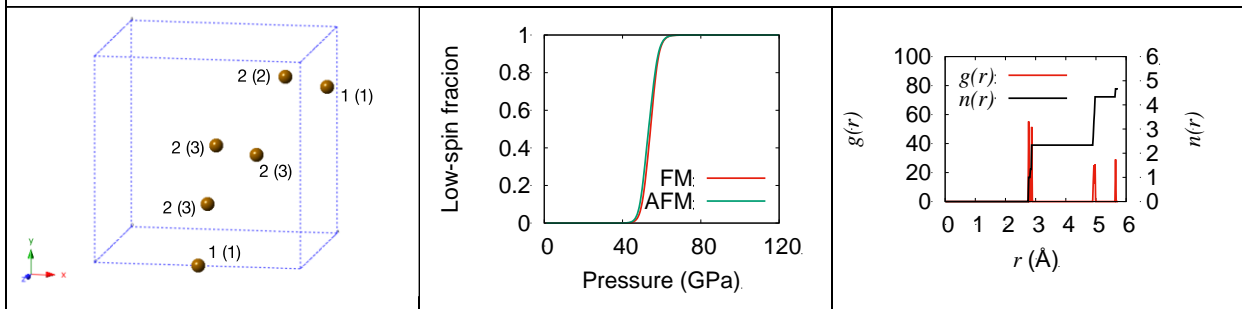


**Model 11****Model 12****Model 13****Model 14****Model 15**

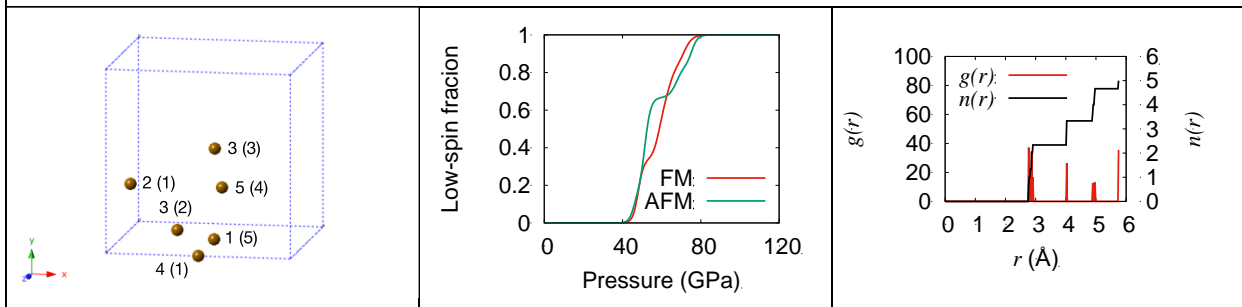
**Model 16**



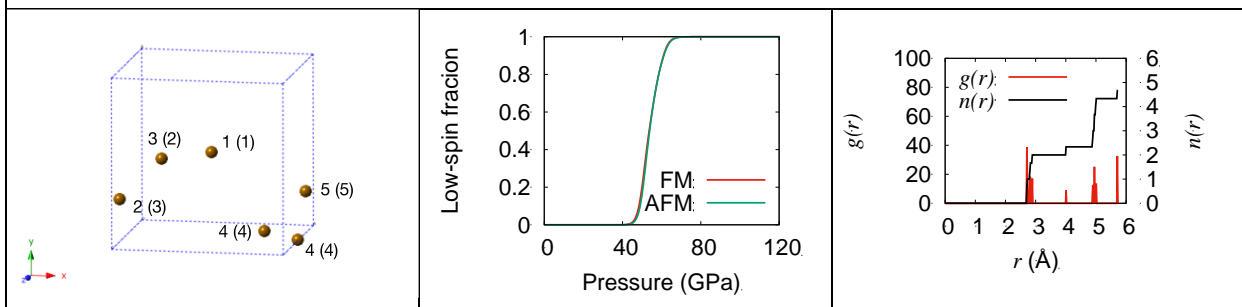
**Model 17**



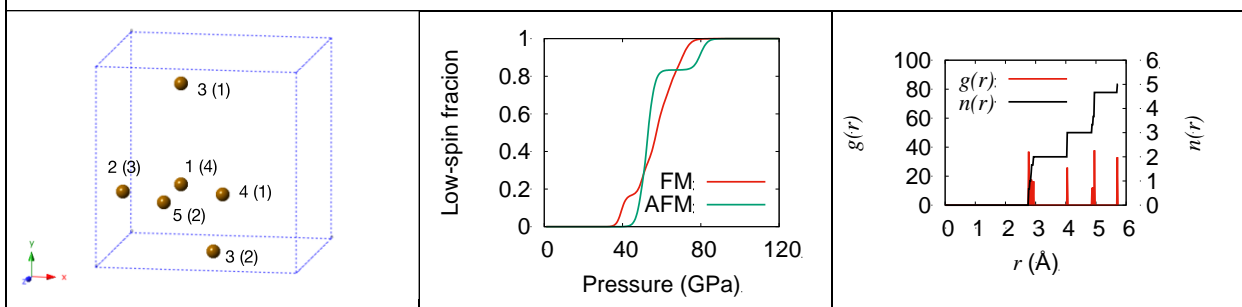
**Model 18**

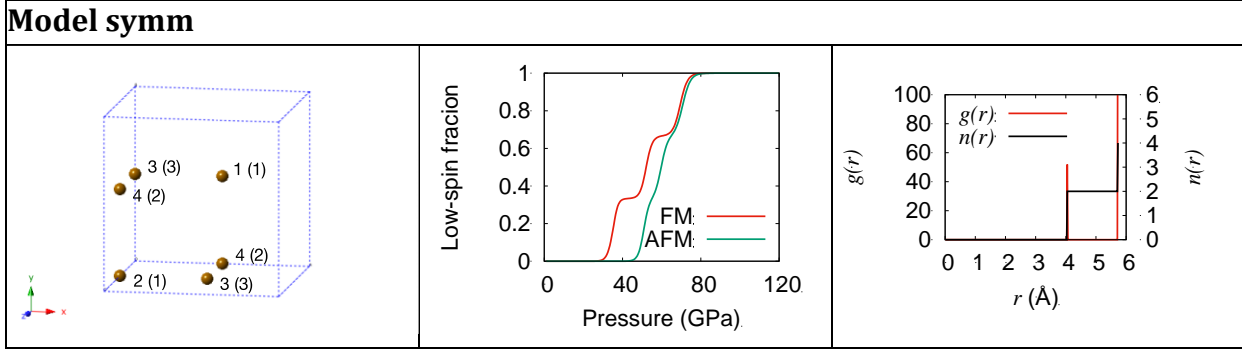


**Model 19**

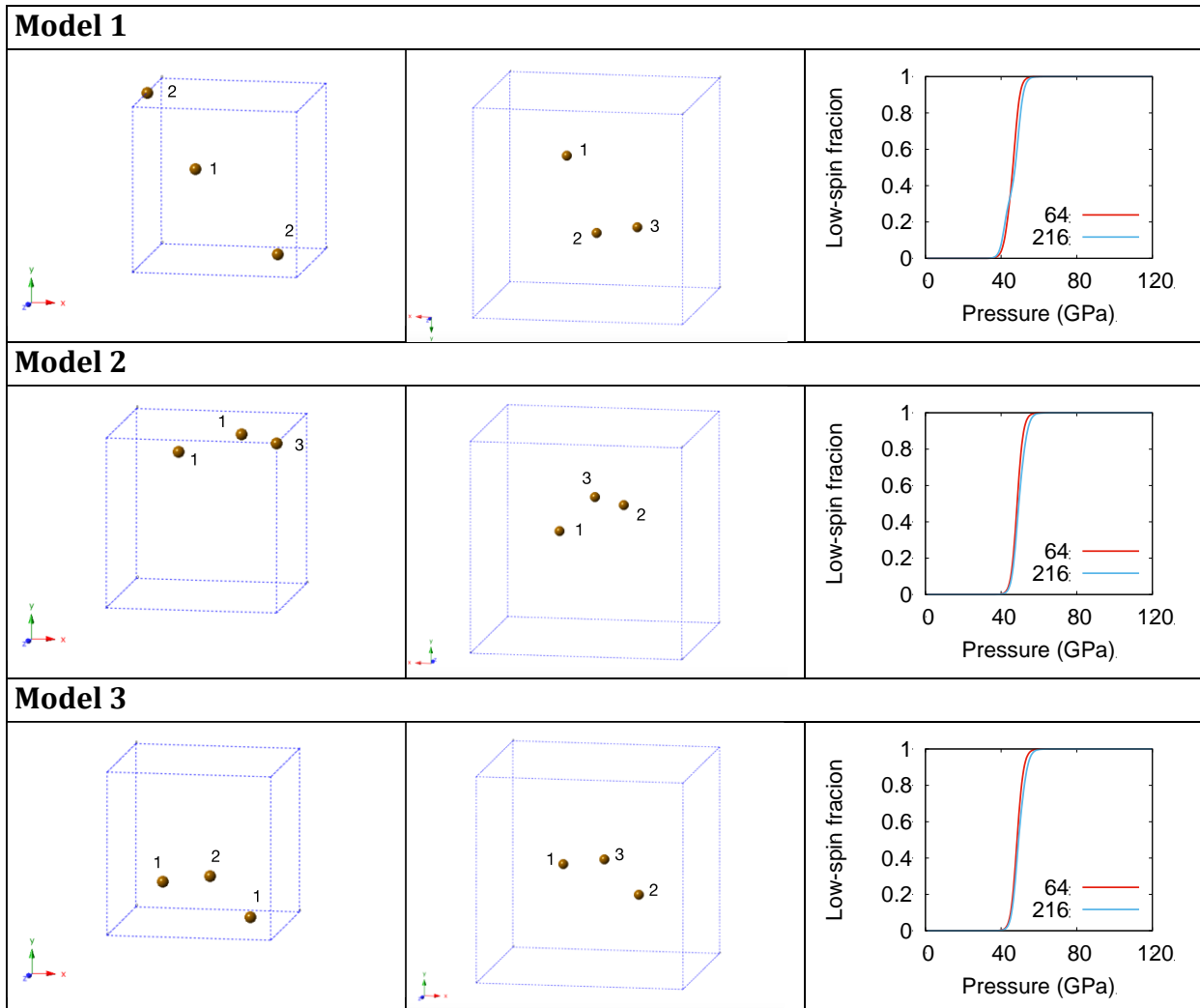


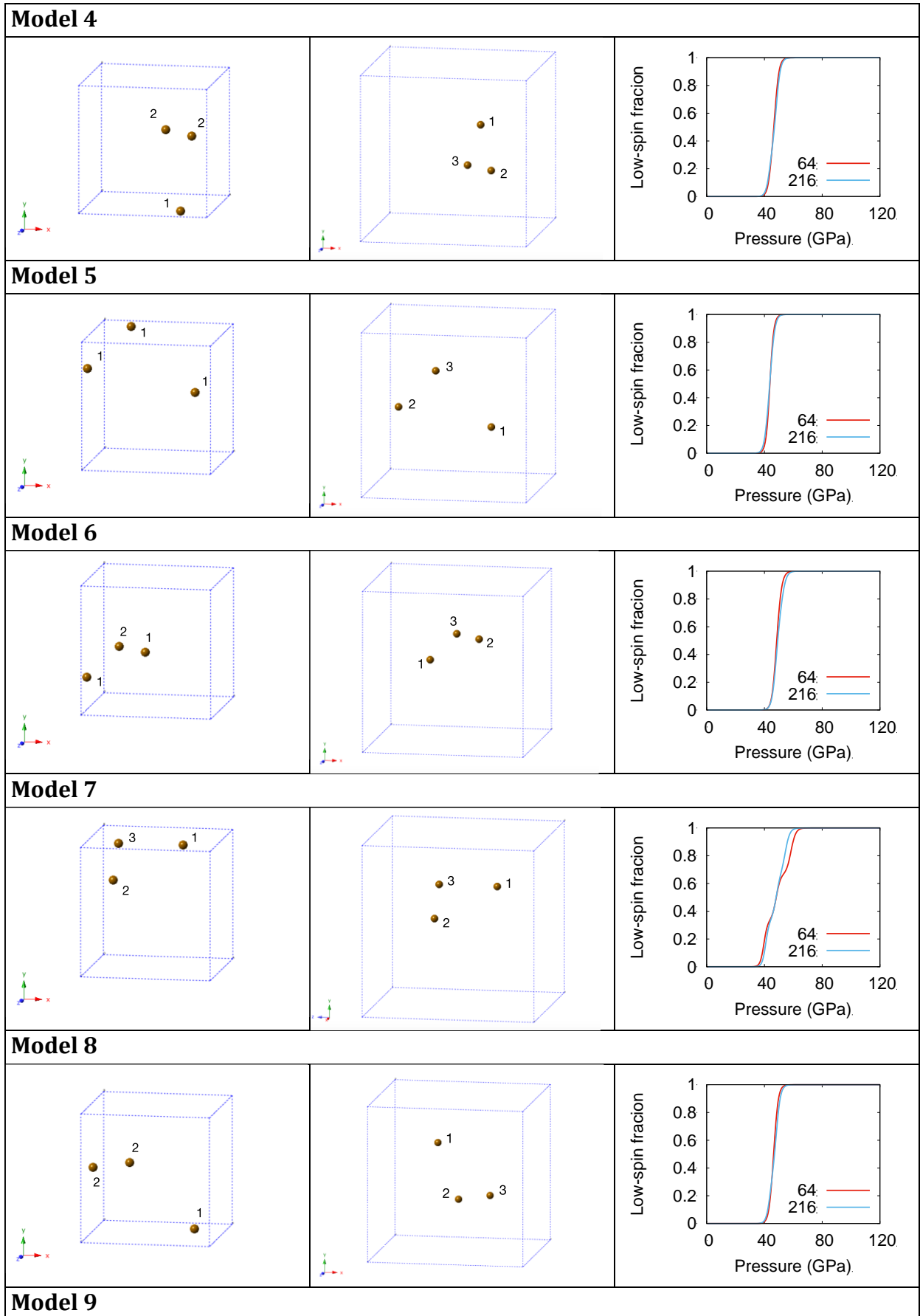
**Model 20**

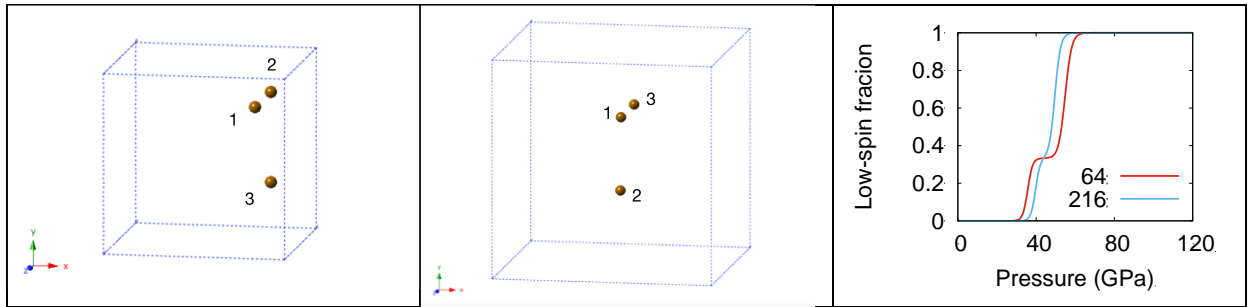




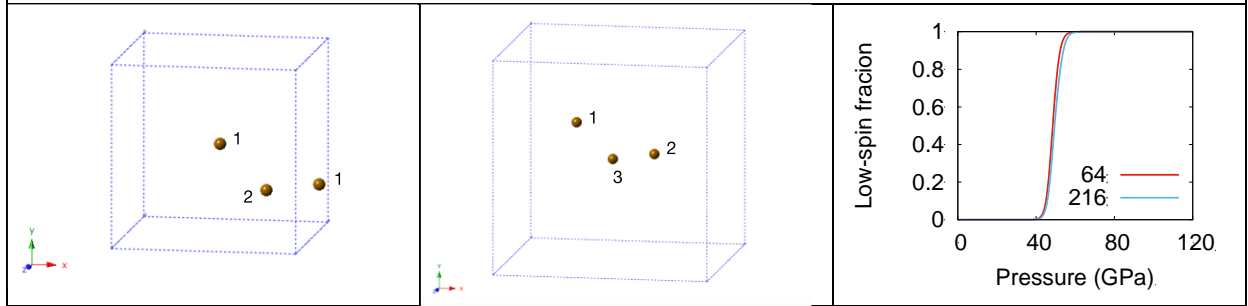
**Table 5. 4:** Iron arrangement for 64-atom (left), and 216-atom (middle) models and low-spin fraction at 300K (right), for models with an  $(\text{Mg}_{0.90625}\text{Fe}_{0.09375})\text{O}$  composition. Labels on iron atoms indicate the order that they undergo spin crossover. If iron atoms have the same number it indicates simultaneous spin crossover. Only results for the FM state are shown.



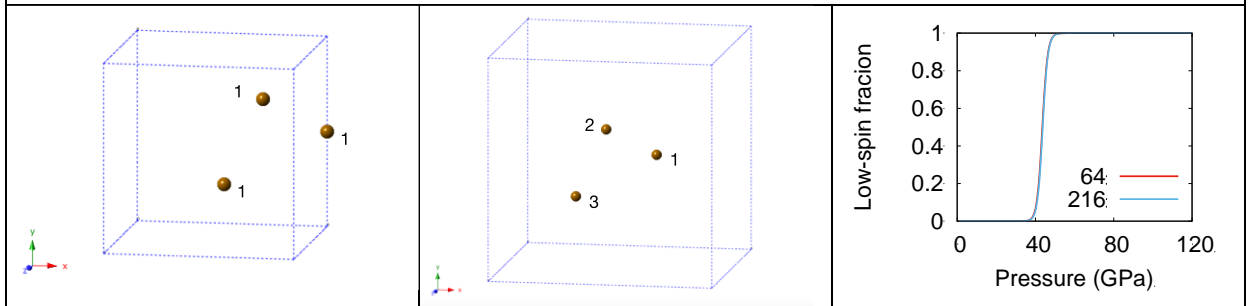




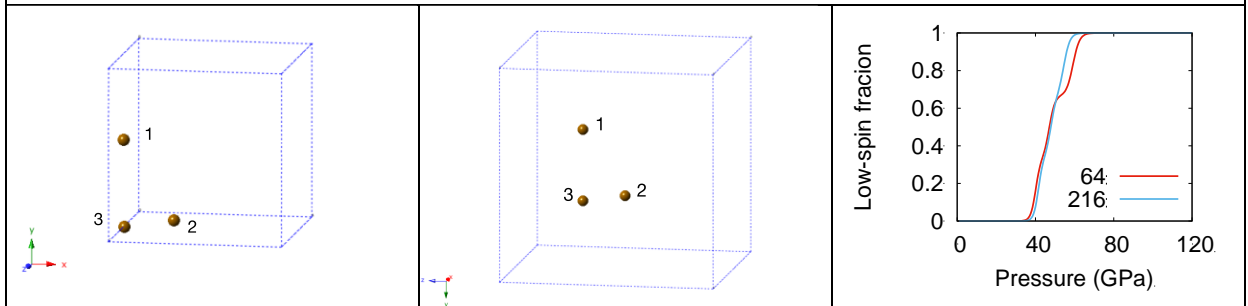
**Model 10**



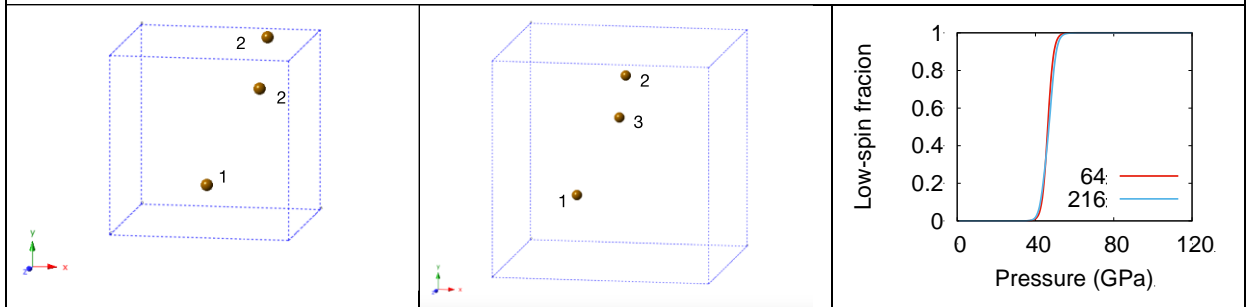
**Model 11**



**Model 12**

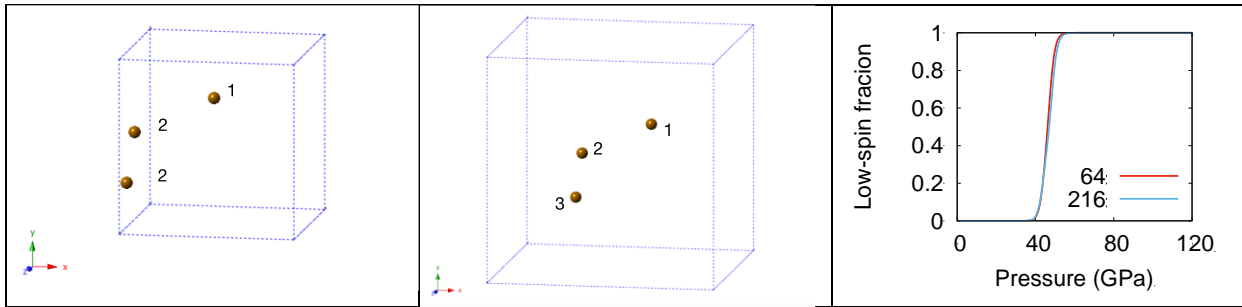


**Model 13**

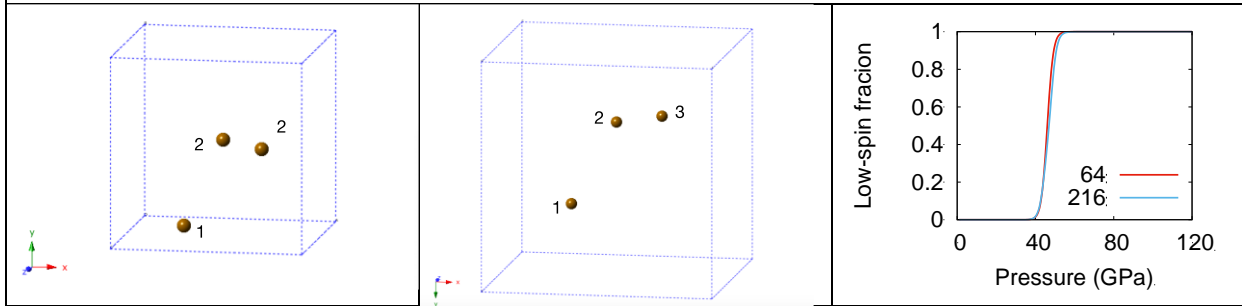


**Model 14**

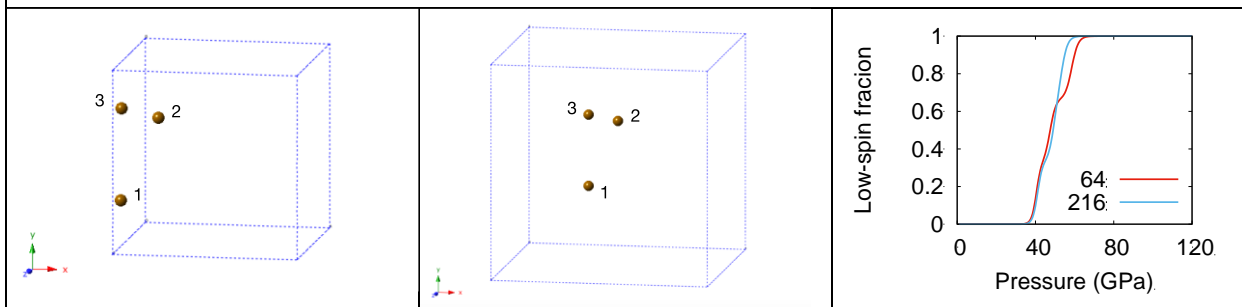
**Chapter 5. ELASTIC SOFTENING OF FERROPERICLASE ACROSS THE SPIN CROSSOVER**



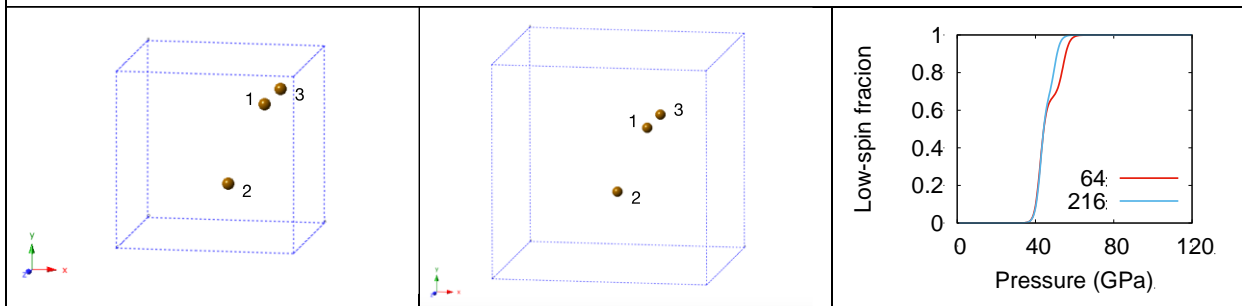
**Model 15**



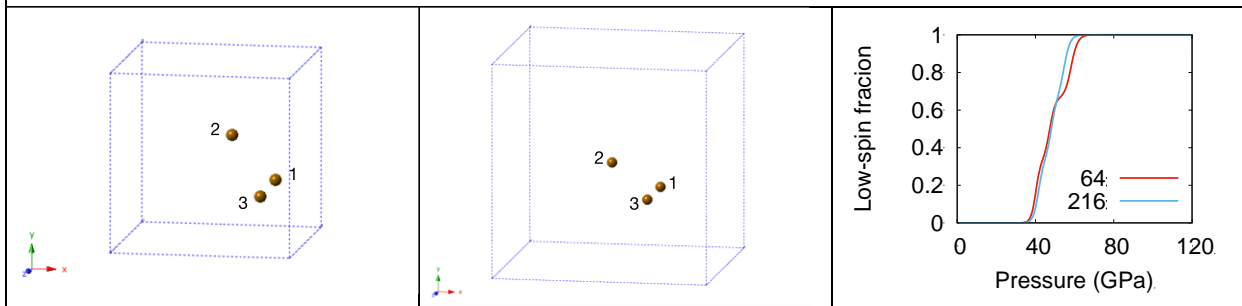
**Model 16**



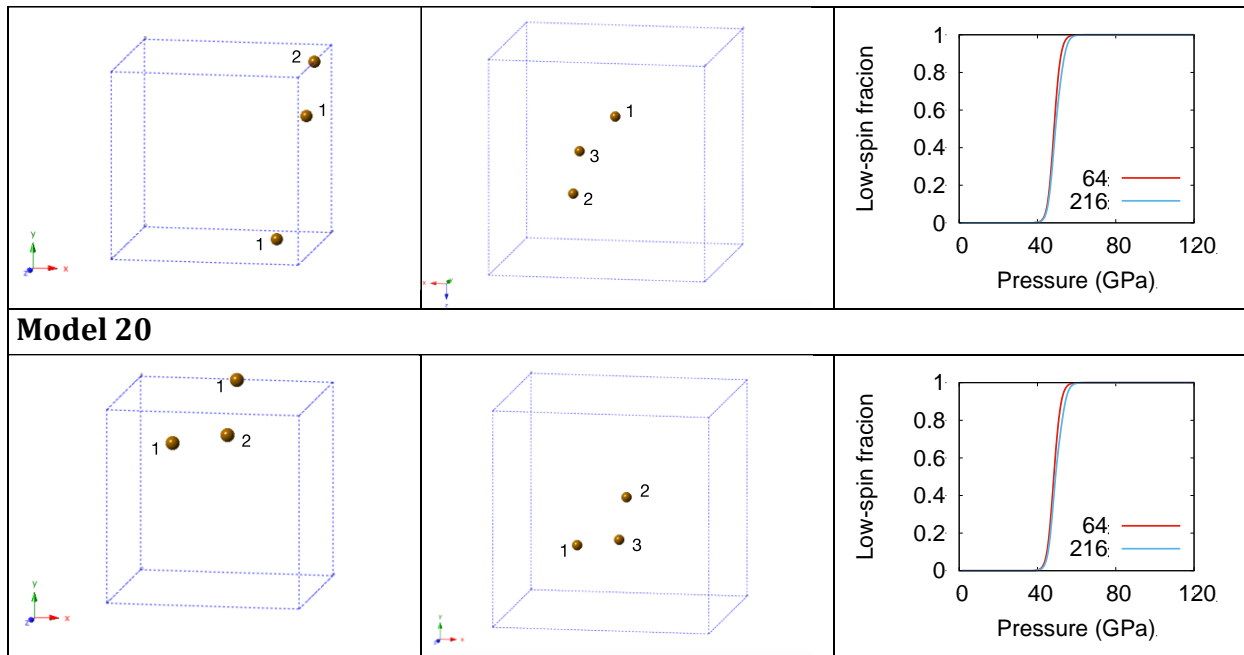
**Model 17**



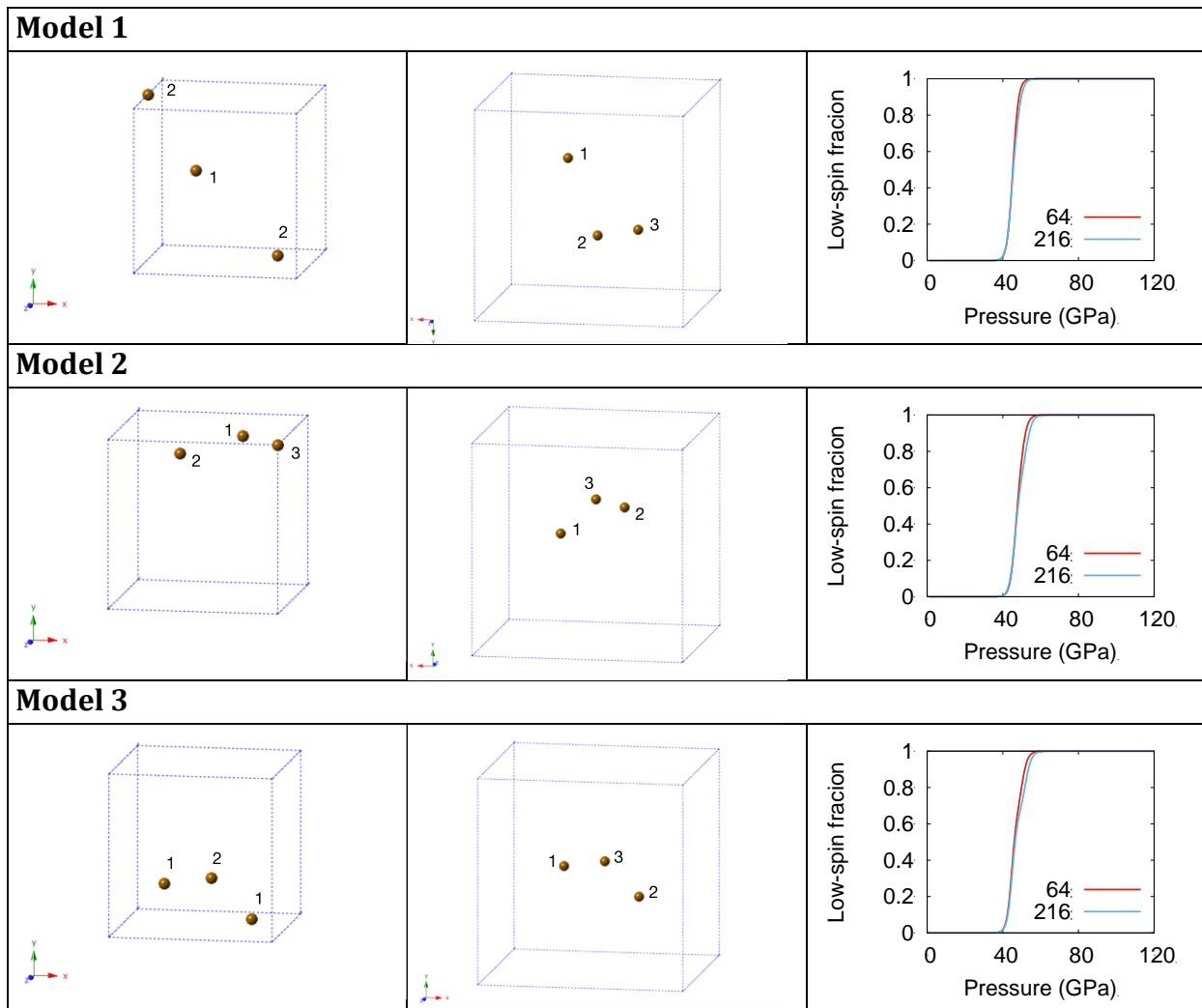
**Model 18**

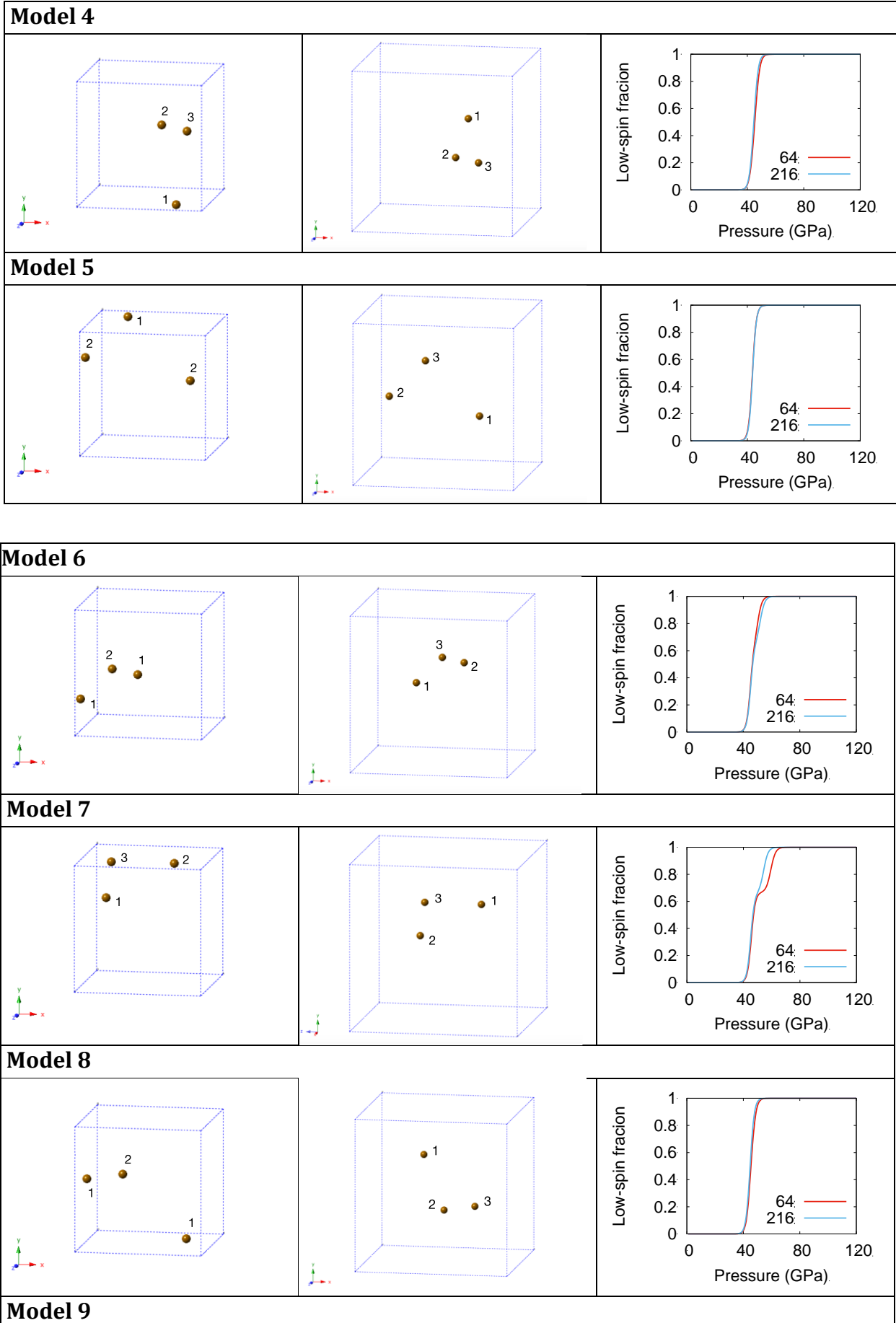


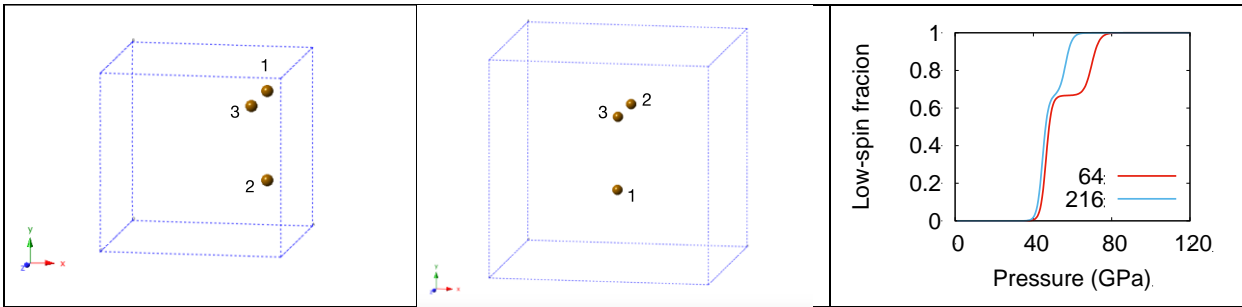
**Model 19**



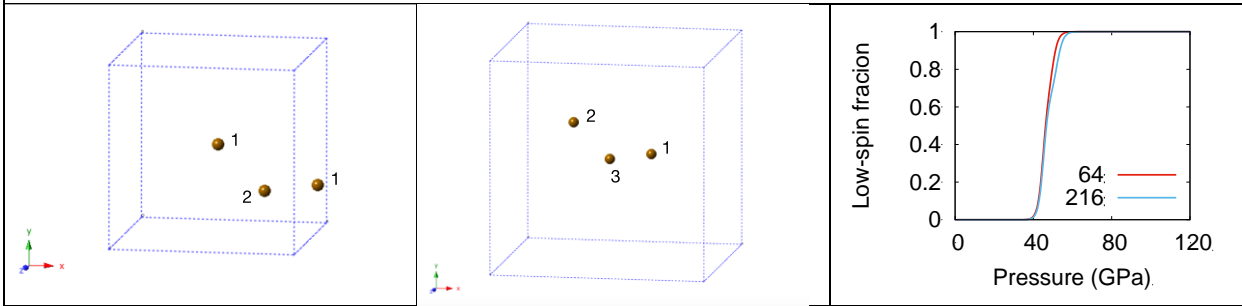
**Table 5.5:** Iron arrangement for 64-atom (left), and 216-atom (middle) models and low-spin fraction at 300K (right), for models with an  $(\text{Mg}_{0.90625}\text{Fe}_{0.09375})\text{O}$  composition. Labels on iron atoms indicate the order that they undergo spin crossover. If iron atoms have the same number it indicates simultaneous spin crossover. Only results for the AFM state are shown.



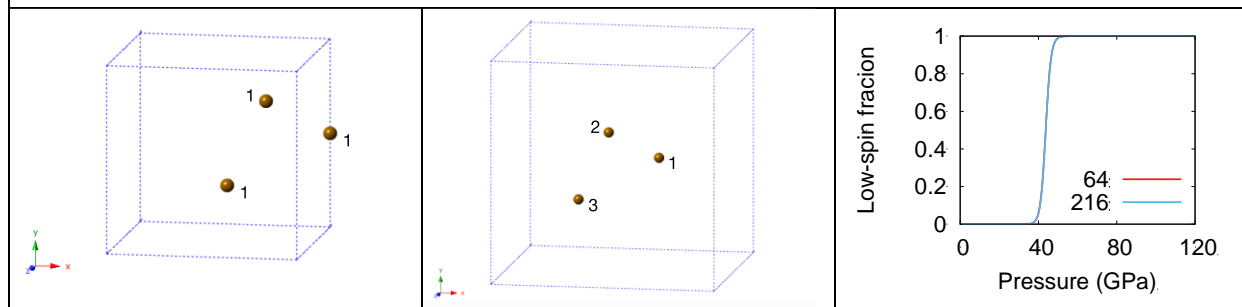




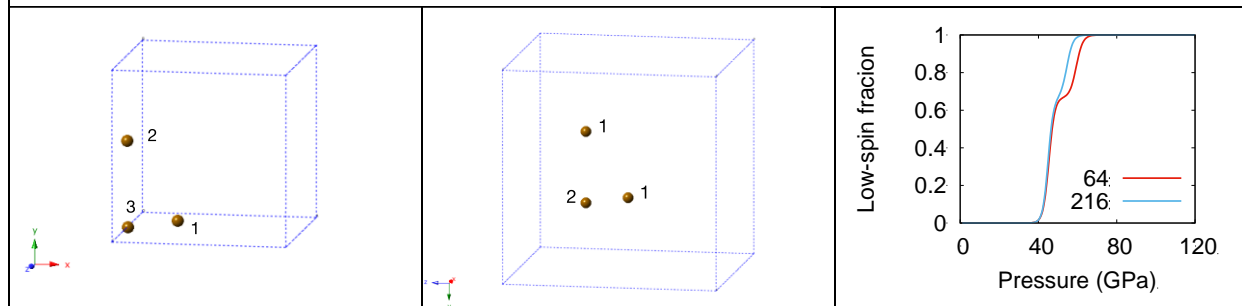
**Model 10**



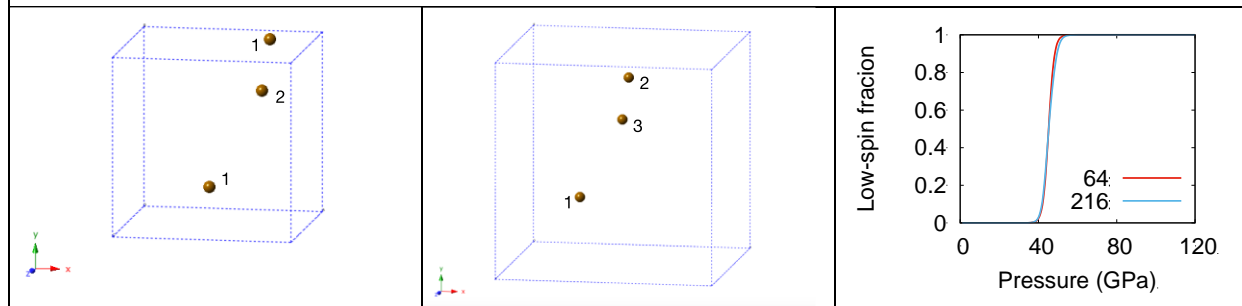
**Model 11**



**Model 12**

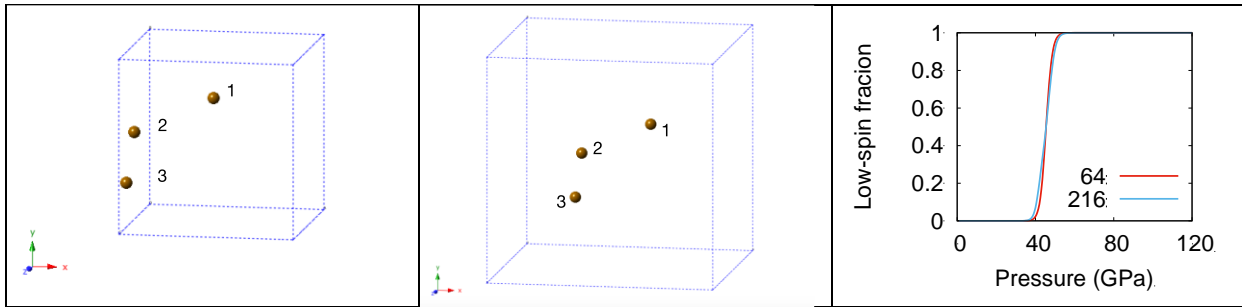


**Model 13**

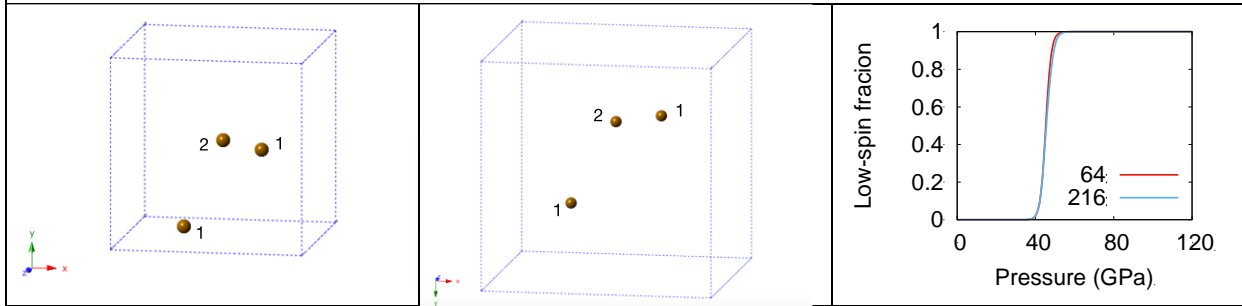


**Model 14**

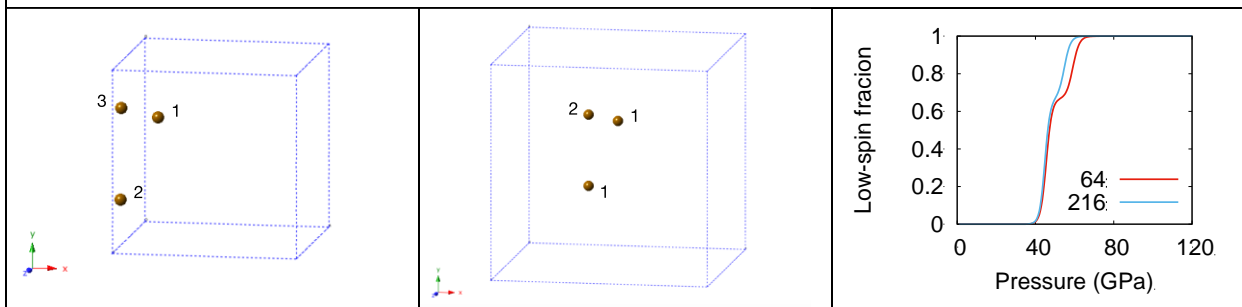
**Chapter 5. ELASTIC SOFTENING OF FERROPERICLASE ACROSS THE SPIN CROSSOVER**



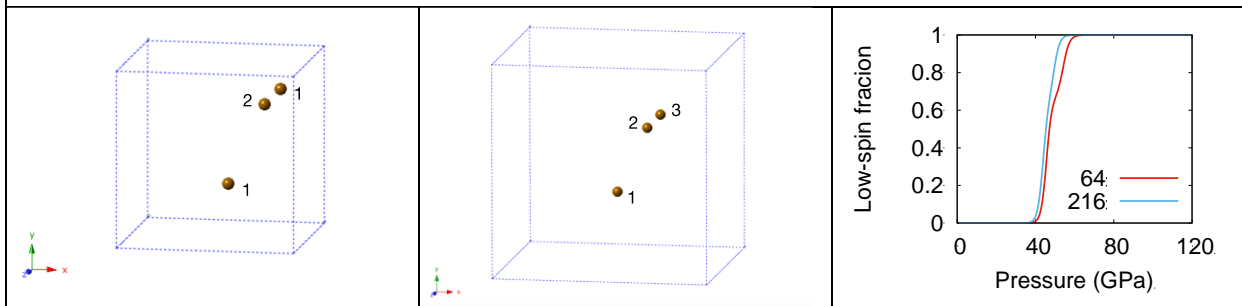
**Model 15**



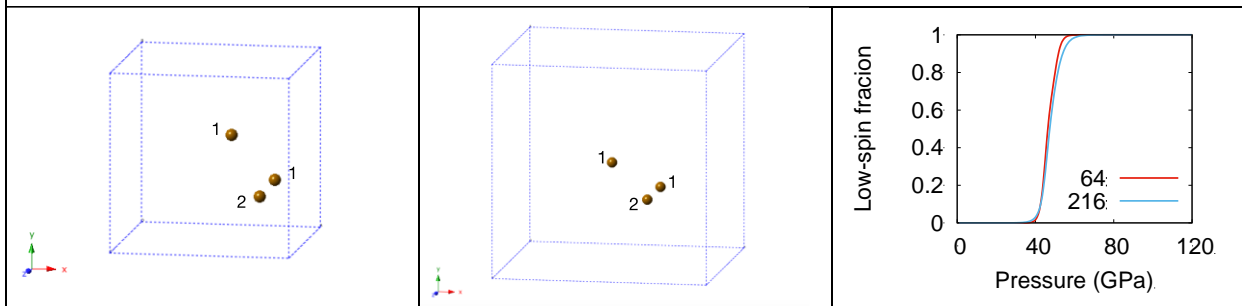
**Model 16**



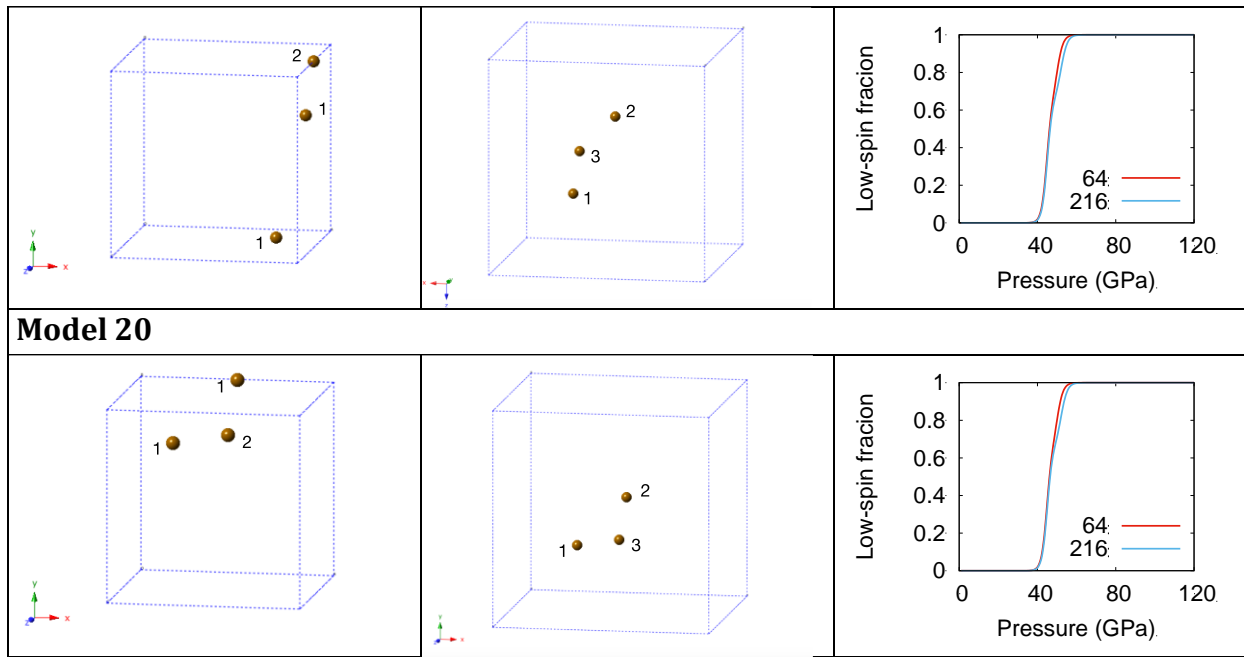
**Model 17**



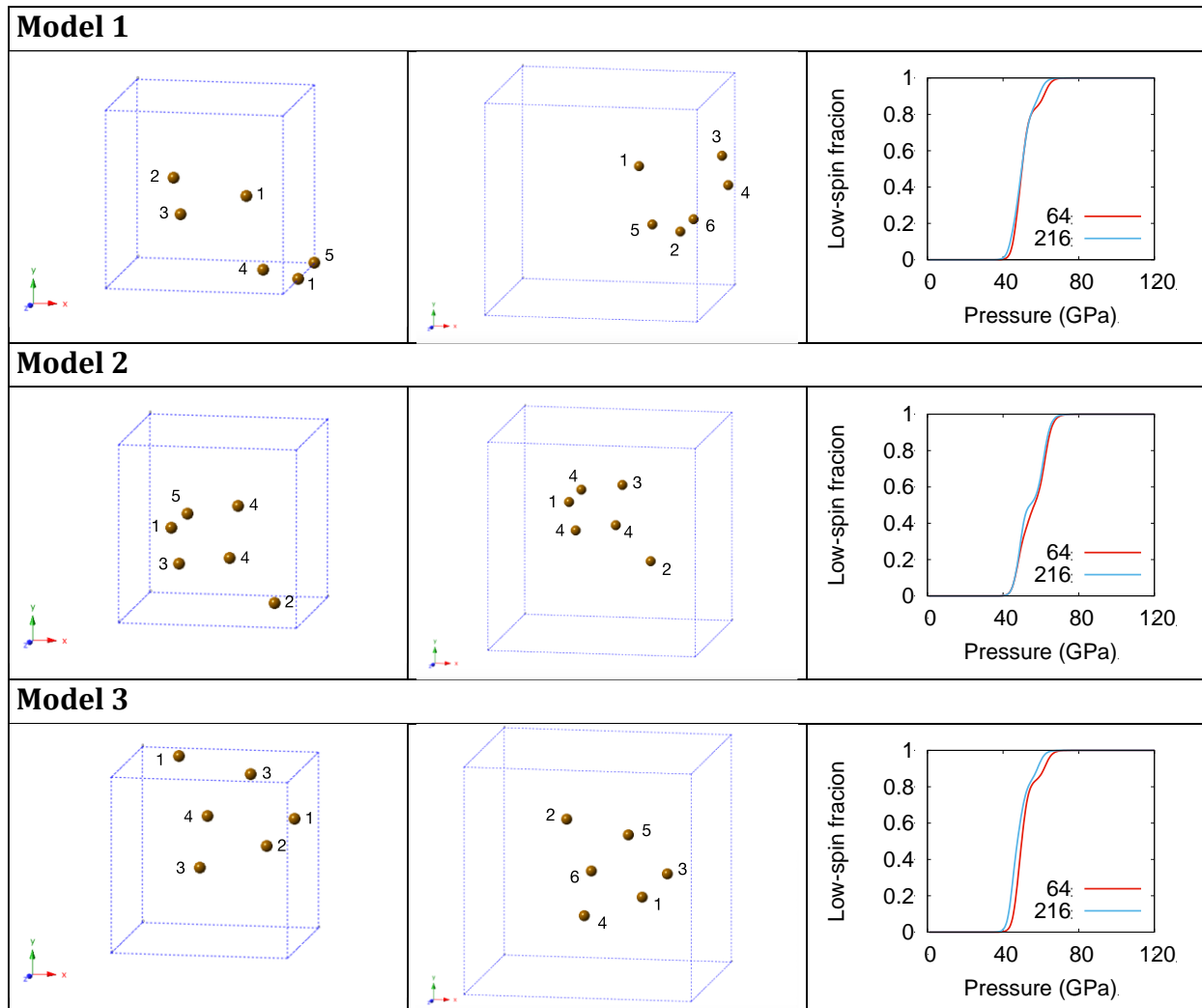
**Model 18**

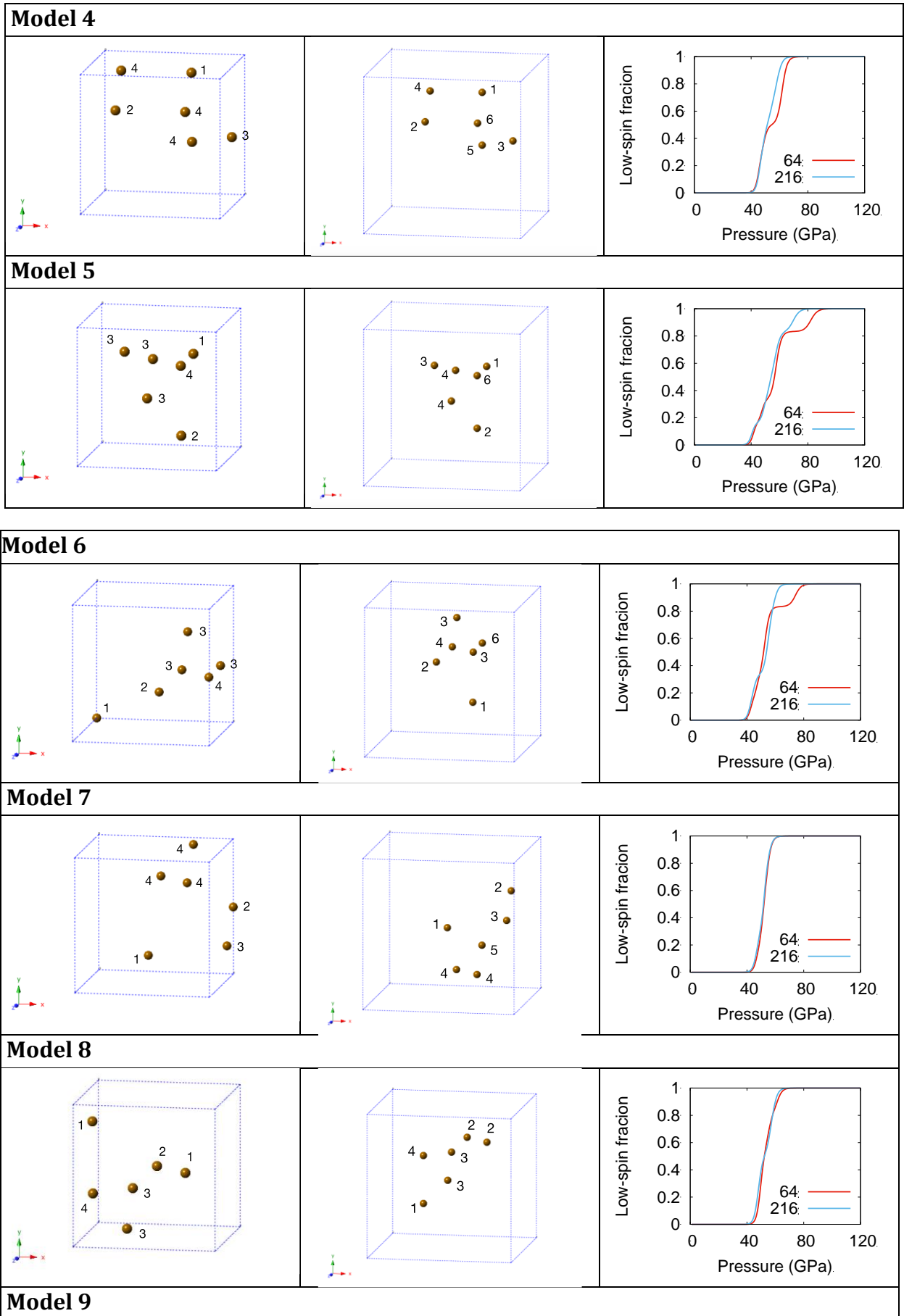


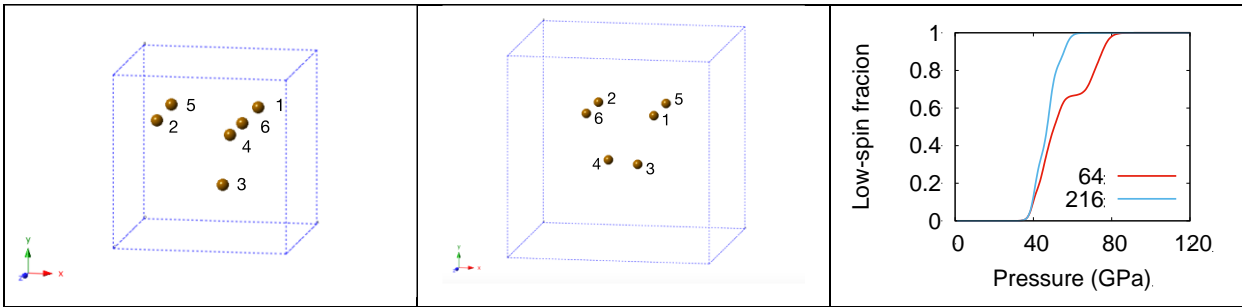
**Model 19**



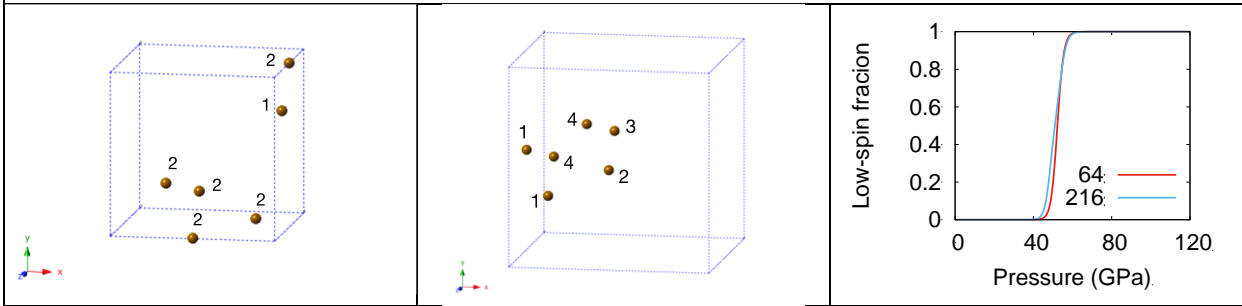
**Table 5.6:** Iron arrangement for 64-atom (left), and 216-atom (middle) models and low-spin fraction at 300K (right), for models with an  $(\text{Mg}_{0.8125}\text{Fe}_{0.1875})\text{O}$  composition. Labels on iron atoms indicate the order that they undergo spin crossover. If iron atoms have the same number it indicates simultaneous spin crossover. Only results for the FM state are shown.



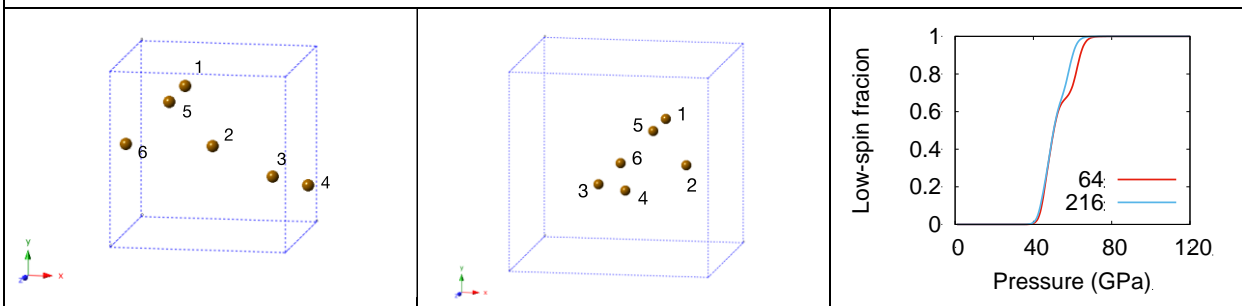




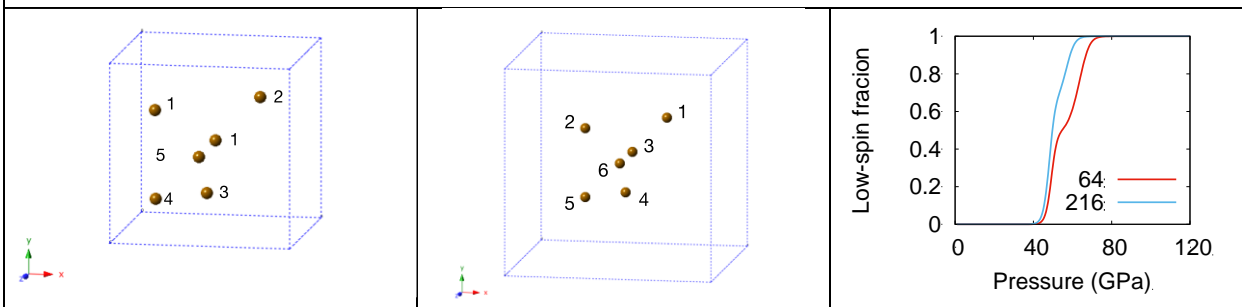
**Model 10**



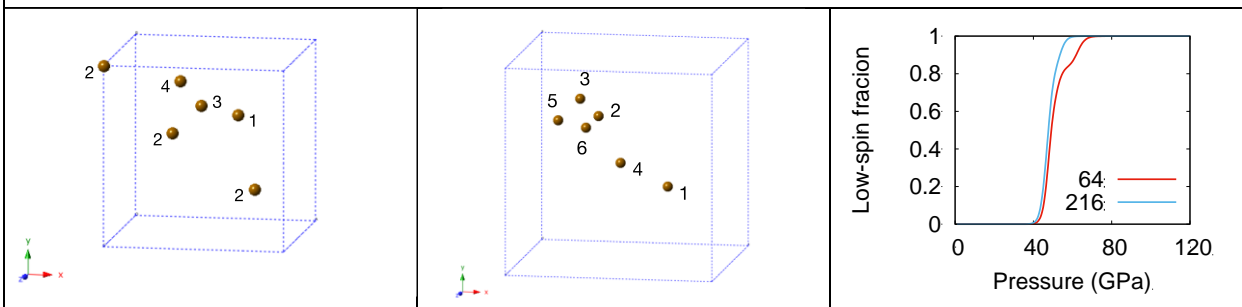
**Model 11**



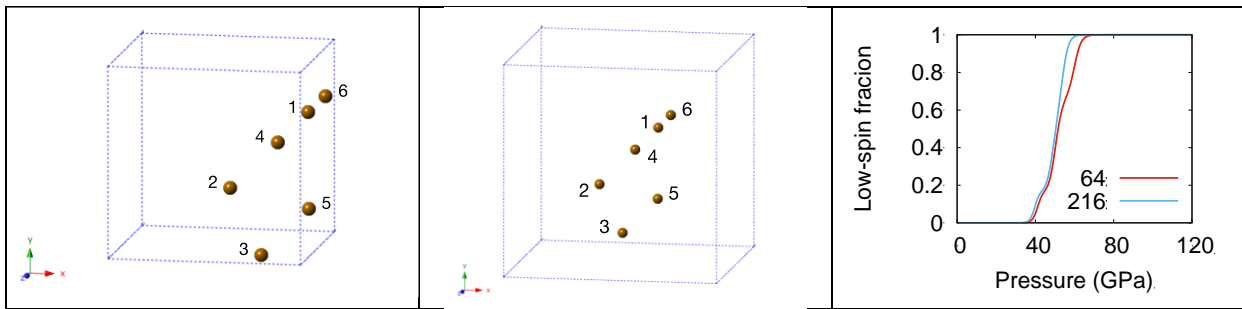
**Model 12**



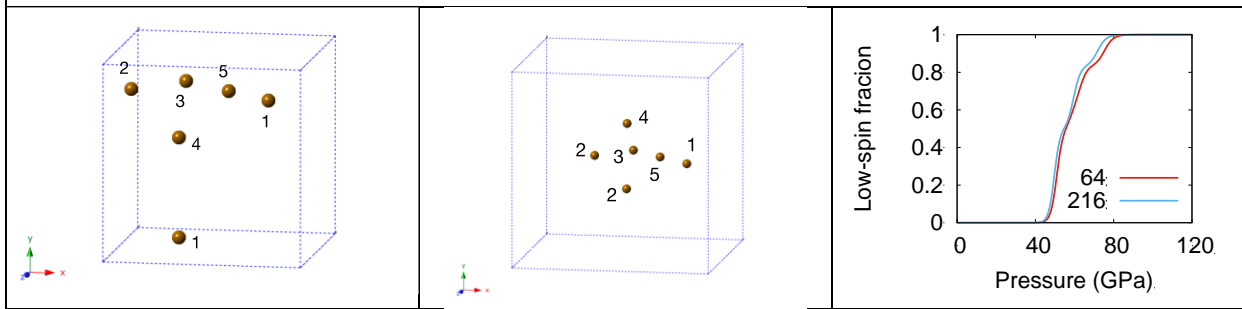
**Model 13**



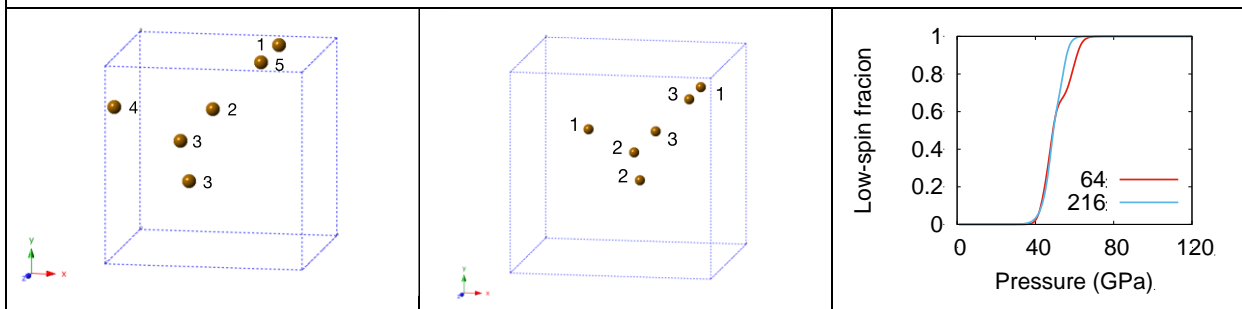
**Model 14**



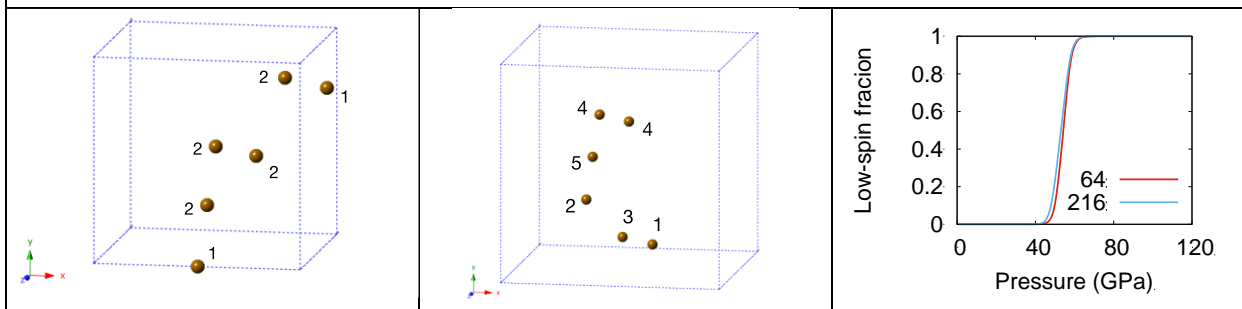
**Model 15**



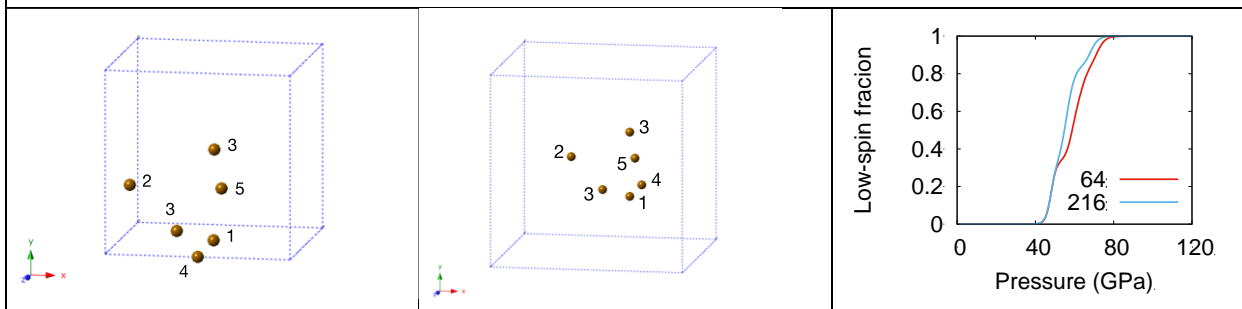
**Model 16**



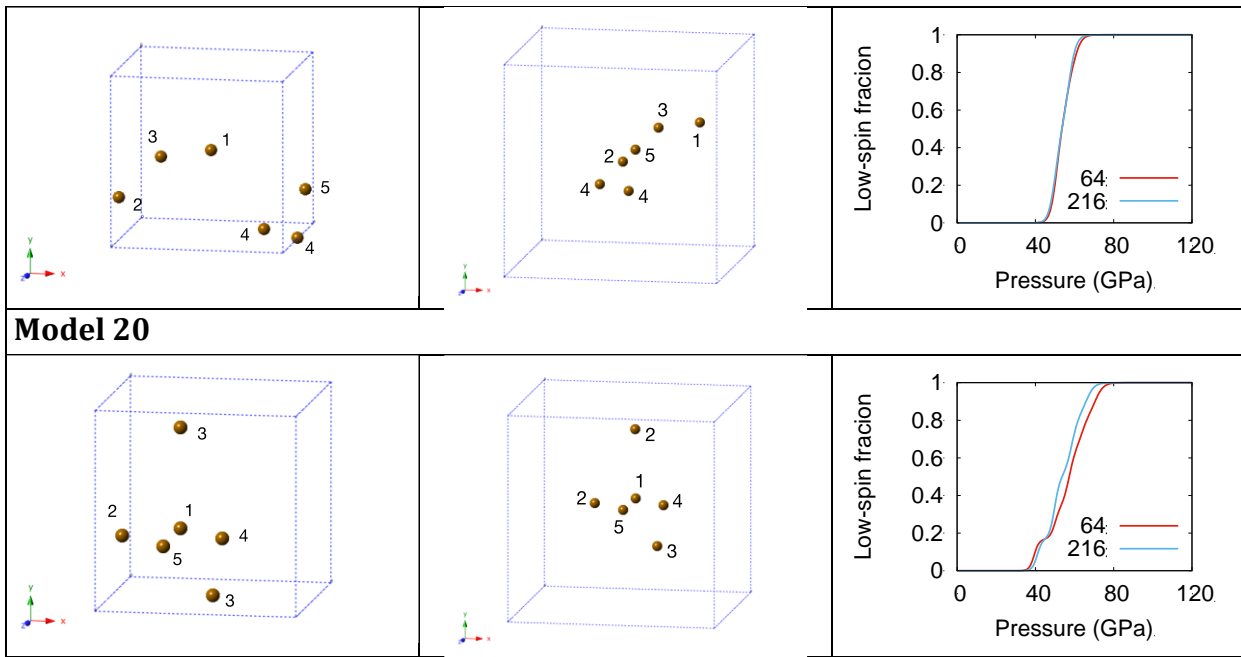
**Model 17**



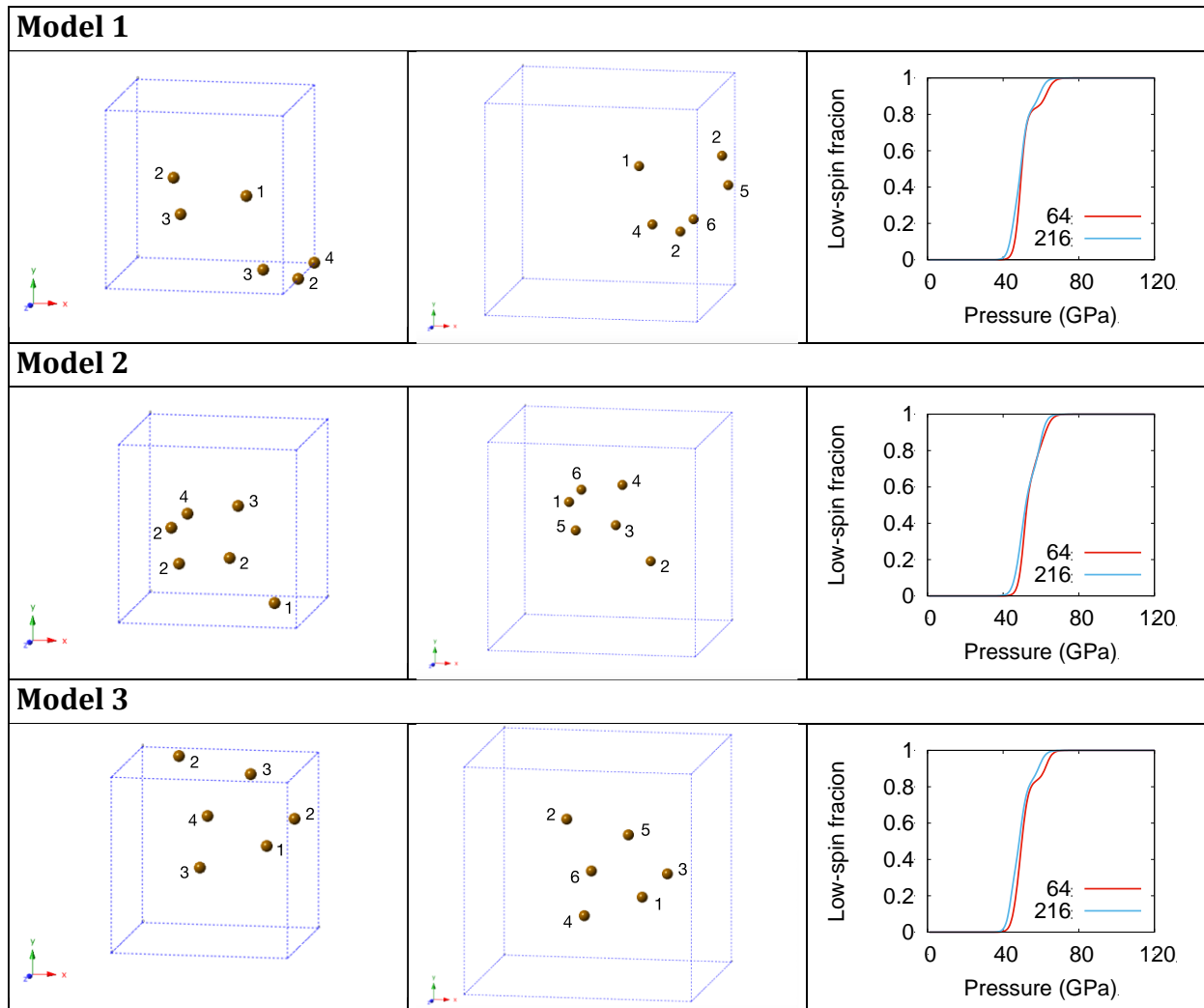
**Model 18**

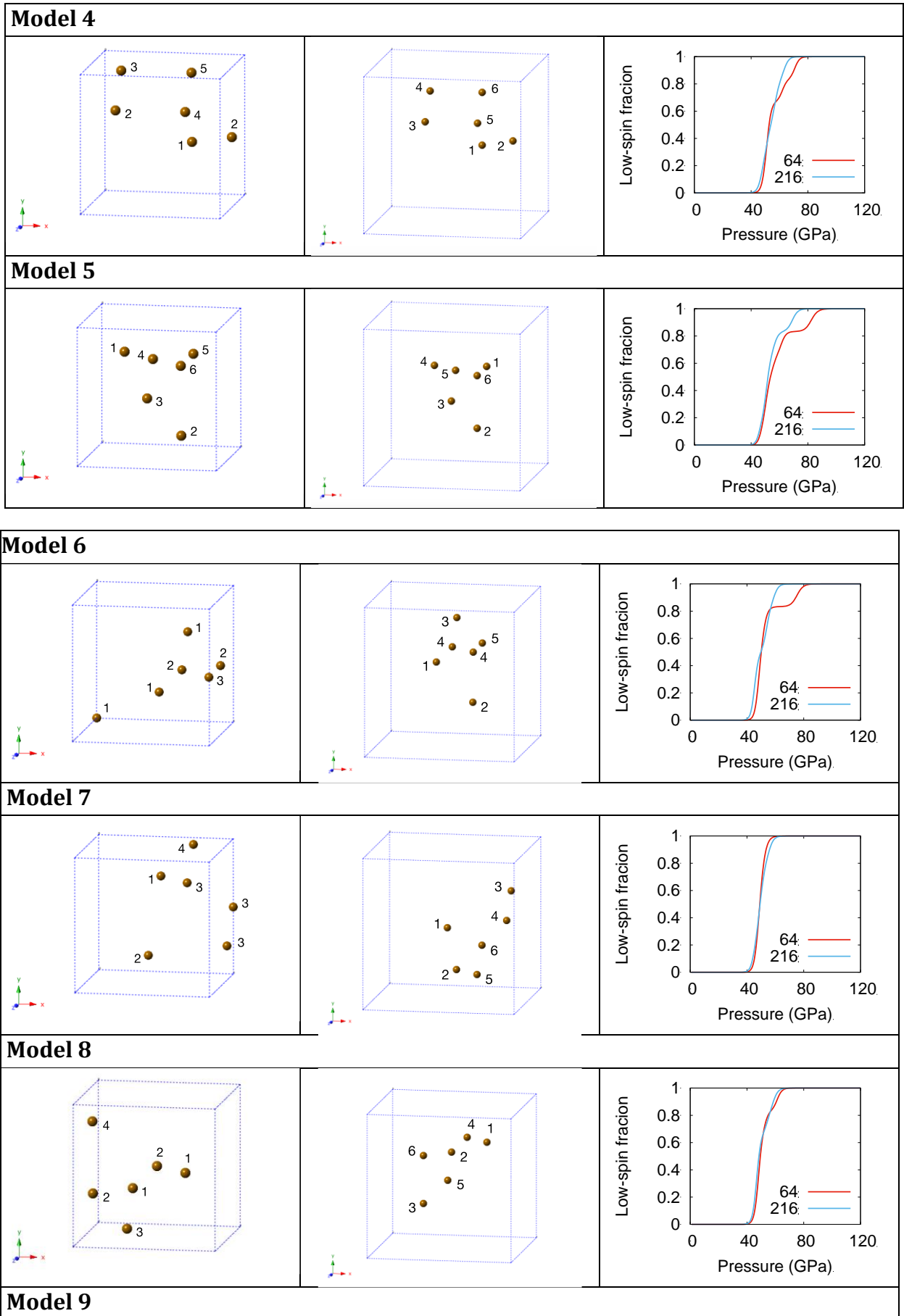


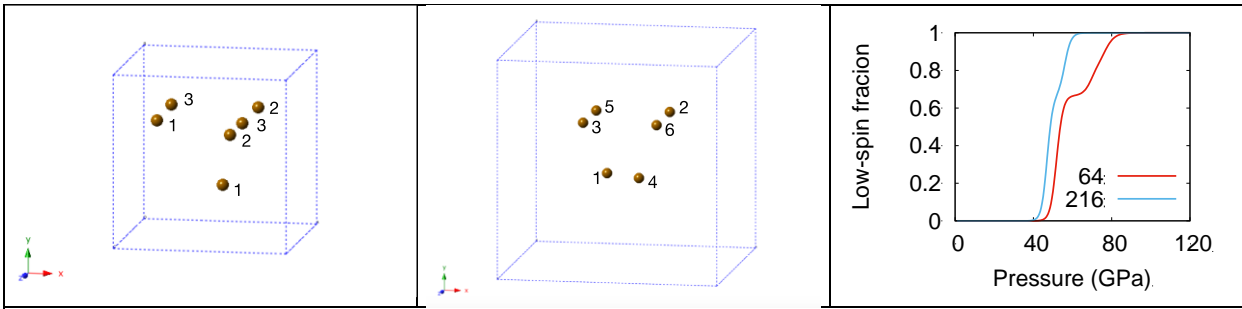
**Model 19**



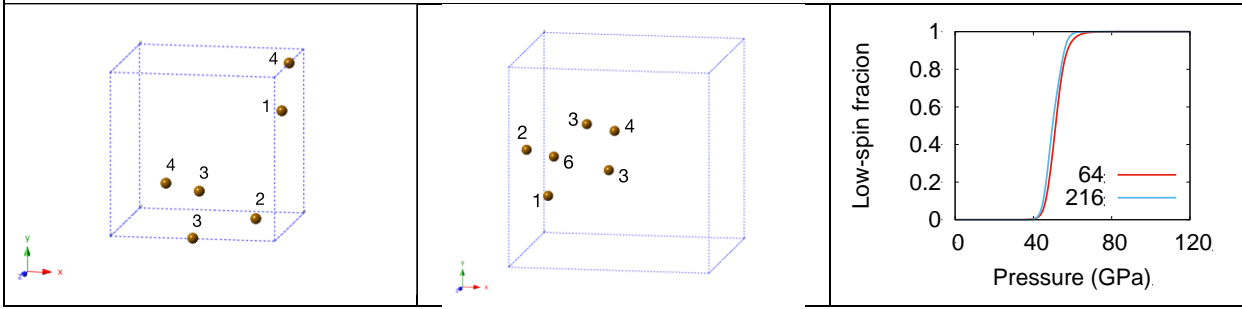
**Table 5.7:** Iron arrangement for 64-atom (left), and 216-atom (middle) models and low-spin fraction at 300K (right), for models with an  $(\text{Mg}_{0.8125}\text{Fe}_{0.1875})\text{O}$  composition. Labels on iron atoms indicate the order that they undergo spin crossover. If iron atoms have the same number it indicates simultaneous spin crossover. Only results for the AFM state are shown.



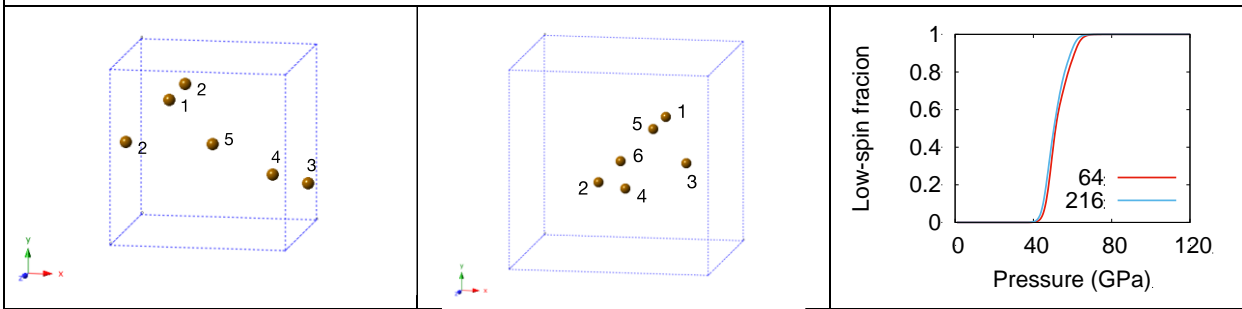




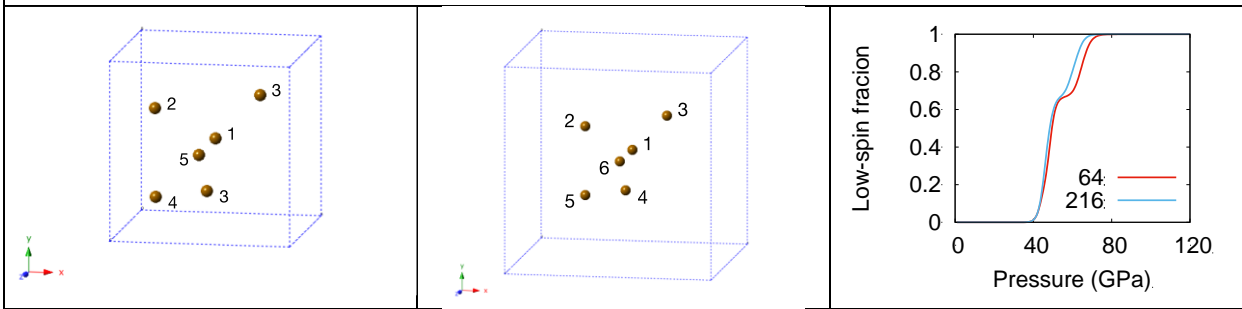
**Model 10**



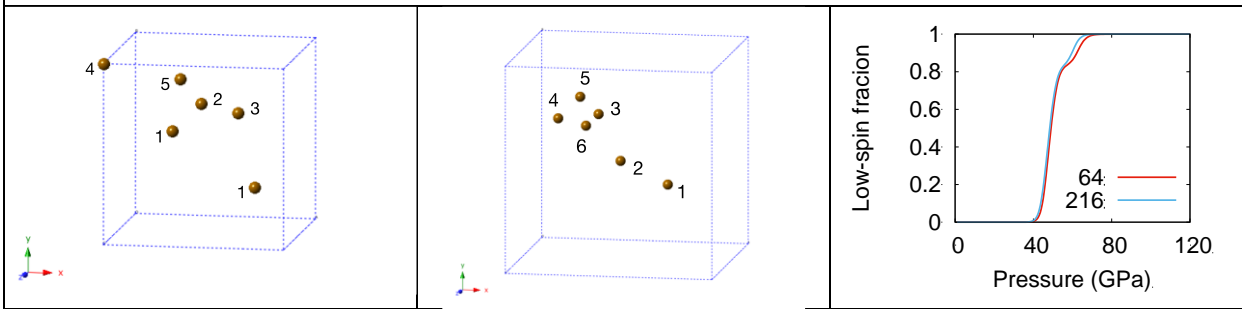
**Model 11**



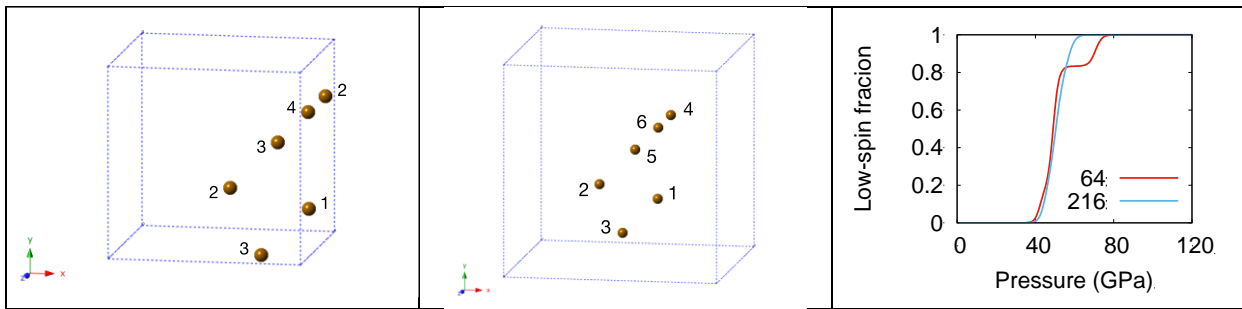
**Model 12**



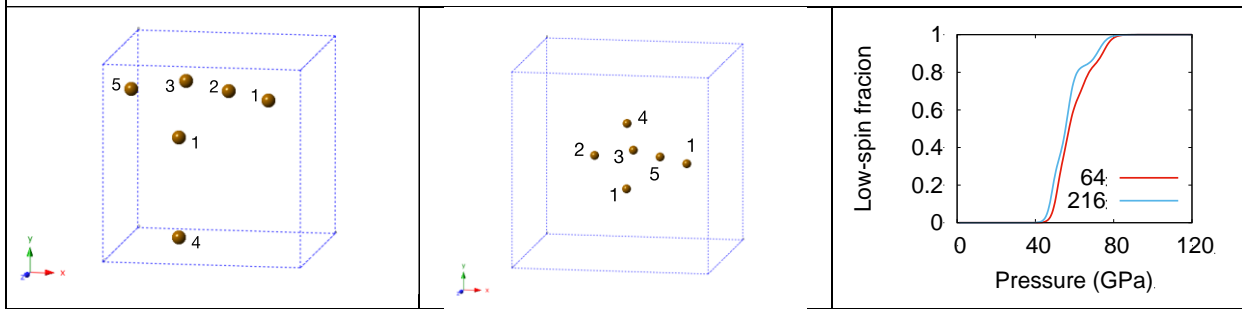
**Model 13**



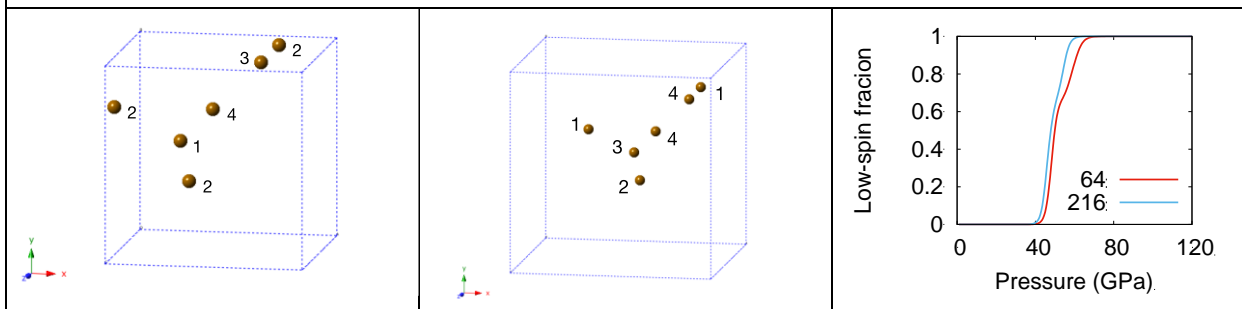
**Model 14**



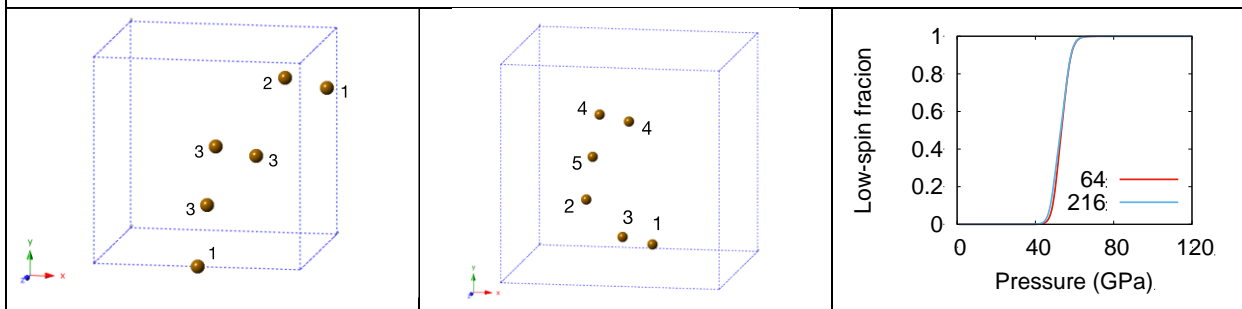
**Model 15**



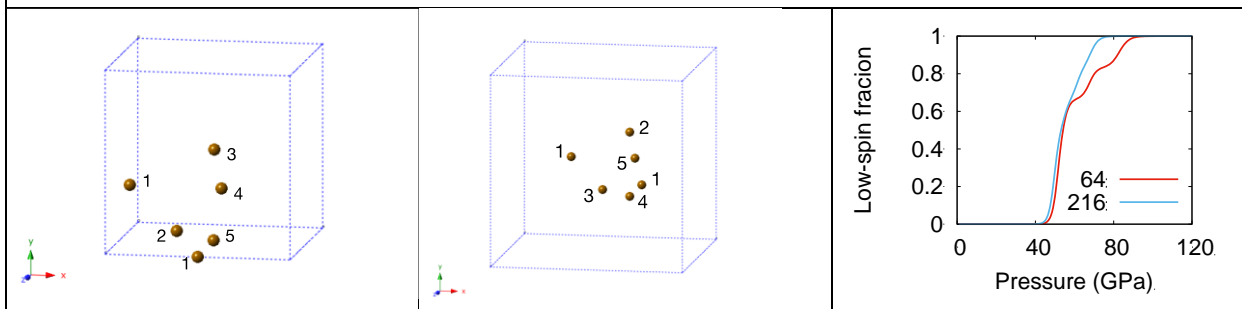
**Model 16**



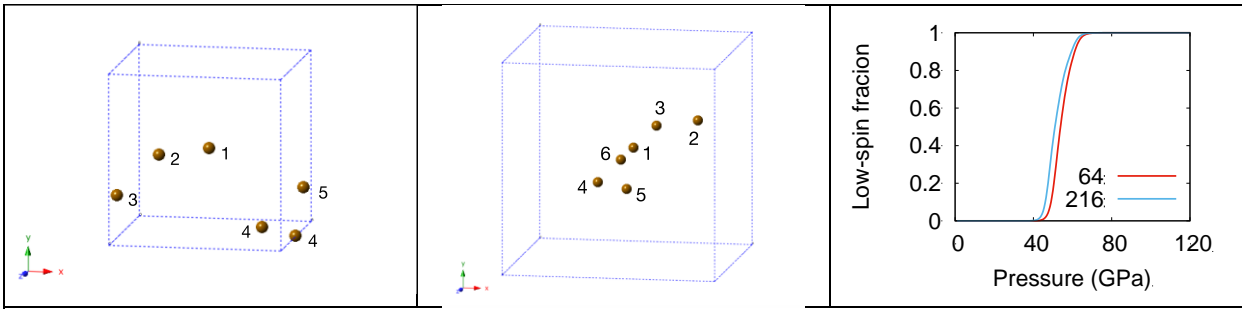
**Model 17**



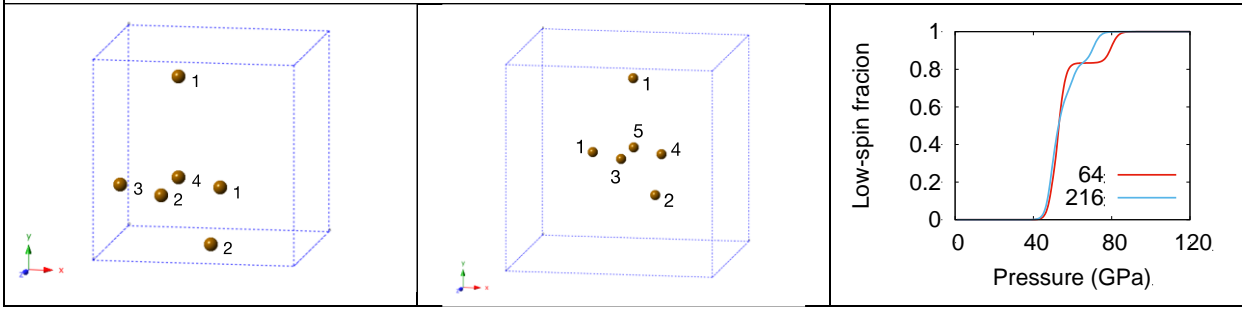
**Model 18**



**Model 19**



**Model 20**



**References:**

Humphrey, W., A. Dalke and K. Schulten (1996). "VMD: Visual molecular dynamics." Journal of Molecular Graphics **14**(1): 33-38.



## Chapter 6

# A resistively-heated dynamic diamond anvil cell (RHdDAC) for fast compression X-ray diffraction experiments at high temperatures

A. S. J. Méndez<sup>1,2</sup>, H. Marquardt<sup>3</sup>, R. J. Husband<sup>1</sup>, I. Schwark<sup>1</sup>, J. Mainberger<sup>1</sup>, K. Glazyrin<sup>1</sup>, A. Kurnosov<sup>2</sup>, C. Otzen<sup>1</sup>, N. Satta<sup>2</sup>, J. Bednarcik<sup>4</sup>, and H.-P. Liermann<sup>1</sup>

<sup>1</sup>Photon Sciences, Deutsches Elektronen-Synchrotron (DESY), 22607 Hamburg, Germany; <sup>2</sup>Bayerisches Geoinstitut BGI, University of Bayreuth, 95440 Bayreuth, Germany; <sup>3</sup>Department of Earth Sciences, University of Oxford, OX1 3AN Oxford, UK; <sup>4</sup>Department of Condensed Matter Physics, Institute of Physics, P.J. Šafárik University, 041 54 Košice, Slovakia

Corresponding author: Alba San José Méndez (alba.mendez@desy.de)

This chapter has been published as:

Mendez et al. (2020) *Rev. Sci. Instrum.* **91**, 073906.<sup>3</sup>

### Abstract

A resistively-heated dynamic diamond anvil cell (RHdDAC) setup is presented. The setup enables dynamic compression of samples at high temperatures by employing a piezoelectric actuator for pressure control and internal heaters for high temperature. The RHdDAC facilitates precise control of compression rates and was tested in compression experiments at temperatures up to 1400 K and pressures of  $\sim 130$  GPa. The mechanical stability of metallic glass gaskets composed of a FeSiB alloy was examined at simultaneous high-pressure/temperature conditions. High-temperature dynamic compression experiments on H<sub>2</sub>O ice and (Mg,Fe)O ferropericlase were performed in combination with time-resolved x-ray diffraction measurements to characterize crystal structures and compression behaviors. The employment of high brilliance synchrotron radiation combined with two fast GaAs LAMBDA detectors available at the Extreme Conditions Beamline (P02.2) at PETRA III (DESY) facilitates the collection of data with excellent pressure resolution. The pressure-temperature conditions achievable with the RHdDAC, combined with its ability to cover a wide range of compression rates and perform tailored compression paths, offers perspectives for a variety of future experiments at extreme conditions.

---

<sup>3</sup> <https://aip.scitation.org/doi/10.1063/5.0007557>

## **6.1 INTRODUCTION**

Diamond Anvil Cells (DACs) are broadly used in (geo-)physics, chemistry, and materials science to explore material properties at extreme conditions of pressure ( $P$ ). The development of membrane-driven DACs and DACs driven by piezoelectric actuators (dynamic DACs, dDACs) has led to an increasing interest in performing experiments under dynamic compression.<sup>1-14</sup> In particular, the recent combination of the dDAC with time-resolved x-ray diffraction experiments at synchrotron sources to study the crystal structure evolution and compression behavior of samples is highly promising. It has been shown that compression rates of  $>100$  TPa/s can be achieved,<sup>15</sup> demonstrating the potential of the dDAC to access compression (strain) rates that bridge the gap between traditional static DAC experiments and dynamic shock/ramp compression measurements. dDACs have been used to study compression-rate dependencies and kinetics of phase transitions,<sup>10,16</sup> probe metastable phases,<sup>4,6</sup> and simulate processes during impact events.<sup>14</sup> Besides the ability to vary compression rates, the dDAC also enables the application of customized compression paths. Recent work applied sinusoidal pressure-oscillations to a solid sample, on top of a base pressure, to measure its elastic response.<sup>17</sup> While these works have proven the potential of the dDAC, experiments have so far been limited to room temperature conditions due to the temperature sensitivity of the piezo actuator driver.

However, to address research questions related to the deep Earth and other planetary bodies, as well as in physics, chemistry and materials sciences, achieving experimental conditions of simultaneous high-pressure ( $P$ ) and-temperature ( $T$ ) is essential. High- $P/T$  experiments with DACs are more complicated because of the high- $T$  degradation of the DACs and the contamination of the sample. A specific example is the experimental challenge encountered in high- $T$  DAC experiments on H<sub>2</sub>O ice. At high temperature, reactions between the H<sub>2</sub>O sample and different metals that are regularly used as gasket materials, pressure markers or as laser absorbers in laser-heated DACs are likely to occur.<sup>18-20</sup> Lin et al. performed in situ high- $P/T$  Raman spectroscopy and synchrotron x-ray diffraction experiments employing static DACs to examine the behavior of H<sub>2</sub>O ice VII in the vicinity of its melting curve.<sup>19</sup> In these experiments, different gasket materials including Re were tested. They observed the appearance of additional Raman peaks at 35 GPa and 1040 K consistent with those of  $\epsilon$ -O<sub>2</sub><sup>21</sup> that may have been formed as a product of H<sub>2</sub>O dissociation induced by a reaction with Re. Similar difficulties were encountered in experiments with lithium in DACs. Frost et al. performed high-temperature dynamic compression across the melting of lithium employing a diamond anvil cell coupled with a gas membrane.<sup>22</sup> Lithium damage to the anvil culets had restricted the  $P$ - $T$  conditions achieved in previous experimental studies. Frost et al. extended the experimental conditions at which lithium had been studied and argued that fast compression permits the experiment to be conducted on a shorter timescale than that of lithium-induced diamond anvil failure. Thus, faster

compression may facilitate the collection of high- $P/T$  x-ray diffraction data in the DAC in cases where the sample is unstable and reacts with the anvils or gasket material.

Here we present a resistively-heated dynamic Diamond Anvil Cell (RHdDAC) developed at the Extreme Conditions Beamline (ECB, P02.2) at PETRA III (DESY). The RHdDAC is able to dynamically compress samples at temperatures up to at least 1400 K. Simultaneous collection of x-ray diffraction data with an excellent pressure resolution is possible by the employment of the GaAs LAMBDA detectors.<sup>23</sup> We discuss applications of the RHdDAC setup to the study of H<sub>2</sub>O ice and (Mg,Fe)O ferropericlaase at high- $P/T$ .

## 6.2 THE HIGH-TEMPERATURE DYNAMIC DIAMOND ANVIL CELL

The RHdDAC setup is based on a modified version of a symmetric piston cylinder type DAC suitable for housing a resistive heater.<sup>24</sup> The DAC is equipped with diamond anvils (type Ia standard design  $x=3.25$  from Almax easyLab) glued to a tungsten carbide seat on the upstream side and a cubic boron nitride (c-BN) seat on the downstream side (Fig. 6.1a). The heating system in the RHdDAC employs rigid graphite heaters, similar to those used previously.<sup>25</sup> The graphite heaters employed in this study have been manufactured at DESY and consist of disks of 11 mm in diameter and 1.2 mm thick with a conical aperture of 104° in the center that allows the heaters to be placed around the diamond-anvils (Fig. 6.1b). In order to prevent heat transport to the cell and electrical insulation, the graphite heaters are isolated from the diamond-anvil-supporting seats by ceramic rings that are glued to the seats with air set cement (OMEGABOND™ 400). The ceramic rings measure 12 mm in diameter and 0.5 mm in height. In contrast to flexible graphite heaters that were used in previous setups,<sup>26-28</sup> the employment of rigid graphite heaters facilitates an easier and cleaner sample loading, in particular when it comes to liquid samples because the gasket can be placed more stably on the diamonds. Type-R thermocouples are mounted on the anvil pavilion close to the tip of the diamonds for temperature measurements (referred to as T1 on the downstream side and T2 on the upstream side). The Rh-Pt alloy has a melting temperature of 1873 K, setting an upper limit for the maximum temperature measurement in the current RHdDAC experiments. The wires of the thermocouples are separately guided out of the heating area through two grooves engraved in the bottom faces of the heaters (Fig. 6.1b). In order to electrically insulate the thermocouples, the wires are coated and fixed to the diamond-anvils with ceramic adhesive (Cotronics Resbond 989 from Polytec PT). The adhesive has a low thermal conductivity of 2.16 W/(m·K) and serves also as a thermal insulator. Two 4.7 mm thick and 68 mm long molybdenum rods with flat tips, are inserted in the DAC through two socket head screws made of aluminum oxide in order to keep the rods electrically insulated from the DAC body. The aluminum oxide screws have a major diameter of 10 mm and an inner diameter of 5 mm through which the rods pass through

## Chapter 6. A RESISTIVELY-HEATED DYNAMIC DIAMOND ANVIL CELL

(Fig. 6.2a). The flat tips of the rods are connected to the stiff graphite heater through sheets of flexible graphite to ensure a good electrical contact with the heaters on both sides. The resulting resistance of the heater is below  $\sim 0.5 \Omega$ . The molybdenum rods are connected to a DC power supply (8V, 220A, Agilent 6671A) through copper connectors (Fig. 6.2b).

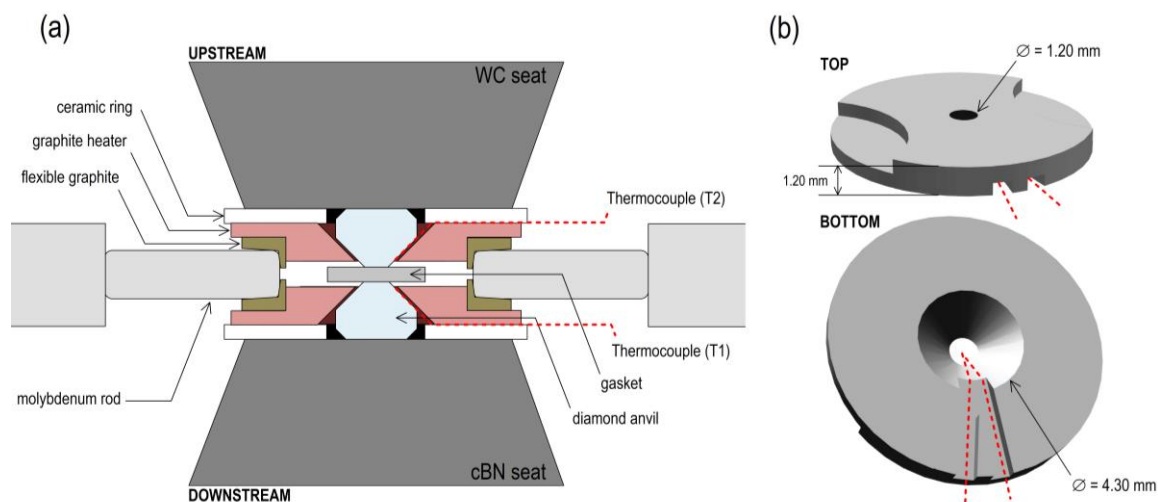


**Figure 6.1:** (a) Cross-section of the inside of the symmetric DAC showing the seated diamond anvils and the heating assembly. (b) 3D illustration of the rigid graphite heater, top and bottom views. The location of the thermocouples is indicated by dashed red lines.

The piezoelectric actuator (PEA) is coupled to the resistively-heated DAC in a similar way as described in Ref. 15. The PEA is enclosed in a hardened stainless-steel case that is open at both ends. The symmetric DAC equipped with the heating system or resistive-heated DAC (hereafter referred to as RHDAC) is inserted into the downstream end by means of a cap with bayonet lock (Fig. 6.2a). The exterior of the cap is connected to a water-cooled aluminium holder (Fig. 6.3a). The upstream end is closed through an end cap with fine threading that is tightened to engage the PEA with the RHDAC and pre-compress the sample if required. We choose a 60 mm long piezo stack actuator with a 9 mm through-hole (PIC255, a modified lead zirconate titanate from PI Ceramic GmbH) that is compliant with the space limitations of the experimental setup at the Extreme Conditions Beamline ECB.<sup>29</sup> The Curie temperature of the chosen piezoelectric material is 350°C, according to the manufacturer specifications. To avoid depolarization of the piezoelectric material, the recommended operating temperature is  $< 50\%$  of the Curie temperature, i.e. 175°C. In order to avoid heating of the PEA above this temperature it is thermally insulated from the RHDAC by a hardened stainless steel plate of 30 mm thickness that is filled with ceramic insulation and encircled by a copper pipe at the interface between the RHDAC and the PEA (Fig. 6.2b). The PEA is connected to an amplifier via a standard high voltage feedthrough (SHV-20 interface). When the PEA expands, it transmits the force to the piston of the RHDAC by pushing on the cooling plate. In addition, a box like water-cooled jacket is placed

around the PEA-housing (Fig. 6.3a). The water-cooled jacket consists of an outer aluminium case that is similar to the RHDAC cooling holder connected to a water chiller that is set to a cooling temperature of 5°C. In order to monitor the temperature in the PEA-housing, two Pt100 temperature sensors were placed on the PEA, close to the interface with the cooling plate (T3), and on the outer part of the cooling jacket (T4).

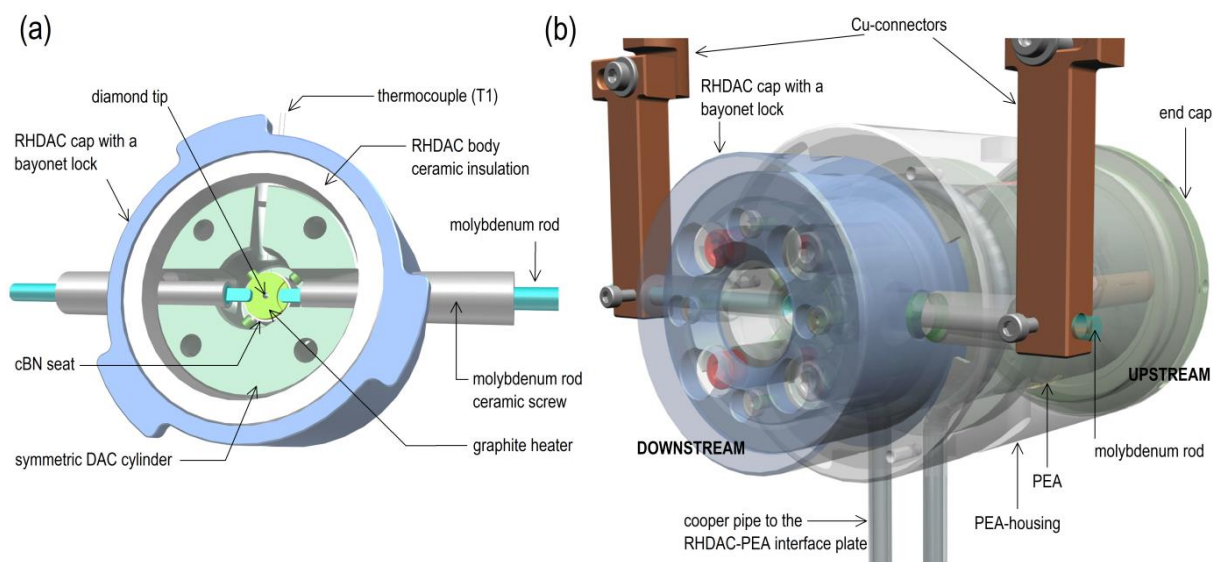


**Figure 6.2:** Illustration of the connection of the DAC to the piezoelectric actuator. (a) Attachment of the symmetric DAC cylinder to the cap with a bayonet lock viewed from above. (b) Attachment of the RHDAC into the PEA-housing viewed from the downstream end.

The RHdDAC assembly is permanently attached to the top lid of a vacuum vessel that was constructed to minimize the heat loss through air convection and avoid oxidation of the setup as well as diamond graphitization. All the electrical connections (T1-T4, copper pins and PEA SHV-20 interface) and water pipes are guided through the lid of the vacuum chamber as shown in Fig. 6.3a. The vacuum vessel consists of a water-cooled stainless-steel chamber with a volume of 4.5 l, equipped with two Kapton windows that are located on the upstream and downstream sides (Fig. 6.3b) to let the incident beam and diffracted x-rays pass. The total weight of the RHdDAC assembly together with the vacuum vessel is about 35 kg.

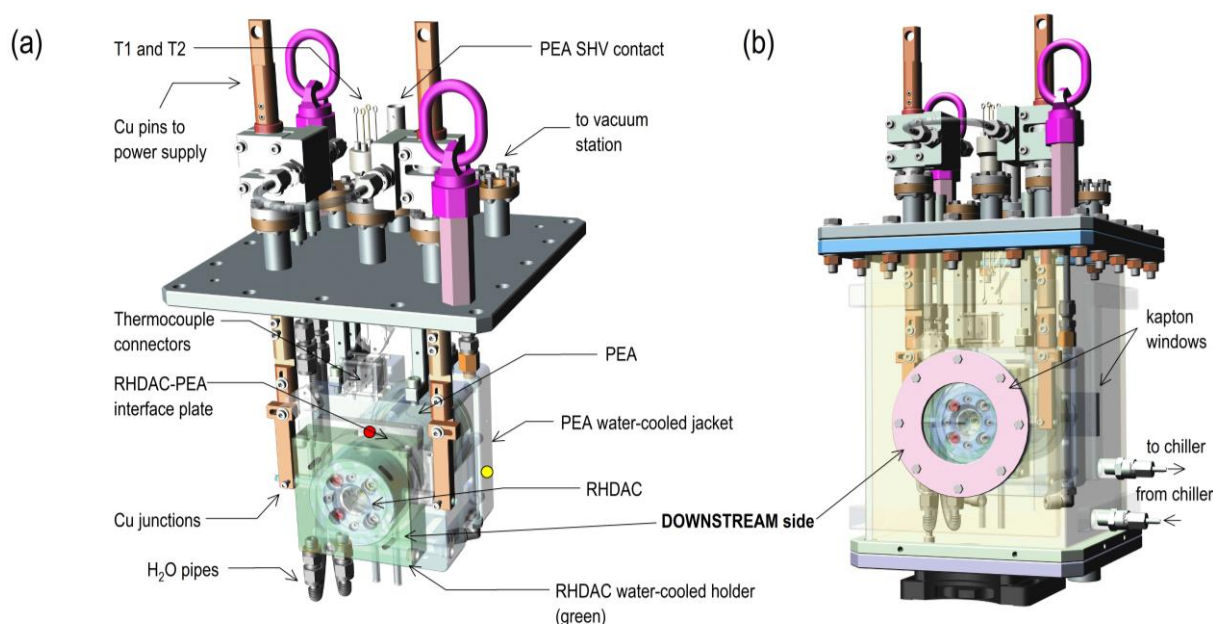


**Figure 6.3:** (a) RHDAC connected to the lid of the vacuum vessel. Red and yellow circles indicate approximate positions of T3 and T4 in the setup, respectively. (b) RHDAC inserted into the vacuum vessel.

### 6.3 EXPERIMENTAL METHOD

Monochromatic synchrotron high-energy radiation was used for time-resolved x-ray diffraction measurements at the Extreme Conditions Beamline P02.2 at PETRA III.<sup>29</sup> The center of the sample chamber was aligned to a Compound Refractive Lenses (CRL) focused x-ray beam of 2 (h)  $\mu\text{m}$  x 8 (v)  $\mu\text{m}$  (FWHM). In order to avoid the emergence of parasitic diffraction peaks due to the low-Z character of the samples in comparison to the high-Z Re gasket, inserts of metallic glass disks in the Re gaskets were employed. 50  $\mu\text{m}$  diameter holes were drilled in a 30  $\mu\text{m}$  thick foil of an amorphous alloy ( $\text{Fe}_{0.79}\text{Si}_{0.06}\text{B}_{0.15}$ ) using a Micro Electric Discharge Machine (EDM). Disks were cut around the holes with an outer diameter of 96  $\mu\text{m}$  employing a laser micromachining tool so that the disks can be inserted in the Re gasket hole of 109  $\mu\text{m}$ . Re and metallic glass are engaged by applying a small pressure with the diamond-anvils. Figure 6.4 shows a metallic glass gasket loaded with H<sub>2</sub>O and Au powder. An integrated diffraction pattern of the sample in comparison to a pattern of the sample loaded in a typical Re gasket is shown in Fig. 6.4b. There is no significant contribution of the amorphous gasket to the background of the diffractogram. Before closing the cell loaded with the sample, the piston cylinder parts of the symmetric DAC are coated with Molykote lubricant paste in order to reduce friction between the cell parts at high temperatures.

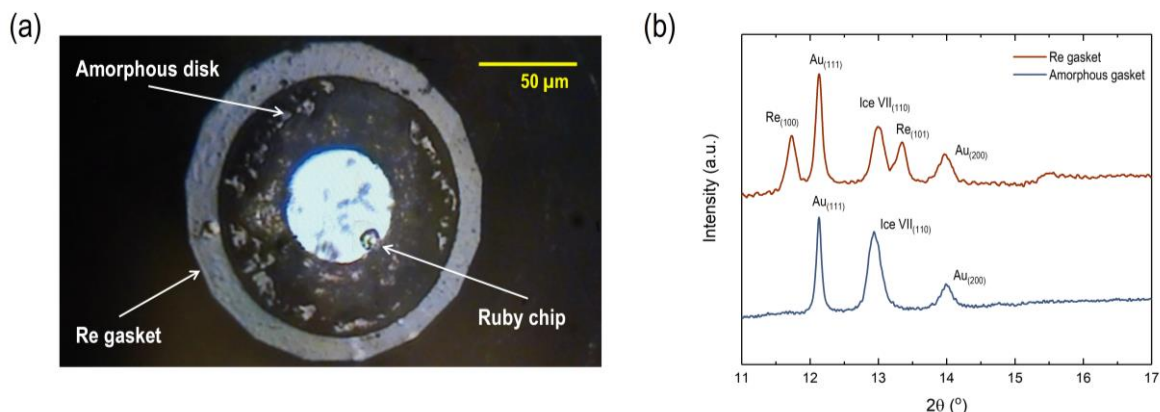


**Figure 6.4:** (a) Picture of the sample chamber in a DAC viewed through the diamond culet. The loaded sample is  $\text{H}_2\text{O}$  along with Au powder. (b) Raw integrated diffraction patterns from two samples containing  $\text{H}_2\text{O}$  ice and Au powder loaded in a Re gasket (top) and an amorphous gasket (bottom). A detector artifact appears in the top pattern as a bump at  $15.5^\circ$ .

Two GaAs 2.3 MPixel LAMBDA detectors were employed to perform fast time-resolved collection of x-ray diffraction images.<sup>23</sup> Each of the detectors can collect x-ray diffraction images at a maximum repetition rate of 2 kHz. The detectors are used simultaneously and positioned in the horizontal on both sides of the incident x-ray beam, with each detector capturing about 20 % of the Debye–Scherrer diffraction rings. Sample to detector distance (SDD) and tilting of the detectors are calibrated using a  $\text{Cr}_2\text{O}_3$  standard from NIST (674b). Different exposure times can be employed on each detector to obtain data sets with different time resolution during the same experiment.

A cartoon showing the control circuit for the RHdDAC setup at the ECB is illustrated in Fig. 6.5 and is similar to that described in Ref. 15. The DC power supply is connected to the graphite heaters and can be controlled remotely from the control room. Temperatures T1 and T2 are measured with a cold junction corrected multimeter (Keithley 3706A) and remotely monitored from the control room. T3 and T4 are read inside the experimental hutch with a data logger (RDXL 6SD from OMEGA) compatible with Pt100 temperature sensors that can display and record temperature as a function of time. The vacuum vessel is connected to a vacuum pump that achieves pressures of  $10^{-5}$  mbar at room temperature in the vessel and keeps the pressure below  $10^{-3}$  mbar throughout the experiment at high temperatures. A water chiller (SL6 from Julabo) is used for cooling of the PEA-housing and the vacuum vessel. The PEA is connected to an amplifier (1000V, 7A; Piezosystem Jena GmbH), which is controlled remotely from the control room through a waveform generator (Agilent 33522B). Arbitrary voltage-time waveforms can be created (*see* Performance and Application) by using the Agilent Benchlink waveform builder software from Keysight and sent to the PEA via the waveform generator.

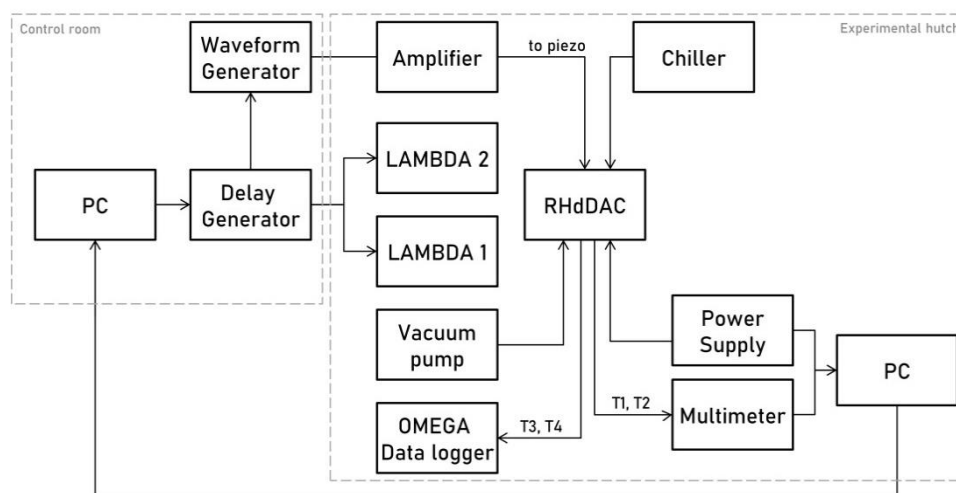
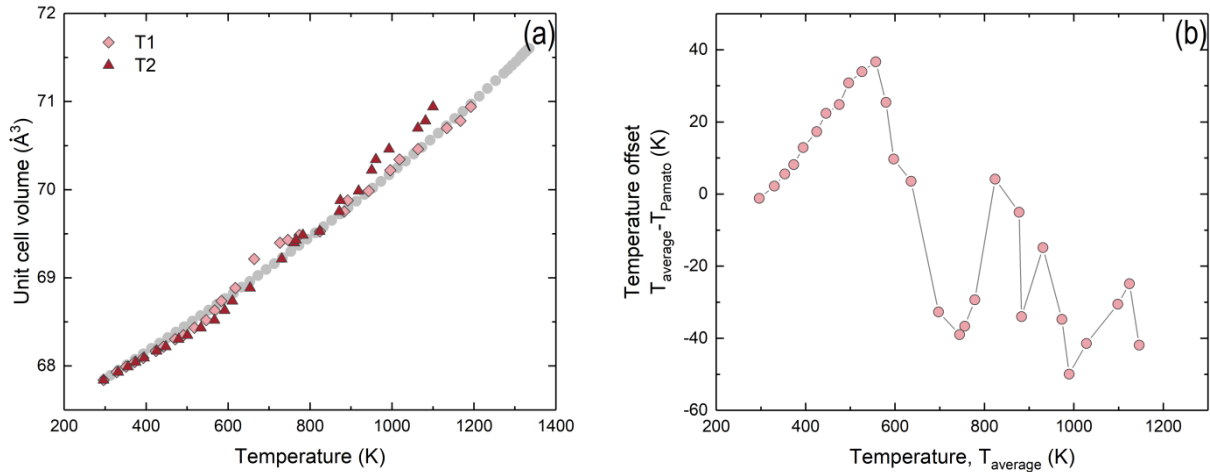


Figure 6.5: Schematics of the experimental setup for RHdDAC experiments at the ECB.

## 6.4 PERFORMANCE AND APPLICATION

### A. Thermal expansion of Au

Even though thermocouples T1 and T2 are placed close to the tip of the diamonds, there may be a temperature difference between the thermocouple reading and the real temperature of the sample. We measured the thermal expansion of Au at room pressure to evaluate a possible temperature offset between the thermocouple readings and the sample. The temperature dependence of the lattice parameter of Au is well described in the literature and it has a melting temperature of 1337 K,<sup>30-32</sup> making it a good temperature standard. Au powder (99.99 % pure from Sigma Aldrich) was loaded into a pre-indented Re gasket with 300  $\mu\text{m}$  culet diamonds, where the sample chamber was only partially filled to avoid pressure increase during heating. The RHdDAC setup was assembled following the described procedure (*see* section III.B) and the end cap was tightened in order to ensure a good contact between PEA and DAC. Two set screws between the piston and cylinder of the DAC prevented any pressure increase at high temperatures. Temperature was increased in 50 K steps up to a maximum temperature of 1200 K and diffraction images were collected after each temperature increment. The unit cell volume of Au was derived from the (111), (200), (220) and (311) reflections and compared to measurements from the literature (Fig. 6.6).<sup>32</sup> Our results indicate a temperature difference smaller than  $\pm 50$  K (Fig. 6.6b), showing that there is an efficient heating of the sample in the RHdDAC.



**Figure 6.6:** (a) Experimental determined unit cell volumes of Au as a function of the temperatures reading from thermocouples T1 and T2 (diamonds and triangles) in comparison with experimental data from Ref. 32 (solid circles). (b) Temperature offset with respect to Ref. 32 as a function of the average temperature of T1 and T2.

#### B. High pressure isotherms across the Ice VII-Ice X stability fields

H<sub>2</sub>O is a major constituent of planetary bodies in the outer Solar System, and a wide range of exoplanets, where it condenses and crystallizes in different forms of ice at high pressures and temperatures. Establishing the boundaries between the different high-pressure phases such as ice VII, ice X and the superionic phase of ice at high temperatures, is of great importance in planetary science. We have explored the capabilities of the RHdDAC by compressing H<sub>2</sub>O ice VII at 450, 625, 865 and 1043 K up to pressures of 110 GPa, i.e. across the stability fields of ice VII, ice X, and possibly in the superionic phase (Fig. 6.7). High pressures were generated by using beveled diamonds with 150 μm diameter culets. Pre-indented Re gaskets were equipped with inserts of metallic glass as described above. Milli-Q H<sub>2</sub>O was loaded in the RHdDAC together with Au powder (99.99% pure from Sigma Aldrich) as a pressure marker and a ruby chip to control the pressure in the sample during pre-compression up to 15 GPa. Temperature was increased in steps of approximately 100 K until reaching the target temperature, collecting diffraction at each step. Pressure significantly increased with temperature in all the experiments possibly due to the overall thermal expansion of the RHdDAC parts. Once the target temperature was reached, the sample was continuously compressed using the PEA actuator, while collecting time-resolved x-ray diffraction data. Trapezoidal voltage-time waveforms were applied with compression rates ranging from 0.1-0.3 GPa/s permitting comparably long exposure times of 500 ms while still achieving an excellent fine stepped pressure coverage with an average pressure spacing of about 0.2 GPa. Each *P-T* path explored in our experiments (Fig. 6.7), including heating to the desired temperature before compressing with the PEA, was completed in about 40 minutes. In RHdDAC experiments, experimental times are limited by the temperature of the PEA and/or sample stability. We noticed that for temperatures below 900 K, the heat transfer to the PEA is

efficiently counteracted by the cooling system, enabling experimental times of several hours. For experiments at temperatures above 900 K, experimental times may be reduced significantly due to a rising temperature of the PEA. Additionally, the contact between heaters and molybdenum rods may change due to deformation during compression causing temperature fluctuations. However, these temperature fluctuations can be easily corrected by slightly re-adjusting the voltage.

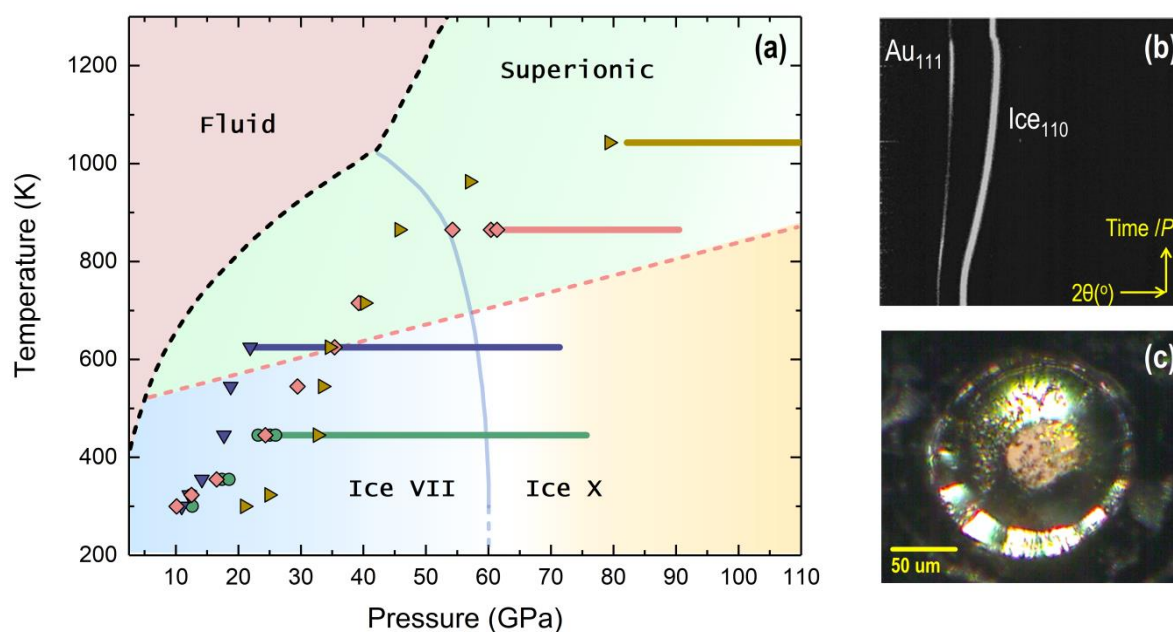


**Figure 6.7:** (a) Experimental conditions reached during the experiments superimposed on the phase diagram of H<sub>2</sub>O. Symbols (triangles, diamonds and circles) represent experimental conditions where diffraction data were collected while increasing the temperature and lines depict the pressure range covered during the dynamic compression at constant  $T$ . Pressure was determined from the (111) diffraction line of gold using published equation of state parameters (Ref. 36). A solid blue line defines the ice VII-ice X boundary from Ref. 33. Dashed pink and black lines define the low temperature superionic phase boundary from Ref. 33 and the melting curve of ice from Ref. 37, respectively. (b) A typical contour plot showing the time-evolution of diffraction patterns (peaks) collected at 625 K; the x-axis represents the diffraction angle ( $2\theta$ ) and the y-axis is time that is related to pressure (Time/ $P$ ). (c) Picture of the sample in the RHDAC after heating up to 1043 K in a metallic glass gasket setup. The sample remained centered during compression indicating that the employed gasket configuration was mechanically stable at high pressures and temperatures.

According to previously determined phase boundaries,<sup>32</sup> the achieved  $P$ - $T$  conditions in our experiments are in the stability field of superionic ice. Data analysis is ongoing in order to confirm the observed H<sub>2</sub>O ice phases in our experiments and their compression behavior. No signs of recrystallization of the metallic glass gasket at the sample-gasket edge were observed in our x-ray diffraction patterns. Furthermore, and in contrast with widely used boron-epoxy amorphous gaskets,<sup>34,35</sup> no reaction products between sample and gasket were detected in our experiments by x-ray diffraction and Raman spectroscopy measurements. The comparably short duration of the experiment may have prevented, or at least significantly reduced, the occurrence

of chemical reactions and/or H<sub>2</sub>O in the solid phases may not be as reactive at high temperatures as suggested previously.<sup>33</sup>

### C. (Mg, Fe)O pressure oscillations under lower mantle conditions

(Mg,Fe)O is the second most abundant mineral in Earth's lower mantle.<sup>38</sup> The characterization of its elastic response is crucial to interpret seismic observations in terms of the mineralogy and dynamics of Earth's deep mantle. Using the RHdDAC, high-temperature pressure oscillation experiments were performed in order to study the elastic response of (Mg<sub>0.8</sub>Fe<sub>0.2</sub>)O ferropericlase and constrain the bulk modulus directly from the collected diffraction data, following the approach outlined in Marquardt et al. (2018).<sup>17</sup> Powder of (Mg<sub>0.8</sub>Fe<sub>0.2</sub>)O was synthesized from stoichiometric mixtures of reagent grade MgO and Fe<sub>2</sub>O<sub>3</sub> treated in a gas-mixing furnace at 1250°C at an oxygen fugacity of 2 log units below the fayalite-magnetite-oxygen (FMQ) buffer.<sup>39</sup> The sample was mixed with fine-grained platinum powder used as a pressure marker (99.99% pure from Sigma Aldrich). A metallic glass disk with a 50 μm hole was inserted in a Re gasket pre-indented to a thickness of 30 μm with 150 μm culet diamonds. The (Mg<sub>0.8</sub>Fe<sub>0.2</sub>)O-Pt mixture was loaded into the gasket hole and pre-compressed to 10 GPa without pressure-transmitting medium. The RHdDAC with the loaded sample was attached to the PEA and the sample was further compressed by 1-2 GPa by tightening the end cap in order to ensure good contact between RHdDAC and PEA. After achieving a good vacuum and stable cooling conditions, the sample was heated up to 1400 K, taking diffraction images every 50 K. At each *P-T* step, four sinusoidal pressure oscillations with a frequency of 0.2 Hz were applied to the sample over a total time of 20 s. Diffraction images were continuously collected by the LAMBDA detectors with single image exposure times of 200 ms. In this experiment, the LAMBDA detectors were positioned off-center with respect to the incident x-ray beam in order to enhance the 2θ range coverage, enabling observation of a larger number of x-ray diffraction lines (Fig. 6.8a). For a preliminary analysis, the strongest peaks, the (200) line of ferropericlase and the (111) line of platinum, were chosen to derive the unit cell volume and the pressure, respectively (Fig. 6.8b). The collected data demonstrate the potential of the RHdDAC to directly quantify the sample's bulk modulus at high-temperature and pressures of the core-mantle-boundary, according to its thermodynamic definition ( $K = -V \cdot \partial P / \partial V$ ).

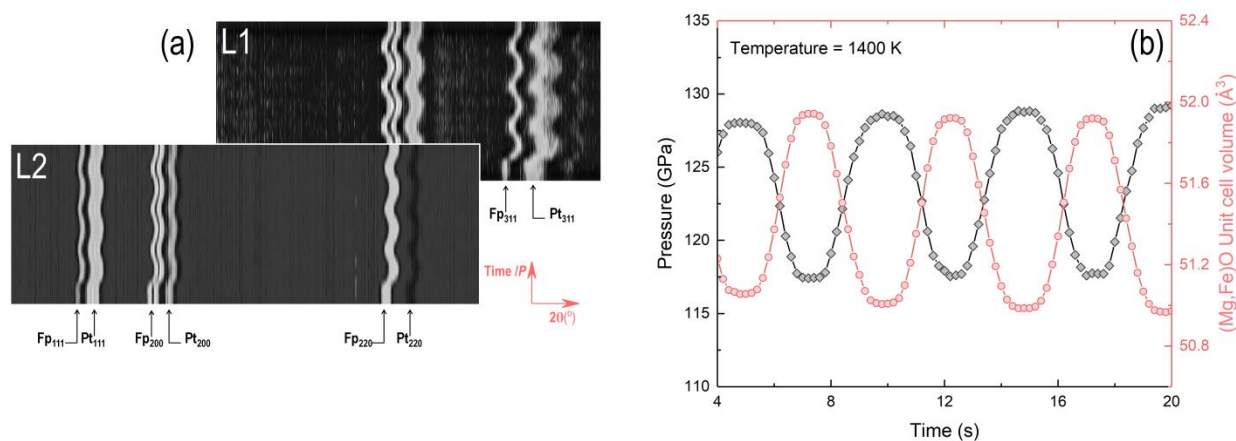


**Figure 6.8:** (a) Contour plots from LAMBDA1 (L1) and LAMBDA2 (L2) showing the oscillating diffraction lines; the x-axis represents the diffraction angle ( $2\theta$ ) and the y-axis is time that is related to pressure (Time / P). (b) Platinum pressure and unit cell volume of ferropericase as a function of time. Pressure was determined using published equation of state parameters (Ref. 36). The response of both phases, platinum and ferropericase, is in phase throughout the duration of the experiment.

## 6.5 CONCLUSIONS

In this paper, we present a resistively-heated piezo actuator-driven DAC (RHdDAC) for compression of samples at temperatures up to 1400 K that was developed at the Extreme Conditions Beamline (ECB), PETRA III (DESY). We demonstrate the current capabilities of the novel setup for time-resolved x-ray diffraction measurements. We used the RHdDAC to explore the phase diagram of  $H_2O$  ice and were able to collect a large amount of x-ray diffraction data over a wide range of  $P$ - $T$  conditions while minimizing the duration of the experiments. Examination of the samples after the experiments suggested that fast compression may inhibit contamination reactions or induced diamond failure processes at high temperatures. We also collected x-ray diffraction data in the (presumably) low spin phase of ferropericase by applying sinusoidal pressure oscillations with a frequency of 0.2 Hz at 1400 K in order to determine the sample's bulk modulus at high temperatures and lowermost mantle pressures. These experiments demonstrate the versatility of the RHdDAC setup. Our experiments further show the potential of metallic glass gasket inserts, which remained mechanically and chemically stable within the explored  $P$ - $T$  range, for x-ray diffraction measurements of low- $Z$  materials. Expansion of the maximum temperature accessible with this setup will be possible by achieving a better understanding of the high- $T$  performance of the PEA and improving its thermal isolation.

## Acknowledgements

This research was supported through the DFG Research Unit FOR 2440 (grant MA4534/5-1). We acknowledge DESY (Hamburg, Germany), a member of the Helmholtz Association HGF, for the provision of experimental facility PETRA III and beamline P02.2. We acknowledge B. Winklers and the BMBF project (reference 05K13RF1) that purchased the laser cutting machine for preparing the gaskets.

## References

- <sup>1</sup> W.J. Evans, C.-S. Yoo, G.W. Lee, H. Cynn, M.J. Lipp, and K. Visbeck, *Review of Scientific Instruments* **78**, 073904 (2007).
- <sup>2</sup> G.W. Lee, W.J. Evans, and C.-S. Yoo, *Proceedings of the National Academy of Sciences* **104**, 9178 (2007).
- <sup>3</sup> J.-Y. Chen and C.-S. Yoo, *Proceedings of the National Academy of Sciences* **108**, 7685 (2011).
- <sup>4</sup> J.-Y. Chen and C.-S. Yoo, *J. Phys.: Conf. Ser.* **377**, 012109 (2012).
- <sup>5</sup> D. Tomasino and C.-S. Yoo, *Appl. Phys. Lett.* **103**, 061905 (2013).
- <sup>6</sup> J.-Y. Chen, M. Kim, C.-S. Yoo, H.-P. Liermann, and W.J. Evans, *J. Phys.: Conf. Ser.* **500**, 142006 (2014).
- <sup>7</sup> Z. Konôpková, A. Rothkirch, A.K. Singh, S. Speziale, and H.-P. Liermann, *Phys. Rev. B* **91**, 144101 (2015).
- <sup>8</sup> S.V. Sinogeikin, J.S. Smith, E. Rod, C. Lin, C. Kenney-Benson, and G. Shen, *Rev. Sci. Instrum.* **86**, 072209 (2015).
- <sup>9</sup> J.S. Smith, S.V. Sinogeikin, C. Lin, E. Rod, L. Bai, and G. Shen, *Rev. Sci. Instrum.* **86**, 072208 (2015).
- <sup>10</sup> C. Lin, J.S. Smith, S.V. Sinogeikin, C. Park, Y. Kono, C. Kenney-Benson, E. Rod, and G. Shen, *J. Appl. Phys.* **119**, 045902 (2016).
- <sup>11</sup> E.-R. Carl, U. Mansfeld, H.-P. Liermann, A. Danilewsky, F. Langenhorst, L. Ehm, G. Trullenque, and T. Kenkmann, *Meteorit Planet Sci* **52**, 1465 (2017).
- <sup>12</sup> E.-R. Carl, H.-P. Liermann, L. Ehm, A. Danilewsky, and T. Kenkmann, *Meteorit Planet Sci* **53**, 1687 (2018).
- <sup>13</sup> A. Černok, K. Marquardt, R. Caracas, E. Bykova, G. Habler, H.-P. Liermann, M. Hanfland, M. Mezouar, E. Bobocioiu, and L. Dubrovinsky, *Nat Commun* **8**, 15647 (2017).
- <sup>14</sup> M. Sims, S.J. Jaret, E.-R. Carl, B. Rhymer, N. Schrodte, V. Mohrholz, J. Smith, Z. Konopkova, H.-P. Liermann, T.D. Glotch, and L. Ehm, *Earth and Planetary Science Letters* **507**, 166 (2019).
- <sup>15</sup> Zs. Jenei, H.P. Liermann, R. Husband, A.S.J. Méndez, D. Pennicard, H. Marquardt, E.F. O'Bannon, A. Pakhomova, Z. Konopkova, K. Glazyrin, M. Wendt, S. Wenz, E.E. McBride, W.

## **Chapter 6. A RESISTIVELY-HEATED DYNAMIC DIAMOND ANVIL CELL**

- Morgenroth, B. Winkler, A. Rothkirch, M. Hanfland, and W.J. Evans, *Review of Scientific Instruments* **90**, 065114 (2019).
- <sup>16</sup> G.W. Lee, W.J. Evans, and C.-S. Yoo, *Phys. Rev. B* **74**, 134112 (2006).
- <sup>17</sup> H. Marquardt, J. Buchen, A.S.J. Mendez, A. Kurnosov, M. Wendt, A. Rothkirch, D. Pennicard, and H.-P. Liermann, *Geophys. Res. Lett.* **45**, 6862 (2018).
- <sup>18</sup> B. Schwager, L. Chudinovskikh, A. Gavriluk, and R. Boehler, *J. Phys.: Condens. Matter* **16**, S1177 (2004).
- <sup>19</sup> J.-F. Lin, *Geophys. Res. Lett.* **32**, L11306 (2005).
- <sup>20</sup> A. Sano, E. Ohtani, T. Kondo, N. Hirao, T. Sakai, N. Sata, Y. Ohishi, and T. Kikegawa, *Geophys. Res. Lett.* **35**, L03303 (2008).
- <sup>21</sup> M. Santoro, E. Gregoryanz, H. Mao, and R.J. Hemley, *Phys. Rev. Lett.* **93**, 265701 (2004).
- <sup>22</sup> M. Frost, J.B. Kim, E.E. McBride, J.R. Peterson, J.S. Smith, P. Sun, and S.H. Glenzer, *Phys. Rev. Lett.* **123**, 065701 (2019).
- <sup>23</sup> D. Pennicard, S. Smoljanin, F. Pithan, M. Sarajlic, A. Rothkirch, Y. Yu, H.P. Liermann, W. Morgenroth, B. Winkler, Z. Jenei, H. Stawitz, J. Becker, and H. Graafsma, *J. Inst.* **13**, C01026 (2018).
- <sup>24</sup> B. Li, C. Ji, W. Yang, J. Wang, K. Yang, R. Xu, W. Liu, Z. Cai, J. Chen, and H. Mao, *Proc Natl Acad Sci USA* **115**, 1713 (2018).
- <sup>25</sup> Z. Du, L. Miyagi, G. Amulele, and K.K.M. Lee, *Review of Scientific Instruments* **84**, 024502 (2013).
- <sup>26</sup> H.-P. Liermann, S. Merkel, L. Miyagi, H.-R. Wenk, G. Shen, H. Cynn, and W.J. Evans, *Review of Scientific Instruments* **80**, 104501 (2009).
- <sup>27</sup> J. Immoor, H. Marquardt, L. Miyagi, F. Lin, S. Speziale, S. Merkel, J. Buchen, A. Kurnosov, and H.-P. Liermann, *Earth and Planetary Science Letters* **489**, 251 (2018).
- <sup>28</sup> J. Immoor, H. Marquardt, L. Miyagi, S. Speziale, S. Merkel, I. Schwark, A. Ehnes, and H.-P. Liermann, *Review of Scientific Instruments* **91**, 045121 (2020).
- <sup>29</sup> H.-P. Liermann, Z. Konôpková, W. Morgenroth, K. Glazyrin, J. Bednarčík, E.E. McBride, S. Petitgirard, J.T. Delitz, M. Wendt, Y. Bican, A. Ehnes, I. Schwark, A. Rothkirch, M. Tischer, J. Heuer, H. Schulte-Schrepping, T. Kracht, and H. Franz, *J Synchrotron Rad* **22**, 908 (2015).
- <sup>30</sup> O.L. Anderson, D.G. Isaak, and S. Yamamoto, *Journal of Applied Physics* **65**, 1534 (1989).
- <sup>31</sup> R.O. Simmons and R.W. Balluffi, *Phys. Rev.* **125**, 862 (1962).
- <sup>32</sup> M.G. Pamato, I.G. Wood, D.P. Dobson, S.A. Hunt, and L. Vočadlo, *J Appl Crystallogr* **51**, 470 (2018).
- <sup>33</sup> E. Sugimura, T. Komabayashi, K. Ohta, K. Hirose, Y. Ohishi, and L.S. Dubrovinsky, *The Journal of Chemical Physics* **137**, 194505 (2012).
- <sup>34</sup> J.-F. Lin, J. Shu, H. Mao, R.J. Hemley, and G. Shen, *Rev. Sci. Instrum.* **74**, 6 (2003).

- <sup>35</sup> A.D. Rosa, M. Merkulova, G. Garbarino, V. Svitlyk, J. Jacobs, Ch.J. Sahle, O. Mathon, M. Munoz, and S. Merkel, *High Pressure Research* **36**, 564 (2016).
- <sup>36</sup> Y. Fei, A. Ricolleau, M. Frank, K. Mibe, G. Shen, and V. Prakapenka, *Proceedings of the National Academy of Sciences* **104**, 9182 (2007).
- <sup>37</sup> A.F. Goncharov, C. Sanloup, N. Goldman, J.C. Crowhurst, S. Bastea, W.M. Howard, L.E. Fried, N. Guignot, M. Mezouar, and Y. Meng, *The Journal of Chemical Physics* **130**, 124514 (2009).
- <sup>38</sup> T. Irifune and T. Tsuchiya, in *Treatise on Geophysics* (Elsevier, 2015), pp. 33–60.
- <sup>39</sup> H. Marquardt and L. Miyagi, *Nature Geosci* **8**, 311 (2015).



## **Eidesstattliche) Versicherungen und Erklärungen**

(§ 9 Satz 2 Nr. 3 PromO BayNAT)

Hiermit versichere ich eidesstattlich, dass ich die Arbeit selbstständig verfasst und keine anderen als die von mir angegebenen Quellen und Hilfsmittel benutzt habe (vgl. Art. 64 Abs. 1 Satz 6 BayHSchG).

(§ 9 Satz 2 Nr. 3 PromO BayNAT)

Hiermit erkläre ich, dass ich die Dissertation nicht bereits zur Erlangung eines akademischen Grades eingereicht habe und dass ich nicht bereits diese oder eine gleichartige Doktorprüfung endgültig nicht bestanden habe.

(§ 9 Satz 2 Nr. 4 PromO BayNAT)

Hiermit erkläre ich, dass ich Hilfe von gewerblichen Promotionsberatern bzw. –vermittlern oder ähnlichen Dienstleistern weder bisher in Anspruch genommen habe noch künftig in Anspruch nehmen werde.

(§ 9 Satz 2 Nr. 7 PromO BayNAT)

Hiermit erkläre ich mein Einverständnis, dass die elektronische Fassung meiner Dissertation unter Wahrung meiner Urheberrechte und des Datenschutzes einer gesonderten Überprüfung unterzogen werden kann.

(§ 9 Satz 2 Nr. 8 PromO BayNAT)

Hiermit erkläre ich mein Einverständnis, dass bei Verdacht wissenschaftlichen Fehlverhaltens Ermittlungen durch universitätsinterne Organe der wissenschaftlichen Selbstkontrolle stattfinden können.

Bayreuth, 18. November 2020,

.....

